Hydroelastic waves and their interaction with fixed structures

Paul Brocklehurst

Thesis submitted for the degree of Doctor of Philosophy

School of Mathematics
University of East Anglia
Norwich, NR4 7TJ
England

September 2012

Abstract

A selection of problems are presented which study the interaction of hydroelastic waves with fixed structures. A thin floating elastic plate model is considered which primarily represents a continuous floating ice sheet, but may also be applied to very large floating platforms. The incident hydroelastic waves are assumed to either propagate from long–distance towards the structures or be generated by a moving load. All aspects of the subsequent interaction are studied in detail. The elastic plate is clamped to the fixed vertical structures to model an ice sheet frozen to the structure boundary.

Both linear and nonlinear formulations are admitted for a selection of two– and three–dimensional problems. For the linear problems, selection of appropriate integral transforms leads to explicit analytical solutions in terms of integral quadratures. For the nonlinear case, the numerical solution is found by application of Green's second identity combined with a boundary element method. The resulting deflection fields are analysed as well as the strain in the ice sheet due to curvature from the hydroelastic waves. Particular attention is paid to the strain at the ice–structure boundary. The integral transforms also lead to concise expressions for the horizontal and vertical wave forces impacting on the structure. It is shown that these forces may reach a substantial magnitude and must be taken into account for the design of structures in ice–covered water.

Several assumptions are utilised which allow the problems to be mathematically treatable while retaining accuracy. Realistic effects such as viscoelasticity and fluid stratification are studied. The solutions are investigated in detail under the variation of physical parameters of the fluid, the ice sheet and the incident/load–generated waves, based on realistic values from cold climate regions.

Acknowledgements

There are several people I would like to thank for their contribution to the thesis. My primary supervisor, Alexander Korobkin, never failed to instantly provide the perfect solution to any problems I encountered. This has led to my belief in his mathematical omniscience. In addition, his enthusiasm for the subject and affable manner made him a privilege to work with. My secondary supervisor, Emilian Părău, was invaluable: he is a talented and dedicated mathematician whose door was always open for guidance. I could not have asked for a better supervisory team and I've learned a great deal from them both. I would also like to acknowledge Luke Bennetts and Michael Meylan for their comments and advice at various conferences. Mark Cooker's revision of the thesis was extremely thorough and helpful.

I will always have fond memories of my PhD experience in Norwich, largely due to the excellent company of Matt, Ben M., Ben H., Nina & Vicky. I enjoyed every minute of house–sharing with Rob. I am extremely thankful for Hannah's support and companionship. My parents are wonderful people to whom I owe tremendous gratitude.

Contents

Chapter 1

Introduction

1.1 Preliminaries

That waves exist in ice sheets is a surprising revelation for some, owing to the misconception that ice is rigid. In fact, the ice cover of the Arctic Ocean has been shown to be in almost perpetual motion. The constant swell, ebb, and flow of the ocean upon which the ice rests causes small–amplitude waves to propagate through the ice sheet. The study of the behaviour of ice has a long and fascinating history, but the naturally emerging trend is the consideration of ice as an elastic material. Development of this elastic theory allowed the fluid-ice interaction to become well understood, and the literature available is now rich and diverse. However, fewer studies are available on the interaction of these "hydroelastic" waves with rigid structures. This thesis is concerned with such interactions, driven by the expected need for offshore wind farms, drilling rigs and oil/gas platforms to be built in ice–covered waters, among other applications.

The introduction is arranged as follows. Section 1.2 summarises the progress thus far in the field with a literature review. It is arranged in a roughly chronological order, with some effort to group similar topics. Focus here is more on the subject matter rather than the solution methodology, which is discussed further in Section 1.3. Section 1.4 explains some theoretical assumptions utilised within the thesis with justification for their usage. Section 1.5 presents an outline of each chapter within the thesis, accompanied by more specific literature discussion. Section 1.6 discusses the intended applications of each chapter, as well as expanding on the more general applications of hydroelasticity.

1.2 Literature review

The first foray into the field is widely accredited to Greenhill (1887) as far back as the 19th century. He considered an elastic beam resting on fluid of finite depth, even describing the dispersion of ice–coupled waves. The idea was later extended by Ewing & Crary (1934), beginning a series of papers that experimentally studied

flexural waves in expansive ice sheets. Some earlier models of wave-ice interaction were simplified "mass–loading" models that did not account for the elastic or inelastic behaviour of the ice. Weitz & Keller (1950) and Peters (1950) were among such studies, treating the ice sheet as a disconnected set of mass points on the surface. Such models were considered to be fundamentally flawed and were thus superseded by the elastic counterpart. Stoker (1957) studied surface gravity wave interaction with a thin floating elastic sheet, though the equations assumed a shallow water model. Kouzov (1963a) studied acoustic waves propagating through compressible fluid bounded by two thin elastic plates. In an innovative study Kouzov (1963b) also solved the problem of hydroelastic wave diffraction at a crack in an elastic plate. One of the early attempts to model ocean wave penetration into sea ice is given by Hendrickson & Webb (1963).

Meanwhile, various experiments were undertaken, verifying the presence of waves in ice sheets. Press & Ewing (1951); Press et al. (1951); Oliver et al. (1954), in a series of experiments, created ice–coupled waves artificially. Hunkins (1962) conducted experiments at four drifting research stations, detecting waves of long period 15–60 seconds. The waves had small–amplitude and long wavelengths, and it was concluded that such waves propagate with little attenuation throughout the Arctic. Robin (1963) conducted shipborne wave recorder experiments in the Weddell sea, and similar conclusions were drawn as to the period and amplitude of waves and their penetration into large sheets of ice. Wadhams (1972) also conducted experiments on ice wave attenuation; in this case measurements were obtained by upwards sonar from a submarine.

Considered by many as a pioneering study in usage of the thin-elastic plate model, Evans & Davies (1968) fully solved problem of wave reflection and transmission by a semi–infinite elastic plate in finite water. This work is a somewhat obscure technical report, originally intended to have military applications, but is often accredited for kick–starting the subsequent fervour in the field. They treated the problem as time–harmonic, but the explicit solution was too complex to be computed. The authors were forced to resort to a shallow–water approximation.

Much of the theory regarding waves in ice sheets has spawned from studies in the Marginal Ice Zone (MIZ). This is an area at the intersection of ice fields and open ocean where the ice is not continuous, but rather made up of smaller ice floes. The interaction of these smaller floes with incoming ocean waves, and indeed the interaction of the floes with each other, has been studied extensively. While not directly related to this thesis, which considers continuous ice, studies regarding this topic were instrumental in establishing hydroelastic theory. Early measurements in the MIZ were conducted by Wadhams (1975), who used airborne laser profiling to measure swell. The response of a single ice floe to swell were measured by Squire & Martin (1980) and Goodman et al. (1980).

The accompanying hydroelastic theory was being developed in tandem, led by such authors as Squire; the works of Squire (1984c,d,b,a) being excellent examples.

The dispersion relations considered here were more detailed than in previous work in the field. Bates & Shapiro (1980) studied long–period waves in an ice cover, using the elastic plate model. Several studies were also under way in Russia, Timokov & Kheisin (1987) being one example. Studies concerned with the complicated interactions in the MIZ became more common: works concerning the breakup of ice floes are found by Squire & Martin (1980) and Goodman et al. (1980). Work concerning floe collision is given by Martin & Becker (1987, 1988), Crocker (1992) and Rottier (1992).

In an important series of papers, Fox & Squire (1990, 1991b, 1994) studied waves at the sea–ice boundary. They were the first authors to correctly match the potentials across the boundary, superseding earlier work which was incompletely matched. The thin plate equation was utilised, now thoroughly established as the optimal model for the ice cover. The model assumes that the velocity potential is periodic and can be expressed in terms of time–independent part, which many future papers adopted. The reflection and transmission coefficients, describing the wave energy reflected and transmitted by the ice relative to the incident free–surface wave, were studied for various parameters. In a related model, Meylan & Squire (1993a,b) solve the finite–length floe version of this problem, using a different solution methodology. The model predicted perfect transmission for certain values of the ice wavelength and floe diameter. The problem was later solved for finite depth (Meylan & Squire, 1994).

No hydroelastic literature review is complete without reference to the study of moving loads on an ice sheet. Such studies have a plethora of applications, discussed in Section 1.6. Wilson (1958) pioneered the theoretical treatment of moving loads on ice sheets, and Kerr (1976) gives an early review of the research on this topic. Experiments were conducted by Takizawa (1985) and Squire et al. (1988). The theory was further developed by Davys et al. (1985) and later Schulkes et al. (1987). Schulkes & Sneyd (1988) considered the time–dependent version of the problem, with most earlier work assuming periodic motion. Hosking et al. (1988) introduces viscoelasticity in an attempt to better match the theory with experiments. The problem was later revisited in three–dimensions by Milinazzo et al. (1995), and by Părău & Vanden-Broeck (2011) to incorporate nonlinear effects. In addition, Duffy (1996) studied the generation of internal ocean waves at the interface of a two–layer fluid by a moving load on an ice sheet. The comprehensive book by Squire et al. (1996) studies the subject in greater detail.

Primarily the above papers utilised the standard thin elastic plate model, outlined later in Section 1.4. Others attempted to incorporate the more inhomogeneous aspects of ice. Fox & Squire (1991a) attempted to model thick elastic plates, with comparison to the thin elastic plate model. Wadhams & Holt (1991) studied waves in frazil and pancake ice, alternate forms of ice consisting of small crystals. Some authors attempted to model the slight attenuation of ice waves over long distances: Wadhams (1973) using the explanation of hysteresis due to Norton creep; Bates &

Shapiro (1980) and Squire & Fox (1992) using linear viscoelasticity. A sophisticated model incorporating inhomogeneous, non–idealised features of ice was attempted by Marchenko (1996, 1997); Marchenko & Voliak (1997).

The work on ocean wave penetration into ice sheets by Fox & Squire (1994) was reworked by Sturova (1999), including a study of oblique angles of wave incidence. Barrett & Squire (1996) further extend the work by considering an abrupt change in ice rigidity, density or thickness. Sahoo et al. (2001) considered the same problem with different edge conditions, and Kim & Ertekin (1998) used a different set of orthogonal eigenfunctions which resulted in an improvement in numerical efficiency.

The field of hydroelasticity continued to expand, aided in part by the interest in Very Large Floating Structures (VLFS), which can be modelled using the same thin elastic plate model. These VLFS are explained further in Section 1.6, and for now we only recognise their contribution to the literature. Wu et al. (1995) is an early example of solution by eigenfunction expansion. Kashiwagi (1998) solved the propagation of waves through a VLFS using an alternate method. The application of plate theory to VLFS led to new challenges for authors: reducing the elastic response of the platforms to incoming waves (Khabakhpasheva & Korobkin, 2002); fixing the platform to the bottom of the ocean using a spring (Korobkin, 2000); the response of the platforms to tsunamis or larger amplitude waves (Masuda & Miyazaki, 1999). Andrianov & Hermans (2003) studied the influence of water depth on the platform response. Utsunomiya et al. (1998) analysed the response to waves of a VLFS near a breakwater. The review papers by Kashiwagi (2000) and Watanabe et al. (2004) further summarise the progress in this field.

Entering the 21st century, the field showed no signs of stagnation. Further experimental findings exemplified the continuing demand for ice–related studies. Exploiting modernising technology, Schulz-Stellenfleth & Lehner (2002) took measurements of waves damped by sea ice using space–borne synthetic aperture radar images of the MIZ. Further observations were made in the Okhotsk Sea using an ultrasonic sounder. Downer & Haskell (2001) studied ice floe kinematics in the Ross Sea. Marko (2003) studied ice draft, ice velocity, ice concentration and current profile data inside the Sea of Okhotsk ice pack. This study was motivated by intense wave occurrences in 1998 which produced high–amplitude waves. A survey of recent changes in the thickness of Arctic sea ice was presented by Wadhams (2004). Emerging warming trends exhibited in the Arctic, and the international concern regarding global climate change, has led to further interest into ice–wave behaviour. Serreze et al. (2007) investigates the shrinking Arctic ice cover due to this warming; Kwok et al. (2009b) documents the reducing ice thickness. As a consequence of such trends, we can expect higher amplitude waves, and waves that are able to penetrate further into the pack ice (Squire, 2007).

Returning to the problem of wave reflection/transmission at the ice–water boundary, three–dimensional scattering by ice sheets was studied by Balmforth & Craster (1999) in a frequently referenced paper. Explicitly building the edge–conditions

into the analysis, they were able to solve fully the problem by revisiting the method of Evans & Davies (1968). Tkacheva (2004) provide another study, also revisiting the Weiner–Hopf method. There was further study by Teng et al. (2001), using an eigenfunction approach, who stated the energy conservation relation for free, simply–supported and built–in edge conditions. Utilising residue calculus techniques, the problem was also studied by Linton & Chung (2003), who included the case of waves incident from the ice into the ocean, as well as the reverse. Chung & Linton (2005) extended the problem further by considering wave transmission across a gap between two plates.

One problem subject to recent attention is that of wave propagation across a crack in an ice sheet. The problem was touched on in an earlier referenced paper by Barrett & Squire (1996), but it was studied first in more detail by Squire & Dixon (2000) for infinite depth. Simple formulae were derived for the reflection and transmission coefficients across the crack. The authors report a strong dependence on wave period in their results, with perfect transmission across the crack occurring for certain values of the period. Squire & Dixon (2001) extend the problem to consider multiple cracks. Evans & Porter (2003) revisited the crack problem in two–dimensions, for finite depth, obtaining an explicit solution. The same authors also consider the multiple crack problem, finding that large resonant motion can occur in the strip between two cracks. Porter & Evans (2007) generalise the problem to consider a finite number of straight cracks, and are forced to approximate a solution using Galerkin's method. The fascinating resultant wave fields are evidence of the power of the model.

Several authors endeavour to expound the dynamics of finite ice floe interaction with ocean waves (as opposed to a continuous or semi–infinite ice sheet). Meylan (2002) studied the wave response of a single ice floe of arbitrary geometry. The fully three–dimensional problem was solved explicitly for fluid of infinite depth. The author concludes that ice floe stiffness is the most important factor in determining ice floe motion, scattering, and force. Peter et al. (2004) studied a circular ice floe in fluid of finite depth. Peter & Meylan (2004) consider multiple floe interaction for floes of arbitrary shapes. Their infinite depth formulation changes the sum of the discrete roots of the dispersion relation into an integral.

As the theory continued to evolve, the models became more complex, taking into account various subtleties in the physical formulation that were simplified in the past. An example is given by Williams & Squire (2004), who allow the ice to vary spatially; variable ice thickness, pressure ridges, changes of material property, and open/refrozen holes in the ice are all considered. Williams & Squire (2006) study scattering at the boundary between three floating sheets of arbitrary thicknesses. Bennetts (2007) investigated the scattering of waves in ice of variable thickness. Several authors have studied the effect of variable bottom topography, as opposed to a flat bed; Wang & Meylan (2002) and Belibassakis & Athanassoulis (2005) being two examples. Porter & Porter (2004) combined both varying ice thickness and

varying bottom topography in an accomplished manner. Brevdo & Il'ichev (2006) investigates the effect of wind stress on a viscoelastic ice plate, and in addition the water is assumed to be weakly compressible.

Implicit in the vast majority of the above references is the assumption of zero draught. This assumption asserts that the ice is constantly in contact with the underlying fluid, and that the bottom of the ice sheet is flat. These assumptions in turn also imply that no submergence of the ice is possible. Examples of studies that incorporate non–zero draught include Andrianov (2005), Williams & Squire (2008) and Bennetts (2007). The effect of submergence of an ice sheet was studied by Williams & Porter (2009).

Further research into the MIZ is ongoing, and more recent example are cited here. Kohout & Meylan (2008) study arrangements of ice floes in two dimensions, working towards a wave attenuation model. They also derive a floe breaking model. Meylan & Masson (2006) investigated wave scattering in the MIZ by presenting a linear Boltzmann equation. In a more numerically–based study, Ogasawara & Sakai (2006) utilise a boundary element method and finite element method approach to analyse the characteristics of waves in the MIZ. Bennetts et al. (2010) present a three-dimensional model of wave attenuation in the marginal ice zone. Dumont et al. (2011) introduced a model for the MIZ, combining wave scattering theory with a floe–breaking parametrisation. Vaughan & Squire (2011) study wave propagation through a field of ice floes with particular interest on the ice–fracturing capability of the waves. Williams et al. (2012) attempt to include ice–sheets in a larger scale model for wave interaction in the MIZ, contriving a probability–based method for the possibility of ice fracture.

With the earlier referenced impact of global warming in mind, there has been further progression from modelling continuous ice sheets towards more detailed interactions with smaller floes. Bennetts & Squire (2009) investigated wave scattering by multiple arrays of circular ice floes, which are allowed to have realistic draught. Two–dimensional and three–dimensional models are compared. Bennetts & Squire (2010) further investigated this problem, this time allowing the ice to vary in thickness through the upper and lower surfaces. In a related study, Peter & Meylan (2009) studied wave scattering by vast fields of elastic bodies. Vaughan et al. (2009) investigated the decay of flexural gravity waves along the boundary between ice and sea, with the aim of replicating the attenuation that occurs while also accounting for heterogeneity in the ice sheet.

The inverse of the problem of a solitary finite ice floe is that of an ice polynya. A polynya is an opening or lake within an otherwise continuous ice sheet. Such problems have also received some attention, owing to the prevalence of polynyas throughout ice covered regions. Bennetts et al. (2009) studied wave scattering by an ice polynya. Bennetts & Williams (2010) extended the problem to consider polynyas of arbitrary shape. Results are compared for differently shaped polynyas over a range of relevant wavenumbers. The wave elevation within the polynya is

also studied.

Studies that incorporate nonlinear effects are far less common than linear studies, owing to the difficulty of treatment of the equations involved. The complicated, high–order equations and boundary conditions involved in hydroelasticity already provide a challenge for authors; introduction of nonlinearity further complicates the problem. Here we provide several examples of nonlinear studies. Early examples are found in Forbes (1986, 1988), the latter using a Galerkin method to find a solution. Peake (2001) studies the nonlinear stability of a fluid–loaded elastic plate. Hegarty & Squire (2004) addressed large–amplitude waves in a solitary ice floe; nonlinear terms are present in the fluid and elastic plate equations, the small–amplitude linearisation of previous work being no longer valid. A solution is found via perturbation expansion and matching methods. Părău & Dias (2002) provide another early example, investigating weakly nonlinear effects in the study of a moving load on an ice sheet. The solution is based on dynamical systems theory. Hegarty & Squire (2008) extend their previous work by using a boundary element method to solve large–amplitude wave propagation through an ice floe. Părău & Vanden-Broeck (2011) further investigate ice response to a moving load by applying Green's theorem and using a boundary element method, based on the work of Forbes (1989). In this study the ice is linear, but the fluid equations are fully nonlinear. Bonnefoy et al. (2009) utilise a nonlinear higher order spectral method in an application to the same problem.

In the previous few years, research is ongoing into a multitude of topics within hydroelasticity, manifesting itself in a burgeoning understanding of the dynamics of ice sheets. For example, Meylan & Sturova (2009) investigated the motion of an elastic plate that is released from rest and the solution allowed to evolve. Three different solution methods were presented and compared. The authors of Hassan et al. (2009) incorporate plate submergence, studying the plate deflection at oblique and normal incidence. The submergence problem was subsequently studied by Williams & Meylan (2011) for a semi–infinite plate, who also discussed the problem of wave scattering by a rigid submerged dock. Continuing the trend for increasing realism in ice modelling, Sturova (2009) studied the time dependent response of a heterogeneous ice plate, resting on fluid of finite depth. Ehrenmark & Porter (2012) assessed hydroelastic wave scattering over a plane incline. Xu & Lu (2009) report an optimisation of the eigenfunction matching method for the wave scattering by a semi–infinite plate problem. Athanassoulis & Belibassakis (2009) introduce a new system of equations for the analysis of a thick floating non–uniform ice sheets, incorporating variable bottom topography on the sea bed.

Further progress has been made on the application of nonlinear equations to model the fluid–ice interactions. A finite element model approach was used by Weir et al. (2011) to solve the equations within the fluid and a floating beam. Particular attention was paid to nonlinearity in the beam, exploring different beam theories. The time–dependence of the solution methodology allowed the evolution of the solution to be studied. Nonlinear hydroelastic waves were also modelled by

Plotnikov & Toland (2011) using the Cosserat theory of hyperelastic shells. In a related study Mollazadeh et al. (2011) apply the method of fundamental solutions to the semi–infinite floating elastic plate problem, using fully non–linear equations for the fluid. Nonlinear travelling waves bound between two thin elastic plates were studied by Blyth et al. (2011).

In an attempt to rectify the exiguity of controlled experiments on floating elastic plates, a study was conducted by Montiel et al. (2011). These were the first experiments conducted to record the wave response of a three–dimensional floating disc. The disc was made of expanded PVC, which is claimed to have comparable properties to sea ice when scaled. The goal was to validate the linear elastic plate theory by comparison with a floating elastic disc. The authors report generally good agreement between theory and experiment for the deflection of the disc, with some differences occurring at low frequencies. Related experiments were conducted by Wang & Shen (2010), in this case studying wave propagation through a mixture of grease and pancake ice. Carried out in two wave tanks, the experiments aimed to understand amplitude attenuation in waves through such a medium. The authors compare the results with the viscous ice model of Keller (1998), concluding that such a model is not sufficient to adequately describe the dispersion relation and attenuation.

Some literature is available on the interaction of ice with ocean structures. However, most studies differ in focus from the present study: forces on the cylinder are due to crushing or pushing from ice drifting into the structure. The present study focuses more on *wave* forces on structures in a continuous ice field, and the horizontal drift of the ice is not considered. In addition, the literature referenced here primarily approach the problem from an engineering standpoint, using certain idealisations for the interactions, instead of solving the full sets of fluid and elastic equations and boundary conditions. Nevertheless it is prudent to provide some examples here.

An early study of the crushing of ice into a vertical structure is given by Matlock et al. (1969, 1971). In this simplified model the structure is represented as a spring–mass system. The moving ice sheet is modelled as a rigid base on rollers, carrying a series of cantilevered teeth. The ice impinges on the structure at a prescribed velocity. Sundararajan & Reddy (1973) provides a stochastic analysis of the problem, this time modelling the structure as elastic. An experimental study is given by Tsuchiya et al. (1985) who conducted ice–loading tests on a structure in Hokkaido, Japan. The theory is advanced by Karr et al. (1993) who considered nonlinear effects, incorporating intermittent ice breakage and intermittent contact of the structure with the ice. A more technically involved study is found in Jordaan (2001), incorporating damage mechanics and ice fracture in a finite element model. In the work of Venturella et al. (2011), the earlier Matlock model is expanded via modal analysis. Further reading may be found in the theses by Croteau (1983) and Gürtner (2009), and the books by Sanderson (1988) and Cammaert &

Muggeridge (1988). Contained within are further technical studies and literature reviews, in addition to recommendations on the design of structures to best resist the ice encroachment.

Finally, we present several sources where further reading regarding hydroelastic waves can be found. The early history of the study of ocean waves in ice–covered seas was summarised in the excellent review article by Squire et al. (1995). The review was subsequently updated in Squire (2007) to account for the flurry of activity around the turn of the century. A theme issue entitled "The mathematical challenges and modelling of hydroelasticity" was published following an ICMS workshop of the same name (see Korobkin et al., 2011); many of the papers contained within are relevant to the present study. Squire (2011) addresses up–to–date emerging trends, and speculates on the future challenges of hydroelasticity. It is certain that this fascinating field will continue to flourish.

1.3 Methods of solution

A numerous assortment of techniques have been utilised to find a solution for problems within the field of hydroelasticity. In this section we briefly describe the most frequently used of these methods. To begin, we discuss the method of eigenfunction expansion. The generalised method may be traced back to the work of Povzner (1953) and Ikebe (1960). A description of its application to water–wave problems may be found in Linton & McIver (2001). With application to hydroelastic problems, the basic idea is that each root of the dispersion relation (the real roots and the infinite set of imaginary roots) constitutes a vertical "mode". The eigenfunction expansion is the summation of all of the modes to obtain a general solution. The unknown coefficients in the sum must be found by application of various boundary conditions; once the sum is truncated, the resulting system of equations can be solved readily. In problems where regions of fluid are both without and with an ice cover, the eigenfunctions must be matched across the boundaries. The method proves effective and efficient for solving a variety of problems. Fox & Squire (1990) were the first to include all of the evanescent modes and solve the scattering of waves at the ice–ocean boundary. Similar application was made to a finite floating plate by Wu et al. (1995). Evans & Porter (2003) applied the method to model wave scattering by a finite crack in an ice sheet, fully exploiting the symmetry of the problem to provide a concise solution.

Commonly, authors use techniques based on the application of Green's theorem. Authors select an appropriate Green's function G, which can have an integral representation or be expressed as the reciprocal of the distance between so–called "field" and "source" points. G must satisfy Laplace's equation as well as any other equations and boundary conditions in a problem. Employment of Green's second identity allows a solution for the velocity potential to be expressed in terms of integral equations. However, the evaluation of these integrals can present some difficulties, often

being singular due to the nature of the Green's function. Once these are overcome, the method presents a concise and powerful tool, and is widely used throughout applied mathematics. Its application to hydroelastic problems was initially made by Meylan & Squire (1993b), who solved the problem of wave interaction with a finite ice floe. It has subsequently been used by many authors, and is particularly useful when the problem considered involves arbitrary geometry.

Another method that may be applied to hydroelastic problems is the Weiner-Hopf technique. Typically a Fourier transform is applied to the dependent variables. Exploiting the analytic properties of the transform, the functions are then split into two parts, usually denoted by a "+" and a "–". Further manipulations on the functional equations leads to the solution being expressed in terms of integrals. Initially this method was applied by Evans & Davies (1968) for the problem of wave scattering at the ice–ocean boundary, though the resulting solution was found to be cumbersome and complicated. It was later shown by Balmforth & Craster (1999) that the solution may be written in a more straightforward manner. Tkacheva (2001) revisited the method and was able to derive extremely concise expressions for the reflection and transmission coefficients. The method has also notably been used by Chung & Fox (2002) for the same problem, who showed that the solutions of Evans & Davies (1968) can be calculated without numerical computation of the integral transforms by finding the roots of the dispersion equations (Squire, 2007).

In the hydroelastic literature, the use of integral transforms is ubiquitous. They are frequently used in conjunction with one of the other referenced methods, and they provide a valuable tool for a variety of situations. Transforms can sometimes even be used exclusively to derive an explicit solution to problems in hydroelasticity. Integral transforms are especially useful given the high order of the elastic governing differential equations, which reduce to algebraic equations in transformed space. Judicious choice of a particular transform may also assist in dealing with various boundary conditions. After inverse transforms have been performed, the solution is given in terms of integral quadratures. Milinazzo et al. (1995) provide one example, solving the problem of a moving load on an ice sheet in three dimensions by double application of Fourier transforms. Meylan et al. (2004) used Laplace transforms to find an explicit solution to the time–dependent floating elastic plate problem. Fourier transforms are used by Porter & Evans (2007) to solve the diffraction of flexural waves by finite straight cracks in an elastic plate.

As the hydroelastic formulations incorporate more inhomogeneous effects and become more realistic, the associated geometries become asymmetric, and the governing equations more complicated. Consequently authors are forced away from analytic solutions to numerically–driven approaches. One such approach is the so–called spectral method, applied by such authors as Bonnefoy et al. (2009), which writes the solution as a sum of "basis functions", often used in conjunction with a fast Fourier transform. Another approach is the Galerkin technique, utilised for example by Bennetts & Williams (2010) to solve a set of integro–differential equations

by expanding the solution in terms of a set of trial functions. Other methods are more computationally based, such as the boundary element method, used by such authors as Wang & Meylan (2004). The alternative finite element method is conceptually similar, in which a mesh is constructed for computation of the behaviour of the required surface. Korobkin et al. (2011) discusses the advantages of such methods compared with analytical or semi–analytical methods, calling for a combination of both approaches to facilitate further progress in the field.

The above provides a mere sample of the techniques used by hydroelastic modellers. For further reading, one might consult the excellent book by Linton & McIver (2001) which elucidates many of the above methods in reference to water wave scattering theory. The thesis of Bennetts (2007) contains detailed notes on solution methods with application to hydroelastic problems, as does the work of Squire (2007).

1.4 Theoretical assumptions

Ice formation, though a complex process, can be reduced to several distinct stages. The first stage, as turbulent open water begins to freeze, is defined as frazil ice; "a suspension of fine spicules or platelets of ice in water" (Wadhams & Holt, 1991). As the frazil crystals begin to clump together, they form a soupy layer of slurry with ice concentration (by volume) approximately $20-40\%$ (Martin & Kauffman, 1981). From here, further freezing causes the ice to form into a disjoint cover called pancake ice: the action of wind and waves causes the gradual formulation into almost–circular discs some centimeters to tens of centimeters in diameter and several centimeters in thickness (Lange, 1989). The process continues until the ice reaches a continuous state. Through partial melting and refreezing, multiyear ice can solidify further and attain more thickness; the ice thickness distribution in the Arctic ocean is studied in detail by Wadhams (1990). The ice is often interspersed with regions of open water called leads or polynyas, and sometimes the ice buckles forming pressure ridges (Squire et al., 1996).

The structure of this continuous ice is complicated and governed by many contributing factors. In greatest detail it can be described at the atomic level (see Fletcher, 1970; Glen, 1987). The structure of oxygen and hydrogen atoms within the ice is well known due to X-ray crystallography. Throughout the thickness of the ice sheet there exists variation in its properties; Frankenstein & Garner (1967) explain how the ice depends on brine volume, which can be computed from the temperature and salinity. Squire et al. (1996) further describe this brine dependence, with reference to brine pockets and grooves. A temperature gradient may be present throughout the ice, with differences throughout the vertical structure (Fox & Squire, 1994). An up to date synopsis regarding the various properties of ice may also be found in Timco & Weeks (2010).

We now outline the assumptions that we apply to the physically complex ice

sheet described above, and to the fluid foundation, in order to allow the problem to be mathematically treatable. As reviewed in Section 1.2, the general consensus is to represent the ice sheet by an elastic plate, and this is adopted throughout this thesis. Justification for this assumption is common throughout the literature (see Squire et al., 1995) and the elastic behaviour of ice was experimentally confirmed long ago (Press & Ewing, 1951; Oliver et al., 1954). Further, experiments conducted by Squire & Fox (1992); Squire (1984a); Squire et al. (1994) compare favourably with the theory. In particular, Squire (1993b) discusses the usage of the elastic plate model versus the mass–loading model, concluding that the elastic model is superior and especially effective at modelling large ice sheets.

The linear, *thin* plate equation has been studied by many authors in the past (Timoshenko et al., 1959; Ugural, 1981; Ventsel & Krauthammer, 2001; Squire et al., 1996); therefore we choose to only briefly explain its derivation here. The basic assumptions are based on the idea that the waves passing through the plate have small amplitude in comparison with their wavelength, and hence the curvature in the plate is small. In full, the assumptions are (see Ugural, 1981):

- The deflection of the midsurface is small compared with the thickness of the plate, and the square of the slope is therefore negligible
- The midplane remains unstrained subsequent to bending
- Plane segments initially normal to the midsurface remain plane and normal to that surface after the bending, implying that the vertical shear strains are negligible
- The stress normal to the midplane is small compared with the other stress components and may be neglected.

The above are known as Kirchoff's hypothesis (or Kirchoff–Love theory), a simplification of the Euler-Bernoulli plate theory to consider thin plates. Under such assumptions, we may introduce an equation for the equilibrium of the bending and twisting moments for an elastic plate under some external load q. We assume the plate has thickness h and density ρ_i, and occupies the x-y plane. The vertical displacement or *deflection* of the plate is defined by $w(x, y, t)$. From Squire et al. (1996) we then have

$$\frac{\partial^2 M_1}{\partial x^2} + 2\frac{\partial^2 M_{12}}{\partial x \partial y} + \frac{\partial^2 M_2}{\partial y^2} + \frac{\rho_i h^3}{12}\frac{\partial^2}{\partial t^2}\left(\frac{\partial^2 w}{\partial x^2} + \frac{\partial^2 w}{\partial y^2}\right) = \rho_i h \frac{\partial^2 w}{\partial t^2} - q. \tag{1.1}$$

In the above equation, M_1 and M_2 are the bending moments of the plate and M_{12}

is the twisting moment. These may be expressed in terms of the deflection as:

$$M_1 = -EJ\left(\frac{\partial^2 w}{\partial x^2} + \nu\frac{\partial^2 w}{\partial y^2}\right), \tag{1.2}$$

$$M_2 = -EJ\left(\frac{\partial^2 w}{\partial y^2} + \nu\frac{\partial^2 w}{\partial x^2}\right), \tag{1.3}$$

$$M_{12} = -EJ(1-\nu)\,\frac{\partial^2 w}{\partial x \partial y}. \tag{1.4}$$

Here the quantity EJ is known as the flexural rigidity of the elastic plate and ν is Poisson's ratio. E is Young's modulus, a measure of the stiffness of an elastic material, and $J = h^3/12(1-\nu^2)$. We substitute equations (1.2)-(1.4) into equation (1.1) to obtain the linear Euler–Bernoulli thin plate equation:

$$EJ\nabla^4 w + \rho_i h\frac{\partial^2 w}{\partial t^2} = q, \tag{1.5}$$

where the biharmonic operator is the double application of the Laplacian, given by

$$\nabla^2 = \frac{\partial^2}{\partial x^2} + \frac{\partial^2}{\partial y^2},$$
$$\nabla^4 = \nabla^2\nabla^2 = \frac{\partial^4}{\partial x^4} + 2\frac{\partial^4}{\partial x^2 y^2} + \frac{\partial^4}{\partial y^4}.$$

In equation (1.5) we have neglected the effect of rotatory inertia, which must only be included if the loading q is applied suddenly or is of high frequency (Squire et al., 1996), neither of which are true in this thesis. Though it is generally small, we retain the second term in equation (1.5), representing the acceleration of the plate. The equivalent equation governing the deflection for *thick* plates, retaining the effects of rotatory inertia and transverse shears, is given in Fox & Squire (1991a), equation (4). However, the authors note that in application to ice sheet deflections, the thick and thin plate formulations provide essentially identical results. The authors of Balmforth & Craster (1999) concur, stating that it would take a very unusual selection of parameter values for the thick-plate inclusion to have any effect, and conclude that the thin plate model may be used instead with negligible consequence. Hence, we may use equation (1.5) without loss of accuracy.

In application to ice sheets, there is evidence that Young's modulus E varies with depth. This is discussed in full in Kerr & Palmer (1972), who re–express Young's modulus as $E(z)$ (z being the vertical co–ordinate) using Hamilton's variational principle. However, the authors prove that for a variable Young's modulus and a constant Poisson's ratio the resulting formulations for plates and beams are the same as those for the corresponding homogeneous problems, if a modified "relaxed" flexural rigidity EJ is used. This conclusion is shared by Squire et al. (1996). However, little data is available on the distribution $E(z)$ and it is difficult to establish for each case (Kerr & Haynes, 1988). Hence in this thesis we use a constant E, but with reference to the close ties between the inhomogeneous and homogeneous cases

discussed in Kerr & Palmer (1972), this usage is justified. Any variety in the vertical structure of the ice is ignored, and the ice sheet is assumed isotropic, uniform and homogeneous. The ice sheet is also considered to be of infinite extent, covering the entire free surface of the domain.

We proceed to state assumptions applied to the fluid foundation upon which the ice plate rests. Firstly, the fluid is assumed to be in contact with the lower surface ice sheet at all times and for all space. Known as the zero draught assumption, this is adopted by the vast majority of authors in the field (Squire et al., 1995; Watanabe et al., 2004). Given the assumed–small deflections of the ice, the long periods of the waves we will consider, and the infinite extent of the ice sheet, this assumption seems reasonable. The usual assumptions on the fluid apply, in accordance with linear water wave theory (Stoker, 1957; Newman, 1997; Linton & McIver, 2001). The incompressibility of water is assumed. We neglect the viscous effects of the fluid, given that they are negligible for oceanic flow of the amplitude and scale we consider (Phillips, 1977). Hence by Kelvin's theorem the flow is irrotational (Fox & Squire, 1994). This allows the fluid velocity to be expressed as the gradient of the velocity potential. We model the fluid as having finite depth. However, the linear fluid assumptions are not valid in Chapter 6, where the fluid equations are fully nonlinear and we adopt an infinite depth approximation.

Underneath an ice sheet, the vertical structure of the fluid density may vary; the fluid may stratify into layers due to the seasonal melting and freezing of the ice (Squire et al., 1996; Lewis & Walker, 1970). Within these stratified layers, waves may propagate internally under the ice sheet, even forcing ice flexure; this was studied by Czipott et al. (1991). An internal wave was tracked under the ice cover in the Arctic Ocean, reaching pycnocline displacement of up to 36 m. Though the density gradient may be gradual, we assume two distinct layers of different densities under the ice in the manner introduced by Schulkes et al. (1987). Without the presence of an ice cover the problem is well studied, and was originally proposed as early as Lamb (1932). The theory was developed by Linton & McIver (1995) for wave scattering by horizontal cylinders in a two layer fluid. In Chapter 4 we adopt the two–layer formulation and assess its impact with regards to hydroelastic wave interaction with structures.

Another assumption used within the thesis is that the ice has constant thickness. Given the kind of continuous ice we are modelling, and that we assume the plate is thin compared to its wavelengths, this is fair. Throughout the thesis, we use the data set of Squire et al. (1988) for the ice parameters, where the ice was reported as consistently 1.6m thick over a large area, providing further justification. In addition, we assume that the fluid bed is perfectly flat. Given the deep water of the data set of Squire et al. (1988) (a depth of 350 m), it is unlikely that small undulations in the bottom topography will have more than a negligible effect on the deflection of the ice sheet. In general the classical theory of hydroelasticity also adopts these assumptions (Squire et al., 1995), with some examples to the contrary available

more recently (Porter & Porter, 2004; Bennetts, 2007).

A small rate of decay has been cited in the ocean over very long distances (Hunkins, 1962; Robin, 1963; Squire et al., 1995). Initially, we will neglect any wave attenuation in the ice sheet. We consider the motion of the ice sheet relatively close to fixed structures, and hence this assumption seems fair. However, in Chapter 5 we adopt a simple viscoelastic model for improved realism. Viscoelasticity in ice has also been studied by Bates & Shapiro (1980), Hosking et al. (1988) and Squire & Fox (1992) and found to be a good approach to modelling the attenuation.

Finally, throughout the thesis, we are interested in the strain throughout the ice sheet caused by the hydroelastic waves. Strain is defined as a dimensionless, normalized measure of deformation, describing the ratio of deformation to the initial dimension of the ice. The strain in this thesis is calculated within the linear plate theory (Ugural, 1981). If the calculated strain exceeds the so–called "yield strain", the ice is likely to fracture. Ice fracture is reviewed in Squire et al. (1995), and many authors have investigated the conditions under which it occurs. In particular Squire (1993a) investigates breakup in continuous sheets of ice. However, few experimental studies are available, and the exact yield strain of ice is difficult to calculate. Recently Prinsenberg & Peterson (2011) recorded flexural failure induced by swell at the ice edge in the Beaufort Sea. Timco & Weeks (2010) provide a database on the flexural strength of ice, which Williams et al. (2012) attempt to convert into a strain threshold, including a probability based model for the ice fracture. The exact theory of ice breakup is beyond the scope of this thesis and we will adopt a constant yield strain based on the available literature.

1.5 Thesis outline

Here we provide an outline of the thesis. The inclusion of vertical structures complicates the modelling of ice sheets, as we must incorporate wave reflection and diffraction by the structure, as well as satisfy conditions at its boundary. However, due to the framework of assumptions outlined in the above Section 1.4, we will show that solutions may be explicitly derived for a variety of problems.

Chapter 2 presents the most simplified model of hydroelastic interaction with a structure. We consider wave reflection by a vertical wall in two dimensions, where the fluid has an ice cover. The ice is considered to be frozen to the vertical structure. An incident hydroelastic wave approaches the wall, and the subsequent interaction is studied in detail. An analytic solution is found using integral transform methods. Results are presented for the ice deflection and strain in the ice sheet, as well as forces on the structure caused by the hydroelastic waves. This simplified formulation helps provide a firm basis for extension of the model.

Chakrabarti et al. (2003) also studied hydroelastic waves both incident on a vertical wall and due to an oscillating wave-maker. In Chakrabarti et al. (2003), the ice was not fixed to the wall, whereas in the present study, the ice clamping

leads to a specific effect on the ice deflection; moreover, the case of infinite depth was studied as opposed to the finite depth case considered in Chapter 2. One of the methods of solution in Chakrabarti et al. (2003) made effective use of a Fourier cosine transform, which we also utilise in this study. Williams & Squire (2002) studied oblique wave reflection by a vertical wall to which the ice is frozen. The fluid was again assumed to be of infinite depth, and the authors used tools based on Green's second identity to obtain a solution. Unlike the work by Chakrabarti et al. (2003) and Williams & Squire (2002), we study the hydroelastic wave forces on the cylinder, providing explicit formulae for their calculation, which are of practical importance for the design of offshore structures. The work of Chapter 2 was published in the paper by Brocklehurst et al. (2010). Subsequently a similar paper was published by Bhattacharjee & Guedes-Soares (2012), who provide a comparison with the solution of Chapter 2 which is also presented here.

In Chapter 3, we extend the model into three dimensions by considering hydroelastic wave diffraction by a vertical cylinder. The ice is assumed to be frozen to the structure. Utilising a Fourier decomposition and applying a Weber transform, explicit solutions are provided for the ice deflection and velocity potential of the fluid. The strain in the ice at the cylinder-ice boundary is analysed, to assess whether the ice–clamping condition is viable. Expressions for the vertical shear force and the horizontal wave force are also presented.

Water wave scattering by a vertical cylinder was first examined by Omer Jr & Hall (1949), and later McCamy (1954). Mei (1983) obtained a solution by decomposing the potentials of the incident and reflected waves into Fourier series with respect to the azimuthal coordinate. Consideration of arrays of vertical cylinders is now commonplace, pioneered by such authors as Spring & Monkmeyer (1974) and Linton & Evans (1990). The inclusion of an ice cover to diffraction problems involving a vertical cylinder has been studied considerably less. Malenica & Korobkin (2003) considered the problem of water wave interaction with a vertical cylinder frozen into a circular finite ice floe, as opposed to the continuous ice considered in Chapter 3. The efficient technique of eigenfunction expansions in the region covered by the ice flow and in the open water region was used. The work of Malenica & Korobkin (2003) was part of a conference proceedings, and expressions for the strain and forces on the cylinder were not published. The advantages and disadvantages of each method of solution are discussed in Chapter 3. The work of Chapter 3 was published in the paper Brocklehurst et al. (2011).

In Chapter 4, the two–dimensional vertical wall problem of Chapter 2 is repeated, with the inclusion of fluid stratification. The fluid has two distinct layers of different density, as discussed in Section 1.4. We investigate the effect of this stratification on the interaction with the hydroelastic wall. In particular, we assess whether incident waves in the interface between the two fluids can generate reflected waves in the ice cover and vice versa. The effect of two fluid layers on the forces on the wall and the strain in the ice sheet is also studied in detail. Hydroelastic wave studies including

fluid stratification are sparse. The most closely related work to the formulation of Chapter 4 is given by Bhattacharjee & Sahoo (2008), who investigated scattering by a crack in an ice sheet resting on a two–layer fluid.

Chapter 5 studies waves in an ice sheet due to a moving load, in three dimensions. We use a simple model for the viscoelasticity of the ice sheet. The problem is solved by integral transform techniques combined with application of residue calculus theory. We then proceed to model load–induced waves in the vicinity of a vertical wall. The ice is assumed to be frozen to the vertical wall. In both cases the pattern and magnitude of the deflection are studied in detail under a variety of parameters, including the speed of the moving load and the newly introduced viscoelastic parameter. In the vertical wall case, we investigate the effect of variance in the distance of the load from the wall. The strain at the ice–wall boundary is investigated to ascertain under which parameter values the connection is likely to be broken.

The problem of a moving load on a viscoelastic ice–cover was studied by Hosking et al. (1988). The authors use a slightly different viscoelastic formulation to the one considered in Chapter 5, and a solution is found by integral transforms. While the study is thorough and well executed, no three–dimensional plots of the ice deflection are presented, so we present several here for the no–wall case. The problem was revisited by Milinazzo et al. (1995), though the ice was considered purely elastic. However, the primary focus of Chapter 5 is the vertical wall case, which is hitherto unstudied.

In Chapter 6 the moving load model is repeated, but we consider fully nonlinear equations for the fluid motion. The solution is found by application of Green's theorem using a free–surface Green's function, and the solution is then computed numerically using a boundary element method. The solution is based on the method of Părău & Vanden-Broeck (2011), who solved the problem where no vertical wall is present. Comparison is made with the linear model of Chapter 5.

1.6 Applications

Understanding large masses of ice and their dynamics is of crucial importance to humanity. Together, the Antarctic and Greenland ice sheets contain more than 99% of the freshwater ice on Earth. The Antarctic land–ice extends almost 14 million square kilometres, and the Greenland land–ice about 1.7 million square kilometres. If both melted, the global sea level would rise by approximately 70 metres (National Snow and Ice Data Center). Surrounding these is yet more ice in the form of ice shelves, which reach hundreds of metres in thickness (Griggs & Bamber, 2011). We are concerned with polar sea ice, which is thinner (usually approximately 1–3 metres in thickness) and much more seasonally dependent. Sea ice typically covers about 14 to 16 million square kilometers in late winter in the Arctic and 17 to 20 million square kilometers in the Antarctic Southern Ocean (National Snow and Ice

Data Center), though in summer they may reduce significantly through melting. Understanding the dynamics of sea–ice waves forms part of the motivation for this and many other studies referenced in Section 1.2.

The principle application of the first several chapter of this thesis is specifically the interaction of waves in sea ice with offshore structures. Offshore structures come in a variety of types, from rigid to compliant structures (see for example a recent review by El-Reedy, 2012). The design and installation of such structures has been a challenge for generations of engineers. Such structures may be required to resist wave forces due to impinging ice sheets. Recent warming trends in global temperature has led to increased interest in the seasonal variation of sea ice extent (see for example Kwok et al., 2009a). As a consequence of this variation, large bodies of ice may break off and drift from the poles (Arrigo et al., 2002), interacting with existing structures, calling for a need to study further the impact of such interaction.

Also of vital importance is the design of new structures, with the ice interaction in mind. It is common knowledge that the earth's fossil fuels are declining rapidly, and demand will soon outstrip supply. It is also well known that the Arctic contains oil and gas reserves; recently, a review on the subject was conducted by Lloyds Insurance (see Emmerson & Lahn, 2012), discussing current and future projects in the Arctic. Extracting these resources is thus the next logical step. Quoting from Emmerson & Lahn (2012), "the combined effects of global resource depletion, climate change and technological progress mean that the natural resource base of the Arctic is now increasingly significant and commercially viable". Further, the authors state that the Arctic is likely to attract substantial investment over the coming decade, potentially reaching hundreds of billions of dollars or more. An earlier review was conducted in ISO19906 (2010), pertaining to the design and construction of offshore structures in the Arctic and other cold regions. Understanding the hydroelastic wave forces on new structures is therefore of paramount importance.

There is a certain irony that oil and gas industries may now proliferate into the Arctic because of the receding ice cover, when they are purportedly contributors to the increased greenhouse gases that led to such recession. Indeed, Stroeve et al. (2007) claim that "climate models are in near universal agreement that Arctic sea ice extent will decline through the 21st century in response to atmospheric greenhouse gas loading". In view of the theory of global warming, many call for an increase in cleaner, renewable energy. Hence, one application of this thesis is the development of offshore wind farms in ice–covered seas. Ice loads on such structures were the subject of a study by Gravesen et al. (2003), in application to development of offshore wind farms in Denmark and Canada. The study was advanced and published in Gravesen et al. (2005). Offshore wind farms in ice–covered seas were also discussed by Battisti et al. (2006).

As mentioned in Section 1.2, the same equations used to model an ice sheet may be applied to a Very Large Floating Structure (VLFS). These VLFS may have a variety of purposes, from floating airports (see mega–float in Tokyo Bay) to breakwaters,

oil and natural gas platforms, wind and solar power plants or even for habitation (see DeltaSync, floating city). Such structures may become commonplace sooner than many expect, owing to the growing population and increasing need for space (Andrianov, 2005). The present work may be applied to these VLFS, in particular so–called pontoon–type VLFS which are very flexible. The boundary conditions considered in this thesis are suitable for VLFS that are fixed at one boundary. A review of the synergies between VLFS and ice research may be found in Squire (2008).

The thesis is not wholly restricted to ice–covered *ocean* waves. Many applications for this thesis can be found within the context of lake or river ice. This type of ice has different properties to sea ice, owing to the lack of salinity (see Squire et al., 1996). There are studies within the literature of wave interaction with this kind of ice; see for example Xia & Shen (2002). River and lake ice is studied in greater detail in Ashton (1986), who discussed several applications. The interaction of ice with multi–span bridges, piers, or tidal jetties may be modelled by the present study. We may also apply the work to waves in a frozen lake behind a dam. Waves interacting with the side of a river channel, or harbour, are of interest in cold–climate shipping lanes and are examples of further potential application of the thesis.

Chapters (5) and (6) are concerned with moving loads on ice sheets. Such problems have numerous practical applications. The book by Squire et al. (1996) discusses the historical applications, chronicling some early attempts to cross ice passages and, in the late 19th century in Canada, to construct a railway line on the ice. Nowadays, with many research teams based in polar regions, there is need for vehicles to safely drive on the ice, or for aircraft to land on it. Such applications are relevant to the present study. The problem is curious in that there exists a critical speed which, if matched by the speed of the load, exaggerated and potentially dangerous ice response can occur.

We consider moving load problems that occur in the vicinity of a vertical wall. This particular problem has multiple applications throughout cold climate regions. For example, there exists a class of vehicles termed icebreakers which are designed specifically to fracture the ice (see for example Ashton, 1986). For example, an air–cushioned vehicle similar to a hovercraft may be driven on the ice to intentionally incite fracture. Applications for this type of vehicle may be found in harbours, rivers and canals where ships need to transport cargo but are restricted by ice growth in winter. Further, there are several accounts of flooding due to ice blockage in rivers in parts of Canada, Alaska and Russia. She et al. (2007) studied such events in reference to ice jam events on the Athabasca River. Nzokou et al. (2009) has studied wave interaction with an ice cover on a river, in order to model ice breakup. Better understanding of this phenomenon combined with application of ice–breaking vehicles may help avoid future disasters. In the present study we investigate the strain in the ice and the dependence of the solution on the load speed and distance from the wall. The wall may represent a river bank or the wall of a canal or harbour.

Chapter 2

Two-dimensional hydroelastic wave interaction with a vertical wall

2.1 Introduction

We begin our investigation by studying the problem of linear hydroelastic wave reflection by a vertical wall in two dimensions. We will use this model to demonstrate the formulation of hydroelastic problems and illustrate some of the techniques used throughout this thesis. This will provide a firm basis for expanding to more complicated formulations. We will consider an incident wave propagating through a hydroelastic plate towards a vertical wall. The plate extends semi–infinitely and floats on water of finite depth. In general we shall refer to the hydroelastic plate as an ice sheet, although it could also represent a VLFS. The plate is clamped to the wall, to imitate an ice sheet frozen to an ocean structure or a VLFS fixed in place.

Various assumptions used in this chapter are stated here (see Section 1.4 for justification). Firstly the fluid is assumed to be ideal, incompressible and inviscid, with irrotational motion. We assume that the plate is in contact with the fluid at all time (there is no gap between the lower edge of the plate and the fluid below). The ice sheet has constant thickness. The fluid bed is considered perfectly flat and perpendicular to the vertical wall. The vertical wall is rigid and impermeable. The incident hydroelastic wave is assumed to be regular and periodic.

We investigate how the hydroelastic wave interacts with the vertical wall and derive an exact solution for the velocity potential in the fluid and the deflection of the hydroelastic plate. The behaviour of the solution under variation of the physical parameters will be analysed in detail. We will pay particular attention to the deflection in the vicinity of the vertical wall, and the specific effect of the ice–clamping condition. The elastic strain caused by the deflection of the plate will be studied, along with the horizontal and vertical forces acting on the vertical wall. Section 2.2 contains the mathematical formulation of the problem and defines the relevant

parameters. We then outline the boundary value problem to be solved. Section 2.3 demonstrates the method of solution. Numerical results are then presented and discussed in Section 2.4. A summary and conclusion of the chapter is given in Section 2.5.

2.2 Formulation

2.2.1 Schematic and parameters

The geometry of the problem and co-ordinate system are shown in Figure 2.1. We

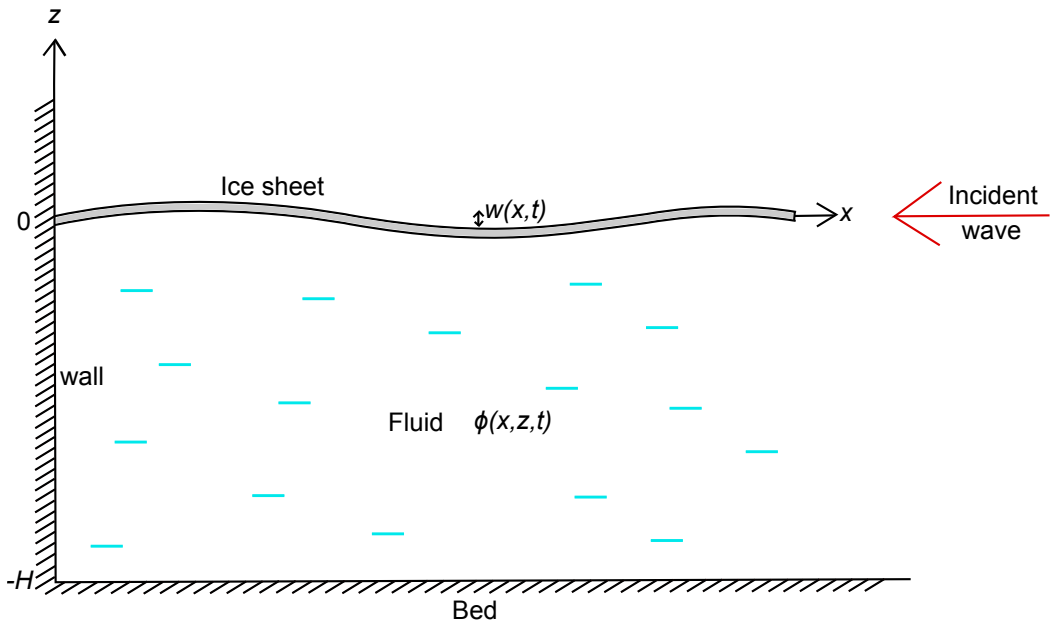

Figure 2.1: Schematic of a semi–infinite ice sheet meeting a vertical wall.

introduce Cartesian coordinates with the x-axis being along the ice sheet at rest and the z-axis directed vertically upwards along the wall. Time is denoted by t. The fluid bed is flat and the fluid has depth H. The pressure in the fluid is represented by $p(x, z, t)$, and the density of the fluid by ρ. The irrotational fluid velocity $\mathbf{V}(x, z, t)$ is equal to the gradient of the velocity potential $\phi(x, z, t)$, hence $\nabla\phi = \mathbf{V}$. The vertical deflection of the ice sheet (the distance the ice sheet is displaced relative to its position at rest) is denoted by $w(x, t)$. The ice has mass per unit length M, where $M = \rho_i h$, ρ_i is the ice density and h is the ice thickness. The ice sheet has flexural rigidity EJ, where E is Young's modulus and $J = h^3/[12(1 - \nu^2)]$, where ν is Poisson's ratio. The incident wave parameters are: a, wave amplitude; ω, wave frequency; k, wavenumber and c, phase velocity. The acceleration due to gravity is denoted g, and the imaginary number is given by $i^2 = -1$.

Though the amount of physical parameters involved in the problem may seem numerous, they are necessary to fully describe the details of the elastic plate and fluid, and they will be re–used in every chapter of this thesis. In Section 2.2.5 we reduce the amount of parameters via nondimensionalisation. Typical values for each physical parameter can be found in Table 2.1. The primary focus of this chapter is for

Parameter	(a) McMurdo Sound	(b) Lake Saroma
g	$9.8\ \mathrm{ms}^{-2}$	$9.8\ \mathrm{ms}^{-2}$
H	350 m	6.8 m
h	1.6 m	0.17 m
ν	0.3	0.33
E	$4.2 \times 10^9\ \mathrm{Nm}^{-2}$	$5.1 \times 10^8\ \mathrm{Nm}^{-2}$
J	$0.375\ \mathrm{m}^3$	$4.6 \times 10^{-4}\ \mathrm{m}^3$
ρ_i	$917\ \mathrm{kgm}^{-3}$	
ρ	$1024\ \mathrm{kgm}^{-3}$	$1026\ \mathrm{kgm}^{-3}$
M	$1467.2\ \mathrm{kgm}^{-2}$	$155.89\ \mathrm{kgm}^{-2}$

Table 2.1: Values of typical parameters taken from measurements at (a) McMurdo Sound, Antarctica (Squire et al., 1988) and (b) Lake Saroma, Japan (Takizawa, 1985). For the data set (b), the ice density is absent from Takizawa (1985) and we hence assume the value $\rho_i = 917\ \mathrm{kgm}^{-3}$. The fluid for (a) is ocean water, and for (b) is a brackish mixture of salt–water and fresh–water.

hydroelastic waves in oceans and the data from McMurdo sound is most pertinent, but the data from Lake Saroma is presented for comparison. Typical values of the incident wave parameters will be discussed later.

2.2.2 Governing Equations and boundary conditions

We now state the governing differential equations for the velocity potential and plate deflection, and give boundary conditions based on the physical situation. Due to our assumptions for the fluid stated in Section 2.1, the conservation of mass equation $\nabla.\mathbf{V} = 0$ means that the potential $\phi(x, z, t)$ is a solution of Laplace's equation in the fluid (see for example Linton & McIver, 2001),

$$\nabla^2\phi = 0, \qquad (x > 0,\ -H \leq z \leq 0). \tag{2.1}$$

Here the Laplacian ∇^2 is given by

$$\nabla^2 = \frac{\partial^2}{\partial x^2} + \frac{\partial^2}{\partial z^2}.$$

Two boundary conditions on ϕ are due to the rigid wall:

$$\phi_x = 0, \qquad (x = 0,\ -H \leq z \leq 0), \tag{2.2}$$

and due to the impermeability of the bed:

$$\phi_z = 0, \qquad (x > 0,\ z = -H). \tag{2.3}$$

Conditions (2.2) and (2.3) ensure no flow through the wall and the bed respectively. Here and in the rest of the thesis, subscripts of variables represent derivatives. The

linearised kinematic boundary condition is given by

$$\phi_z = w_t, \qquad (x > 0,\ z = 0), \tag{2.4}$$

and the linearised Bernoulli equation yields the hydrodynamic pressure in the fluid, given by

$$p(x, z, t) = -\rho\phi_t - \rho g z, \qquad (x > 0,\ -H \leq z \leq 0). \tag{2.5}$$

The differential equation for the plate deflection is obtained from thin plate theory (see Section 1.4) and is given by

$$EJ\nabla^4 w + Mw_{tt} = p(x, w, t), \qquad (x > 0,\ z = 0). \tag{2.6}$$

In this two–dimensional formulation the biharmonic operator $\nabla^4 = \partial^4/\partial x^4$. Boundary conditions on $w(x, t)$ are due to the ice being clamped at the origin, and hence

$$w = 0, \qquad (x = 0), \tag{2.7}$$

$$w_x = 0, \qquad (x = 0). \tag{2.8}$$

This ensures that at the point where the ice meets the vertical wall, the deflection and slope of the deflection are both zero, implying the ice is fixed there and not free to slide up and down the wall. Throughout this chapter, boundary conditions applied at $x = 0$ are assumed to have approached x from the right (positive x), as the region $x < 0$ is not valid in this problem. The conditions in the far-field will be defined later in the section.

We seek a time–periodic solution of the form (see Squire et al., 1995):

$$\phi(x, z, t) = \Re\Big(\Phi(x, z)e^{-i\omega t}\Big), \tag{2.9}$$

$$w(x, t) = \Re\Big(\frac{i}{\omega}W(x)e^{-i\omega t}\Big), \tag{2.10}$$

where ω is the angular frequency of the problem. $\Phi(x, z)$ and $W(x)$ represent the time–independent parts of the velocity potential and ice deflection. Equations (2.1)-(2.8) can now be rewritten in terms of Φ and W. For example, the hydrodynamic pressure (2.5) on the ice plate is now given by

$$\begin{aligned} p(x, 0, t) &= -\rho\phi_t - \rho g w \\ &= \Re\Big((-\rho(-i\omega)\Phi(x, 0) - \rho g\frac{i}{\omega}W(x))e^{-i\omega t}\Big) \\ &= \Re\Big(i\rho\omega(\Phi(x, 0) - \frac{g}{\omega^2}W(x))e^{-i\omega t}\Big). \end{aligned}$$

We substitute this into the plate equation (2.6):

$$\Re\left(\Big(M\frac{i}{\omega}(-i\omega)^2 W(x) + EJ\frac{i}{\omega}W_{xxxx}\Big)e^{-i\omega t}\right) = \Re\left(i\omega\rho\Big(\Phi(x, 0) - \frac{g}{\omega^2}W(x)\Big)e^{-i\omega t}\right),$$

which leads to

$$EJW_{xxxx} + (\rho g - M\omega^2)W = \omega^2 \rho \Phi(x, 0).$$

Proceeding in this manner, substituting equations (2.9) and (2.10) into the remaining boundary conditions and governing equations (2.1)–(2.8) leads to the following boundary value problem (BVP) for Φ and W:

$$\nabla^2 \Phi = 0, \quad (x > 0,\ -H < z < 0), \tag{2.11}$$

$$\Phi_z = 0, \quad (x > 0,\ z = -H), \tag{2.12}$$

$$\Phi_x = 0, \quad (x = 0,\ -H < z < 0), \tag{2.13}$$

$$EJW_{xxxx} + \big(\rho g - M\omega^2\big)W = \omega^2 \rho \Phi(x, 0), \quad (x > 0,\ z = 0), \tag{2.14}$$

$$W = 0, \quad (x = 0), \tag{2.15}$$

$$W_x = 0, \quad (x = 0), \tag{2.16}$$

$$W = \Phi_z, \quad (x > 0,\ z = 0). \tag{2.17}$$

We now proceed to find expressions for the incident hydroelastic waves.

2.2.3 Incident Waves

The velocity potential of the incident wave that propagates from $x = +\infty$ takes the general form

$$\Phi_{inc}(x, z) = A(z)e^{-ikx}, \tag{2.18}$$

where $A(z)$ unknown. The incident wave must satisfy Laplace's equation (2.11), giving:

$$A_{zz} - Ak^2 = 0,$$

and invoking the bed condition (2.12) means that this has general solution

$$A(z) = A_0 \cosh(k(z + H)),$$

where A_0 is an unknown constant. The coupled incident wave for the plate deflection is given by

$$W_{inc} = \frac{\partial \Phi_{inc}}{\partial z}(x, 0) = A_z(0)e^{-ikx}.$$

Returning briefly to the original form of the deflection $w(x, t)$ by using (2.10), the physical, real part of the incident wave is given by:

$$w_{inc}(x, t) = \Re\Big(\frac{i}{\omega} A_z(0)e^{-i(kx+\omega t)}\Big) = \frac{A_z(0)}{\omega} \sin(kx + \omega t).$$

We see that the amplitude of the wave is given by $a = A_z(0)/\omega$. Hence

$$\omega a = A_0 k \sinh(kH), \tag{2.19}$$

and using equations (2.18) and (2.19) the expressions for the incident waves are:

$$\Phi_{inc}(x,z) = \frac{a\omega}{k}\frac{\cosh(k[z+H])}{\sinh(kH)}e^{-ikx}, \tag{2.20}$$

$$W_{inc}(x) = a\omega e^{-ikx}. \tag{2.21}$$

Together with the plate equation (2.14), the incident waves may be used to derive the dispersion relation which links the incident wave frequency to the incident wavenumber.

2.2.4 Dispersion relation

Substituting $\Phi_{inc}(x,0)$ and $W_{inc}(x)$ into the plate equation (2.14) gives

$$EJ(-ik)^4 a\omega e^{-ikx} + (\rho g - M\omega^2)a\omega e^{-ikx} = \omega^2\rho\frac{a\omega}{k\tanh(kH)}e^{-ikx},$$

which rearranges to

$$EJk^4 + \rho g - M\omega^2 = \frac{\rho\omega^2}{k\tanh(kH)}.$$

Hence, the dispersion relation for hydroelastic waves is given by (see for example Squire et al., 1995)

$$\omega^2 = \frac{\rho g + EJk^4}{M + \dfrac{\rho}{k\tanh(kH)}}. \tag{2.22}$$

For a given frequency ω of the problem, the dispersion relation provides the corresponding value for k as prescribed by hydroelastic wave theory. First solved in full by Fox & Squire (1994), it can be shown that equation (2.22) has one real root, two complex roots and an infinite set of imaginary roots. In this formulation, we are concerned only with the single real root k. The corresponding dispersion relation for free surface gravity waves follows from (2.22) if we allow the ice sheet thickness to tend to zero ($h \to 0$ leading to $M = 0$ and $EJ = 0$). A plot of the phase speed $c = \omega/k$ against k is found in Figure 2.2, for both of the data sets in Table 2.1. We note that there exists a minimum for c regardless of what data is chosen, which we denote c_{min}, corresponding to a value $k = k_{cr}$. In some problems, for example Părău & Dias (2002), the linear theory breaks down close to c_{min}. However, this difficulty seems to be constrained to problems involving waves generated by moving loads. Chapters 5 and 6 of this thesis involve such waves, and c_{min} is further addressed there. In the present problem there are no difficulties when the wavenumber is close to k_{cr}. From Figure 2.2 we see that the data set taken from McMurdo sound gives faster phase speed than that of Lake Saroma. Also, the critical wavenumber k_{cr} is much smaller.

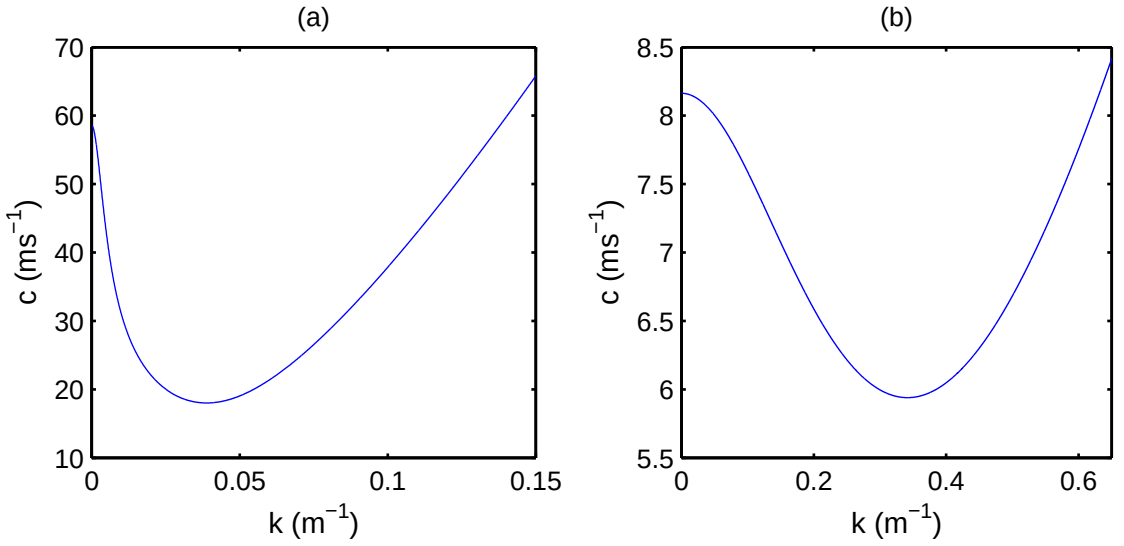

Figure 2.2: The phase speed c plotted against the wavenumber k for the following data sets: (a) McMurdo Sound, (b) Lake Saroma.

Parameter/variable	Dimension
x	$\mathbf{L}$
t	$\mathbf{T}$
k	$\mathbf{L}^{-1}$
E	$\mathbf{M}\mathbf{L}^{-1}\mathbf{T}^{-2}$
J	$\mathbf{L}^{3}$
H	$\mathbf{L}$
ρ	$\mathbf{M}\mathbf{L}^{-3}$
M	$\mathbf{M}\mathbf{L}^{-2}$
g	$\mathbf{L}\mathbf{T}^{-2}$
ω	$\mathbf{T}^{-1}$
a	$\mathbf{L}$
h	$\mathbf{L}$

Table 2.2: The dimensions of the parameters in the problem.

2.2.5 Nondimensionalisation

With the dispersion relation derived, we now nondimensionalise the problem to reduce the number of parameters. Table 2.2 shows the dimensions for the parameters of the problem.

Inspired by the frequent appearance of the term kH in the problem thus far, we will use the depth H as a length scale. In the data from McMurdo sound in Table 2.1(a) the fluid depth is 350 m. Due to the linear formulation of the problem, we will be looking for waves that have a large wavelength in comparison with the wave amplitude, so the choice of H proves suitable as a length scale. We denote dimensionless variables/parameters by an asterisk, and we substitute $k^* = kH$ into the dispersion relation (2.22) to give

$$\frac{g}{\omega^2 H} - \frac{\rho_i h}{\rho H} = \frac{1}{k^* \tanh(k^*)} - \frac{EJ}{H^5 \rho \omega^2} k^{*4}. \tag{2.23}$$

This gives rise to the dimensionless parameter

$$\gamma = \frac{EJ}{H^5 \rho \omega^2},$$

which will appear frequently throughout the problem. The parameter γ depends on the characteristics of the fluid, the plate and the incident wave. It is small and depending on the value of k, γ typically varies from $\mathrm{O}(10^{-5})$ to $\mathrm{O}(10^{-8})$. To summarise, we nondimensionalise thus:

$$z^* = \frac{z}{H}, \quad x^* = \frac{x}{H}, \quad t^* = t\omega, \quad k^* = kH, \quad \gamma = \frac{EJ}{H^5 \rho \omega^2},$$
$$W^*(x^*, t^*) = \frac{W(x,t)}{a\omega}, \quad \Phi^*(x^*, z^*, t^*) = \frac{\Phi(x,z,t)}{Ha\omega}.$$

The asterisks are now dropped and all variables are assumed to be dimensionless in the below analysis. The BVP (2.11)-(2.17) is rewritten in terms of dimensionless quantities as

$$\nabla^2 \Phi = 0, \quad (x > 0,\ -1 < z < 0), \tag{2.24}$$
$$\Phi_z = 0, \quad (x > 0,\ z = -1), \tag{2.25}$$
$$\Phi_x = 0, \quad (x = 0,\ -1 < z < 0), \tag{2.26}$$
$$\gamma W_{xxxx} + \left(\frac{1}{k \tanh(k)} - \gamma k^4 \right) W = \Phi(x,0), \quad (x > 0), \tag{2.27}$$
$$W = 0, \quad (x = 0), \tag{2.28}$$
$$W_x = 0, \quad (x = 0), \tag{2.29}$$
$$W = \Phi_z, \quad (x > 0,\ z = 0). \tag{2.30}$$

Note that we have substituted equation (2.23) into equation (2.27), which reduces the problem to dependence on only two dimensionless parameters, k and γ.

2.2.6 Typical values of wavelength and wave period

At this stage, it is prudent to define typical values of the parameter k, which will be varied frequently throughout the analysis. The period of waves in the Arctic ocean can range from $T = 0.1 - 60$ s for deep water, and most commonly $T = 15 - 60$ s (Hunkins, 1962). This is in agreement with Menemenlis et al. (1995), who measured ocean ice waves of period $T = 20 - 50$ s.

Figure 2.3 shows the wave period and wavelengths plotted against the dimensionless wavenumber k. A range of period $0 - 60$ s corresponds to a range of $k = 1 - 50$. This range of k is equivalent to wavelengths of $0 - 2000$ m. Waves in ice sheets are known to have very long wavelengths; Squire et al. (1995) notes the principal range to be $0 - 500$ m. With these facts in mind, in this chapter we will analyse waves of range $k = 1 - 20$, corresponding to wave period $T = 5 - 50$ s and wavelength $\lambda = 100 - 2000$ m, which is a large enough range to represent typical waves in ice

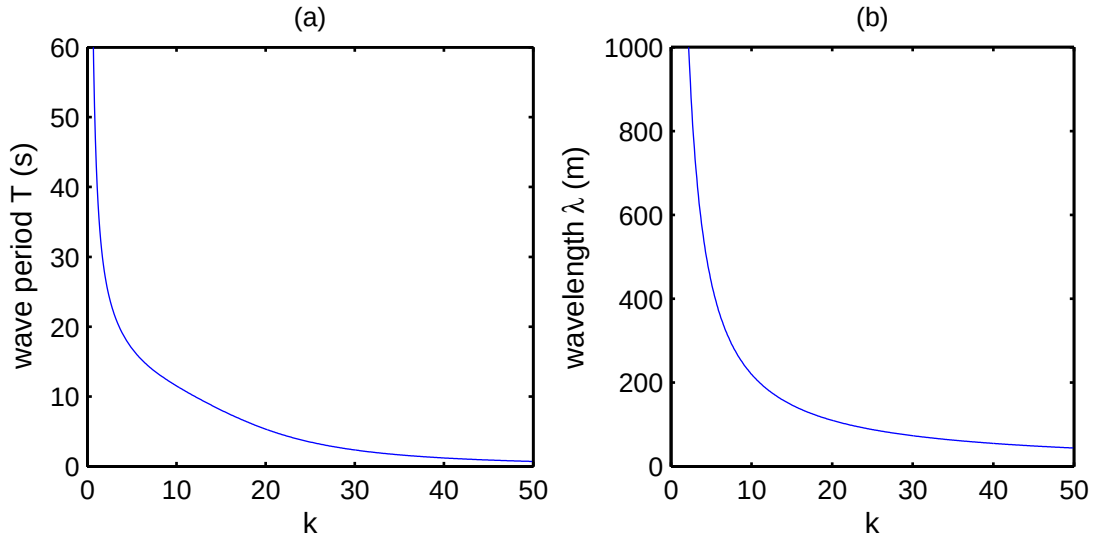

Figure 2.3: (a) The wave period T plotted against the dimensionless wavenumber k. (b) The wavelength λ plotted against the dimensionless wavenumber k. Other parameters are taken from Table 2.1(a).

sheets.

2.2.7 Linear superposition

In dimensionless form, the incident waves (2.20)-(2.21) are

$$\Phi_{inc}(x,z) = \frac{\cosh(k[z+1])}{k\ \sinh(k)}\ e^{-ikx},$$
$$W_{inc}(x) = e^{-ikx}.$$

The incident waves approach the wall from $x = +\infty$, and upon contact with the wall reflected waves are generated which must be accounted for in the solution. The reflected waves take the form

$$\Phi_{ref}(x,z) = a_D \frac{\cosh(k[z+1])}{k\ \sinh(k)}\ e^{ikx},$$
$$W_{ref}(x) = a_D\ e^{ikx},$$

where a_D is the amplitude of the reflected wave, which must be found as part of the solution. By linear superposition, we may express the total potential and deflection as the sum of the incident waves and the reflected waves. However, this would not alone be enough to satisfy all the conditions arising from the presence of a vertical wall. Hence the total form of the potential and deflection are:

$$\Phi(x,z) = \Phi_{inc}(x,z) + \Phi_{ref}(x,z) + \varphi(x,z), \tag{2.31}$$
$$W(x) = W_{inc}(x) + W_{ref}(x) + \hat{w}(x). \tag{2.32}$$

The extra functions $\varphi(x,z)$ and $\hat{w}(x)$ govern the behaviour of the potential and deflection in the vicinity of the vertical wall. We shall require these functions to decay far from the wall, leaving only the incident wave and reflected wave terms in the far field. Note that Φ_{inc}, Φ_{ref}, W_{inc} and W_{ref} all satisfy the governing equations and boundary conditions on z independently; hence, φ and $\hat{w}$ must also satisfy those conditions automatically. The boundary conditions on x require slightly more attention. We substitute equations (2.31) and (2.32) into (2.24)-(2.30) to give the BVP to be solved for the functions $\varphi(x,z)$ and $\hat{w}(x)$:

$$\nabla^2\varphi = 0, \quad (x > 0,\ -1 \le z \le 0), \tag{2.33}$$

$$\varphi_z = 0, \quad (x > 0,\ z = -1), \tag{2.34}$$

$$\varphi_x = i\,\frac{\cosh(k(z+1))}{\sinh(k)}(1 - a_D), \quad (x = 0,\ -1 \le z \le 0), \tag{2.35}$$

$$\gamma\hat{w}_{xxxx} + \left(\frac{1}{k\tanh(k)} - \gamma k^4\right)\hat{w} = \varphi(x,0), \quad (x > 0), \tag{2.36}$$

$$\hat{w} = -(1 + a_D), \quad (x = 0), \tag{2.37}$$

$$\hat{w}_x = ik(1 - a_D), \quad (x = 0), \tag{2.38}$$

$$\varphi_z = \hat{w}, \quad (x > 0,\ z = 0), \tag{2.39}$$

$$\hat{w} \to 0, \quad (x \to \infty), \tag{2.40}$$

$$\varphi \to 0, \quad (x \to \infty). \tag{2.41}$$

The solution to equations (2.33)-(2.41), together with the total forms of the velocity potential and the plate deflection given by equations (2.31) and (2.32), fully describe the behaviour of the coupled ice–fluid system.

2.3 Solution

2.3.1 Fourier transform

To solve the set of equations (2.33)-(2.41) we apply a Fourier cosine transform (see for example Jeffrey, 2002):

$$\varphi^c(\xi,z) = \int_0^\infty \varphi(x,z)\cos(\xi x)\,dx, \tag{2.42}$$

$$w^c(\xi) = \int_0^\infty \hat{w}(x)\cos(\xi x)\,dx. \tag{2.43}$$

The inverse transforms are given by:

$$\varphi(x,z) = \frac{2}{\pi}\int_0^\infty \varphi^c(\xi,z)\cos(\xi x)\,d\xi, \tag{2.44}$$

$$\hat{w}(x) = \frac{2}{\pi}\int_0^\infty w^c(\xi)\cos(\xi x)\,d\xi. \tag{2.45}$$

The reasoning for the choice of a cosine transform instead of the usual Fourier transform is due to the physical situation. As we will see, the cosine transform will leave a term involving $\varphi_x(0,z)$ as a remnant, which is known due to (2.35). The cosine transform is hence the most appropriate transform for the current problem.

2.3.2 Velocity potential

Applying the transform (2.42) to equation (2.33) gives:

$$\int_0^\infty \big(\varphi_{xx} + \varphi_{zz}\big)\cos(\xi x)\,dx = 0,$$
$$\int_0^\infty \big(\varphi_{xx}\big)\cos(\xi x)\,dx + \frac{\partial^2}{\partial z^2}\int_0^\infty \varphi\cos(\xi x)\,dx = 0.$$

Using integration by parts gives

$$\big(\varphi_x\cos(\xi x)\big)_0^\infty - \int_0^\infty \varphi_x(-\xi\sin(\xi x))\,dx + \varphi^c_{zz} = 0,$$

and due to (2.41) this becomes

$$-\varphi_x(0,z) + \xi\int_0^\infty \varphi_x\sin(\xi x)\,dx + \varphi^c_{zz} = 0,$$
$$-\varphi_x(0,z) + \xi\left(\big(\varphi\sin(\xi x)\big)_0^\infty - \int_0^\infty \varphi\cos(\xi x)\xi\,dx\right) + \varphi^c_{zz} = 0,$$

and hence we have

$$\frac{d^2\varphi^c}{dz^2} - \xi^2\varphi^c = \varphi_x(0,z), \quad (-1 < z < 0). \tag{2.46}$$

Applying the transform to equations (2.34) and (2.39) gives two boundary conditions, and we now solve the following boundary value problem for φ^c:

$$\varphi^c_{zz} - \xi^2\varphi^c = i(1-a_D)\frac{\cosh(k(z+1))}{\sinh(k)}, \qquad (-1 < z < 0), \tag{2.47}$$
$$\varphi^c_z = 0, \qquad (z = -1), \tag{2.48}$$
$$\varphi^c_z = w^c(\xi), \qquad (z = 0). \tag{2.49}$$

Here we have used (2.35) to substitute for $\varphi_x(0,z)$. Equation (2.47) has a general solution given by:

$$\varphi^c(\xi,z) = C_1\sinh(\xi(z+1)) + C_2\cosh(\xi(z+1)) + \frac{i(1-a_D)}{k^2-\xi^2}\frac{\cosh(k(z+1))}{\sinh(k)}.$$

Here C_1 and C_2 are unknown functions of ξ. Equation (2.48) means that $C_1 = 0$. The second boundary condition (2.49) becomes

$$\varphi_z(x,0) = w^c(\xi) = C_2\xi\sinh(\xi) + \frac{ik(1-a_D)}{k^2-\xi^2},$$

which rearranges to

$$C_2 = \frac{1}{\xi \sinh(\xi)} \left(w^c(\xi) - \frac{ik(1-a_D)}{k^2 - \xi^2} \right).$$

Hence φ^c is given by

$$\varphi^c(\xi, z) = \frac{\cosh(\xi(z+1))}{\xi \sinh(\xi)} \left(w^c(\xi) - \frac{ik(1-a_D)}{k^2 - \xi^2} \right) + \frac{i(1-a_D)}{k^2 - \xi^2} \frac{\cosh(k(z+1))}{\sinh(k)}. \tag{2.50}$$

We will show later that φ^c is finite at $\xi = k$. Note that this is not the final equation for the potential φ^c because it includes w^c which is unknown at this point. In addition the reflected wave amplitude a_D is yet to be determined.

2.3.3 Plate deflection

Applying the transform (2.43) to the ice plate equation (2.36) gives

$$\gamma \int_0^\infty \hat{w}_{xxxx} \cos(\xi x)\, dx + \left(\frac{1}{k \tanh(k)} - \gamma k^4 \right) w^c = \varphi^c(\xi, 0). \tag{2.51}$$

We can evaluate the far left integral by repetitive integration by parts, and by using equations (2.38) and (2.40) we have:

$$\begin{aligned}
&\int_0^\infty \hat{w}_{xxxx} \cos(\xi x)\, dx \\
&= \big(\hat{w}_{xxx} \cos(\xi x)\big)_0^\infty + \xi \int_0^\infty \hat{w}_{xxx} \sin(\xi x)\, dx \\
&= -\hat{w}_{xxx}(0) + \xi \Big(\big(\hat{w}_{xx} \sin(\xi x)\big)_0^\infty - \int_0^\infty \hat{w}_{xx} \xi \cos(\xi x)\, dx \Big) \\
&= -\hat{w}_{xxx}(0) - \xi^2 \int_0^\infty \hat{w}_{xx} \cos(\xi x)\, dx \\
&= -\hat{w}_{xxx}(0) - \xi^2 \Big(\big(\hat{w}_x \cos(\xi x)\big)_0^\infty + \int_0^\infty \hat{w}_x \xi \sin(\xi x)\, dx \Big) \\
&= -\hat{w}_{xxx}(0) + \xi^2 \hat{w}_x(0) - \xi^3 \int_0^\infty \hat{w}_x \sin(\xi x)\, dx \\
&= -\hat{w}_{xxx}(0) + \xi^2 \hat{w}_x(0) - \xi^3 \Big(\big(\hat{w} \sin(\xi x)\big)_0^\infty - \int_0^\infty \hat{w} \xi \cos(\xi x)\, dx \Big) \\
&= -\hat{w}_{xxx}(0) + \xi^2 ik(1-a_D) + \xi^4 w^c(\xi).
\end{aligned}$$

Hence equation (2.51) becomes

$$\left(\frac{1}{k \tanh(k)} - \gamma k^4 + \gamma \xi^4 \right) w^c(\xi) = \varphi^c(\xi, 0) + \gamma \Big(\hat{w}_{xxx}(0) - \xi^2 ik(1-a_D) \Big). \tag{2.52}$$

Owing to the cosine Fourier transform, we now have an algebraic equation for the deflection w^c instead of a complicated fourth–order differential equation. Using

(2.50) we can now substitute $\varphi^c(\xi,0)$ into equation (2.52) to give:

$$\left(\gamma(\xi^4-k^4)+\frac{1}{k\tanh(k)}-\frac{1}{\xi\tanh(\xi)}\right)w^c(\xi)=$$
$$\frac{i(1-a_D)}{k^2-\xi^2}\left(\frac{1}{\tanh(k)}-\frac{k}{\xi\tanh(\xi)}\right)+\gamma\Big(\hat{w}_{xxx}(0)-\xi^2ik(1-a_D)\Big). \tag{2.53}$$

We notice that the left hand side of equation (2.53) is equal to zero at $\xi=k$ due to the dispersion relation (2.22). Hence, to avoid a singularity we require that the limit of the right hand side as $\xi\to k$ is also equal to zero. We therefore require

$$0=\gamma\Big(\hat{w}_{xxx}(0)-k^3i(1-a_D)\Big)+i(1-a_D)\lim_{\xi\to k}\left(\frac{1}{k^2-\xi^2}\left(\frac{1}{\tanh(k)}-\frac{k}{\xi\tanh(\xi)}\right)\right). \tag{2.54}$$

We assess the limit on the right hand side using L'Hôpital's rule:

$$\begin{aligned}
&\lim_{\xi\to k}\left(\frac{1}{k^2-\xi^2}\left(\frac{1}{\tanh(k)}-\frac{k}{\xi\tanh(\xi)}\right)\right)\\
&=\lim_{\xi\to k}\left(\frac{-1}{2\xi}\left(\frac{k}{\xi^2\tanh(\xi)}+\frac{k}{\xi\cosh^2(\xi)\tanh^2(\xi)}\right)\right)\\
&=\lim_{\xi\to k}\left(\frac{-1}{2\xi}\left(\frac{k}{\xi^2\tanh(\xi)}+\frac{k}{\xi\sinh^2(\xi)}\right)\right)\\
&=\lim_{\xi\to k}\left(\frac{-1}{2\xi}\left(\frac{k}{\xi^2\tanh(\xi)}+\frac{k}{\xi}\left\{\frac{1}{\tanh^2(\xi)}-1\right\}\right)\right)\\
&=\frac{1}{2k}-\frac{1}{2k^2\tanh(k)}-\frac{1}{2k\tanh^2(k)}.
\end{aligned}$$

Substituting this into equation (2.54) gives

$$\gamma\hat{w}_{xxx}(0)=ik^3(1-a_D)\gamma+i(1-a_D)\Big(\frac{1}{2k^2\tanh(k)}+\frac{1}{2k\tanh^2(k)}-\frac{1}{2k}\Big). \tag{2.55}$$

We define the function

$$V(k)=\frac{1}{2k^2\tanh(k)}+\frac{1}{2k\tanh^2(k)}-\frac{1}{2k}, \tag{2.56}$$

and then the right hand side of equation (2.53) now reads

$$i(1-a_D)\left(V(k)+\frac{1}{k^2-\xi^2}\left(\frac{1}{\tanh(k)}-\frac{k}{\xi\tanh(\xi)}\right)+\gamma k^3-\gamma\xi^2k\right).$$

By dividing across the left hand side of (2.53) we can explicitly write the equation for plate deflection as

$$w^c(\xi)=i(1-a_D)Q(\xi), \tag{2.57}$$

where the function $Q(\xi)$ is defined as

$$Q(\xi) = \frac{\xi \tanh(\xi)\Big(V(k) + \gamma k(k^2 - \xi^2)\Big) + \dfrac{1}{k^2 - \xi^2}\left(\dfrac{\xi \tanh(\xi)}{\tanh(k)} - k\right)}{\xi \tanh(\xi)\left(\gamma(\xi^4 - k^4) + \dfrac{1}{k \tanh(k)}\right) - 1}. \tag{2.58}$$

The coefficient a_D which defines the reflected wave amplitude is still undefined. We note that we have two equations for the deflection $\hat{w}(0)$. One is found by applying the inverse transform (2.45) at $x = 0$, giving

$$\hat{w}(0) = \frac{2}{\pi} \int_0^\infty w^c(\xi)\, d\xi.$$

The other is given by equation (2.37), due to the ice–clamping condition. Equating these, we have

$$\hat{w}(0) = -(1 + a_D) = i(1 - a_D)\frac{2}{\pi} \int_0^\infty Q(\xi)\, d\xi.$$

Denoting

$$\chi = \frac{2}{\pi} \int_0^\infty Q(\xi)\, d\xi,$$

we have

$$\begin{aligned} 1 + a_D &= -i\chi(1 - a_D), \\ a_D\Big(1 - i\chi\Big) &= -\Big(1 + i\chi\Big), \\ a_D &= -\frac{1 + i\chi}{1 - i\chi}. \end{aligned} \tag{2.59}$$

Equation (2.59) directly implies that

$$|a_D| = 1, \tag{2.60}$$

which in turn means we can write

$$a_D = e^{i\theta}, \tag{2.61}$$

where θ is the phase shift between the incident and reflected waves. Equation (2.60) corresponds to the energy conservation relation for hydroelastic wave reflection by a vertical wall. To calculate θ, we introduce the parameter α such that

$$e^{i\alpha} = \begin{cases} \frac{1+i\chi}{(1+\chi^2)^{1/2}} & \text{if } \chi > 0, \\ \frac{1-i\chi}{(1+\chi^2)^{1/2}} & \text{if } \chi < 0. \end{cases}$$

For $\chi > 0$, by equations (2.61) and (2.59) we have

$$e^{i\theta} = -e^{2i\alpha} = e^{2i\alpha + i\pi}.$$

If $\chi < 0$, we have

$$ae^{i\theta} = -ae^{-2i\alpha} = ae^{-2i\alpha+i\pi}.$$

We calculate α via the equation

$$\cos(\alpha) = \frac{1}{(1+\chi^2)^{\frac{1}{2}}},$$

and finally

$$\theta = \begin{cases} \pi + 2\alpha & \text{if } \chi > 0, \\ \pi - 2\alpha & \text{if } \chi < 0. \end{cases}$$

The phase shift θ is plotted against k in Figure 2.4. The phase shift tends to 2π in

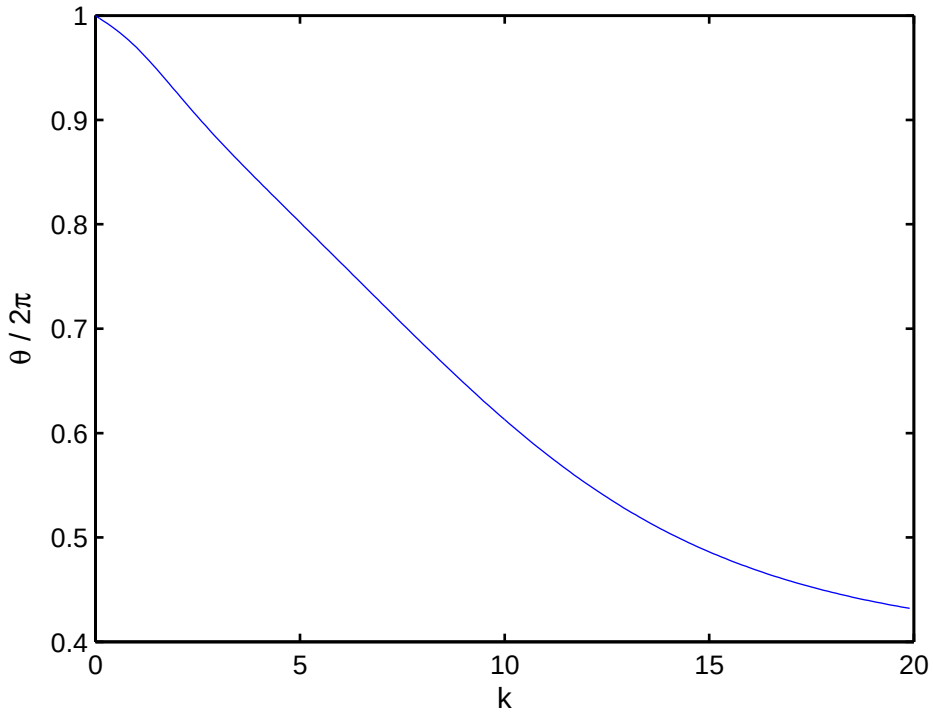

Figure 2.4: The phase shift $\theta/2\pi$ is plotted against k. The values of other parameters are taken from Table 2.1(a).

the limit $k \to 0$. This is expected as the limit $k \to 0$ represents a flat ice surface, and $\theta = 2\pi$ indicates no phase shift.

Equation (2.57) becomes

$$w^c(\xi) = i(1 - e^{i\theta})Q(\xi), \tag{2.62}$$

with $Q(\xi)$ given by equation (2.58). The final solution for the plate deflection is then given by (2.62).

With $w^c(\xi)$ and a_D obtained, the final solution for the velocity potential φ^c is written:

$$\varphi^c(\xi, z) = i(1 - e^{i\theta})L(\xi, z), \tag{2.63}$$

where the function $L(\xi)$ is given by

$$L(\xi, z) = \frac{\cosh(\xi(z+1))}{\xi \sinh(\xi)} \left(Q(\xi) - \frac{k}{k^2 - \xi^2} \right) + \frac{\cosh(k(z+1))}{(k^2 - \xi^2)\sinh(k)}. \tag{2.64}$$

The important functions $Q(\xi)$ and $L(\xi)$ are crucial to determining the behaviour of the solution close to the vertical wall.

2.3.4 $Q(k)$ and $L(k, z)$

The functions $Q(k)$ and $L(k, z)$ contain terms involving the fraction $1/(k^2 - \xi^2)$. These terms could present numerical difficulties close to $\xi = k$. In this section we prove that the functions Q and L are finite at the value $\xi = k$.

Using equation (2.58), we split the equation $Q(\xi)$ into

$$Q(\xi) = \frac{Q_1(\xi) + Q_2(\xi)}{Q_3(\xi)}, \tag{2.65}$$

where we define

$$\begin{aligned}
Q_1(\xi) &= \xi \tanh(\xi) \Big(V(k) + \gamma k (k^2 - \xi^2) \Big), \\
Q_2(\xi) &= \frac{1}{k^2 - \xi^2} \left(\frac{\xi \tanh(\xi)}{\tanh(k)} - k \right), \\
Q_3(\xi) &= \xi \tanh(\xi) \left(\gamma(\xi^4 - k^4) + \frac{1}{k \tanh(k)} \right) - 1.
\end{aligned}$$

Recall that $Q_1(k) + Q_2(k) = 0$ by construction, and $Q_3(k) = 0$ by the dispersion relation. Firstly, the Taylor expansion of $Q_1(\xi)$ close to $\xi = k$ is given by

$$Q_1(\xi) = Q_1(k) + Q_1'(k)(\xi - k) + ...,$$

where dashes indicate differentiation with respect to ξ, and ellipses indicate terms of order $(\xi - k)^2$ and higher. $Q_1'(k)$ is simple to evaluate and Q_1 presents no further difficulties. $Q_2(\xi)$ requires slight manipulation to eliminate the $1/(k^2 - \xi^2)$ term. We rewrite thus:

$$\begin{aligned}
Q_2(\xi) &= \frac{1}{k^2 - \xi^2} \left(\frac{\xi \tanh(\xi)}{\tanh(k)} - k + \xi - \xi \right) \\
&= \frac{\xi - k}{(k + \xi)(k - \xi)} + \xi \left(\frac{\tanh(\xi) - \tanh(k)}{\tanh(k)(k^2 - \xi^2)} \right) \\
&= \frac{-1}{k + \xi} + \frac{\xi}{(k + \xi)\tanh(k)} \left(\frac{\tanh(\xi) - \tanh(k)}{k - \xi} \right).
\end{aligned}$$

It is simpler to expand each part separately about $\xi = k$ using Taylor series:

$$\begin{aligned}
\frac{-1}{k+\xi} &= -\frac{1}{2k} + \frac{1}{4k^2}(\xi - k) + ..., \\
\frac{\xi}{k+\xi} &= \frac{1}{2} + \frac{1}{4k}(\xi - k) + ..., \\
\tanh(\xi) &= \tanh(k) + \frac{1}{\cosh^2(k)}(\xi - k) - \frac{\sinh(k)}{\cosh^3(k)}(\xi - k)^2 + \mathrm{O}(\xi - k)^3,
\end{aligned}$$

which means we can write

$$\frac{\tanh(\xi) - \tanh(k)}{k - \xi} = -\frac{1}{\cosh^2(k)} + \frac{\sinh(k)}{\cosh^3(k)}(\xi - k) + ...,$$

having cancelled the $(k - \xi)$ factor on the right hand side. Hence, after multiplying the terms together, $Q_2(\xi)$ close to $\xi = k$ becomes

$$Q_2(\xi) = Q(k) + A(k)(\xi - k) + ...,$$

where

$$A(k) = \frac{1}{4k^2} + \frac{1}{2\cosh^2(k)} - \frac{1}{4k\sinh(k)\cosh(k)}.$$

The function $Q_3(\xi)$ can also be expanded close to $\xi = k$ using Taylor series as

$$Q_1(\xi) = Q_3(k) + Q_3'(k)(\xi - k) + ...,$$

and the differentiation is again trivial. Hence, with Q_1, Q_2 and Q_3 all expanded, we use (2.65) to write

$$Q(\xi) = \frac{Q_1(k) + Q_1'(k)(\xi - k) + Q_2(k) + A(k)(\xi - k)}{Q_3(k) + Q_3'(k)(\xi - k)} + ...$$

Evaluating the above equation at $\xi = k$ means $Q_1(k) + Q_2(k) = 0$ and $Q_3(k) = 0$. The remaining terms all have a $(\xi - k)$ factor, which cancels leaving

$$Q(k) = \frac{Q_1'(k) + A(k)}{Q_3'(k)}.$$

Performing the differentiation yields the long-winded but exact value of $Q(k)$, given by

$$Q(k) = \frac{\left(\tanh(k) + \frac{k}{\cosh^2(k)}\right) V(k) - 2k^3\gamma\tanh(k) + \frac{1}{4k^2} + \frac{1}{2\cosh^2(k)} - \frac{1}{4k\sinh(k)\cosh(k)}}{\left(\tanh(k) + \frac{k}{\cosh^2(k)}\right)\frac{1}{k\tanh(k)} + 4k^4\gamma\tanh(k)}. \tag{2.66}$$

Using (2.64), the function $L(k,z)$ can now be written

$$L(k,z) = Q(k)\,\frac{\cosh(k(z+1))}{k\sinh(k)} + \lim_{\xi\to k}\frac{1}{k^2-\xi^2}\left(\frac{\cosh(k(z+1))}{\sinh(k)} - \frac{k\cosh(\xi(z+1))}{\xi\sinh(\xi)}\right). \tag{2.67}$$

The second term in this equation requires application of l'Hôpital's rule, which is straightforward and we obtain

$$\lim_{\xi\to k} L(\xi,z) = \frac{(z+1)\sinh(k(z+1)) + 2Q(k)\cosh(k(z+1)}{2k\sinh(k)} - \frac{\cosh(k(z+1))\big(\sinh(k)+k\cosh(k)\big)}{2k^2\sinh^2(k)}. \tag{2.68}$$

The function $Q(\xi)$ given by equation (2.58) is therefore smooth everywhere. The function Q is plotted against ξ in Figure 2.5.

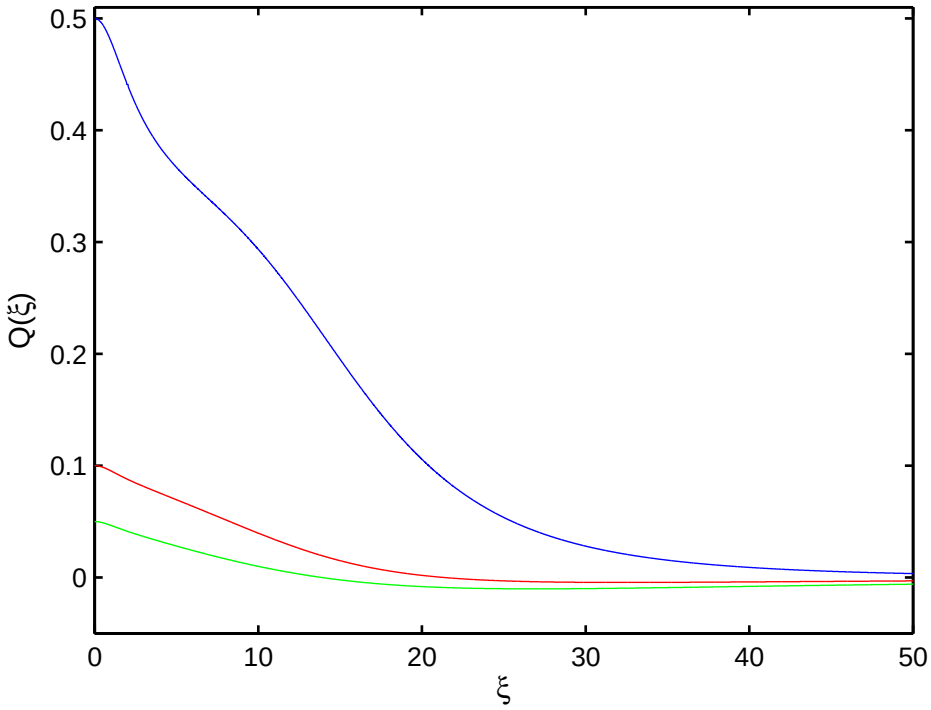

Figure 2.5: The function Q is plotted against ξ for $k = 2$ (blue), $k = 10$ (red), $k = 20$ (green).

We note that $Q(0) = k^{-1}$, and that $Q(\xi)$ decays with order ξ^{-2} as $\xi \to \infty$.

2.3.5 Inverse transforms

Recall that the inverse transforms to return to $x - z$ co-ordinates are given by

$$\varphi(x,z) = \frac{2}{\pi}\int_0^\infty \varphi^c(\xi,z)\cos(\xi x)\,d\xi, \tag{2.69}$$

$$\hat{w}(x) = \frac{2}{\pi}\int_0^\infty w^c(\xi)\cos(\xi x)\,d\xi. \tag{2.70}$$

Here the functions w^c and φ^c are given by (2.62) and (2.63). We can work backwards through the analysis, using equation (2.32) and (2.10) to give the expression for the deflection $w(x,t)$:

$$w(x,t) = \Re\left(e^{-it}\left(ie^{-ikx} + ie^{i(\theta+kx)} + \frac{2}{\pi}(e^{i\theta}-1)\int_0^\infty Q(\xi)\cos(\xi x)\,d\xi \right)\right). \quad (2.71)$$

Defining the integral as

$$g(x) = \int_0^\infty Q(\xi)\cos(\xi x)\,d\xi, \quad (2.72)$$

and taking the real part of (2.71) yields the final solution for the ice deflection:

$$w(x,t) = \sin(kx+t) - \sin(\theta+kx-t) + \frac{2g(x)}{\pi}\big(\cos(\theta-t)-\cos(t)\big). \quad (2.73)$$

We note that the inverse transforms (2.69)-(2.70) (and therefore the integrals involved in the calculation of $g(x)$ and θ) are too complicated to be evaluated analytically, and they are hence calculated numerically. This is achieved using standard integral quadrature techniques. As mentioned previously, the function $Q(\xi)$ decays with order ξ^{-2} as $\xi \to \infty$, causing the integrals to converge rapidly. Figure 2.6 demonstrates an example inverse transform.

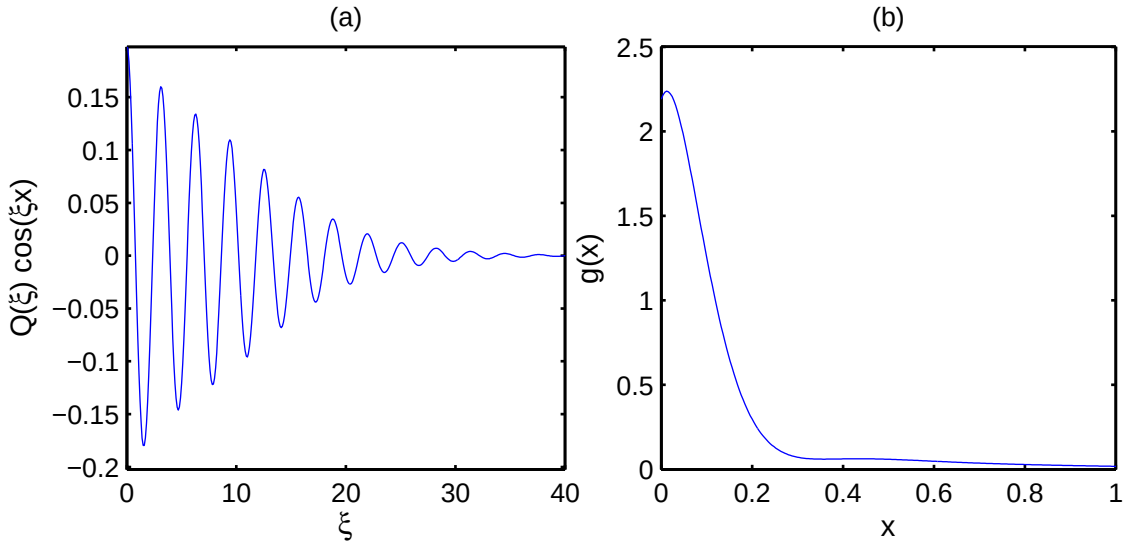

Figure 2.6: (a) The integrand of g is plotted against ξ illustrating its rapid decay. Here $x = 2$. (b) The function $g(x)$ plotted against x. In both cases, $k = 5$ and the remaining parameter values are taken from Table 2.1(a).

Figure 2.6(b) is particularly important, because $g(x)$ represents the part of the solution *not* corresponding to either the incident or reflected waves; the part of the solution to account for the presence of the vertical wall. Figure 2.6(b) shows how far from the wall g has influence.

2.4 Numerical results

In this section, we present numerical results for the ice deflection and the strain in the ice sheet. We also study the vertical shear force on the wall, and the horizontal force. There are many physical parameters in the present problem, defining the properties of the fluid and the ice sheet, that can vary in certain ranges. When presenting results, the data from Table 2.1(a) is used unless stated otherwise. We are particularly interested in varying the wavenumber k, as well as the thickness of the ice sheet, to give a fair representation of waves in ice sheets. We should be careful when varying the fluid depth H, since it was used as a length scale. Therefore when investigating the effect of varying H we must revert to dimensional variables.

We note that the dimensionless solution depends only on two parameters, γ and k. Note that γ contains ω, which depends on k. When varying parameters, we will state the parameters in their dimensional quantity for clarity, then substitute those values to calculate the dimensionless solution. The results are mostly presented in dimensionless variables; however, some results (such as forces on the wall) are best presented dimensionally, to facilitate a physical understanding. We continue to assume that all variables/parameters are dimensionless; for clarity we add the suffix 'dim' to dimensional quantities, which are also accompanied by units.

Since the variables which are periodic in time, the notation "$|\quad|$" is used to indicate the magnitude of a variable with respect to time (the maximum value of the variable for any time). For example, the deflection $w(x,t)$ given by equation (2.73) can be rewritten as

$$w(x,t) = c(x)\sin(t) + d(x)\cos(t), \tag{2.74}$$

for functions $c(x)$ and $d(x)$. Introducing $A(x)$ and $\delta(x)$ such that $c = A\cos(\delta)$ and $d = -A\sin(\delta)$ this can be rewritten more conveniently as

$$w(x,t) = A(x)\cos(t+\delta). \tag{2.75}$$

This allows us to plot the magnitude of the deflection $|w(x)|$, given by $A = \sqrt{c^2 + d^2}$. This procedure removes time as a factor from figures for clarity.

2.4.1 Deflection of the ice sheet

We begin by plotting the ice sheet deflection, given by equation (2.73). Figure 2.7 shows the deflection for three values of the wavenumber k. We see that the ice deflection and slope of the deflection are zero at $x = 0$ as required by the ice–clamping condition. We also note the effect of the ice clamping on the first wave peak. It is smaller in magnitude and wavelength than subsequent waves. For $k = 20$, there is also some disturbance in the subsequent wave peaks, until the deflection settles to a regular wave. This phenomenon is less visible for smaller k values because the wavelength is long enough such that there is only one or two

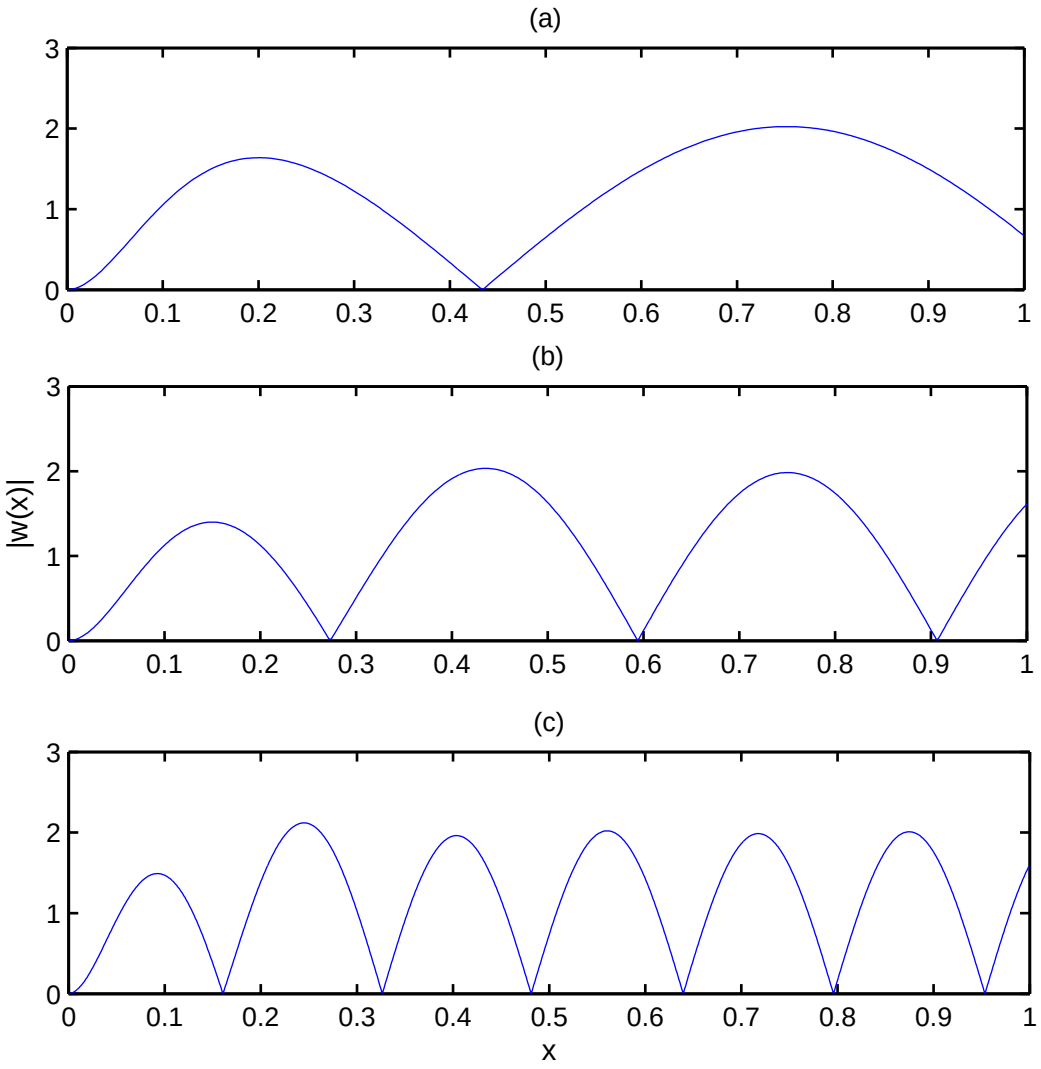

Figure 2.7: The deflection $|w(x)|$ plotted against x for (a) $k = 5$, (b) $k = 10$ and (c) $k = 20$. All other parameters are set to their default value.

wave peaks before the influence of the vertical wall wanes (see Figure 2.6(b)).

We now plot the ice deflection for varying ice thickness, keeping the wavenumber fixed at $k = 10$. This is shown in Figure 2.8. The wave for thickness $h = 1$ m

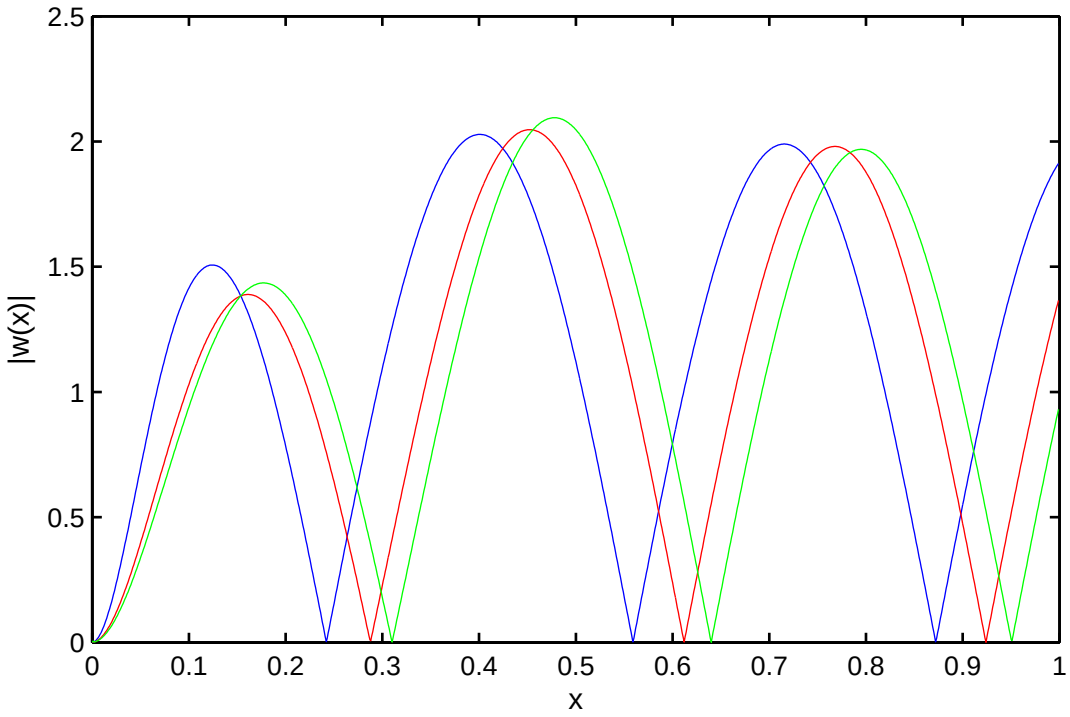

Figure 2.8: The deflection $|w(x)|$ plotted against x for ice thickness $h = 1.0$ m (blue), $h = 2.0$ m (red) and $h = 3.0$ m (green). All other parameters are set to their default value and $k = 10$.

is most strongly affected by the ice clamping, with the wave closest to the wall having smaller wavelength than the waves for thicker ice. This is consistent with expectations, since thinner ice has less flexural rigidity and is hence more malleable. The wave for thickness $h = 3$ m has slightly higher second peak.

We now wish to study the effect of the fluid depth on the ice deflection. Figure 2.9 shows the deflection for four different depths, $H = 50, 100, 200, 300$ m. We see that for deep water, the effect of changing the depth is negligible, demonstrated by the curves for $H = 200$ m and $H = 300$ m being almost identical. As the fluid becomes shallower, we start to see more variance; the depth affects the amplitude of the first peak more than the wavelength, with $H = 50$ m giving the smallest first peak. The overall impact of varying the depth is not as profound as varying the ice thickness.

2.4.2 Strain in the ice sheet

We now turn our attention to the elastic strain ε in the ice sheet. The strain was defined and discussed in Section 1.4. If the computed strain value exceeds the yield strain of ice, the ice sheet is more likely to fracture. Of particular interest in this section is the value of the strain at the vertical wall, as this will determine whether the edge conditions (2.8) are realistic.

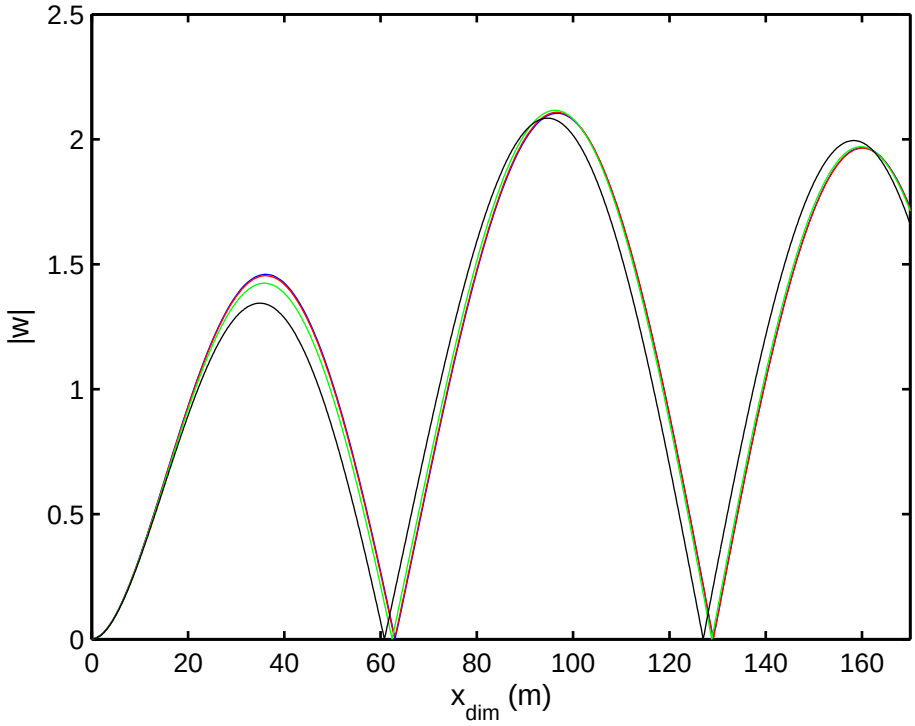

Figure 2.9: The deflection $|w(x)|$ plotted against x for fluid depth $H = 300\,\mathrm{m}$ (blue), $H = 200\,\mathrm{m}$ (red), $H = 100\,\mathrm{m}$ (green) and $H = 50\,\mathrm{m}$ (black). All other parameters are set to their default value and $k_{dim} = 0.05\,\mathrm{m}^{-1}$.

Squire (1993a) dealt with ice–breakup, and the theory was found to be in accordance with Goodman et al. (1980), who used a wire strainmeter to measure the strains in sea ice. An observed fracture strain is reported at $3\,\mathrm{x}\,10^{-5}$, and the theory suggests a crack will propagate if the strain reaches $4.3\,\mathrm{x}\,10^{-5}$. Squire & Martin (1980) determine the fracture strain for Bering Sea ice to be $4.4 - 8.5\,\mathrm{x}\,10^{-5}$. In this chapter we take an estimate of yield strain $\varepsilon_{cr} = 8\,\mathrm{x}\,10^{-5}$.

In dimensionless variables, the strain is calculated by the equation (Ugural, 1981):

$$\varepsilon = \frac{ah}{2H^2}\frac{\partial^2 w}{\partial x^2}. \tag{2.76}$$

It should be noted that calculation of the second derivative in (2.76) is not straightforward. According to (2.73), we need to evaluate the second derivative of the function $g(x)$ given by (2.72), where $Q(\xi) = \mathrm{O}(1/\xi^2)$ as $\xi \to \infty$. We define a new function $q(\xi)$ as

$$q(\xi) = Q(\xi) + \frac{k}{\xi^2 + 1}, \tag{2.77}$$

where $q(\xi) = \mathrm{O}(1/\xi^3)$ as $\xi \to \infty$. Then

$$\begin{aligned}\frac{\partial^2 g(x)}{\partial x^2} &= \frac{\partial^2}{\partial x^2}\int_0^\infty (q - \frac{k}{\xi^2+1})\cos(\xi x)\,d\xi \\ &= \frac{\partial^2}{\partial x^2}\Big(\int_0^\infty q(\xi)\cos(\xi x)\,d\xi - \int_0^\infty \frac{k\cos(\xi x)}{\xi^2+1}\,d\xi\Big) \\ &= -\int_0^\infty \xi^2 q(\xi)\cos(\xi x)\,d\xi - k\frac{\partial^2}{\partial x^2}\left(\frac{\pi}{2}e^{-x}\right) \\ &= -\int_0^\infty \xi^2 q(\xi)\cos(\xi x)\,d\xi - \frac{k\pi}{2}e^{-x},\end{aligned}$$

where the last integral can be numerically evaluated. Here we have used the standard result from Gradshteyn & Ryzhik (2007):

$$\int_0^\infty \frac{\cos(yx)}{y^2+1}\,dy = \frac{\pi}{2}e^{-x}. \tag{2.78}$$

The strain can then be calculated by differentiating equation (2.73) and using (2.76) to give

$$\begin{aligned}\varepsilon = \frac{ah}{2H^2}\Bigg(&-k^2\sin(kx+t) + k^2\sin(\theta+kx-t) \\ &- \frac{2}{\pi}\big(\cos(\theta-t)-\cos(t)\big)\left(\int_0^\infty \xi^2 q(\xi)\cos(\xi x)\,d\xi - \frac{k\pi}{2}e^{-x}\right)\Bigg).\end{aligned}$$

To begin, we plot the maximum strain with respect to time $|\varepsilon|$ against x, for $k = 5$ and $k = 10$. This is shown in Figure 2.10. The most striking feature of this figure is that the strain is far higher at the point where the ice meets the vertical wall than for the rest of the strain profile. This is due to the ice–clamping condition. If fracture occurs, it is likely to do so at $x = 0$. We note that the strain has a linear dependence on the wave amplitude; it is arbitrarily chosen as $a = 1$ cm for this graph. The strain is below its yield value ε_{cr} for both values of k for the current parameters. We also see that away from the wall, the strain is higher for larger k; this is of course expected, since shorter wavelength causes more curvature in the ice and hence more strain.

With the knowledge that the strain is highest at the ice-wall connection, we may now plot the maximum strain (the strain at $x = 0$) for each k. This is shown in Figure 2.11 for varying values of the ice thickness. The strain is finite in the $k \to 0$ limit. In general the maximum strain increases as the waves become shorter, though there exists a non-zero k for each curve that gives minimum strain for each thickness. For long waves, the highest maximum strain is given by thinner ice. However, this is reversed as the waves become shorter, and for short waves, thicker ice gives more strain at the ice-wall boundary.

The maximum strain is plotted against k for varying fluid depth H in Figure 2.12. Depth variation is not as important as ice thickness in determining the strain

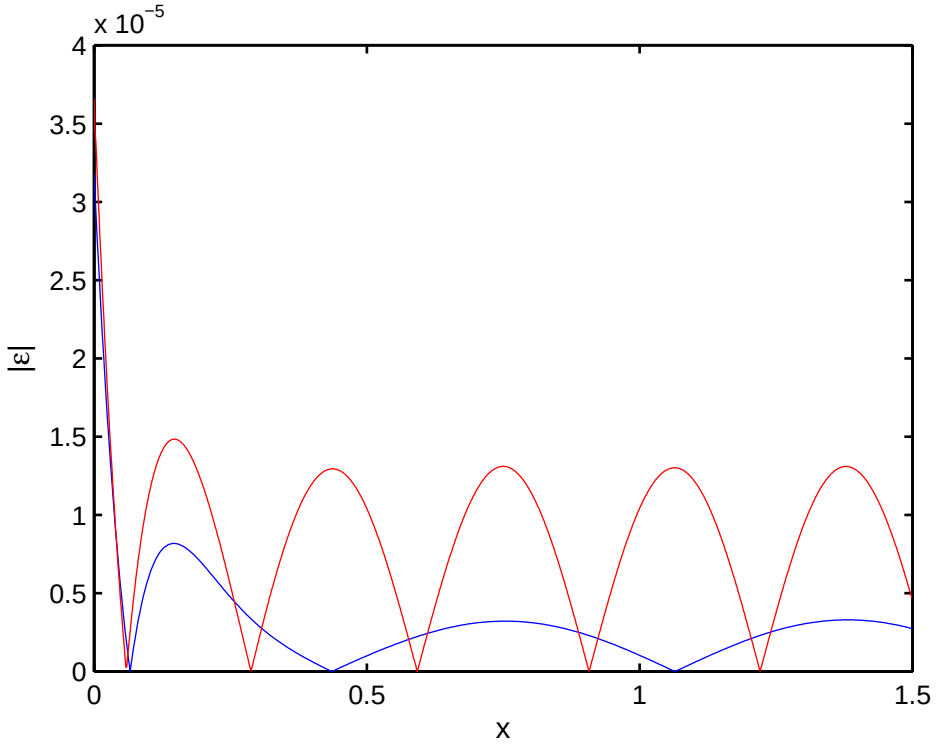

Figure 2.10: The strain $|\varepsilon|$ is plotted against x for $k = 5$ (blue) and $k = 10$ (red). All other parameters are set to their default value and the amplitude is chosen as $a = 1\,\text{cm}$.

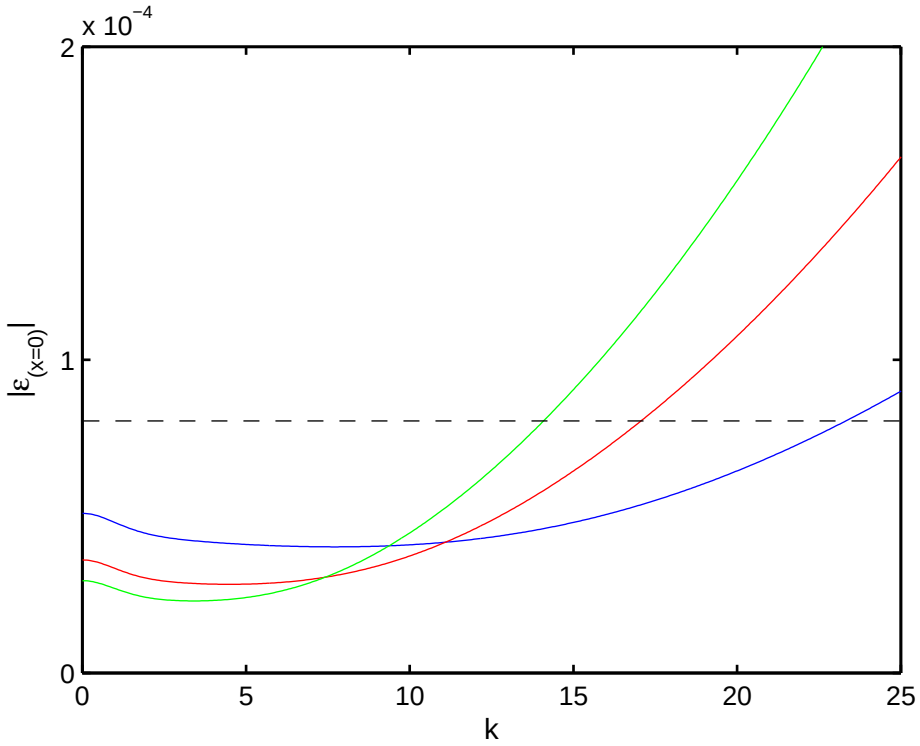

Figure 2.11: The maximum strain $|\varepsilon_{(x=0)}|$ is plotted against k for ice thickness $h = 1.0\,\text{m}$ (blue), $h = 2.0\,\text{m}$ (red) and $h = 3.0\,\text{m}$ (green). The dashed line indicates the critical strain $|\varepsilon_{cr}|$. All other parameters are set to their default value and the amplitude is chosen as $a = 1\,\text{cm}$.

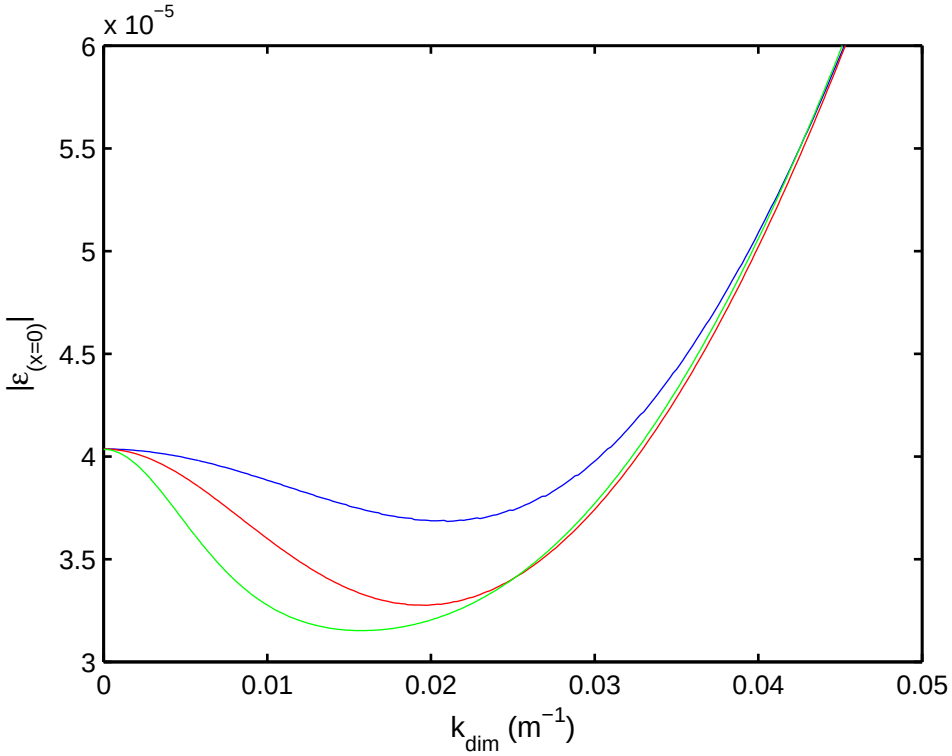

Figure 2.12: The maximum strain $|\varepsilon_{(x=0)}|$ is plotted against k for fluid depth $H = 50\,\mathrm{m}$ (blue), $H = 100\,\mathrm{m}$ (red) and $H = 200\,\mathrm{m}$ (green). All other parameters are set to their default value and the amplitude is chosen as $a = 1\,\mathrm{cm}$.

along the wall, which is expected due to the results for the ice deflection. The depth only influences longer waves from approximately $k_{dim} = 0 - 0.04\,\mathrm{m}^{-1}$ (corresponding to $\lambda \approx 0 - 150\,\mathrm{m}$). We see that shallower water causes more strain within this range, but all three curves coalesce in the limit $k_{dim} \to 0$ and when $k_{dim} > 0.04\,\mathrm{m}^{-1}$.

Because the amplitude was chosen rather arbitrarily in the preceding analysis of the strain, we now investigate the wave amplitude in more detail to allow a broader understanding. Due to the linear dependence of the strain on wave amplitude, we can plot the maximum allowable amplitude while retaining a strain of $|\varepsilon_{cr}|$. This is shown in Figure 2.13. The maximum allowable strain at $x = 0$ is compared with the maximum allowable strain far from the wall for comparison. As k grows, only waves of a few centimetres are permitted.

2.4.3 Shear force on the wall

One of the physical forces on the wall caused by the motion of the ice sheet is the vertical shear force. Due to the ice–clamping condition, the ice exerts a lifting force on the wall, something that must be considered in the design of ocean structures in ice–covered water. The shear force is defined in dimensionless variables as (Ugural, 1981)

$$V^{SH} = -w_{xxx}(0,t) \tag{2.79}$$

The dimensional shear force is given by $V^{SH}_{dim} = (aEJ/H^3)V^{SH}$. Fortunately, we do not have to perform the differentiation of $\hat{w}$: the third derivative can be calculated

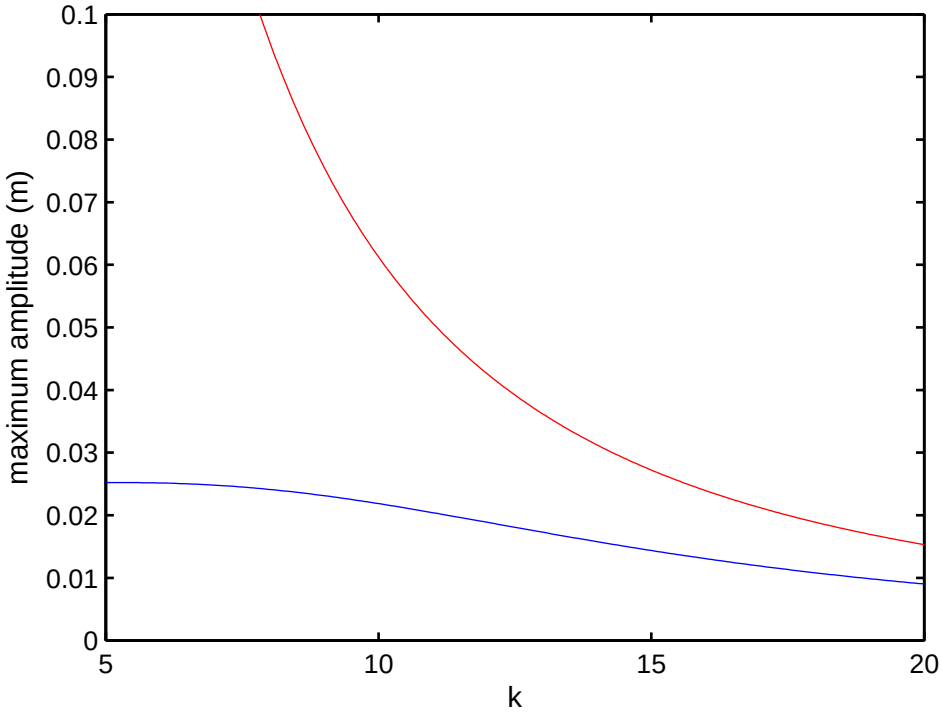

Figure 2.13: The maximum allowable wave amplitude, calculated to ensure the strain $|\varepsilon| = 8 \times 10^{-5}$. The blue curve shows the maximum amplitude for the strain at $x = 0$, and the red curve shows the maximum amplitude for waves far from the wall.

by equation (2.55). This allows us to circumvent any convergence issues that may have arisen due to this differentiation. We have, from equations (2.10) and (2.32):

$$\begin{aligned} V^{SH} &= -\Re\left(i\frac{\partial^3 W(0)}{\partial x^3}e^{-it}\right) = -\Re\left(ie^{-it}\left(\frac{\partial^3 W_{inc}}{\partial x^3} + \frac{\partial^3 W_{ref}}{\partial x^3} + \frac{\partial^3 \hat{w}}{\partial x^3}\right)_{x=0}\right) \\ &= -\Re\Big(ie^{-it}\Big((-ik)^3 + (ik)^3 a_D + w_{xxx}(0)\Big)\Big) \\ &= -\Re\Big(ie^{-it}\Big(i(1-e^{i\theta})(2k^3 + \gamma^{-1}V(k))\Big)\Big). \end{aligned}$$

We then substitute using (2.55) and take the maximum shear force over time to give, after some algebra:

$$|V^{SH}| = \sqrt{2 - 2\cos(\theta)}\left(2k^3 + \frac{1}{2k^2\gamma\tanh(k)} + \frac{1}{2k\gamma\sinh^2(k)}\right). \tag{2.80}$$

Figure 2.14 shows the dimensional shear force plotted against the wavenumber k. The ice can exert a significant lifting force on the vertical wall. We see that the shear force is finite in the limit $k \to 0$ (an expression for this limit is given in Brocklehurst et al., 2010), and as k increases the shear force decreases to a minimum before increasing monotonically. Thicker ice generates more vertical force; this is congruent with our expectations since thicker ice has more contact with the wall. The sensitivity of the force to the ice thickness is more pronounced as the waves become shorter.

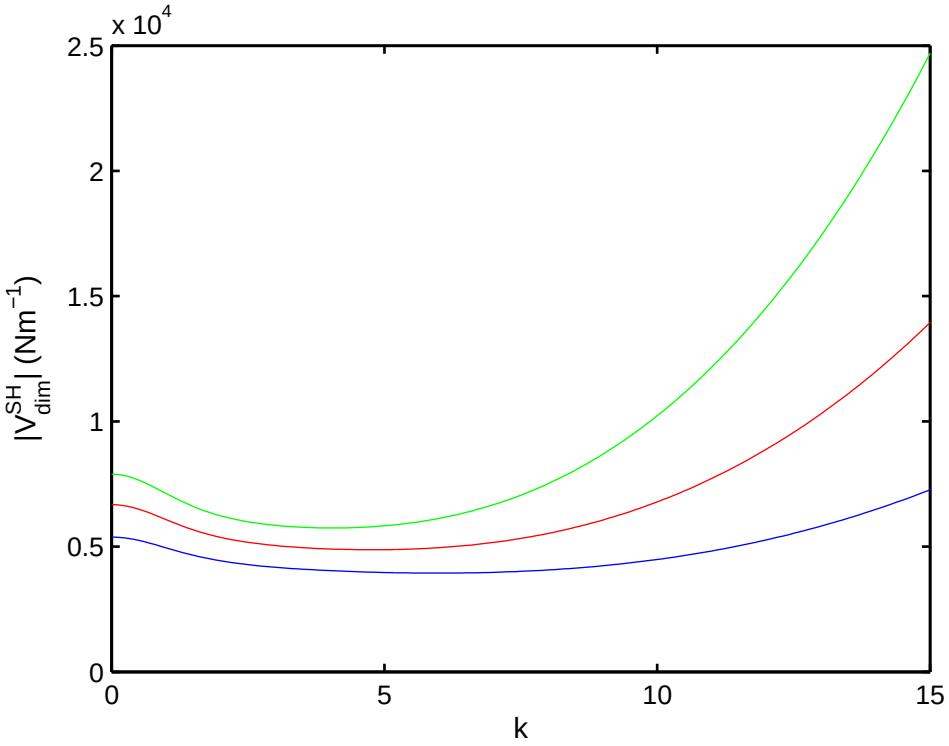

Figure 2.14: The vertical shear force is plotted against k for ice thickness $h = 1.5\,\mathrm{m}$ (blue), $h = 2.0\,\mathrm{m}$ (red) and $h = 2.5\,\mathrm{m}$ (green). Here the incident wave amplitude is $a = 1\,\mathrm{cm}$ and the other parameters are set to their default value.

We now vary the depth H, as shown in Figure 2.15. For shorter waves the effect of depth variance is magnified. Shallower water causes a large increase in vertical force: this is physically plausible since the structure is closer to the ice surface, and since the cross-sectional area over which the force is applied is shorter, the force is increased. For long waves the depth has little effect and the three curves coalesce.

2.4.4 Horizontal force

The horizontal force on a structure is another quantity with practical importance in ocean engineering. It can be calculated readily by integrating the pressure over the surface of the wall. The pressure in the fluid is given by (2.5), and we define the dimensional hydrodynamic horizontal force F as

$$F_{dim} = F^h_{dim} + F^w_{dim}. \tag{2.81}$$

Here F^h_{dim} is the hydrostatic wave force component given by

$$F^h_{dim} = -\rho g H^2 \int_{-1}^{0} z\,dz = \frac{\rho g H^2}{2}. \tag{2.82}$$

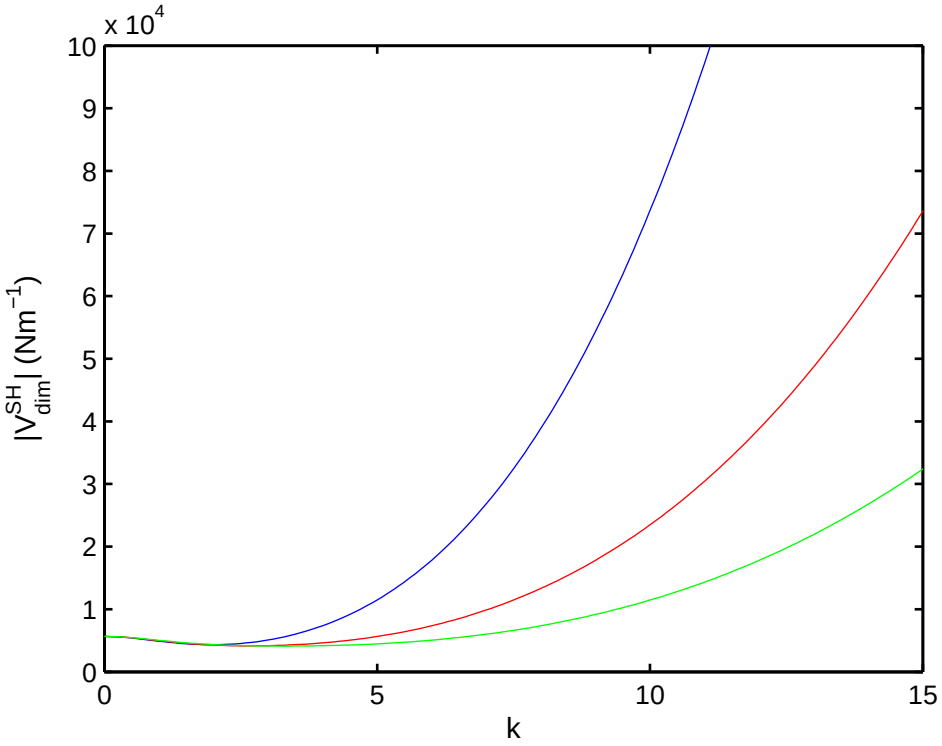

Figure 2.15: The vertical shear force is plotted against k for fluid depth $H = 100\,\mathrm{m}$ (blue), $H = 150\,\mathrm{m}$ (red) and $H = 200\,\mathrm{m}$ (green). Here the incident wave amplitude is $a = 1\,\mathrm{cm}$ and the other parameters are set to their default value.

F^h_{dim} is the constant force on the wall due to the fluid at rest. We are interested in the horizontal wave force component F^w, given in dimensionless variables by

$$F^w = -\int_{-1}^{0} \frac{\partial \phi(0,z,t)}{\partial t} dz. \tag{2.83}$$

Here $F^w = F^w_{dim}/(\rho H^2 a\omega^2)$.

We require $\phi_t(0,z,t)$, which is calculated using equation (2.9); $\Phi(0,z)$ is then calculated using (2.31). The required function $\varphi(0,z)$ is then calculated by performing an inverse transform of the solution (2.63) using (2.44). Hence we have:

$$\begin{aligned}\phi_t(0,z,t) &= \Re(-i\Phi(0,z)e^{-it}) \\ &= \Re\Bigg((-i\cos(t)+\sin(t))\Big(\frac{\cosh(k(z+1))}{\sinh(k)}(1+e^{i\theta}) \\ &\quad + \frac{2i}{\pi}(1-e^{i\theta})\int_0^\infty L(\xi,z)\,d\xi\Big)\Bigg).\end{aligned} \tag{2.84}$$

The function $L(\xi,z)$ is given by equation (2.64). The value of $L(k)$ was already calculated by equation (2.68), but we note that L also has a removable singularity in the limit $\xi \to 0$, where double application of l'Hôpital's rule gives:

$$\lim_{\xi\to 0} L(\xi,z) = -V(k) - 2\gamma k^3 + \frac{\cosh(k(z+1))}{k^2\sinh(k)}.$$

The horizontal wave force component $|F_w|$ is then obtained by taking the real part and magnitude of (2.84) and then using equation (2.83).

F^w is plotted against k in Figure 2.16. The behaviour of F^w as k varies is similar

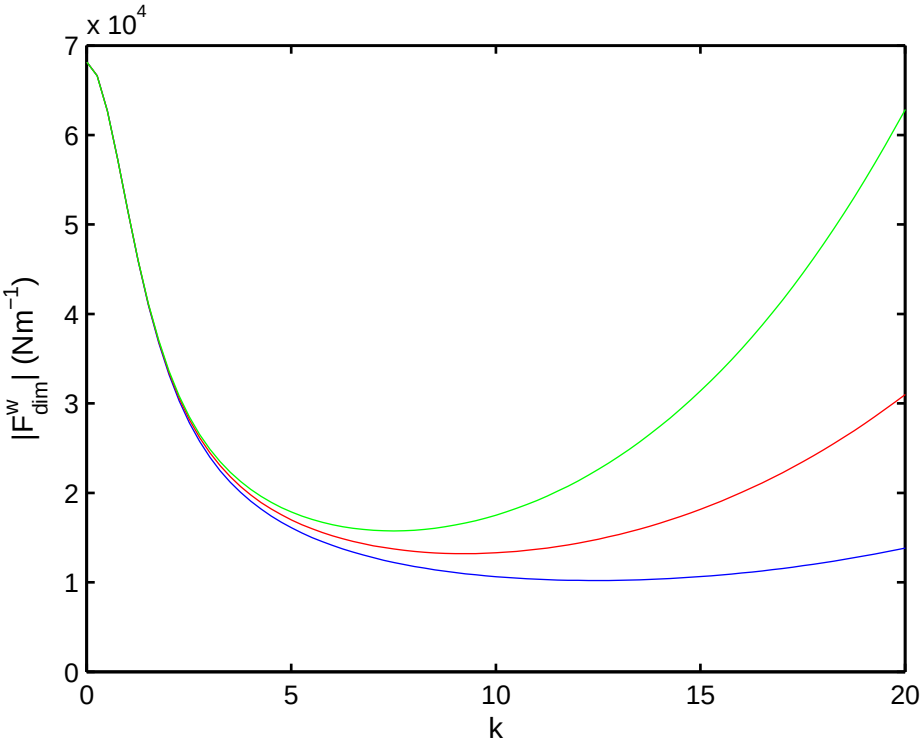

Figure 2.16: The horizontal wave force is plotted against k for ice thickness $h = 1.0$m (blue), $h = 1.5$ m (red) and $h = 2.0$ m (green). Here the incident wave amplitude is $a = 1$ cm and the other parameters are set to their default value.

to that of V^{SH}; it is finite in the limit $k \to 0$, and as k increases F^w decreases to a minimum before increasing monotonically. However, the difference between low and high values of k is more pronounced than for the shear force, and within the range of k considered the force is highest at $k = 0$. Differences due to changes in ice thickness become more noticeable as k grows. The horizontal wave force component is comparable in magnitude to the vertical shear force. However it is small in comparison to the hydrostatic wave force F^h_{dim}, which is equal to 6.1×10^8 Nm^{-1} for the default data set. However we note that F^h is proportional to the square of the fluid depth, which is quite deep for the McMurdo Sound data set.

We are interested in investigating F^w further, to ascertain which terms in equation (2.31) contribute the most to the total wave force. Therefore we split F^w into

$$F^w(t) = F^a(t) + F^b(t),$$

where F^a is the contribution from the incident and reflected wave parts, and F^b is the contribution from $\varphi(0, z)$. $|F^w|$, $|F^a|$ and $|F^b|$ are plotted against k in Figure 2.17(a). Both $|F^a|$ and $|F^b|$ give a significant contribution to the total horizontal wave force component $|F^w|$. For long waves, we see that F^a has a much higher influence, and then decays as k grows, whereas F^b behaves conversely. Hence the

ice–clamping condition has a greater contribution to the horizontal force as the waves become shorter in wavelength.

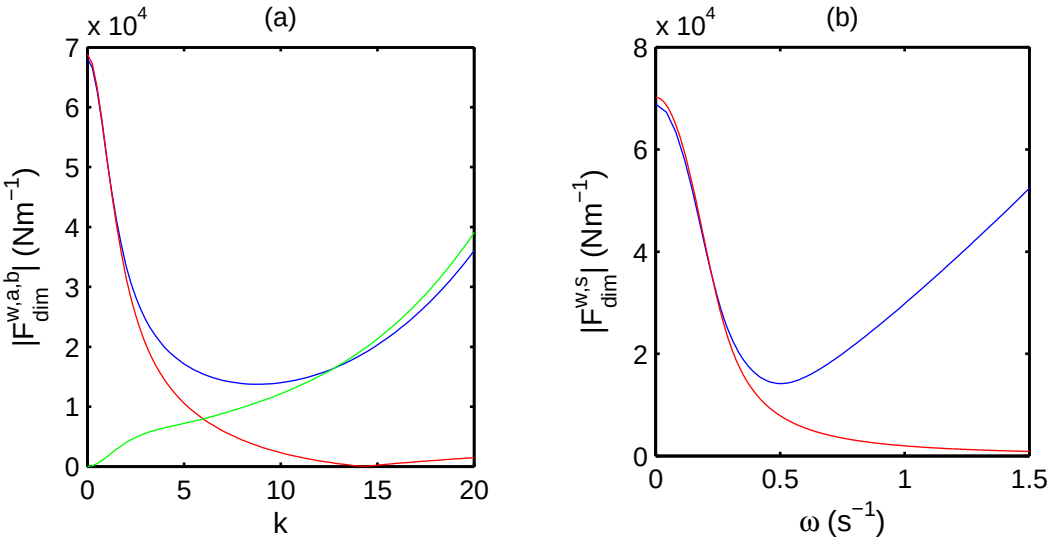

Figure 2.17: (a) The different contributions to the horizontal wave force are plotted against k: $|F^w|$, the total wave force (blue); $|F^a|$, the wave force due to the incident and reflected wave parts (red); $|F^b|$, the wave force due to the function φ (green). (b) The horizontal wave force components plotted against wave frequency ω: for the ice case, $|F^w|$ (blue); the free–surface case $|F^s|$ (red). In both (a) and (b) the incident wave amplitude is $a = 1$cm and the other parameters are set to their default value.

We are interested in how the presence of an ice sheet influences the horizontal force on the wall. To achieve this, we must calculate the horizontal wave force component again, this time without an ice sheet present. This involves reformulating the problem to that of free surface waves incident on a vertical wall. This is a simple procedure and can be achieved by taking the problem outlined in Section 2.2.2 and setting $a_D = a$, $J = 0$ and $M = 0$. The end conditions (2.8) are not valid as there is no ice sheet. Hence in equations (2.31) and (2.32) there is no need for the extra functions $\varphi(x, y)$ and $\hat{w}(x)$, the dispersion relation (2.22) becomes $\omega^2 = gk\tanh(kH)$, and the solution is then given by

$$\Phi = \frac{\cosh(k(z+1))}{k\sinh(k)}(e^{ikx} + e^{-ikx}),$$
$$W = e^{ikx} + e^{-ikx}.$$

Using (2.81) and (2.83), the horizontal wave force for the free surface case (denoted F^s) is then found as

$$|F^s_{dim}| = \frac{2H^2\omega^2\rho a}{k^2} = \frac{2\rho a H g\tanh(k)}{k}. \tag{2.85}$$

For comparison of $|F^s|$ with $|F^w|$, we consider incident waves of the same amplitude (which we take as $a = 0.01$ m) and the same wave frequency with and without an ice cover. Previous figures plotted the forces against k, but here we use ω as the

horizontal axis. The wave frequency ω is consistent for such comparison, whereas the wavenumber k is not, due to the different dispersion relations. Figure 2.17(b) compares $|F^s|$ and $|F^w|$ on the same graph. For low wave frequency the horizontal force on the wall is almost the same between the ice and free surface cases. As wave frequency increases the difference becomes more pronounced, and the presence of the ice causes significantly higher force.

2.5 Summary

The problem of hydroelastic wave interaction with a vertical wall in two dimensions was solved within linear theory. The fluid was of finite depth and the ice was clamped to the vertical wall. The Euler-Bernoulli thin plate equation was used to model the ice sheet, and the fluid was modelled by linear water wave theory. The velocity potential and ice deflection were separated into time-independent functions, which were then decomposed into parts representing the incident wave, reflected wave and extra functions to account for the conditions caused by the presence of an ice cover. The extra functions $\hat{w}$ and φ describe the behaviour of the solution in the vicinity of the vertical wall. The hydroelastic dispersion relation was derived. The BVP was rewritten in terms of $\hat{w}$ and φ. Physical parameters such as the flexural rigidity, thickness of the ice, the fluid depth and others were combined into two dimensionless parameters k^* and $\gamma = EJ/(\rho\omega^2 H^5)$, which define the behaviour of the fluid-structure interaction.

The problem was solved analytically by Fourier cosine transforms. The solution was presented in terms of infinite integral quadratures, which converge quickly. The phase shift between the incident and reflected waves was found as part of the solution. Numerical results were then presented for the ice deflection and strain in the ice sheet, as well as the vertical and horizontal forces on the vertical wall.

The ice sheet deflection was plotted for various parameters. The deflection is zero and its slope is zero where the ice is clamped to the vertical wall. The first wave peak in the deflection is the smallest due to this clamping. For larger values of k, the highest deflection is the second wave peak from the wall. Changing the ice thickness, or other parameters contained within γ, has a significant effect on the shape and magnitude of ice deflection.

The strain in the ice sheet was calculated and analysed for different wavenumbers and fluid depths. The ice clamping introduces a limit on the incident wave amplitude, in order for the strain in the ice sheet to remain below critical yield. This limit means the amplitude must be considerably lower than it would be in the absence of ice clamping, but allows waves of smaller wavelength to be analysed. The strain is highest at the vertical wall where the clamping takes place. The strain in the ice sheet begins finite for very long waves, decreases slightly as k increases, and then increases monotonically for shorter waves.

Forces on the vertical wall caused by the incident hydroelastic waves were calcu-

lated. The consideration of such forces is crucial in the design of off-shore structures. The vertical shear force on the wall that the ice causes was calculated, and changes in γ and k were investigated. As k increases from zero, the shear force begins finite and then decreases to a minimum before rising with k. The horizontal force acting on the wall was also calculated. The wave force component was found to be of the same order as the shear force. Comparison was made to the horizontal wave force with no ice sheet present, to demonstrate the increased force the ice sheet causes.

If this formulation were to be applied to the ocean, where constant ice flexure is caused by tides, a crack could possibly appear at the ice-wall boundary due to the induced strain. As shown in Section 2.4.2 this is highly dependent on the wave amplitude and wavenumber k. The problem could then be easily reformulated with different boundary conditions to reflect this change. The analysis of the free-edge problem is very similar to that in the present paper but the function $Q(\xi)$ is slightly different. However, considering applications in frozen lakes where the incident wave amplitude would be smaller, the strain at the ice-structure connection may not be above the yield strain and the model holds.

The model and solution outline in this chapter provides a firm basis for extension. While the model is linearised and many assumptions are made to simplify the problem, we have gained familiarity and experience with all aspects of the formulation and solution of hydroelastic problems. We may now proceed to complicate the model by incorporating more realistic effects.

2.5.1 Comparison with other authors

The work presented in Chapter 2 was published in the article Brocklehurst et al. (2010). Shortly afterwards, a similar paper was published by Bhattacharjee & Guedes-Soares (2012) entitled "Flexural gravity waves over a floating ice sheet near a vertical wall". The problem studied was linear two-dimensional wave reflection by a vertical wall in fluid of finite depth. Bhattacharjee & Guedes-Soares (2012) considered the wall as both rigid and harmonically oscillating. They also considered three different edge conditions at the ice-wall boundary: free edge, simply supported and clamped conditions. The problem was solved by eigenfunction expansion. For the clamped condition case, the authors presented a comparison with the solution of the present solution of Chapter 2. The authors presented graphs of the ice deflection and the strain in the ice with both solutions compared and found the solutions to be in excellent agreement. This comparison is shown in Figure 2.18.

Given that the solution methods were different, this provides verification to both.

2.5.2 Comparison with other methods of solution

When comparing the present method to the method based on Green's functions developed by Williams & Squire (2002), both methods provide analytical solutions. Eigenfunction expansions such as those used by Evans & Porter (2003) or Bhat-

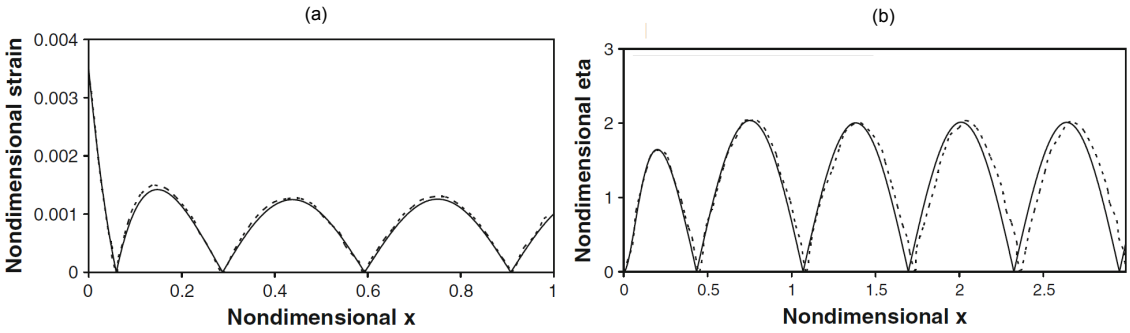

Figure 2.18: (a) The strain in the ice against x for $k = 10$. (b) The deflection against x for $k = 5$. Comparison of the solution of Bhattacharjee & Guedes-Soares (2012) (solid line) with that of the present solution (dashed line). This figure was reproduced from Bhattacharjee & Guedes-Soares (2012), in which $\eta = w$.

tacharjee & Guedes-Soares (2012) could also be used as an alternative approach. The solution in the present method is provided in terms of integral quadratures, whereas an eigenfunction expansion defines the solution in terms of infinite series. Methods based on Green's functions inevitably require numerical computation of the solution as opposed to the explicit solution provided here. The present method can be also used for free-edge ice cover as can the methods by Williams & Squire (2002) and Evans & Porter (2003). The present method allows an explicit definition of the phase shift between the incident and reflected waves in terms of quadratures. Both alternative methods would require numerical calculation of the phase shift. The use of a Fourier cosine transform also presents a very simple expression for the shear force, avoiding potential issues with the convergence of a third derivative other methods could present. The linear superposition involved in the present solution also allows us to easily compare the contribution from each wave part. In addition, as we will see throughout this thesis, the function $Q(\xi)$ appears in other problems also, and that we are now familiar with its behaviour is beneficial.

Chapter 3

Hydroelastic wave diffraction by a vertical cylinder

3.1 Introduction

We now extend the problem solved in Chapter 2 into three dimensions. We consider a vertical cylinder in fluid of finite depth, in the presence of an infinite ice sheet. This study is motivated by the expected need to build ocean structures in ice-covered water, discussed fully in Chapter 1. The vertical cylinder represents one of the supporting stands of such a structure. The hydroelastic behaviour of the ice sheet is described by linear elastic plate theory, and the fluid flow by the potential flow model, as in Chapter 2. The ice sheet is frozen to the vertical cylinder. Incident hydroelastic waves approach the cylinder and are diffracted and reflected. The two-dimensional hydroelastic incident wave is regular. We are interested in the deflection field, as well as the various forces on the cylinder. The distribution of these forces around the circumference of the cylinder is also studied. The strain at the ice-cylinder interface is of particular interest, and we will estimate whether the ice–clamping condition will be maintained. Key parameters under investigation include the cylinder radius and the wavenumber of the incident wave.

The assumptions discussed in Section 2.1 are applicable here also; the fluid is assumed inviscid and incompressible with irrotational flow. We assume the problem is time–harmonic, allowing us to remove time as a factor from the results. We retain the linear thin plate model, which is extended to three dimensions. The added dimension greatly complicates the problem: we exploit the axisymmetry of the vertical cylinder and introduce polar co-ordinates. As in Chapter 2 it is possible to express the ice deflection and velocity potential as the linear sum of the incident wave, reflected wave and an extra function to account for the boundary conditions due to the presence of a cylinder.

The structure of the chapter is as follows. Section 3.2 describes the mathematical formulation of the problem, and relevant physical parameters are defined. Section 3.3 demonstrates the method of solution. The solutions for the ice deflection and velocity potential of the flow are derived. Section 3.4 presents numerical results,

both for the ice deflection and velocity potential. The strain in the ice sheet is analysed. Important physical forces acting on the cylinder are calculated, which are of concern for the design of structures to be built in ice covered water. These include the horizontal force acting on the cylinder and the vertical shear force caused by the ice–clamping condition. A summary and conclusions are given in Section 3.5.

3.2 Mathematical formulation

3.2.1 Schematic and parameters

The geometry of the problem and co-ordinate system are shown in Figure 3.1. We

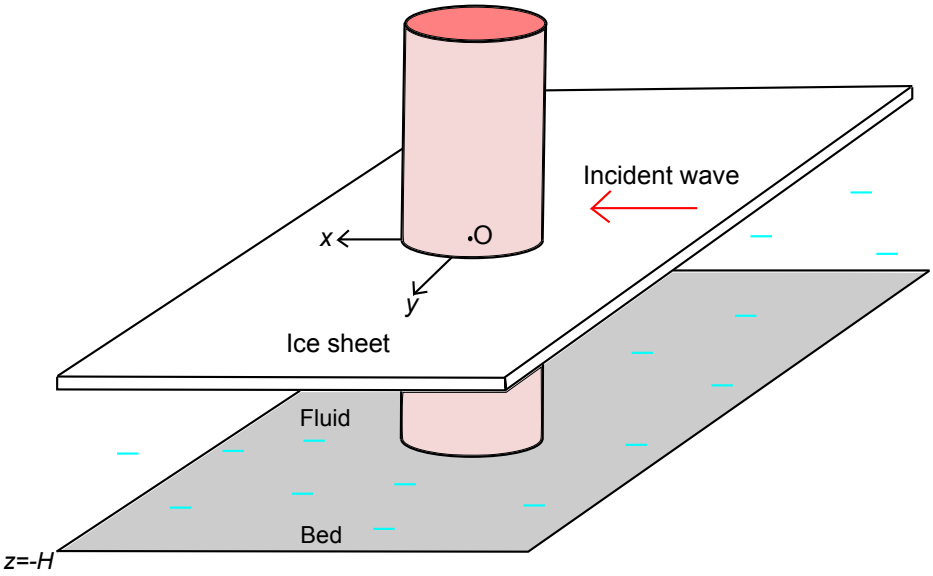

Figure 3.1: Three dimensional schematic of an infinite ice sheet meeting a vertical cylinder in fluid of finite depth.

use Cartesian coordinates with the x– and y–axes being along the ice sheet at rest and the z-axis directed vertically upwards. The positive x–axis is oriented in the same direction as the incident wave. Time is denoted by t. The fluid bed is flat and the fluid has depth H. The vertical cylinder has constant radius b, and the ice sheet is fixed to its surface. We also introduce cylindrical polar co-ordinates, with the origin at the centre of the vertical cylinder, as shown in Figure 3.2. Hence we have $x = r\cos(\theta)$ and $y = r\sin(\theta)$. The fluid and ice sheet occupy the region $r > b$ and $0 \leq \theta \leq 2\pi$.

The pressure in the fluid is represented by $p(r, \theta, z, t)$, and the density of the fluid by ρ. The fluid velocity $\mathbf{V}(r, \theta, z, t)$ is equal to the gradient of the velocity potential $\phi(r, \theta, z, t)$, hence $\nabla\phi = \mathbf{V}$. The vertical deflection of the ice sheet (the ice displacement relative to its position at rest) is denoted by $w(r, \theta, z, t)$. The ice has mass per unit length M, where $M = \rho_i h$, ρ_i is the ice density and h is the ice thickness. The ice sheet has flexural rigidity EJ, where E is Young's modulus and $J = h^3/[12(1-\nu^2)]$, where ν is Poisson's ratio. The incident wave parameters are:

a, wave amplitude; ω, wave frequency; k, wavenumber and c, phase velocity. The acceleration due to gravity is denoted g.

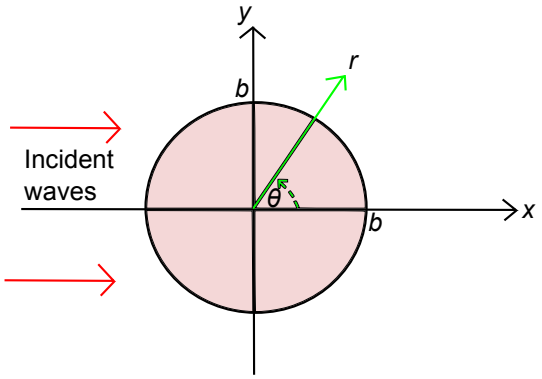

Figure 3.2: Cylindrical polar co-ordinate system.

3.2.2 Governing equations and boundary conditions

The governing equations and boundary conditions are now expressed in polar co-ordinates. The velocity potential satisfies Laplace's equation in the flow region:

$$\nabla^2\phi = 0, \quad (-H < z < 0,\ r > b,\ 0 \leq \theta \leq 2\pi), \tag{3.1}$$

where the Laplacian in polar co-ordinates is given by

$$\nabla^2 = \frac{1}{r}\frac{\partial}{\partial r}\left(r\frac{\partial}{\partial r}\right) + \frac{1}{r^2}\frac{\partial^2}{\partial\theta^2} + \frac{\partial^2}{\partial z^2}. \tag{3.2}$$

The linearised Bernoulli equation gives the pressure in the fluid as

$$p(r,\theta,z,t) = -\rho\phi_t - \rho g z, \quad (-H < z < 0,\ r > b,\ 0 \leq \theta \leq 2\pi), \tag{3.3}$$

where subscripts indicate partial derivatives. Boundary conditions for Laplace's equation (3.1) are due to the rigid vertical wall of the cylinder, the fluid bed, and the linearised kinematic condition on the ice cover respectively:

$$\phi_r = 0, \quad (r = b), \tag{3.4}$$

$$\phi_z = 0, \quad (z = -H), \tag{3.5}$$

$$\phi_z = w_t, \quad (z = 0). \tag{3.6}$$

The deflection of the ice cover is governed by the Bernoulli-Euler thin elastic plate equation:

$$EJ\nabla^4 w + Mw_{tt} = p, \quad (z = 0,\ r > b,\ 0 \leq \theta \leq 2\pi), \tag{3.7}$$

where the biharmonic operator is defined as $\nabla^4 = \nabla^2\nabla^2$. Boundary conditions due to the ice–clamping condition are given by

$$w = 0, \quad (r = b), \tag{3.8}$$

$$w_r = 0, \quad (r = b). \tag{3.9}$$

The conditions in the far field are defined later.

As in Chapter 2, both the ice deflection and the fluid flow are assumed periodic in time with the frequency ω of the incident wave. The solution of the coupled problem (3.1)-(3.9) is sought in the form (see for example Squire *et al.*, 1995):

$$\phi(r, \theta, z, t) = \Re\Big(\Phi(r, \theta, z)e^{-i\omega t}\Big), \tag{3.10}$$

$$w(r, \theta, t) = \Re\Big(\frac{i}{\omega}\, W(r, \theta)e^{-i\omega t}\Big). \tag{3.11}$$

The problem now depends on the time–independent variables Φ and W.

3.2.3 Incident waves and nondimensionalisation

The velocity potential $\Phi_{inc}(r, \theta, z)$ and the deflection $W_{inc}(r, \theta)$ of the incident waves have the form:

$$\Phi_{inc}(r, \theta, z) = \frac{a\omega}{k}\frac{\cosh(k(z + H))}{\sinh(kH)}e^{ikr\cos(\theta)}, \tag{3.12}$$

$$W_{inc}(r, \theta) = a\omega\, e^{ikr\cos(\theta)}. \tag{3.13}$$

These expressions are obtained simply by substituting $x = r\cos(\theta)$ into the expressions for the incident waves derived in Chapter 2, given by equations (2.20) and (2.21). The wave frequency ω and wavenumber k are related by the dispersion relation for hydroelastic waves which is unchanged from equation (2.22):

$$\omega^2\Big(M + \frac{\rho}{k\tanh(kH)}\Big) = \rho g + EJk^4. \tag{3.14}$$

We proceed to nondimensionalise the problem (3.1)-(3.9), using the depth H as a length scale. The following non–dimensional variables and parameters are introduced, denoted by asterisks:

$$r^* = \frac{r}{H}, \quad z^* = \frac{z}{H}, \quad b^* = \frac{b}{H}, \quad t^* = t\omega, \quad k^* = kH,$$
$$W^*(r^*, \theta, t^*) = \frac{W(r, \theta)}{a\omega}, \quad \Phi^*(r^*, \theta, z^*) = \frac{\Phi(r, \theta, z)}{Ha\omega},$$

where k^* is the dimensionless incident wavenumber and b^* is the dimensionless radius of the vertical cylinder. We also retain the dimensionless parameter $\gamma = EJ/\rho\omega^2H^5$ from Chapter 2. In the following analysis the asterisks are dropped and only dimensionless quantities are used if not stated otherwise.

We rewrite the BVP to be solved in terms of $\Phi(r,\theta,z)$ and $W(r,\theta)$ (in dimensionless variables):

$$\nabla^2\Phi = 0, \quad (-1 < z < 0,\ r > b), \tag{3.15}$$

$$\gamma\nabla^4 W + \left(\frac{1}{k\tanh(k)} - \gamma k^4\right) W = \Phi(r,\theta,0), \quad (z = 0,\ r > b), \tag{3.16}$$

$$\Phi_z = 0, \quad (z = -1), \tag{3.17}$$

$$\Phi_z = W, \quad (z = 0), \tag{3.18}$$

$$\Phi_r = 0, \quad (r = b), \tag{3.19}$$

$$W = 0, \quad (r = b), \tag{3.20}$$

$$W_r = 0, \quad (r = b). \tag{3.21}$$

In the above equations $0 \leq \theta \leq 2\pi$.

3.2.4 Decomposition of azimuthal coordinate

The velocity potential of the incident wave (3.12) can be rewritten as (Mei, 1983):

$$\Phi_{inc} = f_0(z) \sum_{n=0}^{\infty} \varepsilon_n i^n J_n(kr)\cos(n\theta), \tag{3.22}$$

where $J_n(kr)$ is the Bessel function of the first kind. We define

$$\varepsilon_n = \begin{cases} 1 & \text{if } n = 0, \\ 2 & \text{otherwise,} \end{cases} \tag{3.23}$$

and the function f_0 is defined as

$$f_0(z) = \frac{\cosh(k(z+1))}{k\sinh(k)}.$$

Equivalently the incident wave for the ice deflection (3.13) can be written

$$W_{inc} = \sum_{n=0}^{\infty} \varepsilon_n i^n J_n(kr)\cos(n\theta). \tag{3.24}$$

We require an expression for the outgoing waves diffracted by the vertical cylinder. It is well known (see for example Mei, 1983) that cylindrical outgoing waves are represented by the Hankel function of the first kind, defined by

$$H_n^{(1)}(kr) = J_n(kr) + iY_n(kr), \tag{3.25}$$

where $Y_n(kr)$ is the Bessel function of the second kind. Only Hankel functions of the first kind appear in this problem and in the analysis below we drop the superscript

in (3.25). Therefore, the diffracted waves are given by

$$\Phi_{dif} = f_0(z) \sum_{n=0}^{\infty} \varepsilon_n i^n a_n^D H_n(kr) \cos(n\theta), \tag{3.26}$$

$$W_{dif} = \sum_{n=0}^{\infty} \varepsilon_n i^n a_n^D H_n(kr) \cos(n\theta), \tag{3.27}$$

where the complex coefficients a_n^D must be determined as part of the solution. Note that the incident and reflected waves satisfy equations satisfy equations (3.15)-(3.18) and correctly describe the far-field behaviour of the hydroelastic waves.

Using linear superposition (as in Section 2.2.7) we may express the total velocity potential and ice deflection as:

$$\Phi(r,\theta,z) = \sum_{n=0}^{\infty} \varepsilon^n \, i^n \cos(n\theta) \Big(f_0(z) J_n(kr) + a_n^D \, f_0(z) H_n(kr) + \varphi_n(r,z) \Big), \tag{3.28}$$

$$W(r,\theta) = \sum_{n=0}^{\infty} \varepsilon^n \, i^n \cos(n\theta) \Big(J_n(kr) + a_n^D \, H_n(kr) + w_n(r) \Big), \tag{3.29}$$

Here we have introduced the unknown functions $\varphi_n(r,z)$ and $w_n(r)$ to describe the flow and ice deflection in the vicinity of the cylinder, owing to the boundary conditions (3.19)-(3.21). The functions $\varphi_n(r,z)$ and $w_n(r)$ are such that they do not give contributions to the wave pattern in the far field (Brocklehurst et al., 2011):

$$\sqrt{r}\varphi_n(r,z) \to 0, \quad \sqrt{r} w_n(r) \to 0, \quad r \to \infty. \tag{3.30}$$

In order to derive the boundary–value problems for the unknown functions $\varphi_n(r,z)$ and $w_n(r)$, where $n \geq 0$, we substitute equations (3.28)-(3.29) into equations (3.15)–(3.21). As noted previously, $J_n(kr)$ and $H_n(kr)$ satisfy the governing equations (3.15)–(3.16) independently, and hence the new functions $\varphi_n(r,z)$ and $w_n(r)$ must also satisfy them. It is convenient to introduce the differential operator

$$S_n < \varphi_n(r,z) >= \left(\frac{\partial^2}{\partial r^2} + \frac{1}{r}\frac{\partial}{\partial r} - \frac{n^2}{r^2} \right) \varphi_n(r,z). \tag{3.31}$$

The resulting n boundary-value problems are formulated as

$$S_n < \varphi_n > + \varphi_{nzz} = 0, \quad (-1 < z < 0,\ r > b), \tag{3.32}$$

$$\gamma S_n^2 < w_n > + \Big(\frac{1}{k \tanh(k)} - \gamma k^4 \Big) w_n = \varphi_n, \quad (z = 0,\ r > b), \tag{3.33}$$

$$\varphi_{nz} = 0, \quad (z = -1,\ r > b), \tag{3.34}$$

$$\varphi_{nr} = -f_0(z) k \big(J_n'(kb) + a_n^D H_n'(kb) \big), \quad (-1 < z < 0,\ r = b), \tag{3.35}$$

$$\varphi_{nz} = w_n, \quad (z = 0,\ r > b), \tag{3.36}$$

$$w_n = -J_n(kb) - a_n^D H_n(kb), \quad (r = b), \tag{3.37}$$

$$w_{nr} = -k J_n'(kb) - a_n^D k H_n'(kb), \quad (r = b). \tag{3.38}$$

In this chapter, primes indicate differentiation *with respect to argument*. We note that the above BVP has no dependence on θ.

3.3 Method of solution

3.3.1 Weber transform

In order to handle the fourth order derivative in equation (3.33) we employ a modified Weber transform (Emmerhoff & Sclavounos, 1992). We may then use the helpful properties of this transform to greatly simplify the differential equations in (3.32)-(3.38) and facilitate a solution. Usually in problems with cylindrical symmetry, a standard Hankel transform proves useful; however, in the present problem the fluid occupies the region $r > b$, and this requires the choice of a Weber transform.

The Weber transform is defined as

$$F(s) = \int_b^\infty r\, f(r)\, Z_n(r, s)\, dr, \tag{3.39}$$

where a function $f(r)$ is defined in $r > b$ and such that $\sqrt{r} f(r) \to 0$ as $r \to \infty$. Here Z_n is given by

$$Z_n(r, s) = J_n(sr) Y_n'(sb) - J_n'(sb) Y_n(sr),$$

and Z_n has the following useful (easily proved) properties:

$$Z_n(b, s) = \frac{2}{\pi s b}, \quad \frac{\partial Z_n}{\partial r}(b, s) = 0, \quad Z_n \to 0 \text{ as } r \to \infty. \tag{3.40}$$

The corresponding inverse transform reads

$$f(r) = \int_0^\infty \frac{F(s)\, s\, Z_n(r, s)}{(J_n'(sb))^2 + (Y_n'(sb))^2}\, ds. \tag{3.41}$$

Defining the integral operator in (3.39) as $F(s) = \mathrm{Web}[f(r)]$, using integration by

parts and the properties above, we now find an expression for $\text{Web}[S_n < f(r) >]$:

$$\begin{aligned}
\text{Web}[S_n < f(r) >] &= \int_b^\infty r f_{rr} Z_n \, dr + \int_b^\infty f_r Z_n \, dr - n^2 \int_b^\infty Z_n \frac{f}{r} \, dr \\
&= \big(r Z_n f_r\big)_b^\infty - \int_b^\infty f_r Z_n \, dr - \int_b^\infty f_r r \frac{\partial Z_n}{\partial r} \, dr \\
&+ \int_b^\infty f_r Z_n \, dr - n^2 \int_b^\infty Z_n \frac{f}{r} \, dr \\
&= -\frac{2 f_r(b)}{\pi s} - \Bigg(\big(r Z_n f\big)_b^\infty - \int_b^\infty f \frac{\partial Z_n}{\partial r} \, dr \\
&- \int_b^\infty r \frac{\partial^2 Z_n}{\partial r^2} f \, dr \Bigg) - n^2 \int_b^\infty Z_n \frac{f}{r} \, dr \\
&= -\frac{2 f_r(b)}{\pi s} + \int_b^\infty \frac{1}{r} \left(r^2 \frac{\partial^2 Z_n}{\partial r^2} + r \frac{\partial Z_n}{\partial r} - n^2 Z_n \right) f \, dr \\
\text{Web}[S_n < f(r) >] &= -\frac{2 f_r(b)}{\pi s} - s^2 \int_b^\infty r f Z_n \, dr,
\end{aligned}$$

and hence we have

$$\text{Web}[S_n < f(r) >] = -s^2 \text{Web}[f(r)] - \frac{2 f_r(b)}{\pi s}. \tag{3.42}$$

Note that in the above, we have substituted

$$-r^2 Z_n = r^2 \frac{\partial^2 Z_n}{\partial r^2} + r \frac{\partial Z_n}{\partial r} - n^2 Z_n,$$

due to the fact that Z_n is a solution to Bessel's equation, since Z_n is a linear combination of J_n and Y_n.

We also require an expression for $\text{Web}[S_n^2 < f(r) >]$. This is achieved by defining $g(r) = S_n < f(r) >$. Using equation (3.42), we then have:

$$\begin{aligned}
\text{Web}[S_n^2 < f(r) >] = \text{Web}[S_n < g(r) >] &= -s^2 \text{Web}[S_n < f(r) >] - \frac{2}{\pi s} g_r(b) \\
&= -s^2 \Big(-s^2 \text{Web}[f(r)] - \frac{2}{\pi s} f_r(b) \Big) - \frac{2}{\pi s} \frac{\partial}{\partial r} (S_n < f(r) >)_{r=b},
\end{aligned}$$

and hence we have

$$\text{Web}[S_n^2 < f(r) >] = s^4 \text{Web}[f(r)] + \frac{2s}{\pi} f'(b) - \frac{2}{\pi s} \frac{\partial}{\partial r} (S_n < f(r) >)_{r=b}. \tag{3.43}$$

With expressions (3.42) and (3.43) derived, we may now proceed to apply the Weber transform to the governing equations and boundary conditions (3.32)-(3.38).

3.3.2 Velocity potential

Applying the Weber transform to (3.32), where $\text{Web}[\varphi_n(r,z)] = \psi_n(s,z)$, and using equations (3.42) and (3.35), we arrive at the differential equation

$$\begin{aligned}\frac{\partial^2\psi_n}{\partial z^2} - s^2\psi_n &= \frac{2}{\pi s}\varphi_{nr}(b,z) \\ &= \frac{P_n}{s}\cosh(k(z+1)),\end{aligned} \tag{3.44}$$

where the coefficients P_n are defined as

$$P_n = \frac{-2}{\pi\sinh(k)}(J_n'(kb) + a_n^D H_n'(kb)). \tag{3.45}$$

The general solution to equation (3.44) is

$$\psi_n(s,z) = \nu_n\sinh(s(z+1)) + \mu_n\cosh(s(z+1)) + \frac{P_n\cosh(k(z+1))}{s(k^2-s^2)}. \tag{3.46}$$

Applying the Weber transform to (3.34) and (3.36), we obtain the boundary conditions

$$\frac{\partial\psi_n}{\partial z} = 0, \qquad (z=-1), \tag{3.47}$$

$$\frac{\partial\psi_n}{\partial z} = W_n, \quad (z=0), \tag{3.48}$$

where $W_n(s) = \text{Web}[w_n(r)]$. Applying the boundary condition (3.47) to the general solution (3.46) we obtain $\nu_n = 0$, and the boundary condition (3.48) implies

$$\mu_n = \frac{1}{s\ \sinh(s)}\left(W_n - \frac{kP_n\sinh(k)}{s(k^2-s^2)}\right).$$

Hence the solution of the boundary-value problem (3.44)-(3.48) is

$$\psi_n(s,z) = \frac{\cosh(s(z+1))}{s\ \sinh(s)}\Big(W_n(s) - \frac{P_n k\sinh(kH)}{s(k^2-s^2)}\Big) + \frac{P_n\cosh(k(z+1))}{s(k^2-s^2)}, \tag{3.49}$$

where W_n and the coefficients a_n^D are to be determined in the next section.

3.3.3 Plate equation

We now apply the Weber transform to the plate equation (3.33) and make use of (3.43) to obtain the following equation for W_n:

$$\gamma\Big(s^4W_n + \frac{2s}{\pi}w_{nr}(b) - \frac{2}{\pi s}\bar{V}_n\Big) + \Big(\frac{1}{k\tanh(k)} - \gamma k^4\Big)W_n = \psi_n(s,0), \tag{3.50}$$

where we define the function

$$\bar{V}_n(k,b) = \frac{\partial}{\partial r}(S_n < w_n(r) >)_{r=b}, \tag{3.51}$$

which will be used below in calculations of the shear force acting on the cylinder due to the clamped condition at $r = b$. Equation (3.50) can be simplified by noting that

$$w_{nr}(b) = -kJ_n'(kb) - ka_n^D H_n'(kb) = \frac{1}{2}\pi k \sinh(k) P_n, \tag{3.52}$$

which follows from (3.38) and (3.45). Inserting (3.52) and (3.49) into the transformed plate equation (3.50) and rearranging the result to factorise $W_n(s)$ on the left-hand side, we find

$$W_n\bigg(\gamma(s^4 - k^4) + \frac{1}{k\tanh(k)} - \frac{1}{s\tanh(s)}\bigg) = \frac{2\gamma}{\pi s}\bar{V}_n - \gamma s k P_n \sinh(k) + P_n \sinh(k)\bigg(\frac{1}{s(k^2 - s^2)}\Big(\frac{1}{\tanh(k)} - \frac{k}{s\tanh(s)}\Big)\bigg). \tag{3.53}$$

Clearly the left-hand side of (3.53) is zero at $s = k$. Hence, to avoid a singularity of the function $W_n(s)$ at this point we require that the limit of the right-hand side is also zero as $s \to k$. This limit can be calculated by applying l'Hôpital's rule to the final term of the right-hand side of (3.53):

$$\begin{aligned}
&\lim_{s\to k}\left(\frac{\coth(k) - k(s\tanh(s))^{-1}}{s(k^2 - s^2)}\right) \\
&= \lim_{s\to k}\left(\frac{-k\Big(-(s\tanh(s))^{-2}(\tanh(s) + s\,\mathrm{sech}^2(s))\Big)}{k^2 - 3s^2}\right) \\
&= \frac{(k\tanh(k))^{-1} + (\sinh^2(k))^{-1}}{-2k^2} \\
&= -\frac{-V(k)}{k},
\end{aligned}$$

where the function $V(k)$ was introduced in equation (2.56).

Equating the right-hand side of (3.53) with zero at $s = k$, we obtain an expression for $\bar{V}_n(k, b)$:

$$\bar{V}_n = \frac{\pi}{2} P_n \sinh(k)\Big(k^3 + \frac{V(k)}{\gamma}\Big). \tag{3.54}$$

Inserting (3.54) into (3.53) and noting that the right–hand side is now also equal to zero at $s = k$, we find that

$$W_n(s) = \frac{P_n \sinh(k)}{s} Q(s). \tag{3.55}$$

Here $Q(s)$ is the same function that appeared in the solution of the equivalent two-dimensional problem of Chapter 2:

$$Q(s) = \frac{s\tanh(s)\big(V(k) + \gamma k(k^2 - s^2)\big) + \frac{1}{k^2 - s^2}\big(\frac{s\tanh(s)}{\tanh(k)} - k\big)}{s\tanh(s)\big(\gamma(s^4 - k^4) + \frac{1}{k\tanh(k)}\big) - 1}. \tag{3.56}$$

The function Q was plotted previously in Figure 2.5. Recall that $Q(k)$ is finite and is given by equation (2.66).

The coefficients a_n^D are still uncalculated. We note that we have two equations for $w_n(b)$; the first comes from boundary condition (3.37):

$$w_n(b) = -J_n(kb) - a_n^D H_n(kb), \tag{3.57}$$

and the second arises from performing an inverse transform (3.41) on the solution (3.55):

$$w_n(b) = P_n \sinh(k) \frac{2}{\pi b} \int_0^\infty \frac{Q(s)}{s\Big((J_n'(sb))^2 + (Y_n'(sb))^2\Big)}\, ds. \tag{3.58}$$

Here we have used the condition $Z_n(b,s) = 2/(\pi sb)$ (see equation (3.40)). Equating (3.57) and (3.58) and substituting for P_n using (3.45), we have

$$-J_n(kb) - a_n^D H_n(kb) = -\frac{2}{\pi}(J_n'(kb) + a_n^D H_n(kb)) \frac{2}{\pi b} \tau_n, \tag{3.59}$$

where

$$\tau_n = \int_0^\infty \frac{Q(s)}{s\big((J_n'(sb))^2 + (Y_n'(sb))^2\big)} ds.$$

By resolving (3.59) into real and imaginary parts and defining

$$\begin{aligned} \chi_n &= \frac{4\tau_n}{\pi^2 b} J_n'(kb) - J_n(kb), \\ \eta_n &= \frac{4\tau_n}{\pi^2 b} Y_n'(kb) - Y_n(kb), \end{aligned} \tag{3.60}$$

we can write

$$a_n^D = \frac{i\chi_n}{\eta_n - i\chi_n}. \tag{3.61}$$

The final solution for the problem is then given by performing inverse Weber transforms on the functions $\psi_n(r,z)$ in (3.49) and $W_n(r)$ in (3.55), and by working backwards through the analysis using equations (3.28)-(3.29) and (3.10)-(3.11). The inverse transforms are too complicated to be evaluated analytically, and must be calculated numerically. In the following section, we outline techniques for doing so.

3.3.4 Numerical techniques for inverse Weber transforms

The inverse transform for the plate deflection is given by

$$\begin{aligned} w_n(r) &= \int_0^\infty \frac{W_n(s)\, s\, Z_n(r,s)}{(J_n'(sb))^2 + (Y_n'(sb))^2}\, ds \\ &= P_n \sinh(k)\, I(r), \end{aligned}$$

where the integral I is defined as

$$I(r) = \int_0^\infty \frac{Q(s)\, Z_n(r,s)}{\zeta}\, ds, \tag{3.62}$$

and we have defined $\zeta = (J_n'(sb))^2 + (Y_n'(sb))^2$. Due to the presence of Bessel functions in its the numerator and denominator, the integrand is extremely oscillatory, and becomes increasingly more so as r grows. Despite the fact that Q decays with order s^{-2} as $s \to \infty$, the convergence of the integrand can be quite slow. Examples of the integrand are plotted in Figure 3.3.

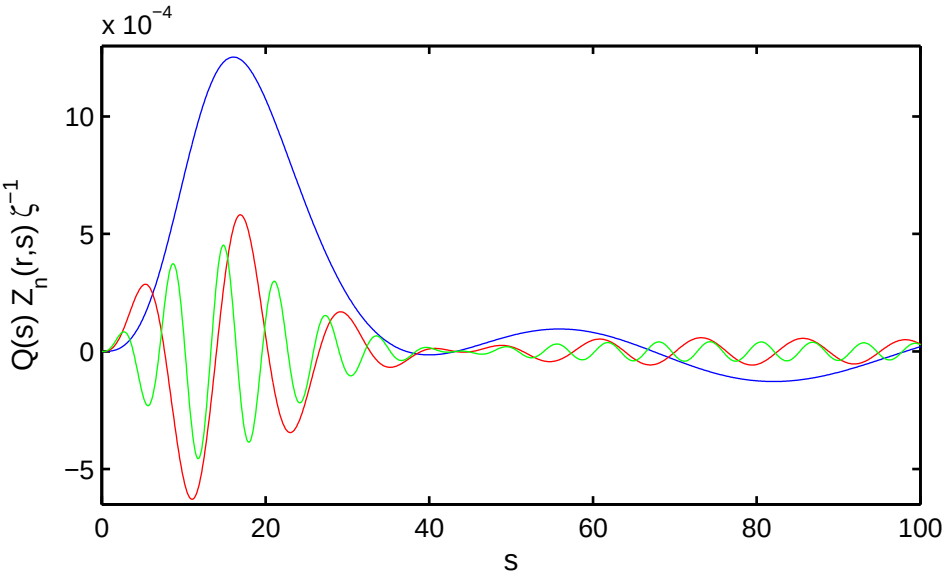

Figure 3.3: The integrand of (3.62) plotted against s for $r = 0.1$ (blue), $r = 0.5$ (red) and $r = 1.0$ (green). The cylinder radius is given by $b = 0.01$, $k = 5$ and $n = 1$. All other parameters are taken from Table 2.1(a).

We are able to improve the convergence of the integral by investigating the behaviour of the integrand as $s \to \infty$. Firstly, the asymptotic expressions for Bessel functions of order n for large argument are given by (Bowman, 1958):

$$J_n(sr) \approx \sqrt{\frac{2}{\pi sr}} \cos\left(sr - \frac{n\pi}{2} - \frac{\pi}{4}\right), \tag{3.63}$$

$$Y_n(sr) \approx \sqrt{\frac{2}{\pi sr}} \sin\left(sr - \frac{n\pi}{2} - \frac{\pi}{4}\right), \tag{3.64}$$

to leading order. Using the differentiation rules for Bessel functions combined with equations (3.63)-(3.64), for large arguments we have

$$\begin{aligned} J_n'(sb) = -J_{n+1}(sb) + \frac{n}{sb} J_n(sb) &\approx \sqrt{\frac{2}{\pi sb}} \cos\left(sb - \frac{\pi}{4} - \frac{(n+1)\pi}{2}\right) \\ &\approx \sqrt{\frac{2}{\pi sb}} \sin\left(sb - \frac{\pi}{4} - \frac{n\pi}{2}\right), \end{aligned} \tag{3.65}$$

and similarly

$$Y_n'(sb) \approx \sqrt{\frac{2}{\pi sb}} \cos\left(sb - \frac{\pi}{4} - \frac{n\pi}{2}\right). \tag{3.66}$$

Hence, using (3.65)-(3.66)an asymptotic expression for Z_n as $s \to \infty$ is given by

$$\begin{aligned} Z_n &= J_n(sr)Y_n'(sb) - J_n'(sb)Y_n(sr) \\ &\approx \sqrt{\frac{2}{\pi sr}}\cos\Big(sr - \frac{n\pi}{2} - \frac{\pi}{4}\Big)\sqrt{\frac{2}{\pi sb}}\cos\Big(sb - \frac{\pi}{4} - \frac{n\pi}{2}\Big) \\ &\quad - \sqrt{\frac{2}{\pi sb}}\sin\Big(sb - \frac{\pi}{4} - \frac{n\pi}{2}\Big)\sqrt{\frac{2}{\pi sr}}\sin\Big(sr - \frac{n\pi}{2} - \frac{\pi}{4}\Big) \\ &= \frac{2}{\pi s\sqrt{br}}\cos\bigg(\Big(sr - \frac{n\pi}{2} - \frac{\pi}{4}\Big) - \Big(sb - \frac{n\pi}{2} - \frac{\pi}{4}\Big)\bigg) \\ &= \frac{2}{\pi s\sqrt{br}}\cos(s(r-b)). \end{aligned} \tag{3.67}$$

Similarly we may find an expression for ζ as $s \to \infty$, given by

$$\begin{aligned} \zeta &\approx \frac{2}{\pi sb}\cos^2\Big(sb - \frac{(n+1)\pi}{2} - \frac{\pi}{4}\Big) + \frac{2}{\pi sb}\sin^2\Big(sb - \frac{(n+1)\pi}{2} - \frac{\pi}{4}\Big) \\ &= \frac{2}{\pi sb}. \end{aligned} \tag{3.68}$$

We note that $Q(s) \sim -ks^{-2}$ as $s \to \infty$. Combining this fact with (3.67) and (3.68), we obtain an expression for the integrand of I as $s \to \infty$:

$$\frac{Q(s)Z_n}{\zeta} \approx -k\sqrt{\frac{b}{r}}\,\frac{\cos(s(r-b))}{s^2}. \tag{3.69}$$

To improve the convergence of I, we now define the function $g(s)$ as

$$g(s) = \frac{Q(s)Z_n}{\zeta} + k\sqrt{\frac{b}{r}}\,\frac{\cos(s(r-b))}{s^2+1}, \tag{3.70}$$

and then I can be rewritten

$$\begin{aligned} I(r) &= \int_0^\infty g(s)\,ds - k\sqrt{\frac{b}{r}}\int_0^\infty \frac{\cos(s(r-b))}{s^2+1}\,ds \\ &= \int_0^\infty g(s)\,ds - \frac{k\pi}{2}\sqrt{\frac{b}{r}}\,e^{b-r}. \end{aligned} \tag{3.71}$$

Here we have used the result in equation (2.78). We note that the integrand in equation (3.71) decays faster than the integrand of equation (3.62) and its behaviour is now less oscillatory as $s \to \infty$, greatly improving the computational efficiency of the problem.

We note that there is some literature on the subject of integrals involving products of Bessel functions. Lucas (1995) considered such integrals for Bessel functions of arbitrary order, using asymptotic expressions and extrapolation on a sequence of partial sums. The author notes that standard infinite integration routines perform extremely poorly when calculating such integrals. However, the integral I in equation (3.62) is more complicated than the integrals considered by Lucas (1995) as it includes the term $(J_n'(sb))^2 + (Y_n'(sb))^2$ in the denominator. Using the technique

outlined above (resulting in equation (3.71)) and using a very fine integration grid, combined with ensuring the integral is truncated to high order, leads to satisfactory accuracy. The efficiency could possibly be improved by using techniques similar to those in Lucas (1995), but such numerical investigation is beyond the scope of this thesis.

When the integrals are calculated and $w_n(r)$ are known, they are substituted into the expression for the total deflection $W(r, \theta)$ given by equation (3.29). This expression is in terms of an infinite sum from $n = 0$ to $n = \infty$. We note that the convergence of this sum is fast: in the calculations we continue to increase n until the magnitude of the contribution from each term is less than 10^{-20}. Usually this occurs between $n = 5$ and $n = 15$.

3.4 Numerical results

In this section we present results for the solution derived in Section 3.3. Results are presented for the ice deflection and strain in the ice sheet, as well as for the magnitude of the shear and horizontal forces acting on the cylinder. Recall that the default data set is given by Table 2.1(a). The wavenumber k and the cylinder radius b are varied frequently, and hence are not assigned a default value but are quoted for each plot. We continue to assume that all variables and parameters are dimensionless unless accompanied by their units. Throughout this section we use the same notation as Section 2.3 to indicate magnitude, to be interpreted as the maximum value with respect to time.

3.4.1 Deflection in the ice sheet

In Section 2.4.1, the deflection results were presented in terms of the magnitude with respect to time. In this three-dimensional formulation, is it clearer to present a snapshot of the deflection for some fixed time. We begin by plotting the deflection for $k = 5$, corresponding to an incident wave of long wavelength $\lambda = 440\,\text{m}$. We also take $b = 0.01$, corresponding to a structure with support cylinder radius $b_{dim} = 3.5\text{m}$. The ice deflection is shown in Figure 3.4.

Recall that the incident wave approaches from $x = -\infty$ and travels in the positive x direction. Because the cylinder radius is small in comparison with the incident wavelength, the effect of the cylinder on the waves is small. However, we see a disturbance in the vicinity of the cylinder among the regular incident waves. The deflection is smallest directly in the wake of the cylinder, as expected. Although it is invisible from this viewpoint, the deflection and slope of the deflection are zero at the contact point between the cylinder and the ice sheet, as prescribed by the ice–clamping condition.

We repeat the calculations, increasing the wavenumber to $k = 10$. Other parameters are the same as for Figure 3.4. The deflection for this case is plotted in Figure

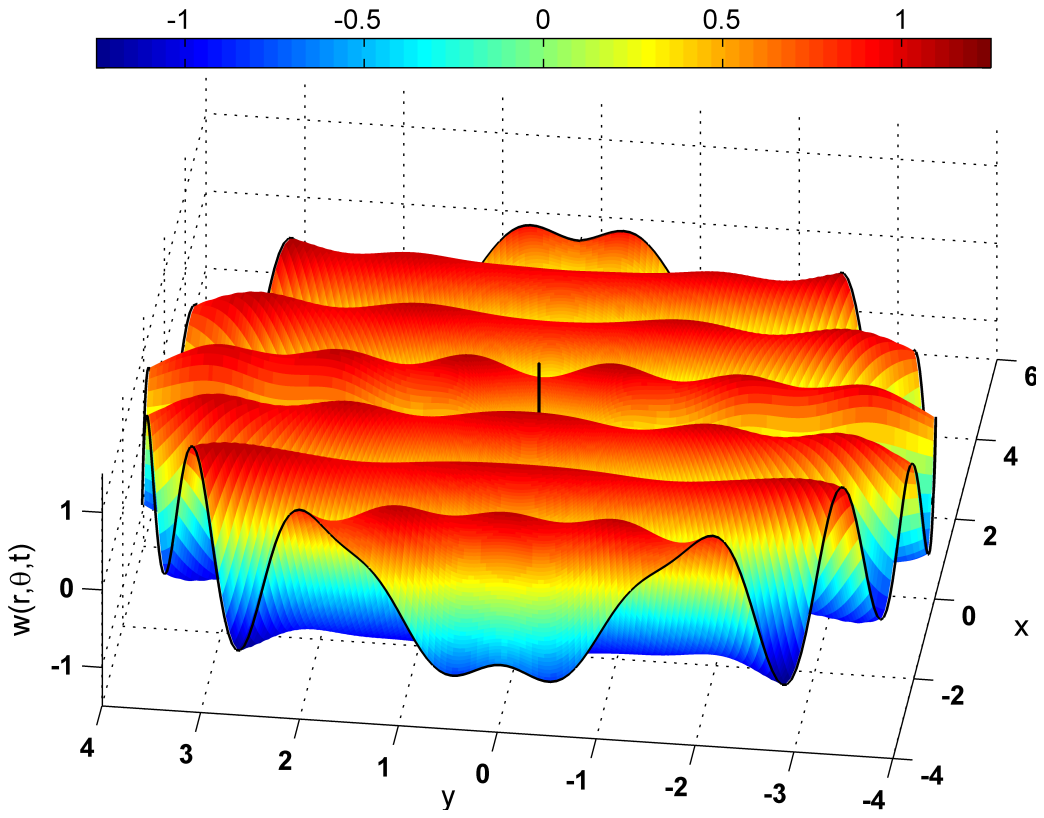

Figure 3.4: The deflection of the ice sheet $w(x, y)$ is plotted against x and y for wavenumber $k = 5$. The cylinder radius is given by $b = 0.01$ and the time is arbitrarily chosen as $t = 3$. The colours indicate the value of w at different positions on the ice sheet (see scale above).

3.5. The smaller wavelength leads to the cylinder having a more profound impact on the deflection of the ice. The perturbations in the vicinity of the cylinder are more pronounced. The deflection directly in the wake of the cylinder is now smaller, and the maximum deflection occurs in the disturbance either side of this wake. In addition there is an increase in the range of the disturbance due to the cylinder. We also note that there is a disturbance in the incident wave before it reaches the cylinder, caused by the outgoing reflected cylindrical waves.

Figures 3.4 and 3.5 were plotted for fixed arbitrary time. We are interested in studying the evolution of the ice deflection over time, with respect to the periodicity of the problem. Figure 3.6 shows the deflection for $k = 20$, evaluated at $t = 0$, $t = 2\pi/3$ and $t = 4\pi/3$. This splits the period into three equally spaced pieces with respect to time. For $k = 20$ the cylinder has a larger influence on the ice deflection, and the effect of diminished deflections behind the cylinder extends over several wavelengths. Figure 3.6(a) shows an incident wave approaching the cylinder. As we reach Figure 3.6(b) the wave splits into two due to the presence of the cylinder and the ice–clamping condition. Figure 3.6(c) completes the set as the wave merges again in the cylinder wake.

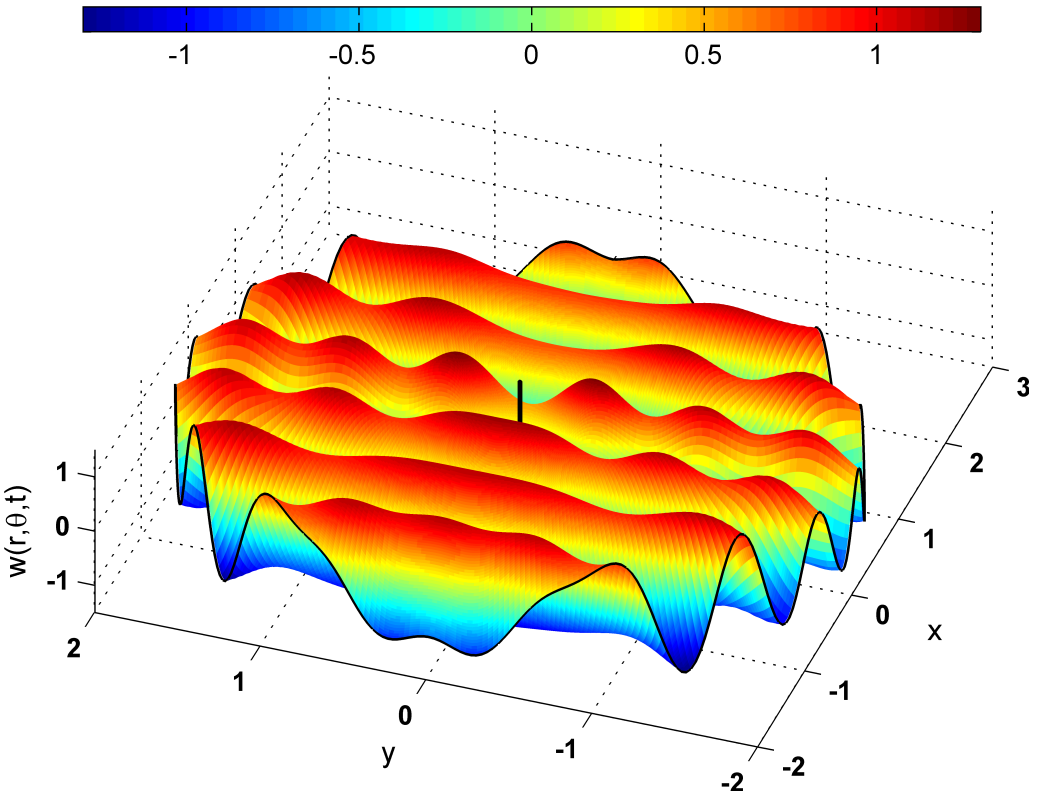

Figure 3.5: The deflection of the ice sheet $w(x, y)$ is plotted against x and y for wavenumber $k = 10$. The cylinder radius is given by $b = 0.01$ and the time is arbitrarily chosen as $t = 3$.

3.4.2 Strain in the ice sheet

We now calculate the strain in the ice sheet. As in Chapter 2, the strain is of particular interest in the present problem as we are interested in whether the clamped–ice condition at $r = b$ can be maintained. In this study we are interested in the radial strain component ε_r, defined as

$$\varepsilon_r = \frac{ah}{2H^2}\frac{\partial^2 w}{\partial r^2}. \tag{3.72}$$

The calculation of the strain is not straightforward. As seen in Section 3.3.4, the inverse Weber transform for the deflection of the ice sheet involves an integrand that behaves with order s^{-2} as $s \to \infty$. Direct calculation of the second derivative with respect to r required for the strain in (3.72) would lead to this integrand being multiplied by s^2, leaving the integral undefined. However, after performing the derivative in equation (3.72), we use the technique to improve the convergence of the integrals outlined in Section 3.3.4. This results in an integrand which behaves with order s^{-1} as $s \to \infty$. The strain can then be calculated without any problems.

Based on the results of Section 2.4.2, the strain is expected to be highest at $r = b$. To begin, we plot the polar distribution of the strain in the ice sheet around the cylinder. Figure 3.7(a) shows the strain ε_r against θ for varying values of the wavenumber k. Firstly we see that the strain is highest at $\theta = \pi$, which is the angle from which the incident wave approaches the cylinder. The minimum value of

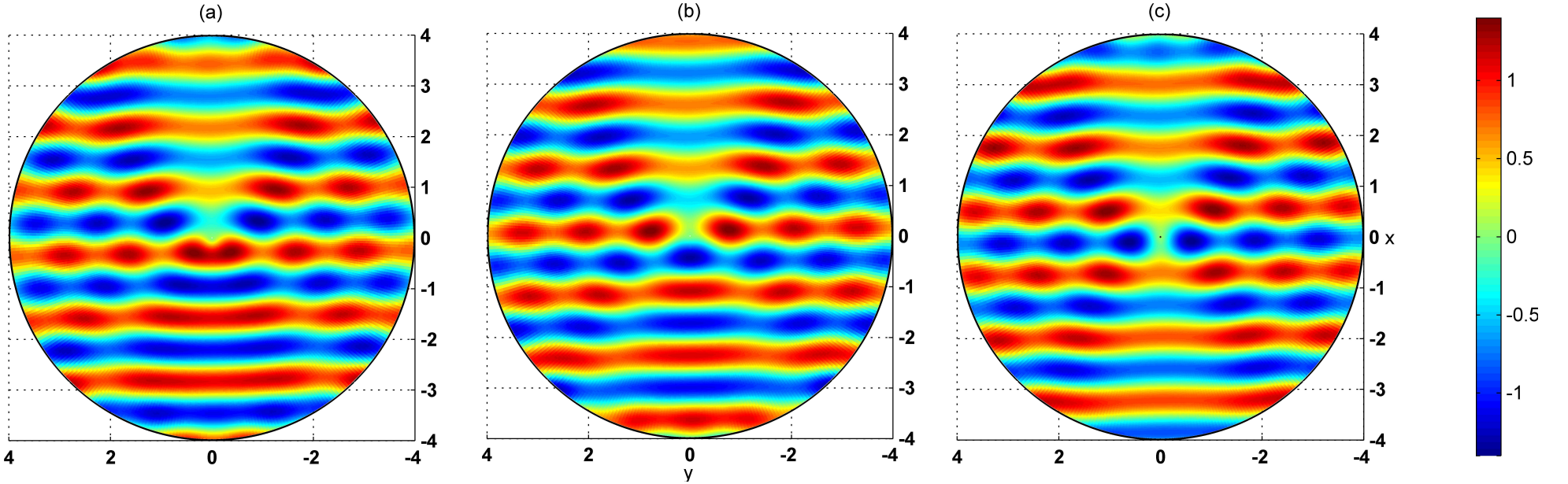

Figure 3.6: The deflection of the ice sheet $w(x, y)$ shown from a vertical viewpoint for $k = 20$ and $b_{dim} = 3.5\,\mathrm{m}$. The three figures show the progression through the period of the problem: (a) $t = 0$, (b) $t = 2\pi/3$, (c) $t = 4\pi/3$.

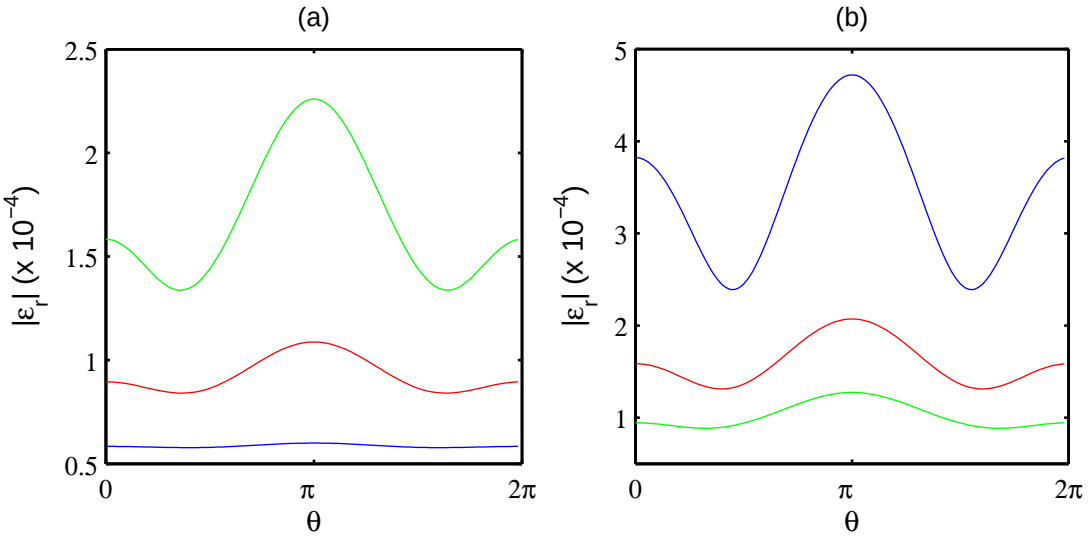

Figure 3.7: (a) The radial strain component ε_r is plotted against θ for $b_{dim} = 3.5\,\text{m}$. Here the wavenumber is given by $k = 2$ (blue), $k = 4$ (red) and $k = 6$ (green). (b) The radial strain component ε_r is plotted against θ for $k = 5$. Here the cylinder radius is given by $b = 2\,\text{m}$ (blue), $b = 3\,\text{m}$ (red) and $b = 4\,\text{m}$ (green). In both cases the amplitude is set to $a = 1\,\text{cm}$ and the remaining parameters are set to their default values.

strain is found at the sides of the cylinder. Increasing the wavenumber k results in an increase in strain, due to the increased curvature caused by the shorter wavelength. The polar variation of the strain is more pronounced for shorter waves.

Figure 3.6(b) shows the strain ε_r against θ for varying values of the cylinder radius b. We see that smaller values of b incite higher strain in the ice sheet. This is to be expected: since the ice is fixed to a smaller area of cylinder, the effect of the passing incident wave is more focused and the resulting strain is higher. For smaller values of b we also see that the strain at $\theta = 0$, behind the cylinder, becomes closer to the strain at $\theta = \pi$.

To investigate further the dependence of the strain in the ice sheet on the parameters k and b, the strain at $\theta = \pi$ is plotted against k, shown in Figure 3.8(a). The strain increases steeply with k, indicating a sensitivity to this parameter. The cylinder radius is also varied, and we see that for longer waves, the value of b is less influential than for shorter waves. Figure 3.8(b) repeats this graph, instead varying the ice thickness h. In the long–wavelength limit $k \to 0$, thinner ice causes the highest strain. However, as k grows, the situation is rapidly reversed and the highest strain is incited by thicker ice. This is similar to the behaviour of the equivalent two–dimensional calculations of Section 2.4.2.

We retain our estimate from Chapter 2 for the yield strain of ice and take $\varepsilon_{cr} = 8 \times 10^{-5}$. Reviewing Figures 3.7-3.8, it seems likely that the connection at $r = b$ will not be maintained unless physical parameters take certain values. For example, the strain amplitude is proportional to the amplitude of the incident wave within the linear theory of hydroelasticity, and hence if the wave amplitude is small enough, the strain may stay below yield. Figures 3.7-3.8 use the arbitrary value

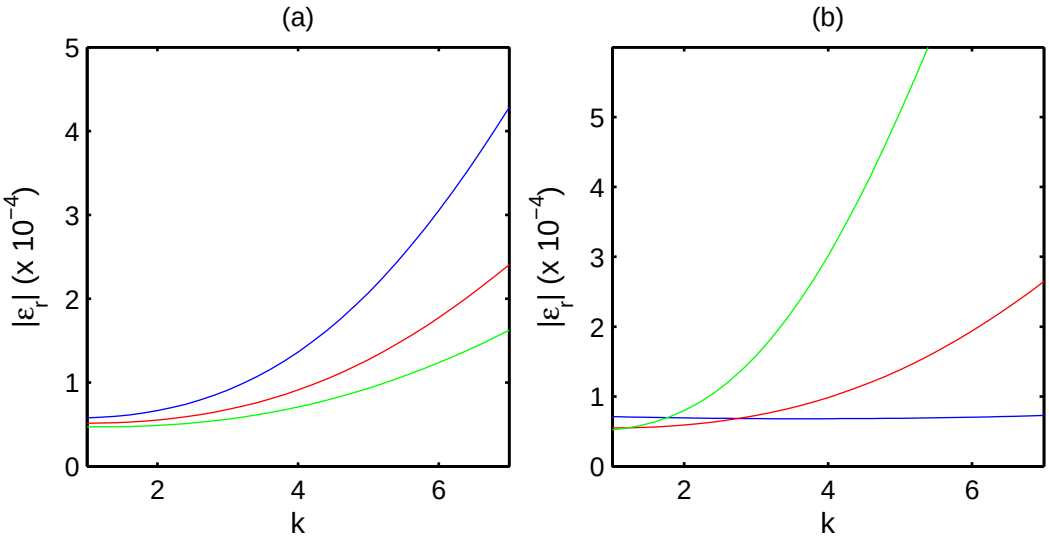

Figure 3.8: (a) The radial strain component ε_r is plotted against k. Here the cylinder radius $b = 3$ m (blue), $b = 4$ m (red) and $b = 5$ m (green). (b) The radial strain component ε_r is plotted against k for $b = 3.5$ m. Here the ice thickness $h = 0.5$ m (blue), $h = 1.5$ m (red) and $h = 2.5$ m (green). In both cases the amplitude $a = 1$ cm and the remaining parameters are set to their default values.

$a = 1$ cm. The strain in the ice sheet also has a sensitive dependence to the parameters k and b. Hence, if the incident waves are long enough, or the cylinder large enough, the strain may stay below yield level and the ice sheet will remain frozen to the cylinder.

3.4.3 Shear force

We now turn our attention to the vertical shear force, the upwards lifting force caused by the ice–clamping condition. The flexure of the ice sheet caused by the incident hydroelastic wave drives the cylinder vertically, threatening to break the connection between the cylinder and the sea bed if the connection is not strong enough. Here we assess the magnitude of this lifting force and factors influencing it.

The vertical shearing force Q_r acting on the cylinder is defined in the non-dimensional variables as (see for example Ugural, 1981)

$$V^r = -\frac{\partial}{\partial r}(\nabla^2 w)_{r=b}, \tag{3.73}$$

where the scale of the shear force is EJa/H^3. Equations (3.11) and (2.30) evaluated at $r = b$ provide

$$V^r(\theta,t) = \Re\Bigg(-ie^{-it}\sum_{n=0}^{\infty}\varepsilon^n\, i^n \cos(n\theta)\Big(\frac{\partial}{\partial r}S_n < J_n(kr) >_{r=b} + a_n^D \frac{\partial}{\partial r}S_n < H_n(kr) >_{r=b} + \frac{\partial}{\partial r}S_n < w_n(r) >_{r=b}\Big)\Bigg). \tag{3.74}$$

The derivatives on the right hand side may be simplified by noting

$$S_n < J_n(kr) >= -k^2 J_n(kr), \quad S_n < H_n(kr) >= -k^2 H_n(kr),$$

and we may substitute

$$\frac{\partial}{\partial r} S_n < w_n(r) >_{r=b} = \bar{V}_n, \tag{3.75}$$

where $\bar{V}_n$ is given by (3.54).

The maximum shear force with respect to time, $|V^r|$, is plotted against θ in Figure 3.9. As expected, the highest shear force is at $\theta = \pi$, the direction from which the incident wave approaches. In Figure 3.9(a) we vary the wavenumber k and find that shorter waves exert more lifting force on the vertical cylinder. In Figure 3.9(b), we vary the cylinder radius b: we see that an increase in the cylinder radius causes a decrease in vertical shear force. The polar behaviour is similar to that of the strain behaviour shown in Figure 3.7(b), which is to be expected as the strain and vertical force are closely linked by their dependence on the ice–clamping condition. The shear force V^r is very sensitive to both parameters k and b.

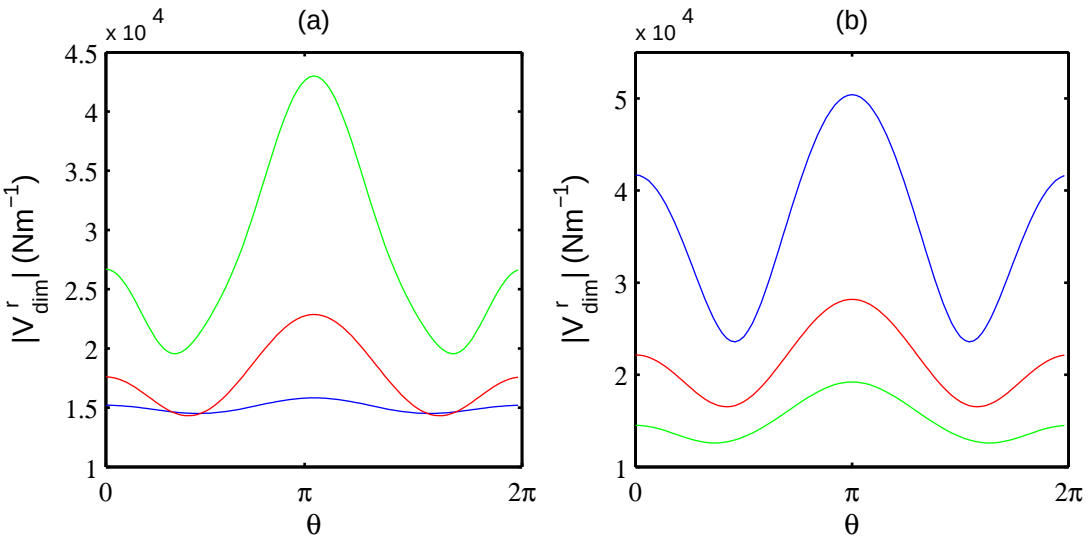

Figure 3.9: (a) The vertical shearing force V^r is plotted against θ for $b_{dim} = 3.5$ m. Here the wavenumber is given by $k = 2$ (blue), $k = 4$ (red) and $k = 6$ (green). (b) The vertical shearing force V^r is plotted against θ for $k = 5$. Here the cylinder radius is given by $b = 2$ m (blue), $b = 3$ m (red) and $b = 4$ m (green). In both cases the amplitude is set to $a = 1$ cm and the remaining parameters are set to their default values.

The total shear force acting on the cylinder is obtained by integrating $V^r(\theta, t)$ with respect to the angular coordinate θ, with the result

$$b \int_0^{2\pi} V^r(\theta, t)\, d\theta = V^T \cos(t + \delta), \tag{3.76}$$

where

$$
\begin{aligned}
V^T &= 2\pi b(u^2+v^2)^{\frac{1}{2}}, \qquad (3.77)\\
u &= J_0'(kb)\Big(2k^3(\beta_0-1)+\frac{V(k)\beta_0}{\gamma}\Big)+Y_0'(kb)\Big(2k^3\alpha_0+\frac{V(k)\alpha_0}{\gamma}\Big),\\
v &= J_0'(kb)\Big(-2k^3\alpha_0-\frac{V(k)\alpha_0}{\gamma}\Big)+Y_0'(kb)\Big(2k^3\beta_0+\frac{V(k)\beta_0}{\gamma}\Big),\\
a_0^D &= \alpha_0+i\beta_0.
\end{aligned}
$$

Note that V^T is the maximum total shear force with respect to time, and the phase shift δ is not studied here. Also note that in the integration of $V^r(\theta,t)$ in (3.76) the only contribution to the result comes from the terms with $n=0$, due to the periodicity of the cosine function. The scale of V^T is equal to EJa/H^2.

The total shear force V^T is plotted against k in Figure 3.10, under variation of the ice thickness. The results are very similar to those of the equivalent two–dimensional problem, shown in Section 2.4.3. The shear force is finite in the long wave limit, and declines to a minimum before rising again with k. There is a sensitive dependence on the ice thickness h, with thicker ice causing higher total shear force.

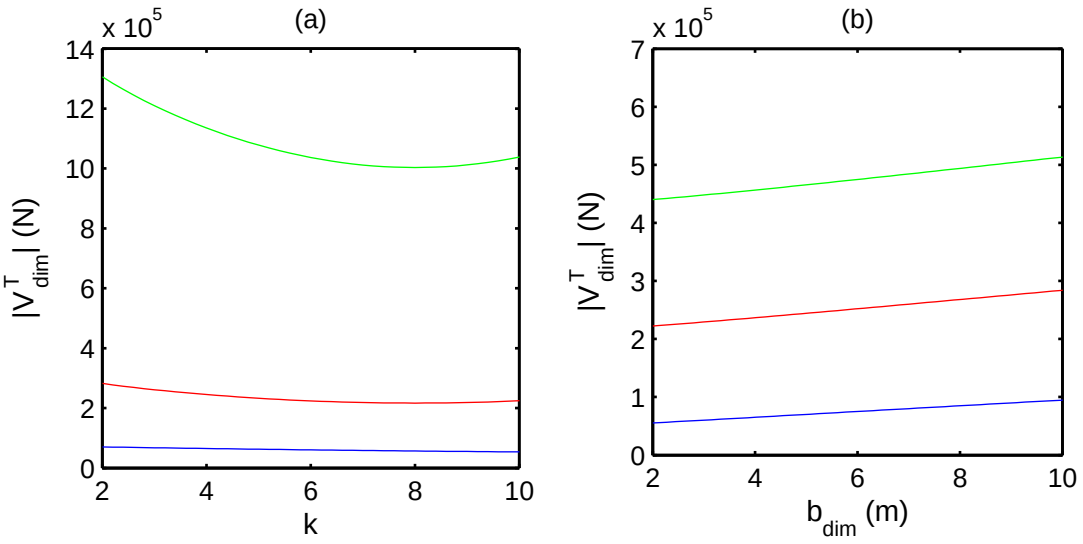

Figure 3.10: (a) The total vertical shearing force V^T is plotted against k for $b=3.5$m. Here the ice thickness is given by $h=0.5$ m (blue), $h=1.5$ m (red) and $h=2.5$ m (green). (b) The total vertical shearing force V^T is plotted against b for $k=5$. Here the ice thickness is given by $h=0.5$m (blue), $h=1.5$m (red) and $h=2.5$m (green). In both cases the amplitude is set to $a=1$ cm and the remaining parameters are set to their default values.

Figure 3.10 shows the total shear force plotted against the cylinder radius b. This relationship is shown to be linear, with a monotonic increase in shear force as the cylinder radius increases. Three values of the ice thickness h are also presented, with thicker ice again causing higher shear force. Figure 3.10 shows that the total shear force can be substantial in magnitude, with upwards lifting forces of order 10^6 N possible.

3.4.4 Horizontal force

We now investigate the other important component of force acting on the cylinder: the horizontal force caused by the incoming incident waves. The component of force in the y direction is zero due to the symmetry of the problem. The component of force in the x direction, F^x, is obtained by integrating the hydrodynamic pressure over the surface of the cylinder:

$$F^x(t) = -b \int_{-1}^{0} \int_{0}^{2\pi} p_D(b, \theta, z, t)\ \cos(\theta) d\theta dz. \tag{3.78}$$

The scale of the force F^x is $a\rho H^3 \omega^2$. Here p_D is the hydrodynamic pressure, which can be calculated from equations (3.3), (3.10) and (3.29) as

$$p_D(b, \theta, z, t) = \Re\Bigg(-ie^{-it} \sum_{n=0}^{\infty} \varepsilon^n\, i^n \cos(n\theta) \Big(f_0(z) J_n(kb) + a_n^D\ f_0(z) H_n(kb) + \varphi_n(b, z) \Big) \Bigg). \tag{3.79}$$

When integrating in (3.78) with respect to θ, we note that only the terms in (3.79) with $n = 1$ contribute to the result, due to the orthogonality of the cosine and sine functions. The contribution from $\varphi_1(b, z)$ in (3.79) is calculated by using (3.49) and inverse Weber transform. After manipulations we find the non-dimensional component of force in the positive x direction:

$$F^x(t) = \bar{F} \cos(t + \delta_f),$$

where

$$\bar{F} = \frac{16}{k^3 b \pi^2 (\chi_1^2 + \eta_1^2)^{\frac{1}{2}}} \int_0^{\infty} \frac{(s^2 - k^2) Q(s) + k}{s^3 \big((J_1'(sb))^2 + (Y_1'(sb))^2 \big)}\, ds \tag{3.80}$$

is the maximum force with respect to time, over one period. The quantities χ_1 and η_1 are given by (3.60).

The force F^x is plotted against k in Figure 3.11(a), for several values of the cylinder radius b. Starting at $k = 2$, as we increase k the horizontal force increases slightly before decreasing to a minimum. As we reach $k = 10$, the force begins to rise again in magnitude. The dependence on the parameter b is once again quite sensitive, with a thicker cylinder causing considerably higher horizontal force, the reasoning for which is apparent.

We wish to compare F^x in the presence of an ice sheet, with the hydrodynamic force acting on a vertical cylinder with no ice sheet present. From Mei (1983), the horizontal force on a vertical cylinder due to incident free surface waves is given by (in dimensionless variables and in the notation of this thesis):

$$F_{fs}^x = \frac{4 \tanh(k)}{k^2 \big((J_1'(kb))^2 + (Y_1'(kb))^2 \big)}, \tag{3.81}$$

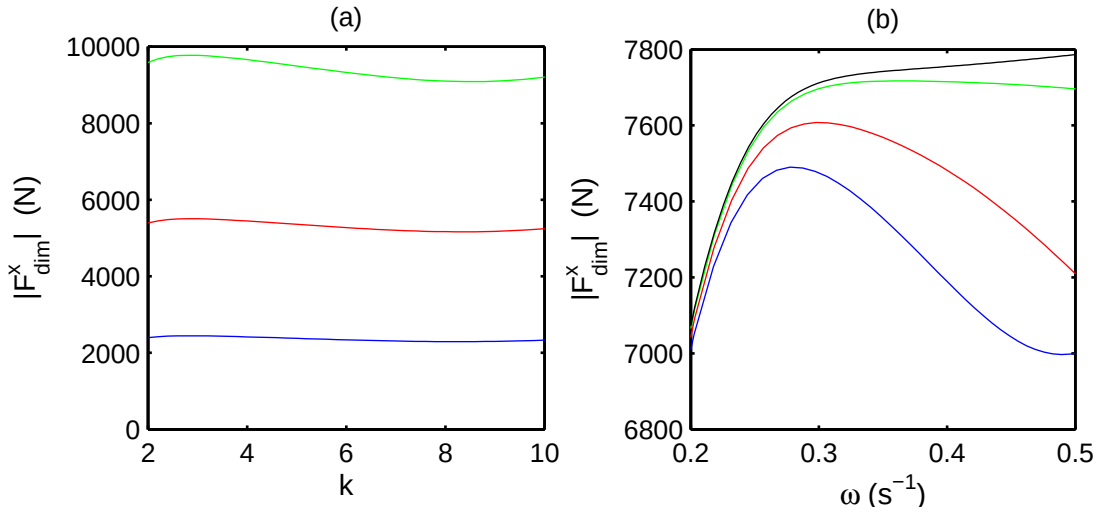

Figure 3.11: (a) The total horizontal wave force F^x is plotted against k. Here the cylinder radius is given by $b = 2\,\mathrm{m}$ (blue), $b = 3\,\mathrm{m}$ (red) and $b = 4\,\mathrm{m}$ (green). (b) The total horizontal wave force F^x is plotted against k. Here the ice thickness is given by $h = 1.6\,\mathrm{m}$ (blue), $h = 0.75\,\mathrm{m}$ (red) and $h = 0.1\,\mathrm{m}$ (green). The black curve represents the free surface horizontal force. In both cases the amplitude is set to $a = 1\,\mathrm{cm}$ and the remaining parameters are set to their default values.

and the dimensional force is obtained by multiplying F^x_{fs} by $ag\rho H^2$. Figure 3.11(b) plots the horizontal force for various ice thicknesses along with the free surface case. Note that the force is plotted against the wave frequency ω, due to the fact that ω is consistent between the ice and no-ice cases, whereas the wavenumber k is not. In contrast to the shear force, thicker ice leads to less horizontal force in the direction of wave propagation. As $h \to 0$ in the present model, the force approaches the equivalent force for the free surface case, as expected. For thicker ice, the force decreases as ω increases, while the opposite is true in the free surface case.

3.5 Summary

The work of Chapter 2 was extended into three dimensions. The problem of hydroelastic wave diffraction by a vertical cylinder was studied within the linear theory of hydroelasticity. In an ice sheet resting on fluid of finite depth, regular waves were incident on a vertical cylinder, to which the ice sheet was frozen. The hydroelastic interaction of the ice waves with the vertical cylinder was studied in detail.

The problem was formulated in polar co-ordinates to exploit the axisymmetry of the physical situation. The governing equations and boundary conditions introduced in Chapter 2 were rewritten in this cylindrical co-ordinate system. The problem was assumed to be time–periodic, allowing the ice deflection and velocity potential to be expressed independently of time. The regular incident wave was expressed in terms of a Fourier series, allowing the decomposition of the azimuthal co-ordinate. The ice deflection and velocity potential were then written as the linear sum of the incident waves, the cylindrical outgoing waves, and an extra function to account for

the boundary conditions on the cylinder.

The resulting boundary value problem was solved by Weber transform. This method leads to the solution being explicitly written in terms of integral quadratures. Numerical results were presented for the ice deflection for varying values of the wavenumber k. The deflection and slope of the deflection were equal to zero at the ice-cylinder boundary, as prescribed by the ice–clamping condition. The presence of the cylinder causes disturbance in the wave profile close to the cylinder, with reduced deflection nearby in the cylinder's wake. The influence of the cylinder becomes more pronounced as the incident wavelength becomes smaller, due to the cylinder radius being small in comparison with this wavelength.

The strain in the ice at the ice-cylinder connection point was also analysed in detail. These strains are generally high, but under certain conditions on the wave amplitude and wavelength the connection may be maintained. It is unlikely that the ice will remain frozen to the cylinder under the constant swell of large–amplitude ocean waves, but in applications involving frozen lakes where one expects smaller wave amplitude, the clamped boundary condition proves realistic. In the event of the ice breaking off from the surface of the cylinder, the problem can be reformulated and solved using the same method, with free edge conditions being considered instead of the fixed edge conditions of the present problem.

Expressions for the vertical shear and horizontal force components were also calculated. We conclude that these forces can reach large magnitudes, even for small–amplitude, long waves. The forces must therefore be considered when designing ocean structures in the presence of an ice cover. The behaviour of these forces under variation of parameters such as the incident wavenumber, the cylinder radius and the ice thickness was studied in detail.

An alternative method of solution that could have been used to tackle the present problem is one utilised by Malenica & Korobkin (2003). The velocity potential in both the free surface and ice–covered regions are expressed in terms of eigenfunction expansions, the eigenvalues of which are the solutions of the corresponding dispersion relation. Because the dispersion relations consist of an infinite number of imaginary roots, the resulting series must be truncated, leading to a linear system of equations for unknown coefficients. The Weber transform and its inherent propensity for symmetry leads to several advantages for solving the present problem. Firstly, the important function $Q(s)$ appeared in the equivalent two–dimensional problem of Chapter 2 and its properties and behaviour are therefore well known. Also $Q(s)$ and its behaviour govern every aspect of the problem, hence familiarity is useful. Also, the Weber transform solution expresses the unknown coefficients a_n^D in terms of exact integral quadrature. The velocity potential and ice deflection are expressed in terms of an infinite sum, but the solution converges extremely quickly, in the sense that few Fourier modes are required. The present method also leads to very concise expressions for the forces on the structure. The total horizontal force given by equation (3.80) is expressed in terms of integral quadrature, the integrand of

which decays rapidly. The total vertical shear force is given by (3.77), and (due to auspicious cancellation during the Weber transform) we are not required to calculate the third derivative, which could have led to convergence difficulties. The force is instead expressed algebraically once the coefficient a_1^D is obtained.

Chapter 4

Hydroelastic wave reflection by a vertical wall in a two-layer fluid

4.1 Introduction

There are many ways to generalise the hydroelastic model in Chapter 2 and attain more realism. One approach is to consider a fluid stratified into two layers of different densities, as opposed to one layer of constant density. The reasoning and justification for choosing this particular complication was discussed in Section 1.4. The physical formulation is very similar to that of Chapter 2, and the assumptions discussed in Section 2.1 apply here also. The incident hydroelastic wave propagates towards the vertical wall, to which the elastic plate is clamped. The elastic plate extends semi–infinitely and the fluid is of finite depth. Because the fluid is now stratified, in addition to the waves propagating in the ice sheet at the surface there are also waves at the boundary between the two layers. These are referred to as "interfacial" or "internal" waves. We will see that there are two wavenumbers for each value of the wave frequency, with one wavenumber representing the surface waves and the second representing the interfacial waves.

We will derive the solution to the hydroelastic wave problem and investigate how the stratification affects the behaviour of the solution. We will investigate whether waves of the interfacial mode can penetrate to the surface, and vice versa. We will consider different cases for the incident waves to investigate whether incident waves of one mode can excite waves of another mode. Also, we compare the solution of the present problem to that of Chapter 2, in order to assess the effect of fluid stratification in problems of hydroelasticity. Section 4.2 recaps the mathematical formulation of the problem and introduces new parameters. We then outline the boundary value problem to be solved. Section 4.3 demonstrates the method of solution. Numerical results are then presented and discussed in Section 4.4. A summary and conclusion of the chapter are given in Section 4.5.

4.2 Mathematical formulation

4.2.1 Schematic and parameters

The geometry of the problem and co-ordinate system are shown in Figure 4.1. The

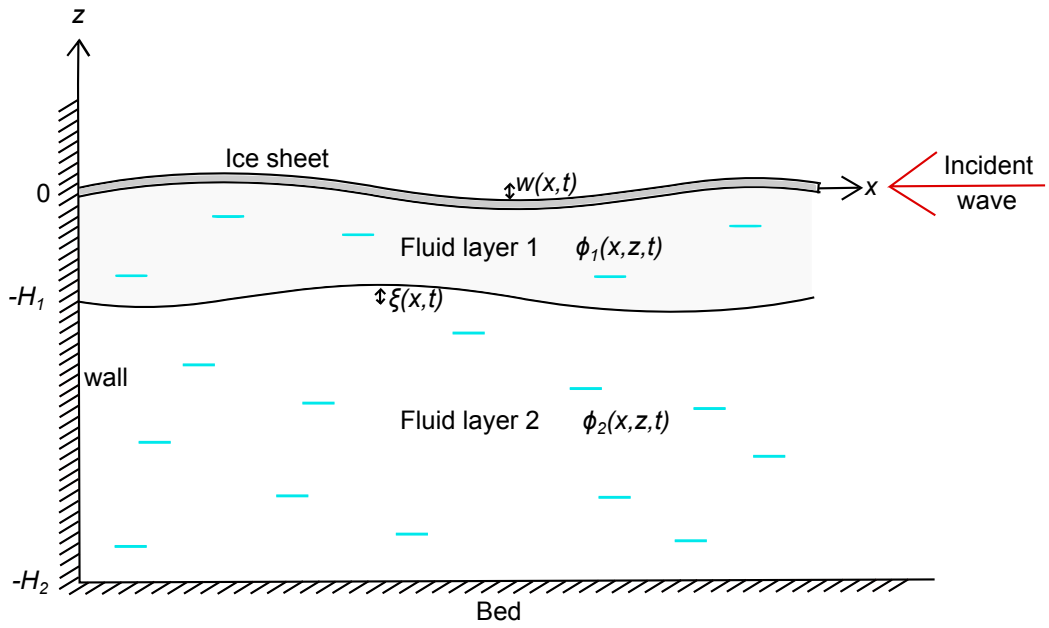

Figure 4.1: Schematic of a semi–infinite ice sheet meeting a vertical wall in a two-layer fluid.

formulation is similar to that outlined in Schulkes et al. (1987) with some notational differences. We introduce Cartesian coordinates with the positive x-axis coinciding with the ice sheet at rest and the z-axis directed vertically upwards along the wall. Time is denoted by t. We denote the upper layer of fluid as layer 1, with density ρ_1 and velocity potential $\phi_1(x, z, t)$. The lower layer of fluid, layer 2, has density ρ_2 and velocity potential $\phi_2(x, z, t)$ where $\rho_1 < \rho_2$. The interface between fluids 1 and 2 at rest is at $z = -H_1$, and the fluid bed is at $z = -H_2$. The deflection of the ice sheet (its vertical displacement relative to its position at rest) is denoted by $w(x, t)$. Similarly the vertical displacement of the interface is denoted by $\xi(x, t)$. The pressure in the fluid is represented by $p(x, z, t)$. Recapping the remaining parameters from Chapter 2: the ice has mass per unit length M, where $M = \rho_i h$, ρ_i is the ice density and h is the uniform ice thickness. The ice sheet has flexural rigidity EJ, where E is Young's modulus and $J = h^3/[12(1 - \nu^2)]$, where ν is Poisson's ratio. The acceleration due to gravity is denoted g. The incident wave parameters are introduced and specified after we establish the form of the incident waves.

4.2.2 Governing equations and boundary conditions

We now derive the governing differential equations for the velocity potentials, plate deflection, and interfacial deflection. We also state the boundary conditions based on the physical situation. The analysis is similar to that of Section 2.2.2, with some additions to account for the two–layer fluid model. The velocity potentials in both

layers must satisfy Laplace's equation in the (linearised) fluid domain:

$$\nabla^2\phi_1 = 0, \qquad (x > 0,\ -H_1 < z < 0), \tag{4.1}$$
$$\nabla^2\phi_2 = 0, \qquad (x > 0,\ -H_2 < z < H_1). \tag{4.2}$$

Boundary conditions at the rigid wall are

$$\phi_{1x} = 0, \qquad (x = 0,\ -H_1 < z < 0), \tag{4.3}$$
$$\phi_{2x} = 0, \qquad (x = 0,\ -H_2 < z < -H_1). \tag{4.4}$$

The condition at the fluid bed is

$$\phi_{2z} = 0, \qquad (x > 0,\ z = -H_2). \tag{4.5}$$

These conditions ensure no flow through the wall and the bed, respectively. The linearised kinematic boundary condition at the ice-fluid boundary is given by

$$\phi_{1z} = w_t, \qquad (x > 0,\ z = 0), \tag{4.6}$$

and the kinematic conditions at the fluid interface are

$$\phi_{1z} = \xi_t, \qquad (x > 0,\ z = -H_1), \tag{4.7}$$
$$\phi_{2z} = \xi_t, \qquad (x > 0,\ z = -H_1). \tag{4.8}$$

The linearised Bernoulli equation for the pressure is combined with the plate equation (see Section 2.2.2) to give

$$EJ\nabla^4 w + Mw_{tt} = -\rho_1 g w - \rho_1\,\phi_{1t}, \qquad (x > 0,\ z = 0). \tag{4.9}$$

The dynamic condition at the interface is:

$$\rho_1(\phi_{1t} + g\xi) = \rho_2(\phi_{2t} + g\xi), \qquad (x > 0,\ z = -H_1). \tag{4.10}$$

Boundary conditions on $w(x,t)$ are due to the ice being clamped at the wall, and hence

$$w = 0, \qquad (x = 0), \tag{4.11}$$
$$w_x = 0, \qquad (x = 0). \tag{4.12}$$

We assume that the flow is time–harmonic with period ω. Therefore we take:

$$\phi_1(x,z,t) = \Re\Big(\Phi_1(x,z)e^{-i\omega t}\Big), \tag{4.13}$$

$$\phi_2(x,z,t) = \Re\Big(\Phi_2(x,z)e^{-i\omega t}\Big), \tag{4.14}$$

$$w(x,t) = \Re\Big(\frac{i}{\omega}W(x)e^{-i\omega t}\Big), \tag{4.15}$$

$$\xi(x,t) = \Re\Big(\frac{i}{\omega}\Xi(x)e^{-i\omega t}\Big). \tag{4.16}$$

For completeness we recast the problem in terms of the unknown variables Φ_1, Φ_2, W and Ξ:

$$\nabla^2\Phi_1 = 0, \quad (x>0,\ -H_1<z<0), \tag{4.17}$$

$$\nabla^2\Phi_2 = 0, \quad (x>0,\ -H_2<z<-H_1), \tag{4.18}$$

$$\Phi_{2z} = 0, \quad (x>0,\ z=-H_2), \tag{4.19}$$

$$\Phi_{1z} = W, \quad (x>0,\ z=0), \tag{4.20}$$

$$\Phi_{1z} = \Phi_{2z} = \Xi, \quad (x>0,\ z=-H_1), \tag{4.21}$$

$$\rho_1(g\Xi - \omega^2\Phi_1) = \rho_2(g\Xi - \omega^2\Phi_2), \quad (x>0,\ z=-H_1), \tag{4.22}$$

$$EJ\nabla^4 W + W(\rho_1 g - \omega^2 M) = \rho_1\omega^2\,\Phi_1, \quad (x>0,\ z=0), \tag{4.23}$$

$$\Phi_{1x} = 0, \quad (x=0,\ -H_1<z<0), \tag{4.24}$$

$$\Phi_{2x} = 0, \quad (x=0,\ -H_2<z<-H_1), \tag{4.25}$$

$$W = 0, \quad (x=0), \tag{4.26}$$

$$W_x = 0, \quad (x=0). \tag{4.27}$$

Conditions as x tends to infinity are not included yet in this formulation, and will be derived in the following section.

4.2.3 Incident waves

We now derive the forms of the incident waves for Φ_1, Φ_2, Ξ and W. This is equivalent to finding expressions for hydroelastic unidirectional waves propagating in a two-layer fluid of finite depth. They must therefore satisfy equations (4.17)-(4.22). We begin by assuming left–travelling waves of the form:

$$\Phi_{1inc} = B(z)\,e^{-ikx}, \tag{4.28}$$

$$\Phi_{2inc} = A(z)\,e^{-ikx}, \tag{4.29}$$

where $A(z)$ and $B(z)$ are to be found. We substitute equations (4.28)-(4.29) into (4.17)-(4.18) to obtain

$$A_{zz} - k^2 A = 0, \tag{4.30}$$

$$B_{zz} - k^2 B = 0. \tag{4.31}$$

In conjunction with the boundary condition (4.19), we find that the general solution to equation (4.30) is

$$A(z) = A_1(k)\cosh(k(z+H_2)), \tag{4.32}$$

where A_1 is a function of k be found. Similarly, the general solution for equation (4.31) is

$$B(z) = B_1(k)\cosh(kz) + B_2(k)\sinh(kz), \tag{4.33}$$

where B_1 and B_2 are both functions of k to be found. Using the interfacial fluid condition (4.21), we find

$$B_2(k) = A_1(k)\frac{\sinh(k(H_2-H_1))}{\cosh(kH_1)} + B_1(k)\frac{\sinh(kH_1)}{\cosh(kH_1)}.$$

Combining equations (4.21) and (4.22) gives

$$\rho_1\left(g\frac{\partial\Phi_{2inc}}{\partial z} - \omega^2\Phi_{1inc}\right) = \rho_2\left(g\frac{\partial\Phi_{2inc}}{\partial z} - \omega^2\Phi_{2inc}\right), \qquad (z=-H_1).$$

Substituting our current expressions (4.28)-(4.29) for Φ_{1inc} and Φ_{2inc} into this equation gives

$$\begin{aligned}\rho_1\Big(gA_1(k)k\sinh(k(H_2-H_1)) - \omega^2\big(B_1(k)\cosh(kH_1) - B_2(k)\sinh(kH_1)\big)\Big)\\ = \rho_2\Big(gA_1(k)k\sinh(k(H_2-H_1)) - \omega^2A_1(k)\cosh(k(H_2-H_1))\Big).\end{aligned}$$

After considerable rearranging we obtain

$$B_1(k) = A_1(k)\frac{\cosh(kH_1)\sinh(k(H_2-H_1))}{\rho_1/\rho_2}\,\theta(k,\omega),$$

where we have defined

$$\theta(k,\omega) = \frac{\rho_1}{\rho_2}\tanh(kH_1) + \coth(k(H_2-H_1)) - \frac{gk(\rho_2-\rho_1)}{\rho_2\omega^2}. \tag{4.34}$$

We define

$$W_{inc}(x) = a\,e^{-ikx}, \tag{4.35}$$

where a is the amplitude of the incident hydroelastic wave. We use the kinematic condition (4.20) to give

$$a = kA_1(k)\Big(\frac{\sinh(k(H_2-H_1))}{\cosh(kH_1)} + \frac{\sinh(k(H_2-H_1))\sinh(kH_1)}{\rho_1/\rho_2}\theta(k,\omega)\Big),$$

which after more rearranging gives

$$A_1(k) = \frac{a(\rho_1/\rho_2)}{k\chi(k,\omega)\sinh(kH_1)\sinh(k(H_2-H_1))},$$

where

$$\chi(k,\omega) = \frac{\rho_1}{\rho_2}\coth(kH_1) + \coth(k(H_2 - H_1)) - \frac{gk(\rho_2 - \rho_1)}{\rho_2\omega^2}. \tag{4.36}$$

Finally, using equation (4.21), we find

$$\frac{\Xi_{inc}}{W_{inc}} = \frac{(\rho_1/\rho_2)}{\chi(k,\omega)\sinh(kH_1)}\,, \tag{4.37}$$

which defines the amplitude ratio between the surface and interfacial waves. This will be studied in more detail later.

Now we have expressions for the constants A_1, B_1 and B_2, we substitute them into (4.32) and (4.33) to find $A(z)$ and $B(z)$. Then, using equations (4.28)-(4.29) and (4.35)-(4.36) the expressions for the incident waves are given by:

$$W_{inc} = a\,e^{-ikx}, \tag{4.38}$$

$$\Xi_{inc} = a\frac{(\rho_1/\rho_2)}{\chi(k,\omega)\sinh(kH_1)}\,e^{-ikx}, \tag{4.39}$$

$$\Phi_{1inc} = \frac{a}{k}\Big(\mu(k,\omega)\cosh(kz) + \sinh(kz)\Big)\,e^{-ikx}, \tag{4.40}$$

$$\Phi_{2inc} = \frac{a(\rho_1/\rho_2)\cosh(k(z+H_2))}{k\chi(k,\omega)\sinh(kH_1)\sinh(k(H_2-H_1))}\,e^{-ikx}. \tag{4.41}$$

Here, $\theta(k,\omega)$ is given by (4.34), $\chi(k,\omega)$ is given by (4.36) and we have defined for brevity

$$\mu(k,\omega) = \frac{1}{\tanh(kH_1)}\frac{\theta(k,\omega)}{\chi(k,\omega)}. \tag{4.42}$$

The incident wave solution (4.38)-(4.41) satisfies equations (4.17)-(4.22).

4.2.4 Dispersion relation

Substituting the incident waves (4.38) and (4.40) into the plate equation (4.23):

$$EJ(-ik)^4 a\,e^{-ikx} + (\rho_1 g - \omega^2 M)a\,e^{-ikx} = \frac{\omega^2\rho_1\mu(k)}{k}a\,e^{-ikx}, \tag{4.43}$$

which rearranges to

$$\omega^2 = \frac{EJk^5 + \rho_1 gk}{Mk + \rho_1\mu(k)}. \tag{4.44}$$

This is the dispersion relation for waves in a two–layer fluid in the presence of an ice cover. It was first derived by Schulkes et al. (1987). The expression for $\mu(k,\omega)$ involves ω^2 terms, and hence the dispersion relation is a quadratic equation in ω^2; it can be rearranged in the form $d_1\omega^4 + d_2\omega^2 + d_3 = 0$, with the real coefficients d_1, d_2 and d_3 being functions of k (this is not performed here but may be found in Schulkes et al., 1987). The two roots are then given by the quadratic formula

$$\omega_\pm^2 = \frac{-d_2 \pm (d_2^2 - 4d_1d_3)^{\frac{1}{2}}}{2d_1}.$$

So for each value of k chosen there are two explicit frequencies ω_+ and ω_-. It can be shown that both roots are positive for any wavenumber k. The two roots are expected because the system has two degrees of freedom, involving surface waves at $z = 0$ and interfacial waves at $z = -H_1$ (Schulkes et al., 1987).

In this study we instead take the approach of fixing a period ω, leading to two positive roots k_1 and k_2, where $k_1 < k_2$. Section 4.2.6 further explains how the two roots are calculated. The root k_1 represents surface waves in the ice cover, and k_2 represents interfacial waves. Though waves of both wavenumbers may exist at either surface, waves of mode k_1 have higher amplitude in the ice cover than waves of wavenumber k_2, so we call k_1 the "surface wavenumber". The same terminology leads to our calling k_2 the "interfacial wavenumber". Figure 4.2(a) shows the phase speed c plotted against k_1 (the surface wavenumber) for varying values of the total depth H_2. Other parameters are taken from the default data set, defined later in Table 4.1. The curve is extremely similar to the corresponding curve for the one-layer model, plotted in Figure 2.2. This indicates that k_1 provides the surface mode. The phase speed continues to grow as k_1 increases, meaning there are two values of k_1 for each value of $c > c_{min}$. Shallower water leads to slower phase speed, although as k_1 increases beyond $0.03\,\mathrm{m}^{-1}$, the depth ceases to influence the phase speed. Note that the top water layer depth H_1 is fixed at 20 m and the phase speed is unaffected by changes in H_1. The corresponding graph for the internal wavenumber k_2 is found

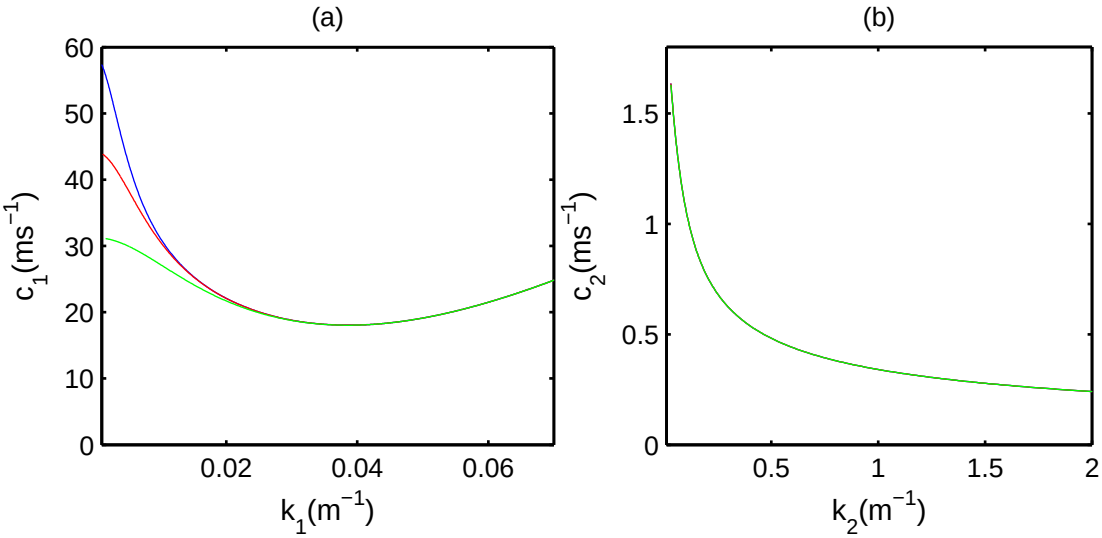

Figure 4.2: (a) The phase speed of the surface waves $c_1 = \omega/k_1$ is plotted against the wavenumber k_1. (b) The phase speed of the interfacial waves $c_2 = \omega/k_2$ is plotted against the wavenumber k_2. In both cases the total depth H_2 is given by $H_2 = 350\,\mathrm{m}$ (blue), $H_2 = 200\,\mathrm{m}$ (red) and $H_2 = 100\,\mathrm{m}$ (green). For all curves, $H_1 = 20\,\mathrm{m}$.

in Figure 4.2(b). The shape of the curve is different and, unlike for the surface mode, there is no stationary point c_{min} and there is only one k_2 value for each c value. It is clear that the second root k_2 is insensitive to the total depth H_2. Comparing the two graphs, we see that the surface waves are considerably faster than the internal waves.

Parameter	Typical value
g	$9.8\,\mathrm{ms}^{-2}$
h	$1.6\,\mathrm{m}$
ν	0.3
E	$4.2\,\mathrm{x}\,10^{9}\,\mathrm{Nm}^{-2}$
J	$0.375\,\mathrm{m}^{3}$
ρ_i	$917\,\mathrm{kgm}^{-3}$
M	$1467.2\,\mathrm{kgm}^{-2}$
ρ_1	$1000\,\mathrm{kgm}^{-3}$
ρ_2	$1024\,\mathrm{kgm}^{-3}$
H_1	$20\,\mathrm{m}$
H_2	$350\,\mathrm{m}$

Table 4.1: Values of typical parameters taken from measurements at McMurdo Sound, Antarctica (Squire et al., 1988), with some additions for the two-layer fluid problem.

Schulkes et al. (1987) noticed that some earlier results can be viewed as limiting cases of the dispersion relation (4.44). For example, if we take $\rho_2 \to \rho_1$ we have $\mu(k) \to \coth(kH_1)$ and we obtain the dispersion relation from Chapter 2, that is, the dispersion relation for an elastic plate resting on a one-layer fluid of finite depth with density ρ_1. This is also the case when we consider the limit $H_1 \to H_2$. Alternatively if we take $H_1 \to 0$, we obtain the dispersion relation for an elastic plate resting on a one-layer fluid of finite depth, but this time with density ρ_2. Also, taking the limit of very small ice thickness leads to $EJ \to 0$ and we recover the dispersion relation for a two-layer fluid of finite depth with no ice cover.

In this study, we will consider various depths H_1 and H_2, in the ranges $5\,\mathrm{m} \leq H_1 \leq 20\,\mathrm{m}$, and $100\,\mathrm{m} \leq H_2 \leq 350\,\mathrm{m}$. The density ratio ρ_1/ρ_2 is open to debate, as there is little literature on the subject of varying fluid density under an ice sheet. Schulkes et al. (1987) take an upper layer density of $\rho_1 = 1024\,\mathrm{kgm}^{-3}$ and a lower layer density of $\rho_2 = 1025.3\mathrm{kgm}^{-3}$. For our study, we will take $\rho_2 = 1024\mathrm{kgm}^{-3}$ and vary ρ_1 between $1000\,\mathrm{kgm}^{-3} \leq \rho_1 \leq 1020\,\mathrm{kgm}^{-3}$, which is a wide enough range to sufficiently demonstrate the effect of fluid stratification under an ice sheet. The default values of each parameter, used to plot all figures, are given in Table 4.1.

Mohapatra & Bora (2009) for illustrative purposes took a density ratio of 0.5 for the two fluid layers, and state "the values of the two roots of the dispersion equation approach the same value ... if we take the ratio of the two densities nearer to 0.97". However, this is incorrect; in fact, the root k_2 grows rapidly in the limit $\rho_1 \to \rho_2$, whereas k_1 is insensitive to changes in ρ_1. This is demonstrated in Figure 4.3.

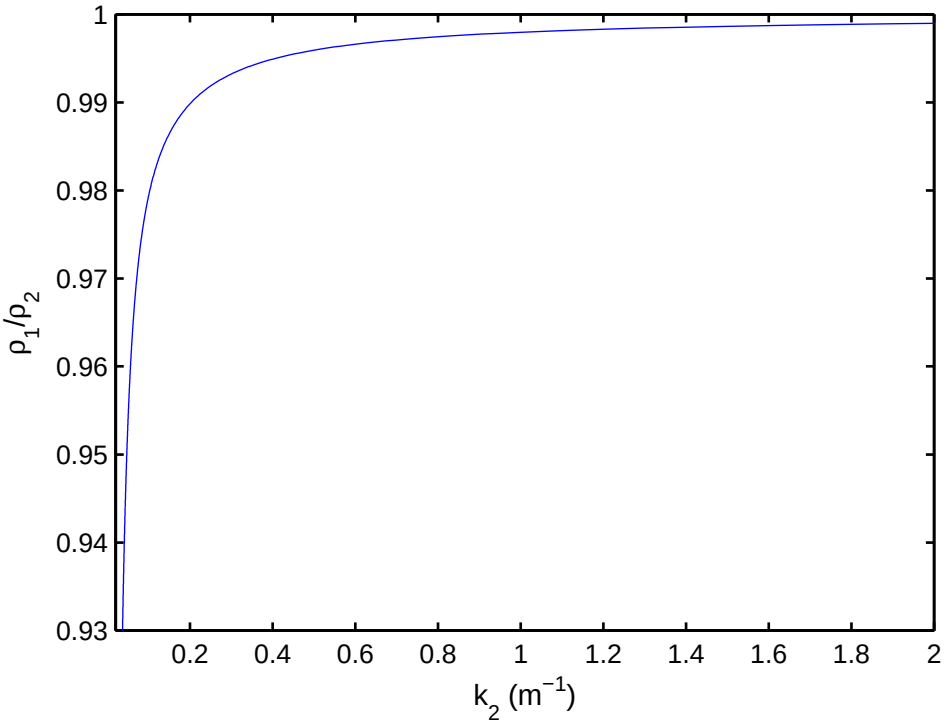

Figure 4.3: The root k_2 plotted against the density ratio ρ_1/ρ_2.

4.2.5 Nondimensionalisation

We define the dimensionless parameters/variables as

$$k^* = kH_2, \quad \bar{\rho} = \frac{\rho_1}{\rho_2}, \quad \bar{H} = \frac{H_1}{H_2}, \quad x^* = \frac{x}{H_2}, \quad z^* = \frac{z}{H_2}, \quad t^* = \omega t,$$
$$\gamma = \frac{EJ}{H_2^5 \rho_1 \omega^2}, \quad \alpha = \frac{\rho_1 g - \omega^2 M}{\rho_1 \omega^2 H_2}, \quad \beta = \frac{\omega^2 H_2}{g(1-\bar{\rho})},$$
$$\Phi_1^* = \frac{\Phi_1}{H_2 a \omega}, \quad \Phi_2^* = \frac{\Phi_2}{H_2 a \omega}, \quad \Xi^* = \frac{\xi}{a\omega}, \quad W^* = \frac{W}{a\omega}.$$

The asterisks are dropped in the analysis below, and all variables are assumed dimensionless unless stated otherwise or accompanied by units. The parameters k_1 and k_2 are also assumed dimensionless.

4.2.6 Notes regarding the roots k_1 and k_2

Because we are fixing a constant ω and using it to calculate the values of k, the functions θ, χ and μ are denoted as functions of k only, though we note that they also contain ω. Now, we further discuss the calculation of the roots k_1 and k_2.

We can rewrite the dispersion relation (4.44) in dimensionless form as

$$f(k) = \gamma k^5 + \alpha k - \mu(k) = 0, \tag{4.45}$$

where α and γ are coefficients defined above which depend on ω^2. Because it is impossible to rearrange the dispersion equation (4.44) to explicitly define k_1 and k_2 algebraically, they are found via iterative root finding. However, we should note

that using root-finding iteration on equation (4.45) to find the roots of $f(k) = 0$ only yields one root for each ω value. We multiply $f(k)$ by $\chi(k)$ and define $g(k) = \chi(k)f(k)$, then we solve $g(k) = 0$: this allows both roots to be found. Figure 4.4

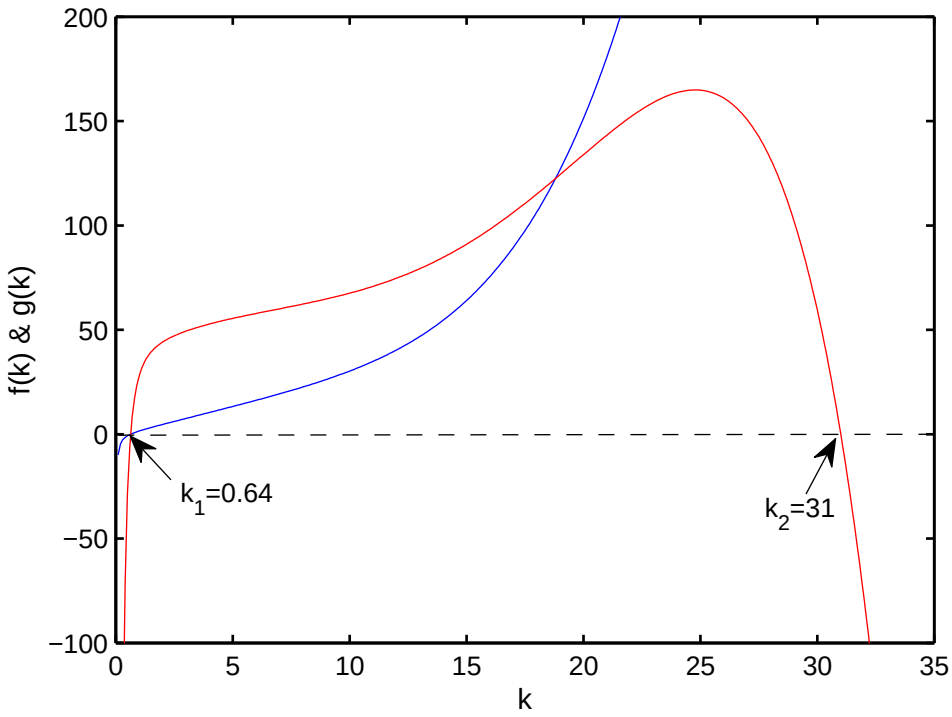

Figure 4.4: The functions $f(k)$ (blue) and $g(k)$ (red) are plotted against k to demonstrate how to find the two roots $k_1 = 0.64$ and $k_2 = 31$. Here ω is fixed at $0.1\ \mathrm{s}^{-1}$, $H_1 = 20$ m and $H_2 = 350$ m.

demonstrates this; the blue curve $f(k)$ correctly finds the root $k_1 = 0.64$, but shoots to infinity as k grows, thus failing to find the root $k_2 = 31$. The explanation for this phenomenon is found in the function $\mu(k) = \coth(k\bar{H})[\theta(k)/\chi(k)]$. Recall that

$$\theta(k) = \bar{\rho}\coth(k\bar{H}) + \coth(k(1-\bar{H})) - \frac{k}{\beta},$$
$$\chi(k) = \bar{\rho}\tanh(k\bar{H}) + \coth(k(1-\bar{H})) - \frac{k}{\beta}.$$

Note that $\theta(k)$ and $\chi(k)$ are very similar and only differ by the first term. Also, in the limit $k \to \infty$, we have $\coth(k\bar{H}) \approx \tanh(k\bar{H}) \approx 1$, and hence $\theta(k) \sim \chi(k) \sim -k/\beta$. We note that $\mu(k)$ is undefined at the point $k = k_{cr}$ where $\chi(k_{cr}) = 0$. This causes problems when plotting the function $\mu(k)$ (see Figure 4.5). As k_2 is generally at least of order 10, the function $\theta(k_{cr})$ is very small also. However, the second root k_2 occurs very close to k_{cr} and is in some sense 'hidden' close to this singularity when we attempt to calculate it. Hence, we need to be very careful when evaluating $\mu(k_2)$ or any term involving $1/\chi(k_2)$.

As in Chapter 2, we are most interested in long surface waves. Muzylev (2007), while studying internal waves under an ice cover in the absence of background currents in the Arctic ocean, considers waves of extremely low frequency, taking a

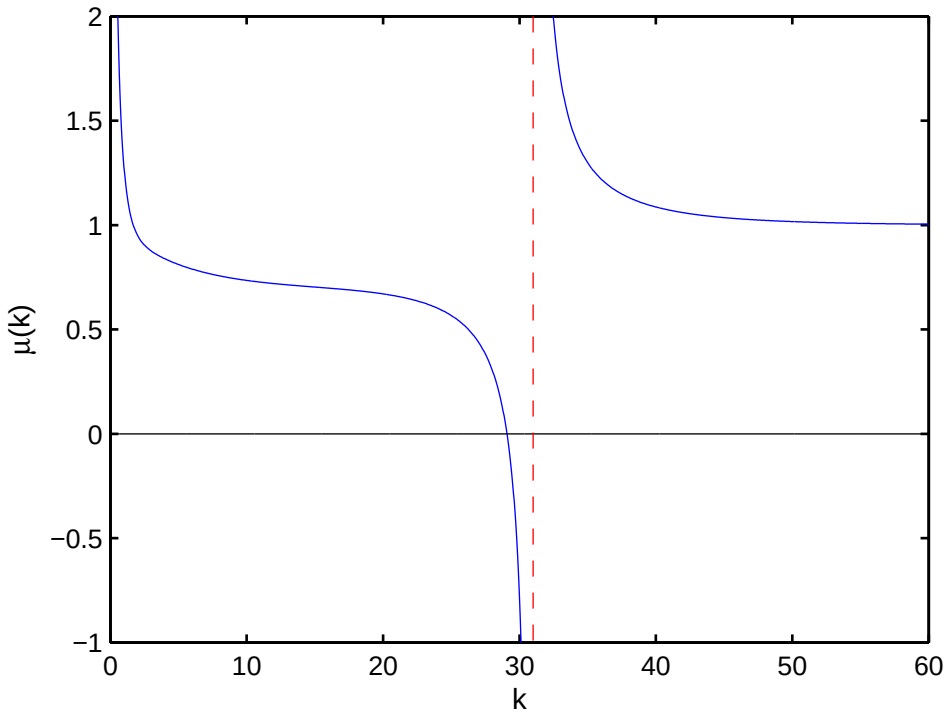

Figure 4.5: The function $\mu(k)$ is plotted against k. The vertical asymptote is where μ is undefined at $k_{cr} = 31.0052$; the root $k_2 = 31.0069$.

maximum period of 12 min and a maximum wavelength of 600 m, in agreement with experimental results. Czipott et al. (1991) studied ice flexure, forced by internal wave packets in the Arctic Ocean; they used tiltmeters to measure a surface wave of period 24 min and wavelength 600 m. Hence it is clear that we must consider very long surface waves: we therefore consider a range of waves from $\omega = 0.05 - 0.2\,\mathrm{s}^{-1}$. The values of k_1 and k_2 are then calculated for each ω. Figure 4.6 shows the wave frequency plotted against the wave period $2\pi/\omega$. The corresponding values of k_1 and k_2 are given in Figure 4.7 for varying values of the density ρ_1 to demonstrate which values of dimensionless k_1 and k_2 correspond to the selected values of ω.

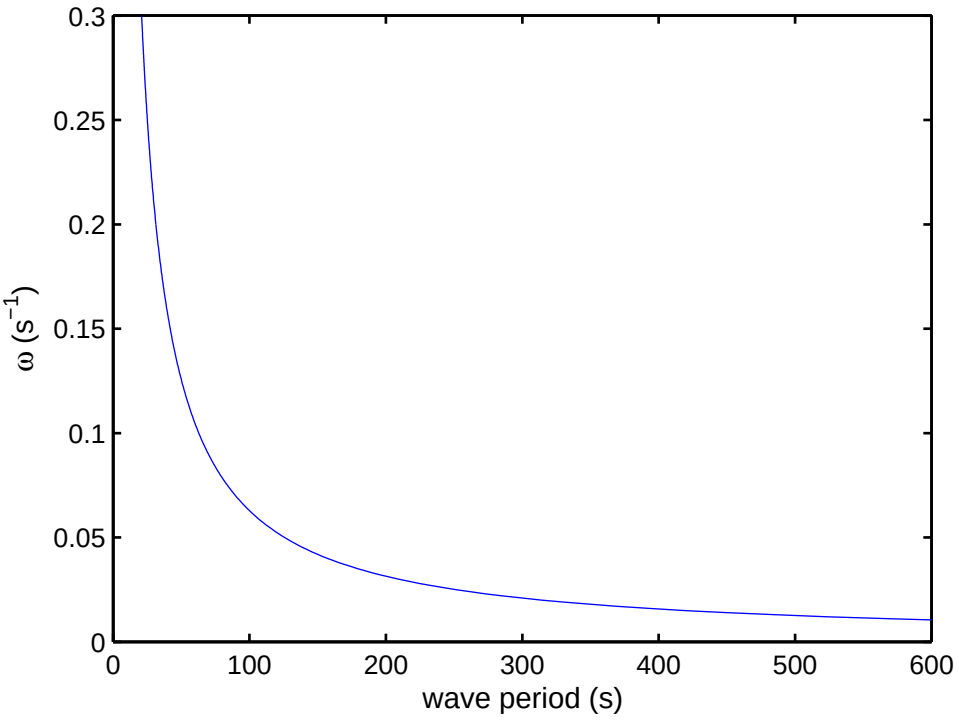

Figure 4.6: The wave frequency ω is plotted against the wave period.

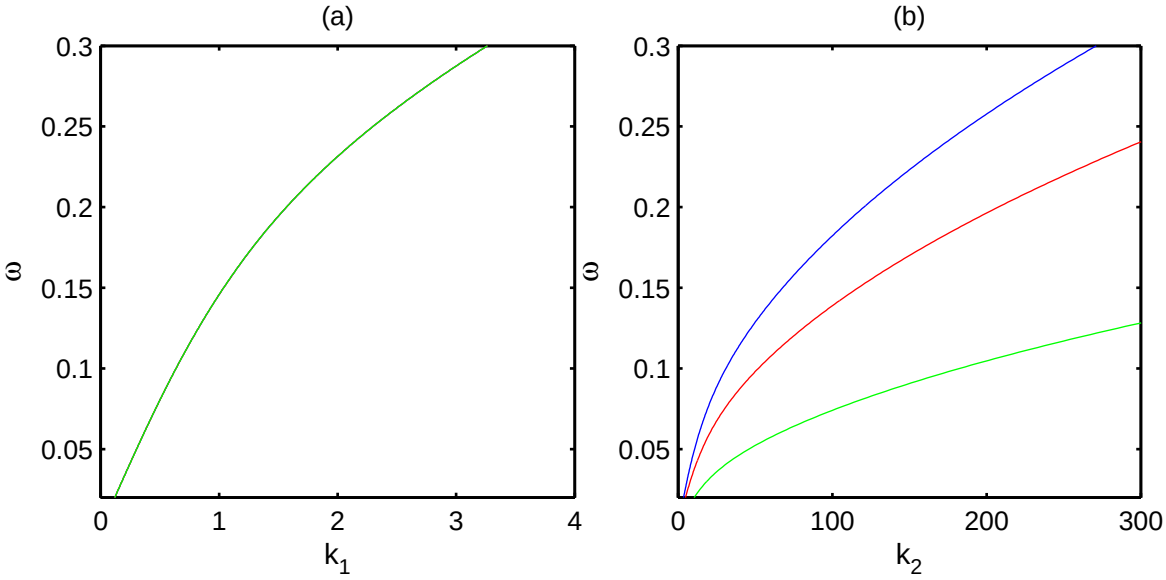

Figure 4.7: The wave frequency ω is plotted against the wavenumbers (a) k_1 and (b) k_2. The density ρ_1 is given by $1000\,\mathrm{kgm}^{-3}$ (blue), $1010\,\mathrm{kgm}^{-3}$ (red) and $1020\,\mathrm{kgm}^{-3}$ (green).

4.2.7 Nondimensional BVP

We rewrite the boundary value problem (4.17)-(4.27) in terms of the dimensionless parameters and variables defined in Section 4.2.5.

$$\nabla^2\Phi_1 = 0, \quad (x > 0,\ -\bar{H} < z < 0), \tag{4.46}$$
$$\nabla^2\Phi_2 = 0, \quad (x > 0,\ -1 < z < -\bar{H}), \tag{4.47}$$
$$\Phi_{2z} = 0, \quad (x > 0,\ z = -1), \tag{4.48}$$
$$\Phi_{1z} = W, \quad (x > 0,\ z = 0), \tag{4.49}$$
$$\Phi_{1z} = \Phi_{2z} = \Xi, \quad (x > 0,\ z = -\bar{H}), \tag{4.50}$$
$$\gamma\nabla^4 W + \alpha W = \Phi_1(x, 0), \quad (x > 0,\ z = 0), \tag{4.51}$$
$$\Phi_{2z} = \beta(\Phi_2 - \bar{\rho}\Phi_1), \quad (x > 0,\ z = -\bar{H}), \tag{4.52}$$
$$\Phi_{1x} = 0, \quad (x = 0,\ -\bar{H} < z < 0), \tag{4.53}$$
$$\Phi_{2x} = 0, \quad (x = 0,\ -1 < z < -\bar{H}), \tag{4.54}$$
$$W = 0, \quad (x = 0), \tag{4.55}$$
$$W_x = 0, \quad (x = 0). \tag{4.56}$$

We note that the boundary value problem depends on the five dimensionless parameters $\bar{H}$, $\bar{\rho}$, α, β and γ which define the physical properties of the ice and the two fluid layers.

4.2.8 Total forms for the potentials & deflections

In a similar manner to Chapter 2, we use linear superposition to express the total forms of Φ_1, Φ_2, Ξ and W. They are expressed as the sum of an incident wave term, a reflected wave term, and an extra function (which decreases to zero in the far field), which describes the motion near the vertical wall. Hence we have

$$\Phi_1(x, z) = \Phi_{1inc}(x, z) + \Phi_{1ref}(x, z) + \varphi_1(x, z), \tag{4.57}$$
$$\Phi_2(x, z) = \Phi_{2inc}(x, z) + \Phi_{2ref}(x, z) + \varphi_2(x, z), \tag{4.58}$$
$$W(x) = W_{inc}(x) + W_{ref}(x) + \hat{w}(x), \tag{4.59}$$
$$\Xi(x) = \Xi_{inc}(x) + \Xi_{ref}(x) + \hat{\xi}(x). \tag{4.60}$$

Given that there are two wavenumbers k_1 and k_2, we will later choose incident waves of one mode or both. The simplest way to proceed is to define, using equations (4.38)-(4.41);

$$f_1(k, z) = \frac{\mu(k)}{k}\cosh(kz) + \frac{\sinh(kz)}{k},$$
$$f_2(k, z) = \frac{\bar{\rho}\cosh(k(z+1))}{k\sinh(k\bar{H})\sinh(k(1-\bar{H}))\,\chi(k)},$$
$$f_3(k) = \frac{\bar{\rho}}{\sinh(k_1\bar{H})\,\chi(k)},$$

and then we take the forms of the incident waves as

$$\Phi_{1inc} = a_1^I \, f_1(k_1, z) \, e^{-ik_1 x} + a_2^I \, f_1(k_2, z) \, e^{-ik_2 x}, \tag{4.61}$$

$$\Phi_{2inc} = a_1^I \, f_2(k_1, z) \, e^{-ik_1 x} + a_2^I \, f_2(k_2, z) \, e^{-ik_2 x}, \tag{4.62}$$

$$W_{inc} = a_1^I \, e^{-ik_1 x} + a_2^I \, e^{-ik_2 x}, \tag{4.63}$$

$$\Xi_{inc} = a_1^I \, f_3(k_1) \, e^{-ik_1 x} + a_2^I \, f_3(k_2) \, e^{-ik_2 x}. \tag{4.64}$$

These equations define the waves propagating towards the vertical wall from $x = +\infty$. Here, the coefficients a_1^I and a_2^I are known constants. We may choose which values to take for a_1^I and a_2^I based on what kinds of incident waves we wish to consider; waves of mode k_1 or k_2 or both. This is discussed more in Section 4.4. The reflected waves are then given by

$$\Phi_{1ref} = a_1^D \, f_1(k_1, z) \, e^{+ik_1 x} + a_2^D \, f_1(k_2, z) \, e^{+ik_2 x}, \tag{4.65}$$

$$\Phi_{2ref} = a_1^D \, f_2(k_1, z) \, e^{+ik_1 x} + a_2^D \, f_2(k_2, z) \, e^{+ik_2 x}, \tag{4.66}$$

$$W_{ref} = a_1^D \, e^{+ik_1 x} + a_2^D \, e^{+ik_2 x}, \tag{4.67}$$

$$\Xi_{ref} = a_1^D \, f_3(k_1) \, e^{+ik_1 x} + a_2^D \, f_3(k_2) \, e^{+ik_2 x}, \tag{4.68}$$

where the unknown coefficients a_1^D and a_2^D are the reflected wave amplitudes that must be found as part of the complete solution.

Note that even if we take incident waves of only *one* mode, the far–field must account for reflected waves of *both* modes. This is due to the vertical wall reflection generating waves of both modes k_1 and k_2. See wave–scattering in a two–layer fluid (without an ice cover), addressed in Linton & McIver (1995).

Using equations (4.61)-(4.68) we may now rewrite the BVP (4.46)-(4.56) in terms of the new variables $\varphi_1(x, z)$, $\varphi_2(x, z)$, $\hat{w}(x)$ and $\hat{\xi}(x)$. We include the far-field condition that all these new variables decay as $x \to \infty$, leaving only the reflected

and incident wave components in the far field.

$$\nabla^2\varphi_1 = 0, \quad (x > 0,\ -\bar{H} \le z \le 0), \tag{4.69}$$

$$\nabla^2\varphi_2 = 0, \quad (x > 0,\ -1 \le z \le -\bar{H}), \tag{4.70}$$

$$\varphi_{2z} = 0, \quad (x > 0,\ z = -1), \tag{4.71}$$

$$\varphi_{1z} = \hat{w}, \quad (x > 0,\ z = 0), \tag{4.72}$$

$$\varphi_{1z} = \varphi_{2z} = \hat{\xi}, \quad (x > 0,\ z = -\bar{H}), \tag{4.73}$$

$$\gamma\nabla^4\hat{w} + \alpha\hat{w} = \varphi_1(x, 0), \quad (x > 0,\ z = 0), \tag{4.74}$$

$$\varphi_{2z} = \beta(\varphi_2 - \bar{\rho}\varphi_1), \quad (x > 0,\ z = -\bar{H}), \tag{4.75}$$

$$\begin{aligned}\varphi_{1x} &= i(a_1^I - a_1^D)k_1 f_1(k_1, z) \\ &+ i(a_2^I - a_2^D)k_2 f_1(k_2, z), \quad (x = 0,\ -\bar{H} \le z \le 0),\end{aligned} \tag{4.76}$$

$$\begin{aligned}\varphi_{2x} &= i(a_1^I - a_1^D)k_1 f_2(k_1, z) \\ &+ i(a_2^I - a_2^D)k_2 f_2(k_2, z), \quad (x = 0,\ -1 \le z \le -\bar{H}),\end{aligned} \tag{4.77}$$

$$\hat{w} = -a_1^I - a_1^D - a_2^I - a_2^D, \quad (x = 0), \tag{4.78}$$

$$\hat{w}_x = ik_1(a_1^I - a_1^D) + ik_2(a_2^I - a_2^D), \quad (x = 0), \tag{4.79}$$

$$\varphi_1, \varphi_2, \hat{w}, \hat{\xi} \to 0, \quad (x \to \infty). \tag{4.80}$$

In the following section we outline the solution to the above boundary value problem.

4.3 Solution

4.3.1 Fourier transform

We apply Fourier cosine transforms defined by:

$$\varphi_1^c(s, z) = \int_0^\infty \varphi_1(x, z)\cos(sx)\,dx, \tag{4.81}$$

$$\varphi_2^c(s, z) = \int_0^\infty \varphi_2(x, z)\cos(sx)\,dx, \tag{4.82}$$

$$w^c(s) = \int_0^\infty \hat{w}(x)\cos(sx)\,dx, \tag{4.83}$$

$$\xi^c(s) = \int_0^\infty \hat{\xi}(x)\cos(sx)\,dx. \tag{4.84}$$

As in the previous Chapters 2 and 3, we aim to use the Fourier cosine transforms to reduce the fourth–order differential equation (4.74) to an algebraic equation. In the following section, an algebraic expression is obtained for the velocity potentials φ_1^c and φ_2^c.

4.3.2 Velocity potentials

Applying the transform to equation (4.69) gives

$$\int_0^\infty [\varphi_{1xx} + \varphi_{1zz}] \cos(sx)\, dx = 0,$$
$$\int_0^\infty [\varphi_{1xx}] \cos(sx)\, dx + \frac{\partial^2}{\partial z^2} \int_0^\infty \varphi_1 \cos(sx)\, dx = 0.$$

Using integration by parts on the left hand integral gives

$$[\varphi_{1x} \cos(sx)]_0^\infty - \int_0^\infty \varphi_{1x}(-s\, \sin(sx))\, dx + \varphi^c_{1zz} = 0,$$

and due to (4.80) this becomes

$$-\varphi_{1x}(0,z) + s \int_0^\infty \varphi_{1x} \sin(sx)\, dx + \varphi^c_{1zz} = 0,$$
$$-\varphi_{1x}(0,z) + s\Big([\varphi_1 \sin(sx)]_0^\infty - s \int_0^\infty \varphi_1 \cos(sx) s\, dx\Big) + \varphi^c_{1zz} = 0,$$

and hence we have

$$\varphi^c_{1zz} - s^2 \varphi^c_1 = \varphi_{1x}(0,z), \quad (-\bar{H} \le z \le 0).$$

Substituting (4.76) on the right hand side gives

$$\varphi^c_{1zz} - s^2 \varphi^c_1 = i(a_1^I - a_1^D) k_1 f_1(k_1, z) + i(a_2^I - a_2^D) k_2 f_1(k_2, z). \tag{4.85}$$

Performing a similar procedure for $\varphi_2(x,z)$ leads to

$$\varphi^c_{2zz} - s^2 \varphi^c_2 = i(a_1^I - a_1^D) k_1 f_2(k_1, z) + i(a_2^I - a_2^D) k_2 f_2(k_2, z). \tag{4.86}$$

The general solutions to the ordinary differential equations with respect to z (4.85) and (4.86) are:

$$\begin{aligned} \varphi^c_1(s,z) &= C_1 \cosh(sz) + C_2 \sinh(sz) \\ &\quad + A_1(s) k_1 f_1(k_1, z) + A_2(s) k_2 f_1(k_2, z), \end{aligned} \tag{4.87}$$
$$\begin{aligned} \varphi^c_2(s,z) &= C_3 \cosh(s(z+1)) + C_4 \sinh(s(z+1)) \\ &\quad + A_1(s) k_1 f_2(k_1, z) + A_2(s) k_2 f_2(k_2, z), \end{aligned} \tag{4.88}$$

where $C_i(s)$ are functions of s and are constant with respect to z, and for brevity we have defined the functions

$$A_1(s) = i \frac{a_1^I - a_1^D}{k_1^2 - s^2},$$
$$A_2(s) = i \frac{a_2^I - a_2^D}{k_2^2 - s^2}.$$

The four boundary conditions come from the Fourier cosine transform of (4.71), (4.72), (4.73) and (4.75) respectively:

$$\varphi^c_{2z} = 0, \qquad (z = -1), \tag{4.89}$$

$$\varphi^c_{1z} = W^c, \qquad (z = 0), \tag{4.90}$$

$$\varphi^c_{1z} = \varphi^c_{2z}, \qquad (z = -\bar{H}), \tag{4.91}$$

$$\varphi^c_{2z} = \beta(\varphi^c_2 - \bar{\rho}\varphi^c_1), \qquad (z = -\bar{H}). \tag{4.92}$$

Now we find $C_i(s)$. We begin with C_4 by substituting (4.89) into general solution (4.88) to find

$$C_4 s + A_1 f_{2z}(k_1, -1) - A_2 f_{2z}(k_2, -1) = 0,$$

which leads to

$$C_4 = 0.$$

Next, for C_2, we substitute (4.90) into (4.87) to give

$$C_2 s + A_1 f_1(k_1, 0) + A_2 f_1(k_2, 0) = w^c,$$

which rearranges to

$$C_2 = \frac{w^c}{s} - A_1 \frac{k_1}{s} - A_2 \frac{k_2}{s}.$$

For C_3, we use condition (4.91) with (4.87) and (4.88):

$$\begin{aligned} -C_1 s \sinh(s\bar{H}) + C_2 s \cosh(s\bar{H}) + A_1 f_{1z}(k_1, -\bar{H}) + A_2 f_{1z}(k_2, -\bar{H}) \\ = C_3 s \sinh(s(1-\bar{H})) + A_1 f_{2z}(k_1, -\bar{H}) + A_2 f_{2z}(k_2, -\bar{H}). \end{aligned} \tag{4.93}$$

This can be rearranged to give

$$\begin{aligned} C_3 = \frac{1}{s \sinh(s(1-\bar{H}))} \Big(& -C_1 s \sinh(s\bar{H}) + C_2 s \cosh(s\bar{H}) \\ & + A_1[f_{1z}(k_1, -\bar{H}) - f_{2z}(k_1, -\bar{H})] + A_2[f_{1z}(k_2, -\bar{H}) - f_{2z}(k_2, -\bar{H})] \Big). \end{aligned}$$

Now, the terms in the two square brackets are both of the form

$$
\begin{aligned}
&f_{1z}(k,-\bar{H}) - f_{2z}(k,-\bar{H}) = \\
&= -\mu(k)k\sinh(k\bar{H}) + k\cosh(k\bar{H}) - \frac{\bar{\rho}k\sinh(k(1-\bar{H}))}{\sinh(k\bar{H})\sinh(k(1-\bar{H}))\,\chi(k)} \\
&= k\cosh(k\bar{H}) - k\cosh(k\bar{H})\frac{\theta(k)}{\chi(k)} - \frac{\bar{\rho}k}{\sinh(k\bar{H})\chi(k)} \\
&= \frac{k}{\chi(k)}\left(\cosh(k\bar{H})[\chi(k)-\theta(k)] - \frac{\bar{\rho}}{\sinh(k\bar{H})}\right) \\
&= \frac{k}{\chi(k)}\left(\cosh(k\bar{H})[\bar{\rho}\coth(k\bar{H}) - \bar{\rho}\tanh(k\bar{H})] - \frac{\bar{\rho}}{\sinh(k\bar{H})}\right) \\
&= \frac{k}{\chi(k)}\left(\frac{\bar{\rho}}{\sinh(k\bar{H})}[\cosh^2(k\bar{H}) - \sinh^2(k\bar{H})] - \frac{\bar{\rho}}{\sinh(k\bar{H})}\right) \\
&= \frac{k}{\chi(k)}\left(\frac{\bar{\rho}}{\sinh(k\bar{H})} - \frac{\bar{\rho}}{\sinh(k\bar{H})}\right) \\
&= 0.
\end{aligned}
$$

Hence we have

$$
C_3 = \frac{1}{s\,\sinh(s(1-\bar{H}))}\Big(-C_1 s\,\sinh(s\bar{H}) + C_2 s\,\cosh(s\bar{H})\Big). \tag{4.94}
$$

Lastly, we use condition (4.92) with (4.87) and (4.88) to give

$$
\begin{aligned}
C_3 s\,\sinh(s(1-\bar{H})) + A_1 f_{2z}(k_1,-\bar{H}) + A_2 f_{2z}(k_2,-\bar{H}) \\
= \beta\Big(C_3\cosh(s(1-\bar{H})) + A_1 f_2(k_1,-\bar{H}) + A_2 f_2(k_2,\bar{H}) \\
-\bar{\rho}\left\{C_1\cosh(s\bar{H}) - C_2\sinh(s\bar{H}) + A_1 f_1(k_1,-\bar{H}) + A_2 f_1(k_2,-\bar{H})\right\}\Big),
\end{aligned}
$$

which rearranges to

$$
\begin{aligned}
C_3\Big(s\,\sinh(s(1-\bar{H})) - \beta\cosh(s(1-\bar{H}))\Big) = -\beta\bar{\rho}C_1\cosh(s\bar{H}) + \beta\bar{\rho}C_2\sinh(s\bar{H}) \\
+A_1[\beta f_2(k_1,-\bar{H}) - \beta\bar{\rho}f_1(k_1,-\bar{H}) - f_{2z}(k_1,-\bar{H})] \\
+A_2[\beta f_2(k_2,-\bar{H}) - \beta\bar{\rho}f_2(k_1,-\bar{H}) - f_{2z}(k_2,-\bar{H})].
\end{aligned}
$$

Evaluating the terms in the square brackets gives

$$
\begin{aligned}
&\beta f_2(k,-\bar{H}) - \beta\bar{\rho} f_1(k,-\bar{H}) - f_{2z}(k,-\bar{H}) = \\
&= \beta\bar{\rho}\Bigg(\frac{\cosh(k(1-\bar{H}))}{\sinh(k\bar{H})\sinh(k(1-\bar{H}))\,\chi(k)} - \frac{\cosh^2(k\bar{H})}{\sinh(k\bar{H})}\frac{\theta(k)}{\chi(k)} \\
&\qquad + \sinh(k\bar{H}) - \frac{k}{\beta\sinh(k\bar{H})\chi(k)}\Bigg) \\
&= \frac{\beta\bar{\rho}}{\chi(k)\sinh(k\bar{H})}\Bigg(\coth(k(1-\bar{H})) - \theta(k)\cosh^2(k\bar{H}) + \chi(k)\sinh^2(k\bar{H}) - \frac{k}{\beta}\Bigg) \\
&= \frac{\beta\bar{\rho}}{\chi(k)\sinh(k\bar{H})}\Bigg(\coth(k(1-\bar{H})) + \Big(\chi(k) - \theta(k)\Big)\sinh^2(k\bar{H}) - \theta(k) - \frac{k}{\beta}\Bigg) \\
&= \frac{\beta\bar{\rho}}{\chi(k)\sinh(k\bar{H})}\Bigg(\coth(k(1-\bar{H})) + \Big(\coth(k\bar{H}) - \tanh(k\bar{H})\Big)\bar{\rho}\sinh^2(k\bar{H}) \\
&\qquad\qquad - \theta(k) - \frac{k}{\beta}\Bigg) \\
&= \frac{\beta\bar{\rho}}{\chi(k)\sinh(k\bar{H})}\Bigg(\coth(k(1-\bar{H})) + \Big(\cosh^2(k\bar{H}) - \sinh^2(k\bar{H})\Big)\bar{\rho}\frac{\sinh(k\bar{H})}{\cosh(k\bar{H})} \\
&\qquad\qquad - \theta(k) - \frac{k}{\beta}\Bigg) \\
&= \frac{\beta\bar{\rho}}{\chi(k)\sinh(k\bar{H})}\Bigg(\coth(k(1-\bar{H})) + \bar{\rho}\tanh(k\bar{H}) - \frac{k}{\beta} - \theta(k)\Bigg) \\
&= \frac{\beta\bar{\rho}}{\chi(k)\sinh(k\bar{H})}\Bigg(\theta(k) - \theta(k)\Bigg) \\
&= 0.
\end{aligned}
$$

Hence we have

$$C_3 = \frac{-\beta\bar{\rho}C_1\cosh(s\bar{H}) + \beta\bar{\rho}C_2\sinh(s\bar{H})}{s\,\sinh(s(1-\bar{H})) - \beta\cosh(s(1-\bar{H}))}. \tag{4.95}$$

We now have two equations (4.94) and (4.95) for C_3 in terms of C_1 and C_2:

$$
\begin{aligned}
C_3\Big(s\,\sinh(s(1-\bar{H})) - \beta\cosh(s(1-\bar{H}))\Big) &= -\beta\bar{\rho}C_1\cosh(s\bar{H}) + \beta\bar{\rho}C_2\sinh(s\bar{H}), \\
C_3\Big(s\,\sinh(s(1-\bar{H}))\Big) &= C_2 s\,\cosh(s\bar{H}) - C_1 s\,\sinh(s\bar{H}).
\end{aligned}
$$

Dividing the first equation by the second gives:

$$1 - \frac{\beta}{s}\coth(s(1-\bar{H})) = \frac{-\beta\bar{\rho}C_1\cosh(s\bar{H}) + \beta\bar{\rho}C_2\sinh(s\bar{H})}{C_2 s\,\cosh(s\bar{H}) - C_1 s\,\sinh(s\bar{H})},$$

Dividing both sides by β and factorising gives:

$$C_2\left(\bar{\rho}\sinh(s\bar{H}) - s\,\cosh(s\bar{H})\left\{\frac{1}{\beta} - \frac{1}{s}\coth(s(1-\bar{H}))\right\}\right)$$
$$= C_1\left(\bar{\rho}\cosh(s\bar{H}) - s\,\sinh(s\bar{H})\left\{\frac{1}{\beta} - \frac{1}{s}\coth(s(1-\bar{H}))\right\}\right),$$

Hence we have

$$C_1 = C_2\frac{\cosh(s\bar{H})}{\sinh(s\bar{H})}\left(\frac{\bar{\rho}\tanh(s\bar{H}) + \coth(s(1-\bar{H})) - \frac{s}{\beta}}{\bar{\rho}\coth(s\bar{H}) + \coth(s(1-\bar{H})) - \frac{s}{\beta}}\right)$$
$$C_1 = C_2\,\mu(s).$$

To summarise, we have established that the functions C_i are given by:

$$C_1 = \frac{w^c\,\mu(s)}{s} - A_1\frac{k_1\mu(s)}{s} - A_2\frac{k_2\mu(s)}{s}, \tag{4.96}$$
$$C_2 = \frac{w^c}{s} - A_1\frac{k_1}{s} - A_2\frac{k_2}{s}, \tag{4.97}$$
$$C_3 = \Big(w^c - A_1k_1 - A_2k_2\Big)\frac{\cosh(s\bar{H}) - \mu(s)\,\sinh(s\bar{H})}{s\,\sinh(s(1-\bar{H}))}, \tag{4.98}$$
$$C_4 = 0. \tag{4.99}$$

The velocity potentials φ_1^c and φ_2^c are then given by substituting (4.96)-(4.99) into the general solutions (4.87) and (4.88). However, the solution is not yet complete as C_1-C_4 are in terms of $w^c(s)$ which is still unknown at this point. In addition the coefficients a_1^D and a_2^D (contained within A_1 and A_2) must be determined.

4.3.3 Plate deflection

Applying the Fourier cosine transform to the ice plate equation (4.74) gives

$$\gamma\int_0^\infty \hat{w}_{xxxx}\cos(sx)\,dx + \alpha w^c = \varphi_1^c(s,0). \tag{4.100}$$

We can evaluate the integral by repetitive integration by parts. Combined with the use of equation (4.80) this gives:

$$\begin{aligned}
&\int_0^\infty \hat{w}_{xxxx}\cos(sx)\,dx \\
&= \big(\hat{w}_{xxx}\cos(sx)\big)_0^\infty + s\int_0^\infty \hat{w}_{xxx}\sin(sx)\,dx \\
&= -\hat{w}_{xxx}(0) + s\Big(\big(\hat{w}_{xx}\sin(sx)\big)_0^\infty - \int_0^\infty \hat{w}_{xx}s\cos(sx)\,dx\Big) \\
&= -\hat{w}_{xxx}(0) - s^2\int_0^\infty \hat{w}_{xx}\cos(sx)\,dx \\
&= -\hat{w}_{xxx}(0) - s^2\Big(\big(\hat{w}_{x}\cos(sx)\big)_0^\infty + \int_0^\infty \hat{w}_{x}s\sin(sx)\,dx\Big) \\
&= -\hat{w}_{xxx}(0) + s^2\hat{w}_x(0) - s^3\int_0^\infty \hat{w}_x\sin(sx)\,dx \\
&= -\hat{w}_{xxx}(0) + s^2\hat{w}_x(0) - s^3\Big(\big(\hat{w}\sin(sx)\big)_0^\infty - \int_0^\infty \hat{w}s\cos(sx)\,dx\Big) \\
&= -\hat{w}_{xxx}(0) + s^2\hat{w}_x(0) + s^4 w^c(s). \qquad (4.101)
\end{aligned}$$

Rearranging, we have

$$w^c(s^4\gamma+\alpha) = \varphi_1^c(s,0) + \gamma(\hat{w}_{xxx}(0) - s^2\hat{w}_x(0)),$$

and substituting for $\varphi_1(s,0)$ using our results from Section 4.3.2 gives:

$$\begin{aligned}
w^c(s^4\gamma+\alpha) = \frac{w^c\mu(s)}{s} - A_1\frac{k_1\mu(s)}{s} - A_2\frac{k_1\mu(s)}{s} \\
+ A_1 f_1(k_1,0) + A_2 f_1(k_2,0) + \gamma(\hat{w}_{xxx}(0) - s^2\hat{w}_x(0)).
\end{aligned} \qquad (4.102)$$

Substituting for $f_1(k,0)$ and using equation (4.79) to substitute for $\hat{w}_x(0)$ we find:

$$\begin{aligned}
w^c\Big(s^4\gamma+\alpha-\mu(s)\Big) = \frac{i(a_1^I-a_1^D)}{k_1^2-s^2}\left(\mu(k_1) - \frac{k_1\mu(s)}{s} - s^2\gamma k_1(k_1^2-s^2)\right) \\
+\frac{i(a_2^I-a_2^D)}{k_2^2-s^2}\left(\mu(k_2) - \frac{k_2\mu(s)}{s} - s^2\gamma k_2(k_2^2-s^2)\right) + \gamma\hat{w}_{xxx}(0).
\end{aligned}$$

We multiply each side of this equation by $s\,\chi(s)\tanh(s\bar{H})$ and we arrive at

$$w^c(s) = \frac{\frac{i(a_1^I-a_1^D)}{k_1^2-s^2}M(k_1,s) + \frac{i(a_2^I-a_2^D)}{k_2^2-s^2}M(k_2,s) + \gamma\hat{w}_{xxx}(0)s\,\chi(s)\tanh(s\bar{H})}{s\,\chi(s)\tanh(s\bar{H})\big(\gamma s^4+\alpha\big) - \theta(s)}. \qquad (4.103)$$

Here the function $M(k,s)$ is defined as

$$M(k,s) = s\,\theta(k)\,\frac{\chi(s)\tanh(s\bar{H})}{\chi(k)\tanh(k\bar{H})} - k\theta(s) - s^3\gamma k(k^2-s^2)\chi(s)\tanh(s\bar{H}). \qquad (4.104)$$

Note that at $s = k$, $M = 0$ algebraically. Hence, terms involving $M(k, s)/(k^2 - s^2)$ in the numerator of (4.103) are not undefined as $s \to k$, but are finite and may be calculated by using l'Hôpital's rule. The function $M(k, s)$ is plotted in Figure 4.8 for both $k = k_1$ and $k = k_2$.

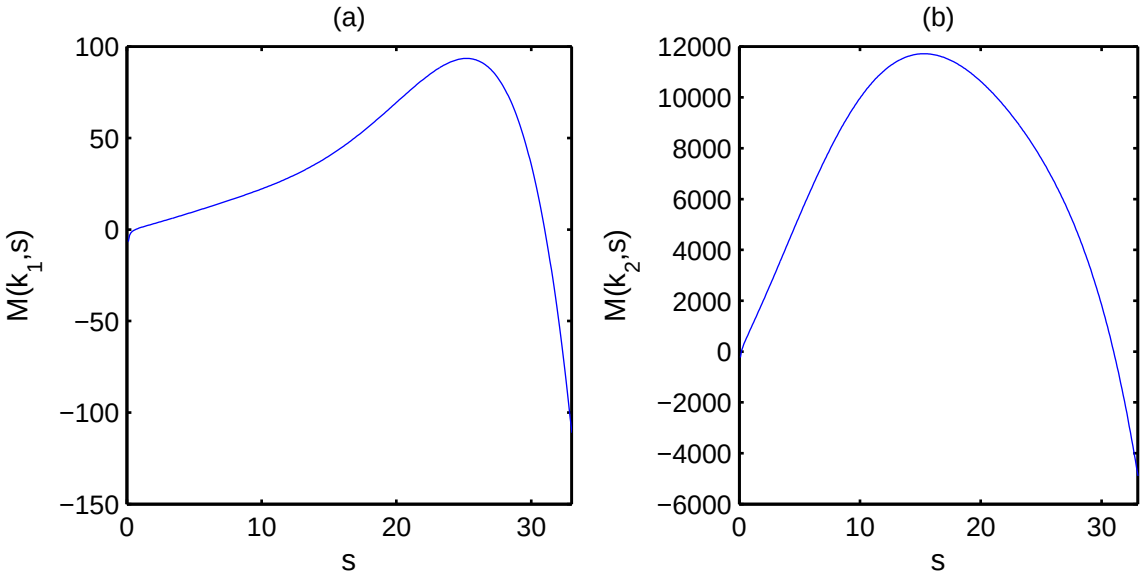

Figure 4.8: The functions (a) $M(k_1, s)$ and (b) $M(k_2, s)$ are plotted against s. The default data set is used for both graphs with $\omega = 0.1\,\mathrm{s}^{-1}$ (giving $k_1 = 0.64$, $k_2 = 31$).

At this stage, there are 3 unknown quantities in equation (4.103), namely a_1^D, a_2^D and $\hat{w}_{xxx}(0)$. We note that the denominator of equation (4.103) is the dispersion relation as a function of s instead of k; therefore, the denominator is equal to zero when $s = k_1$ or $s = k_2$. Hence, we require the numerator to also equal zero when $s = k_1$ and $s = k_2$ to avoid a singularity. We may use this fact to find expressions for two of the unknowns, $\hat{w}_{xxx}$ and a_2^D.

Firstly we assess the limit of the numerator of (4.103) as $s \to k_2$. We require

$$0 = \frac{i(a_1^I - a_1^D)}{k_1^2 - k_2^2} M(k_1, k_2) + i(a_2^I - a_2^D) \lim_{s \to k_2} \frac{M(k_2, s)}{k_2^2 - s^2} + \gamma \hat{w}_{xxx}(0) k_2 \, \chi(k_2) \tanh(k_2 \bar{H}),$$

and we may rearrange to give

$$\hat{w}_{xxx}(0) = -\frac{i(a_2^I - a_2^D)\hat{m}_2 + \frac{i(a_1^I - a_1^D)}{k_1^2 - k_2^2} M(k_1, k_2)}{\gamma \chi(k_2) \tanh(k_2 \bar{H}) k_2}. \tag{4.105}$$

Here we have defined the constant $\hat{m}_2$ as

$$\hat{m}_2 = \lim_{s \to k_2} \frac{M(k_2, s)}{k_2^2 - s^2}. \tag{4.106}$$

This limit can be evaluated easily by applying l'Hôpital's rule. We now evaluate the limit of the numerator in (4.103) as $s \to k_1$, again requiring this limit to equal zero.

This gives

$$0 = i(a_1^I - a_1^D) \lim_{s\to k_1} \frac{M(k_1,s)}{k_1^2 - s^2} + i(a_2^I - a_2^D)\frac{M(k_2,k_1)}{k_2^2 - k_1^2} - \frac{\chi(k_1)\tanh(k_1\bar{H})k_1}{\chi(k_2)\tanh(k_2\bar{H})k_2}\left(i(a_2^I - a_2^D)\hat{m}_2 + \frac{i(a_1^I - a_1^D)}{k_1^2 - k_2^2}M(k_1,k_2)\right). \tag{4.107}$$

We now define

$$\hat{m}_1 = \lim_{s\to k_1} \frac{M(k_1,s)}{k_1^2 - s^2}, \tag{4.108}$$

and we can rearrange (4.107) to give

$$a_2^I - a_2^D = \hat{c}(a_1^I - a_1^D), \tag{4.109}$$

where we have defined the constant $\hat{c}$ as

$$\hat{c} = \frac{\hat{m}_1 - \frac{\chi(k_1)\tanh(k_1\bar{H})k_1}{\chi(k_2)\tanh(k_2\bar{H})k_2}\frac{M(k_1,k_2)}{k_1^2-k_2^2}}{\frac{\chi(k_1)\tanh(k_1\bar{H})k_1}{\chi(k_2)\tanh(k_2\bar{H})k_2}\hat{m}_2 - \frac{M(k_2,k_1)}{k_2^2-k_1^2}}. \tag{4.110}$$

Hence, we now have an expression for the unknown a_2^D in terms of a_1^D, and we can rewrite the solution for the deflection as

$$w^c = i(a_1^I - a_1^D)\, Q(s), \tag{4.111}$$

where

$$Q(s) = \frac{\frac{M(k_1,s)}{k_1^2-s^2} + \hat{c}\frac{M(k_2,s)}{k_2^2-s^2} - \frac{\chi(s)\tanh(s\bar{H})s}{\chi(k_2)\tanh(k_2\bar{H})k_2}\left(\hat{m}_2\hat{c} + \frac{M(k_1,k_2)}{k_1^2-k_2^2}\right)}{s\,\chi(s)\tanh(s\bar{H})\left(\gamma s^4 + \alpha\right) - \theta(s)}. \tag{4.112}$$

The function $Q(s)$ is smooth and is finite at $s = k_1$ and $s = k_2$. This function defines the behaviour of the ice deflection in the vicinity of the vertical wall, allowing all conditions for the problem to be satisfied. Taking the limit of $Q(s)$ as $H_1 \to H_2$ or $H_1 \to 0$ or $\rho_1 \to \rho_2$ will lead to the same function $Q(s)$ derived in the one-layer fluid problem in Chapter 2. Figure 4.9 shows $Q(s)$ plotted against s for various values of the frequency ω.

The solution is still not yet complete as we have yet to find an expression for a_1^D. We note that we have two equations for $\hat{w}(0)$; one is given by equation (4.78), and the other given by performing an inverse transform on equation (4.111) and evaluating at $x = 0$. Hence we have

$$w(0) = -a_1^I - a_1^D - a_2^I - a_2^D,$$
$$w(0) = \frac{2}{\pi} i(a_1^I - a_1^D)\int_0^\infty Q(s)\, ds.$$

Defining $\tau = \frac{2}{\pi}\int_0^\infty Q(s)\, ds$, equating these and substituting for a_2^D using (4.109)

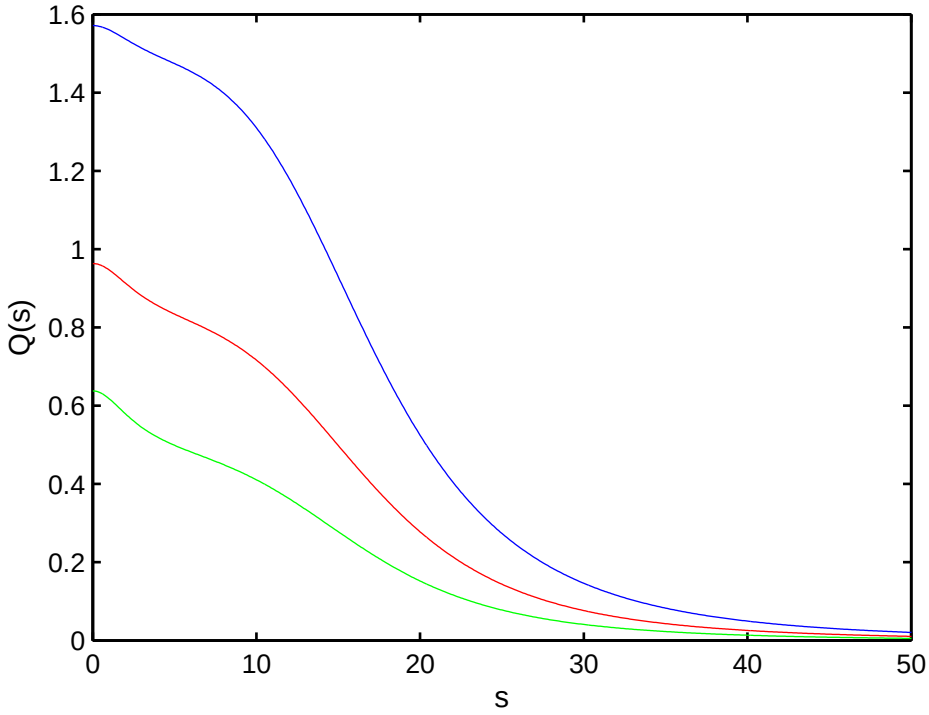

Figure 4.9: The function $Q(s)$ is plotted against s for $\omega = 0.1\mathrm{s}^{-1}$ (blue), $\omega = 0.15\mathrm{s}^{-1}$ (red), $\omega = 0.2\,\mathrm{s}^{-1}$ (green). The remaining parameters are set to their default values.

gives

$$i(a_1^I - a_1^D)\tau = -a_1^I - a_1^D - \hat{c}(a_1^I - a_1^D) - 2a_2^I.$$

We rearrange this to give:

$$a_1^D = \frac{a_1^I(\hat{c} - 1) - 2a_2^I - ia_1^I\tau}{\hat{c} + 1 - i\tau}, \tag{4.113}$$

and a_1^D is now defined in terms of known quantities. Hence, the final solution for the plate deflection is found by inverse Fourier transform of equation (4.111):

$$\hat{w}(x) = \frac{2}{\pi} i(a_1^I - a_1^D) \int_0^\infty Q(s)\, \cos(sx)\, ds. \tag{4.114}$$

4.3.4 Interfacial deflection

Applying the Fourier transform to equation (4.73) gives

$$\xi^c = \varphi_{1z}^c, \qquad (z = -\bar{H}).$$

Using the general solution for φ_{1z} given by (4.87) we have

$$\xi^c(s) = C_2 s\, \cosh(s\bar{H}) - C_1 s\, \sinh(s\bar{H}) + A_1 f_{1z}(k_1, -\bar{H})k_1 + A_2 f_{1z}(k_2, -\bar{H}). \tag{4.115}$$

We substitute for C_1 and C_2 using (4.96) and (4.97), and evaluate f_{1z} to give:

$$\begin{aligned}\xi^c(s) = s\ \cosh(s\bar{H})&\left(\frac{w^C}{s} - A_1\frac{k_1}{s} - A_2\frac{k_2}{s}\right)\\ - s\ \sinh(s\bar{H})&\left(\frac{w^C\mu(s)}{s} - A_1\frac{k_1\mu(s)}{s} - A_2\frac{k_2\mu(s)}{s}\right)\\ + A_1&\Big(-\mu(k_1)k_1\sinh(k_1\bar{H}) + k_1\cosh(k_1\bar{H})\Big)\\ + A_2&\Big(-\mu(k_2)k_2\sinh(k_2\bar{H}) + k_2\cosh(k_2\bar{H})\Big),\end{aligned}$$

$$\begin{aligned}\xi^c(s) = w^c&\Big(\cosh(s\bar{H}) - \mu(s)\ \sinh(s\bar{H})\Big)\\ &+ \frac{i(a_1^I - a_1^D)}{k_1^2 - s^2}k_1\Big(\mu(s)\ \sinh(s\bar{H}) - \cosh(s\bar{H})\\ &+ \cosh(k_1\bar{H}) - \mu(k_1)\sinh(k_1\bar{H})\Big)\\ &+ \frac{i(a_2^I - a_2^D)}{k_2^2 - s^2}k_1\Big(\mu(s)\ \sinh(s\bar{H}) - \cosh(s\bar{H})\\ &+ \cosh(k_2\bar{H}) - \mu(k_2)\sinh(k_2\bar{H})\Big).\end{aligned}$$

We use the expression $\cosh(s\bar{H}) - \mu(s)\sinh(s\bar{H}) = \bar{\rho}/(\chi(s)\sinh(s\bar{H}))$ to simplify and substitute for a_2^D using equation (4.109). This leads us to:

$$\xi^c(s) = i(a_1^I - a_1^D)\bar{\rho}\,L(s), \tag{4.116}$$

where the function $L(s)$ is given by

$$L(s) = \frac{Q(s) + \frac{k_1}{k_1^2 - s^2}\left(\frac{\chi(s)\ \sinh(s\bar{H})}{\chi(k_1)\ \sinh(k_1\bar{H})} - 1\right) + \frac{k_2}{k_2^2 - s^2}\left(\frac{\chi(s)\ \sinh(s\bar{H})}{\chi(k_2)\ \sinh(k_2\bar{H})} - 1\right)}{\chi(s)\ \sinh(s\bar{H})}. \tag{4.117}$$

Note that the bracketed terms in the numerator of (4.117) are zero as $s \to k_1$ and $s \to k_2$ respectively. This means there are no singularities due to the $1/(k^2 - s^2)$ terms in the limits $s \to k$. As noted previously, there is a zero in the denominator where $k = k_{cr}$, leading to $\chi(k_{cr}) = 0$. Hence, we need to verify that the numerator is also zero at this point. Denoting the numerator of $L(s)$ as L_{num}, we have

$$L_{num}(k_{cr}) = Q(k_{cr}) - \frac{k_1}{k_1^2 - k_{cr}^2} - \frac{k_2\hat{c}}{k_2^2 - k_{cr}^2}. \tag{4.118}$$

Returning to the equation for $Q(s)$ given by (4.112), we have

$$Q(k_{cr}) = \frac{\frac{M(k_1,k_{cr})}{k_1^2-k_{cr}^2} + \hat{c}\frac{M(k_2,k_{cr})}{k_2^2-k_{cr}^2}}{-\theta(k_{cr})}, \tag{4.119}$$

and by our definition of the function M given by (4.104) we have $M(k, k_{cr}) = -k\theta(k_{cr})$. Hence,

$$Q(k_{cr}) = \frac{k_1}{k_1^2 - k_{cr}^2} + \hat{c}\frac{k_2}{k_2^2 - k_{cr}^2},$$

and substituting this into (4.119) confirms that $L_{num}(k_{cr}) = 0$ identically.

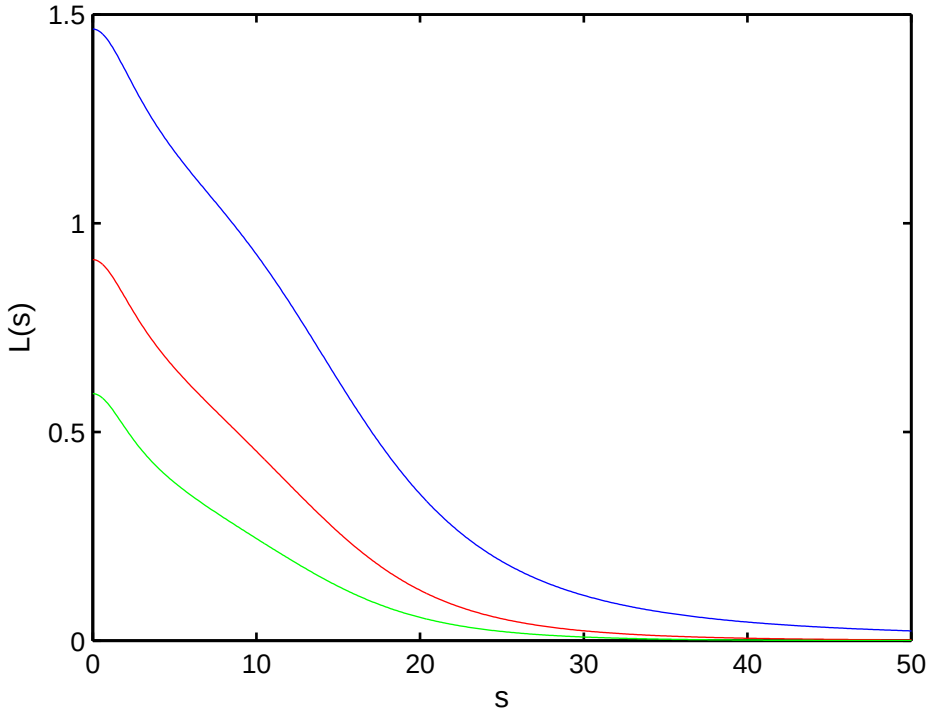

Figure 4.10: The function $L(s)$ is plotted against s for $\omega = 0.1\text{s}^{-1}$ (blue), $\omega = 0.15\text{s}^{-1}$ (red), $\omega = 0.2\,\text{s}^{-1}$ (green). The remaining parameters are set to their default values.

Figure 4.10 shows the functions $L(s)$ plotted against s for varying values of ω. We note that $L(s)$ shows similar characteristics to the function $Q(s)$. Also, $L(s)$ decays rapidly as $s \to \infty$. The final solution for the interfacial deflection is found by inverse Fourier transform of equation (4.116):

$$\hat{\xi}(x) = \frac{2}{\pi} i\bar{\rho}(a_1^I - a_1^D) \int_0^\infty L(s)\ \cos(sx)\, ds. \tag{4.120}$$

4.4 Numerical results

Results are now presented for the solution in Section 4.3. Note that the inverse transforms are too complicated to calculate analytically and hence are calculated numerically. Recall that the default values of the parameters are given by Table 4.1. We consider 3 different cases for the results;

(i) Incident waves with mode k_1 only, representing surface waves. In this case we take the parameters $a_1^I = 1$ and $a_2^I = 0$. This scales the incident surface wave amplitude to 1, allowing us to compare the interfacial response.

(ii) Incident waves with mode k_2 only, representing interfacial waves. In this case we take the parameter $a_2^I = f_3^{-1}(k_2)$. This scales the incident interfacial amplitude to 1, allowing us to compare the surface response.

(iii) Incident waves with modes k_1 and k_2, representing both surface and interfacial waves. In this case, the relationship between a_1^I and a_2^I must be estimated based on realistic observations, of which little is available. We take $a_2^I = f_3^{-1}(k_2)$, scaling the incident k_2 wave amplitude to 1, and choose $a_1^I = 0.01$. This estimates that the incident interfacial wave amplitude is 100 times larger than the incident surface wave amplitude. It should be noted that this ratio represents just one possible choice; results should be more qualitatively interpreted than quantitatively.

We note that the three cases have different amplitude scales, which must be borne in mind when directly comparing results between each case.

4.4.1 Plate & interfacial deflection

We return to the total, non-periodic forms of the deflections $w(x,t)$ and $\xi(x,t)$. We define

$$w_{inv}(x) = \int_0^\infty Q(s)\ \cos(sx)\, ds,$$
$$\xi_{inv}(x) = \int_0^\infty L(s)\ \cos(sx)\, ds.$$

We also express a_1^D in the form $a_1^D = a_R + ia_I$ by multiplying equation (4.113) by the complex conjugate of the denominator. This gives

$$a_R = \frac{a_1^I(\hat{c}-1)(\hat{c}+1) - 2a_2^I(\hat{c}+1) + a_1^I\tau^2}{(\hat{c}+1)^2 + \tau^2}, \tag{4.121}$$

$$a_I = \frac{-2a_1^I\tau - 2a_2^I\tau}{(\hat{c}+1)^2 + \tau^2}. \tag{4.122}$$

We substitute the solutions (4.114) and (4.120) into the total forms for $W(x)$ and $\Xi(x)$ given by equations (4.59) and (4.60), and finally return to the time-dependent

solution using equations (4.15) and (4.16). This gives:

$$
\begin{aligned}
w(x,t) = \sin(t)\Bigg(& a_1^I \cos(k_1 x) + a_2^I \cos(k_2 x) + a_R \cos(k_1 x) - a_I \sin(k_1 x) \\
& + \big(a_2^I - \hat{c}(a_1^I - a_R)\big)\cos(k_2 x) - \hat{c} a_I \sin(k_2 x) + \frac{2}{\pi} a_I w_{inv}(x)\Bigg) \\
& + \cos(t)\Bigg(a_1^I \sin(k_1 x) + a_2^I \sin(k_2 x) - a_I \cos(k_1 x) - a_R \sin(k_1 x) \\
& - \big(a_2^I - \hat{c}(a_1^I - a_R)\big)\sin(k_2 x) - \hat{c} a_I \cos(k_2 x) + \frac{2}{\pi}(a_1^I - a_R) w_{inv}(x)\Bigg),
\end{aligned}
$$

$$
\begin{aligned}
\xi(x,t) = \sin(t)\Bigg(& a_1^I f_3(k_1)\cos(k_1 x) + a_2^I f_3(k_2)\cos(k_2 x) + a_R f_3(k_1)\cos(k_1 x) \\
& - a_I f_3(k_1)\sin(k_1 x) + \big(a_2^I - \hat{c}(a_1^I - a_R)\big) f_3(k_2)\cos(k_2 x) \\
& - \hat{c} a_I f_3(k_2)\sin(k_2 x) + \frac{2}{\pi} a_I \xi_{inv}(x)\Bigg) + \cos(t)\Bigg(a_1^I f_3(k_1)\sin(k_1 x) \\
& + a_2^I f_3(k_2)\sin(k_2 x) - a_I f_3(k_1)\cos(k_1 x) - a_R f_3(k_1)\sin(k_1 x) \\
& - \big(a_2^I - \hat{c}(a_1^I - a_R)\big) f_3(k_2)\sin(k_2 x) - \hat{c} a_I f_3(k_2)\cos(k_2 x) \\
& + \frac{2}{\pi}(a_1^I - a_R)\xi_{inv}(x)\Bigg).
\end{aligned}
$$

Note that the moduli of the deflections were calculated in the same way as Chapter 2 to remove time as a factor from the plots.

Case (i): $a_1^I = 1$, $a_2^I = 0$.

We first investigate the case where we consider only incident waves of mode k_1, that is, incident waves of the surface mode.

Figure 4.11 shows the plate and interfacial deflection for the frequency $\omega = 0.2\,\mathrm{s}^{-1}$. Firstly we notice that the deflection and the slope of the deflection are 0 at the point $x = 0$, as required by the ice–clamping conditions. The ice deflection shows similar characteristics to the equivalent one-layer problem: the vertical wall affects the shape of the first wave peak closest to the wall. We notice that the interfacial deflection is similar in amplitude to the plate deflection. There is no appearance of the mode k_2 for this value of ω. This is because k_2 is large enough that the parameter $\hat{c}$ is very small, which dampens any term involving the interfacial mode.

Figure 4.12 shows the deflections for the frequency $\omega = 0.1\,\mathrm{s}^{-1}$. For the plate deflection, we notice the increased wavelength of k_1 and there is also slightly more disturbance in the first wave peak closest to the wall. For the interfacial deflection we

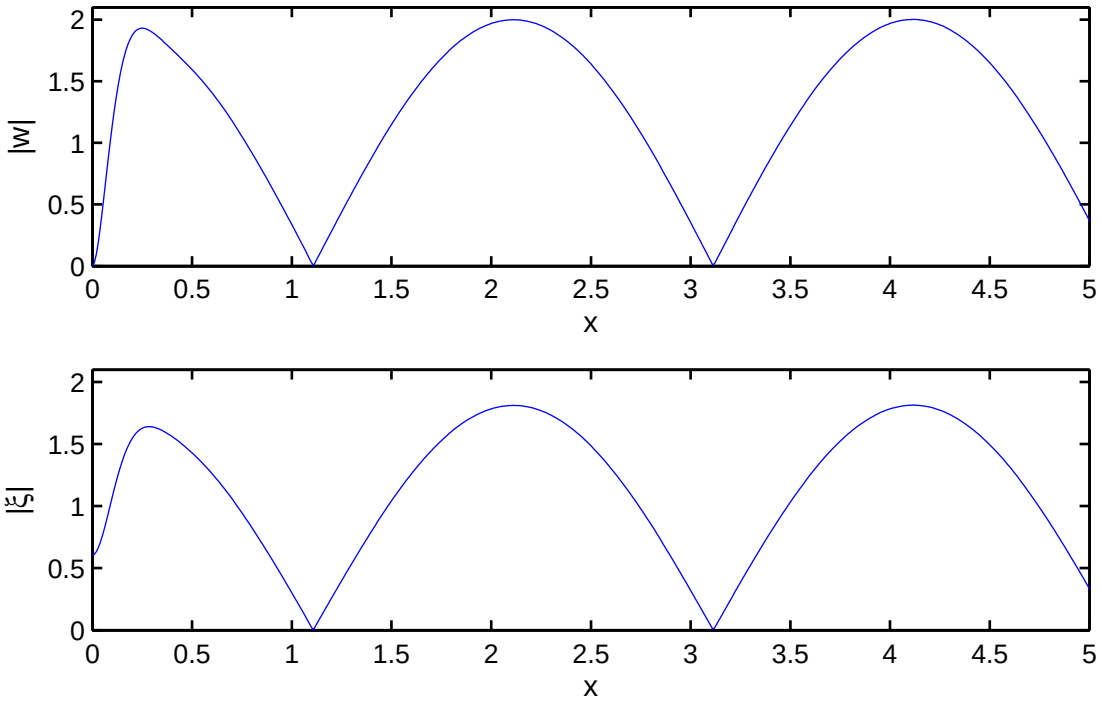

Figure 4.11: Case (i): The plate deflection $|w(x)|$ and the interfacial deflection $|\xi(x)|$ are plotted against x. Here $\omega = 0.2\,\mathrm{s}^{-1}$, leading to $k_1 = 1.57$, $k_2 = 120.48$. The remaining parameters are set to their default values.

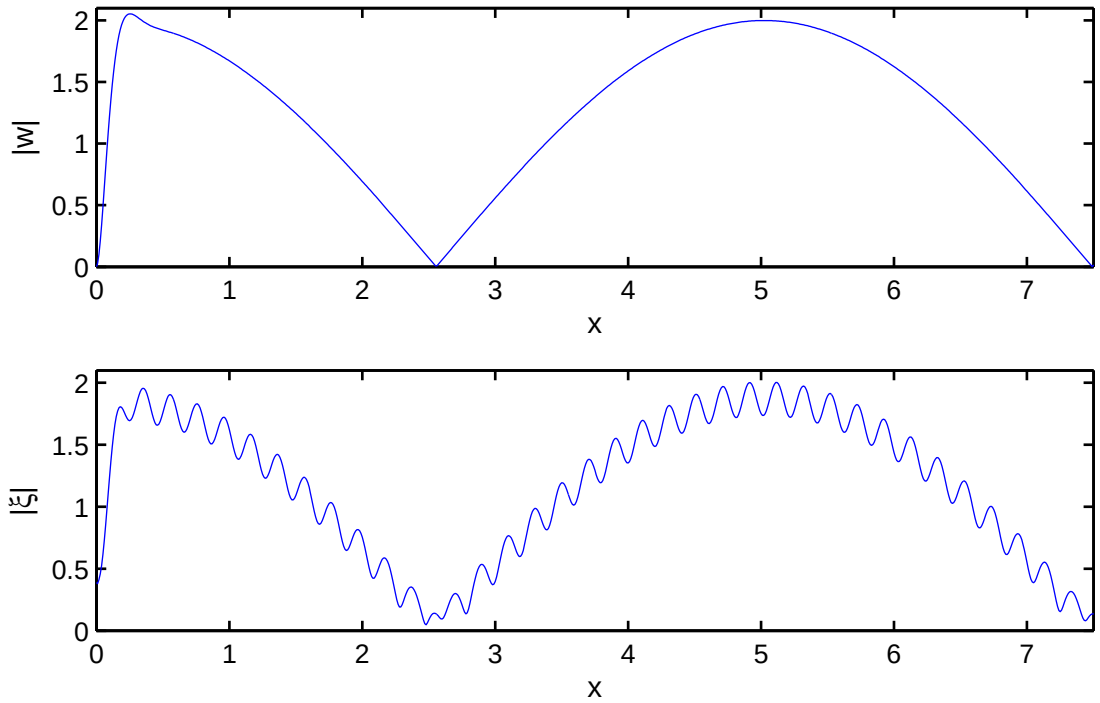

Figure 4.12: Case (i): The plate deflection $|w(x)|$ and the interfacial deflection $|\xi(x)|$ are plotted against x. Here $\omega = 0.1\,\mathrm{s}^{-1}$, leading to $k_1 = 0.64$, $k_2 = 31.01$. The remaining parameters are set to their default values.

now notice waves of mode k_2 appearing, characterised by their smaller wavelength. This is entirely due to the ice–wall interaction, as there were no incident waves of mode k_2. They are still small in amplitude due to the parameter $\hat{c}$.

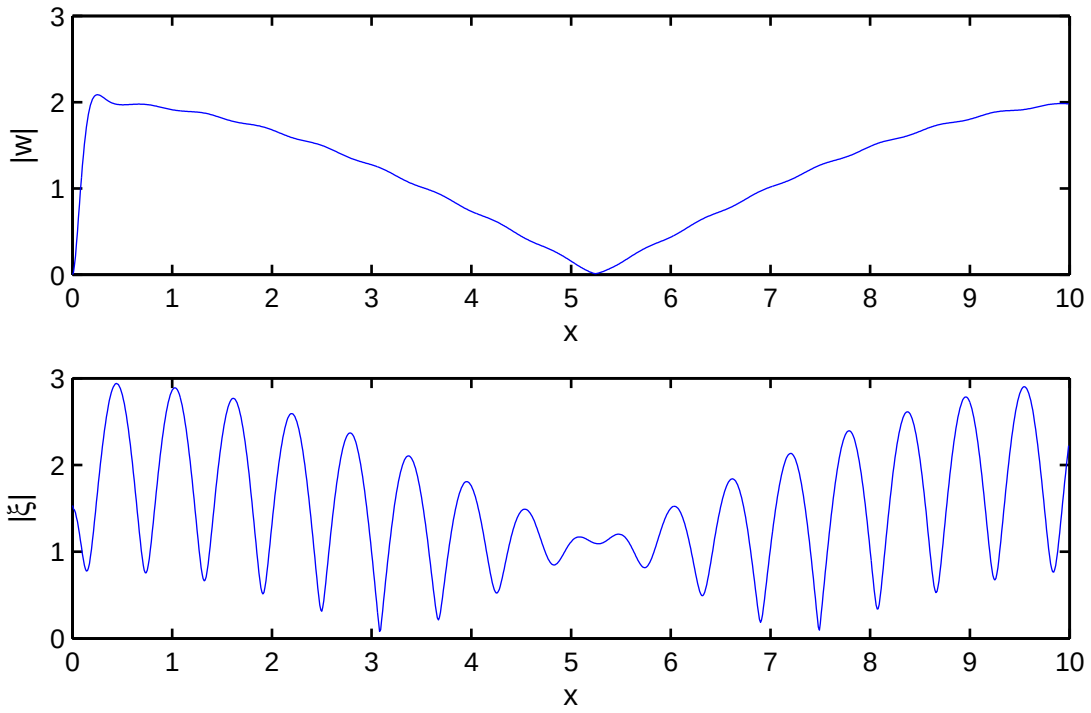

Figure 4.13: Case (i): The plate deflection $|w(x)|$ and the interfacial deflection $|\xi(x)|$ are plotted against x. Here $\omega = 0.05\,\mathrm{s}^{-1}$, leading to $k_1 = 0.30$, $k_2 = 10.70$. The remaining parameters are set to their default values.

Figure 4.13 shows the deflections for the frequency $\omega = 0.05\,\mathrm{s}^{-1}$. This value of ω causes surface waves of very long wavelength. For the plate deflection, we observe a slight disturbance caused by interfacial waves of mode k_2 almost propagating to the surface. For the interfacial deflection we notice that k_2 waves now have larger amplitude and have become more prevalent.

We would like to investigate the effect of changing various parameters on the amplitude of the generated waves of mode k_2. It is not practical to re–plot the deflection each time. Instead we investigate the coefficient a_2^D which represents the k_2 mode wave amplitudes. Calculating a_2^D will give the amplitude of the k_2 waves generated by the ice–wall interaction. We calculate the modulus $|a_2^D|$ to give the maximum value of a_2^D with respect to time. Using equation (4.109) and the values $a_1^I = 1$, $a_2^I = 0$, we have

$$|a_2^D| = |\hat{c}(1 - a_1^D)| = \sqrt{\left(\hat{c}(1 - a_R)\right)^2 + \left(\hat{c}a_I\right)^2}.$$

Here a_R and a_I are given by equations (4.121) and (4.122), where $a_1^D = a_R + ia_I$.

The coefficient $|a_2^D|$ is plotted against ω in Figure 4.14(a), representing the generated k_2 waves *at the surface*. Recall that the scale in this case is relative to $a_1^I = 1$. This confirms the behaviour shown in Figures 4.11-4.13; waves of mode k_2 of significant amplitude are only generated for low values of ω. We see that a more

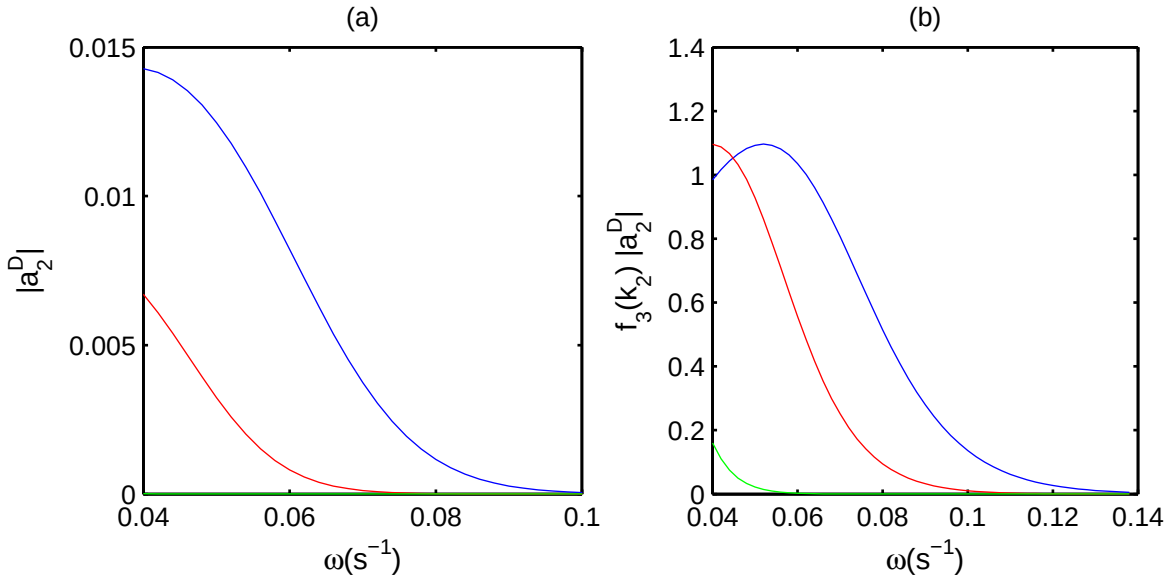

Figure 4.14: Case (i): The coefficients (a) $|a_2^D|$ and (b) $f_3(k_2)|a_2^D|$ are plotted against ω, where the density ρ_1 is given by $1000\,\mathrm{kgm}^{-3}$ (blue), $1010\,\mathrm{kgm}^{-3}$ (red) and $1020\,\mathrm{kgm}^{-3}$ (green).

pronounced density difference between the two layers permits generated k_2 waves of higher amplitude. This is because as ρ_1 approaches ρ_2, k_2 grows and hence the waves have much smaller wavelength which cannot propagate through the elastic surface. Figure 4.15(a) shows the effect the parameter H_1 has on this coefficient. Interestingly the value $H_1 = 10\,\mathrm{m}$ seems to generate the highest k_2 wave amplitudes. It is clear that depth H_1 has a noticeable affect on $|a_2^D|$ for low values of ω. As ω increases beyond $0.1\ \mathrm{s}^{-1}$ however, all of the curves tend to zero regardless of the value of H_1.

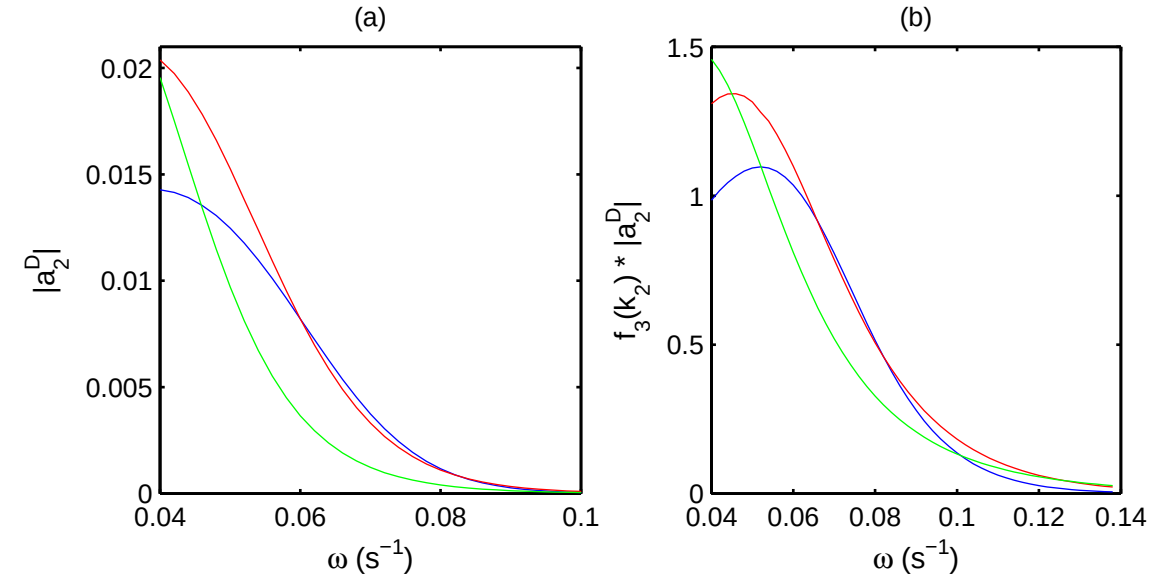

Figure 4.15: Case (i): The coefficients (a) $|a_2^D|$ and (b) $f_3(k_2)|a_2^D|$ are plotted against ω, where the depth H_1 is given by 20 m (blue), 10 m (red) and 5 m (green).

The coefficient $f_3(k_2)|a_2^D|$ is plotted against ω in Figure 4.14(b), representing the generated k_2 waves *at the interface*. As confirmed in Figure 4.13, for low values of ω

the generated k_2 wave has similar amplitude to the incident k_1 wave. Interestingly the curve representing $\rho_1 = 1000\,\mathrm{kgm}^{-3}$ has a maximum value close to $\omega = 0.55\,\mathrm{s}^{-1}$. Lowering the density ρ_1 has less affect at the interface because waves of smaller wavelength are permitted here. However as we reach $\rho_1 = 1020\,\mathrm{kgm}^{-3}$, $f_3(k_2)|a_2^D|$ has considerably smaller amplitude. Figure 4.15(b) shows the effect of the parameter H_1 on $f_3(k_2)|a_2^D|$; we see that changing H_1 has more impact for lower values of ω.

Case (ii): $a_1^I = 0$, $a_2^I = f_3^{-1}(k_2)$. We now investigate the case of incident waves of only mode k_2, representing interfacial incident waves.

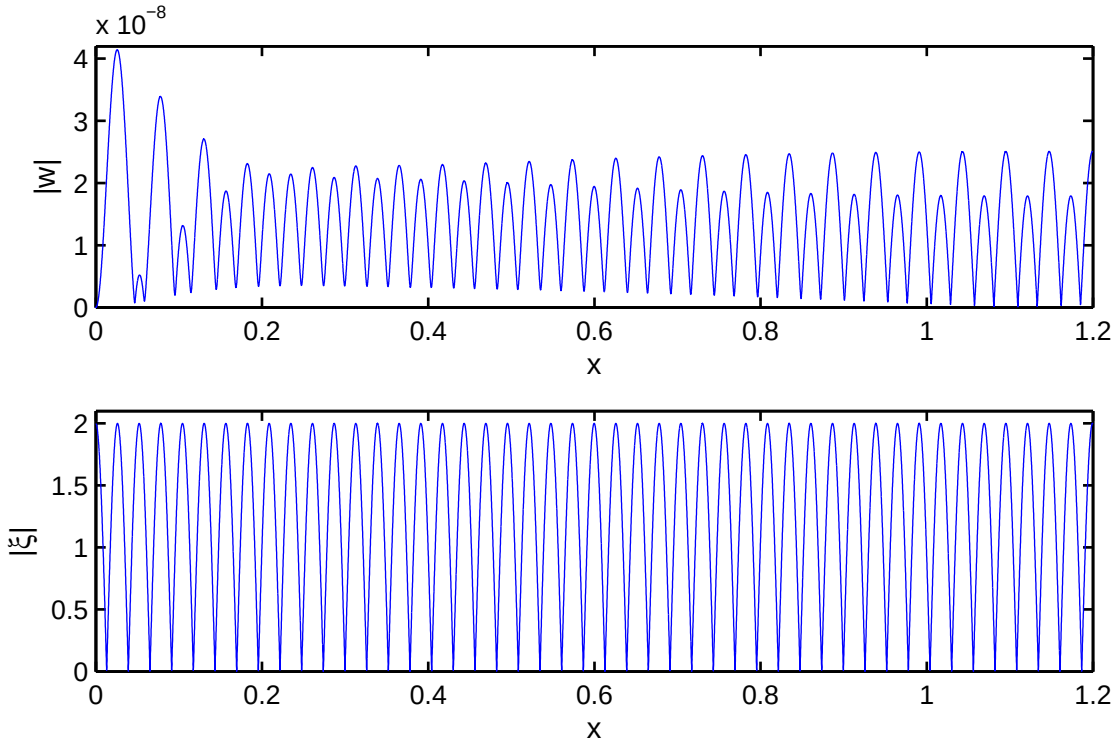

Figure 4.16: Case (ii): The plate deflection $|w(x)|$ and the interfacial deflection $|\xi(x)|$ are plotted against x. Here $\omega = 0.2\,\mathrm{s}^{-1}$, leading to $k_1 = 1.57$, $k_2 = 120.48$. The remaining parameters are set to their default values.

Figure 4.16 shows the deflections for the frequency $\omega = 0.2\,\mathrm{s}^{-1}$. We notice that the surface deflection is negligible for this value of ω, being smaller than the interfacial deflection by a factor 10^{-8}. Even if the interfacial deflection were 10m, the surface deflection would be 0.0005 mm, which is clearly too small to be considered. Studying the interfacial deflection we notice that the mode k_2 is dominant and the mode k_1 has no significant effect on the deflection.

Figure 4.17 shows the deflections for the frequency $\omega = 0.1\,\mathrm{s}^{-1}$. The surface deflection is now smaller than the interfacial deflection by a factor 10^{-3}. By the discrepancy in the size of each wave peak we can see that the mode k_1 exists at the surface, although its effect is quite small. The interfacial deflection is again unaffected by the mode k_1.

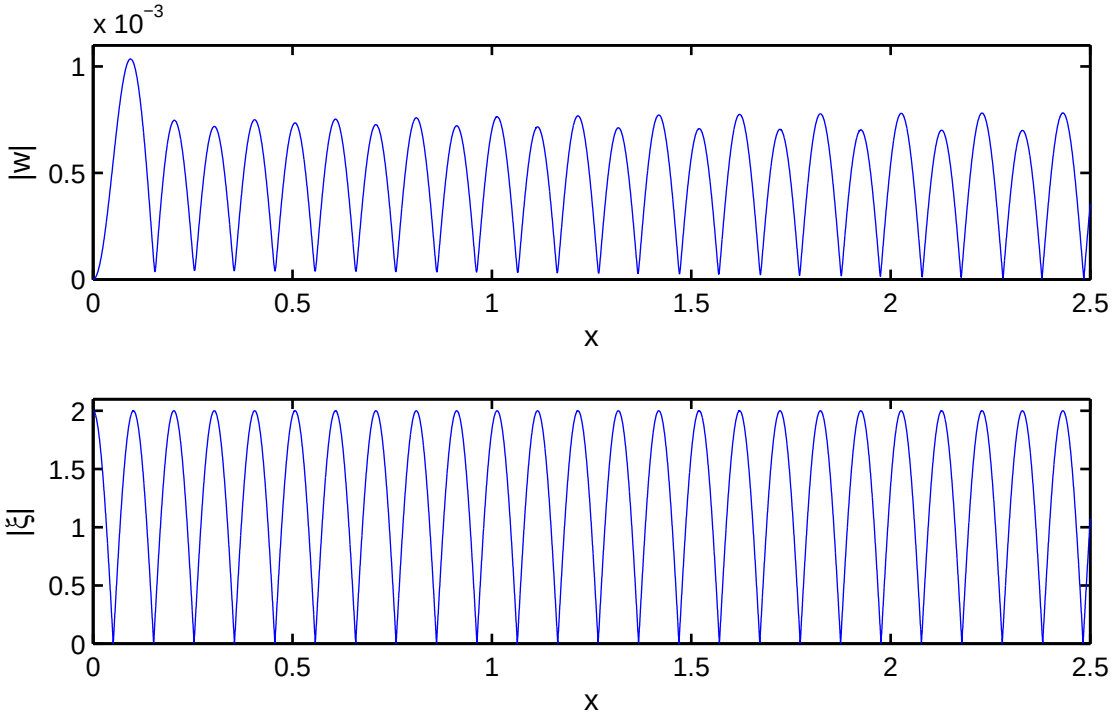

Figure 4.17: Case (ii): The plate deflection $|w(x)|$ and the interfacial deflection $|\xi(x)|$ are plotted against x. Here $\omega = 0.1\,\mathrm{s}^{-1}$, leading to $k_1 = 0.64$, $k_2 = 31.01$. The remaining parameters are set to their default values.

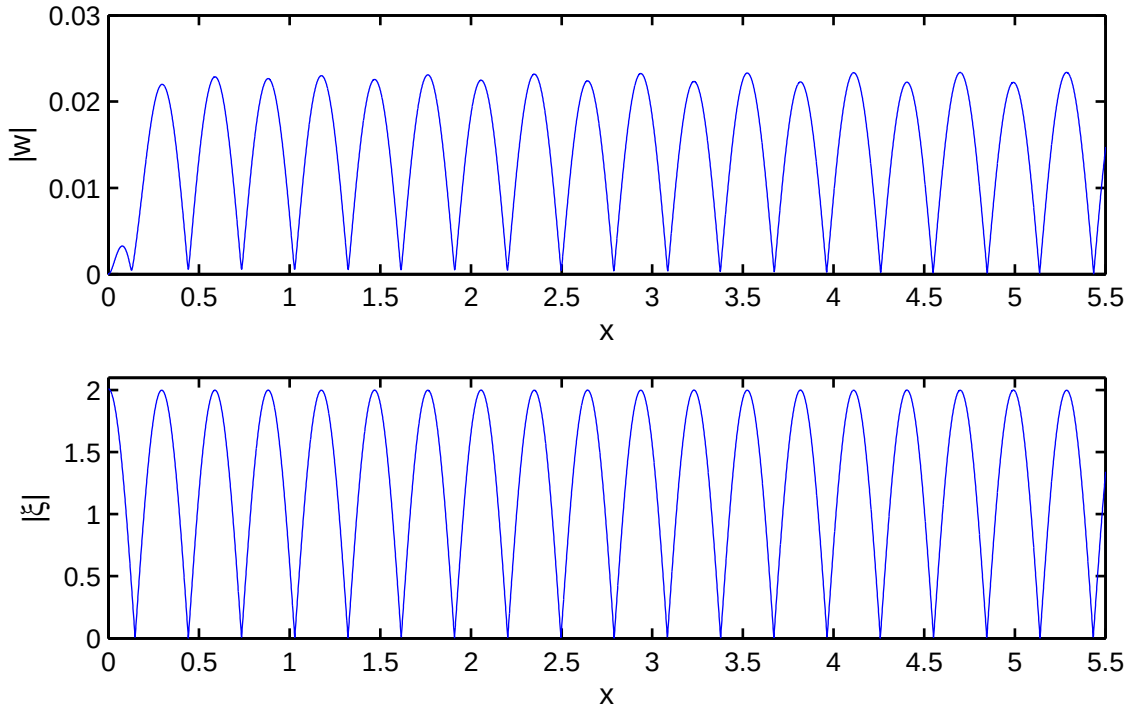

Figure 4.18: Case (ii): The plate deflection $|w(x)|$ and the interfacial deflection $|\xi(x)|$ are plotted against x. Here $\omega = 0.05\,\mathrm{s}^{-1}$, leading to $k_1 = 0.30$, $k_2 = 10.70$. The remaining parameters are set to their default values.

Figure 4.18 shows the deflections for the frequency $\omega = 0.05\,\mathrm{s}^{-1}$. We see that the surface deflection now has significant amplitude compared to the interfacial deflection. However, the wave mode k_1 still has a negligible effect on the surface and interfacial deflections. This implies that incident waves of mode k_2 fail to generate significant waves of mode k_1. However, waves of mode k_2 can exist with significant amplitude on the surface, given that the wavelength is long enough.

We now investigate the coefficient $|a_1^D|$, which shows more clearly the amplitude of generated waves of mode k_1. This is calculated by

$$|a_1^D| = \sqrt{aR^2 + aI^2},$$

where a_R and a_I are given by equations (4.121) and (4.122).

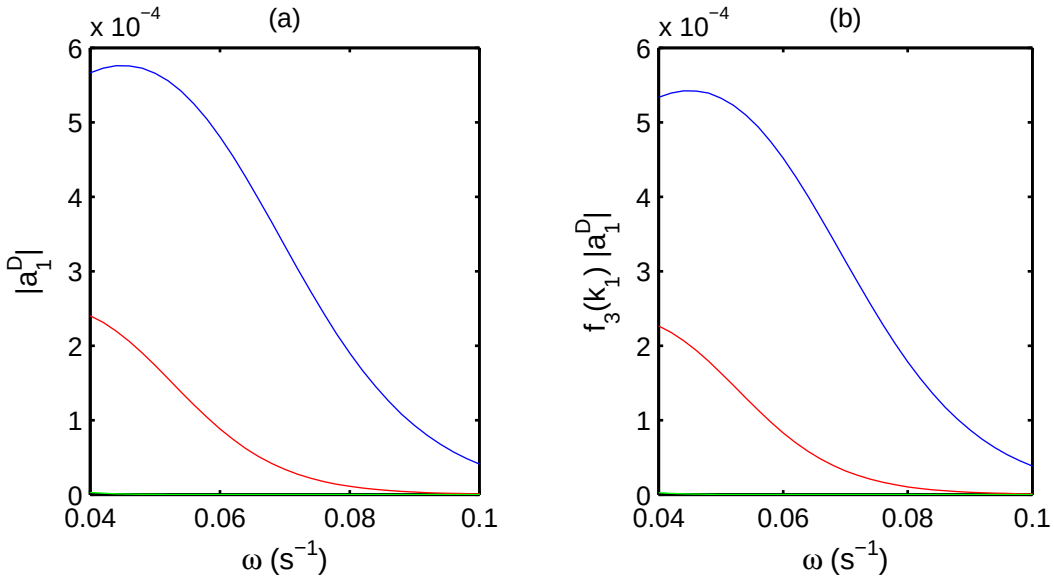

Figure 4.19: Case (ii): The coefficients (a) $|a_1^D|$ and (b) $f_3(k_1)|a_1^D|$ are plotted against ω, where the density ρ_1 is given by $1000\,\mathrm{kgm}^{-3}$ (blue), $1010\,\mathrm{kgm}^{-3}$ (red) and $1020\mathrm{kgm}^{-3}$ (green).

Figure 4.19(a) shows the coefficient $|a_1^D|$, representing the generated k_1 waves *at the surface*, plotted against ω. Figure 4.19(b) shows $f_3(k_1)|a_1^D|$ plotted against ω. In both cases the density ρ_1 is varied. Recall that the incident k_2 wave at the interface is scaled to 1 (so $f_3(k_2)a_2^I = 1$). In general the k_1 amplitudes are much smaller than the incident k_2 amplitudes, though this is expected as the surface response is constrained by the elasticity of the ice sheet. As expected, the more pronounced the density difference between the two layers, the higher the amplitude of the generated k_2 waves. Figure 4.20 shows the same plot, this time varying H_1. Again it seems that the middle depth $H_1 = 10\,\mathrm{m}$ causes the highest k_1 amplitude.

Case (iii): $a_1^I = 0.01$, $a_2^I = f_3^{-1}(k_2)$. We now investigate the case where there is an incident wave for both k_1 and k_2.

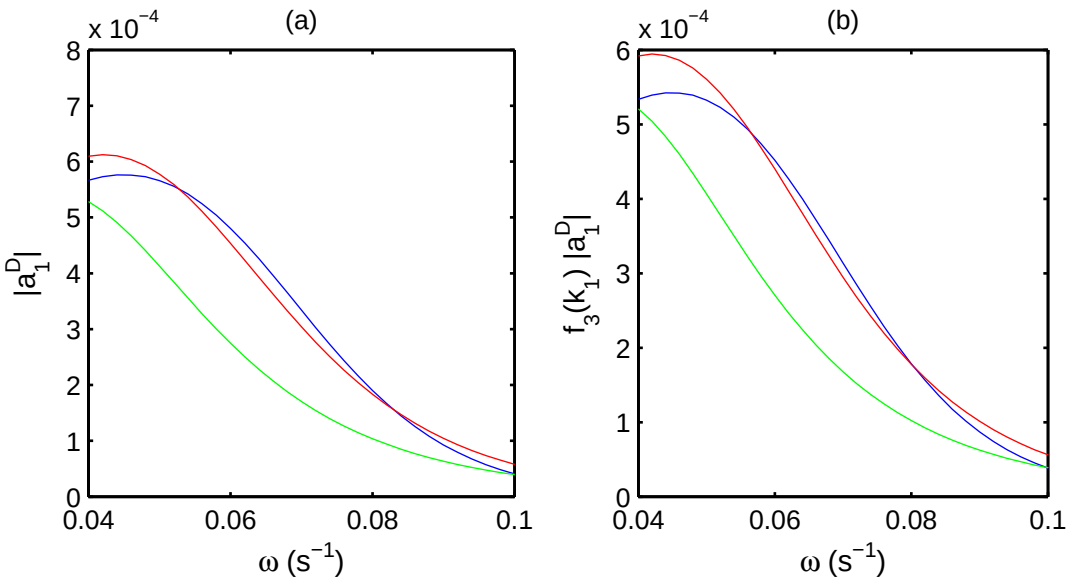

Figure 4.20: Case (ii): The coefficients (a) $|a_1^D|$ and (b) $f_3(k_1)|a_1^D|$ are plotted against ω, where the depth H_1 is given by 20 m (blue), 10 m (red) and 5 m (green).

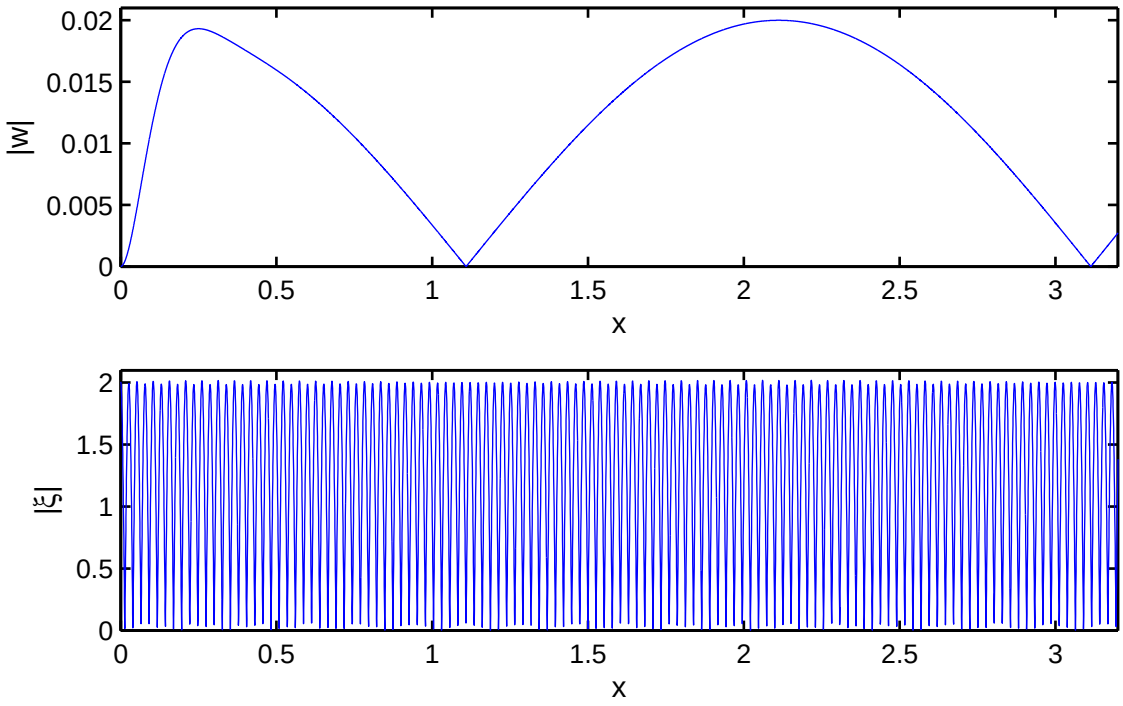

Figure 4.21: Case (iii): The plate deflection $|w(x)|$ and the interfacial deflection $|\xi(x)|$ are plotted against x. Here $\omega = 0.2\,\mathrm{s}^{-1}$, leading to $k_1 = 1.57$, $k_2 = 120.48$. The remaining parameters are set to their default values.

Figure 4.21 shows both deflections for the frequency $\omega = 0.2\,\mathrm{s}^{-1}$. We see that k_1 dominates the surface deflection and k_2 dominates the interfacial deflection, and the other mode is negligible in each case.

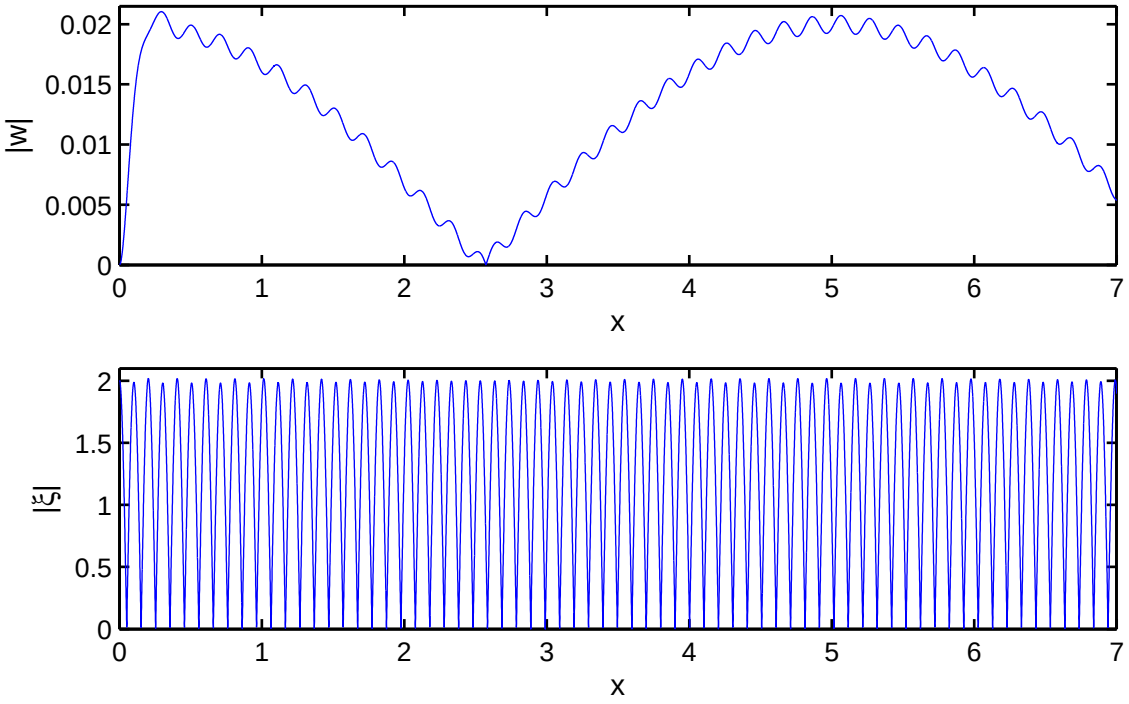

Figure 4.22: Case (iii): The plate deflection $|w(x)|$ and the interfacial deflection $|\xi(x)|$ are plotted against x. Here $\omega = 0.1\,\mathrm{s}^{-1}$, leading to $k_1 = 0.64$, $k_2 = 31.01$. The remaining parameters are set to their default values.

Figure 4.22 shows both deflections for the frequency $\omega = 0.1\,\mathrm{s}^{-1}$. We see that waves of mode k_2 start to appear on the surface, although they have much smaller amplitude than the waves of mode k_1. The interfacial deflection remains dominated by the mode k_2.

Figure 4.23 shows both deflections for the frequency $\omega = 0.05\mathrm{s}^{-1}$. At the surface, the waves of each mode now have comparable amplitude. Higher amplitude k_2-waves are possible due to the long wavelengths caused by this value of ω. Throughout all values of ω, we see a slight variation in the peaks of the interfacial deflection, indicating that the surface mode is present although negligible compared to the interfacial mode.

4.4.2 Strain in the ice sheet

We are interested in the strain in the ice sheet for several reasons. Firstly, we would like to investigate whether the ice–clamping condition is realistic, or whether there is too much strain at $x = 0$ for the clamping to be maintained. Secondly, we would like to compare with Chapter 2 to investigate what effect a two-layer fluid has on the ice strain, compared to a one-layer model. We would also like to study all cases (i)-(iii) to compare the strain caused by each.

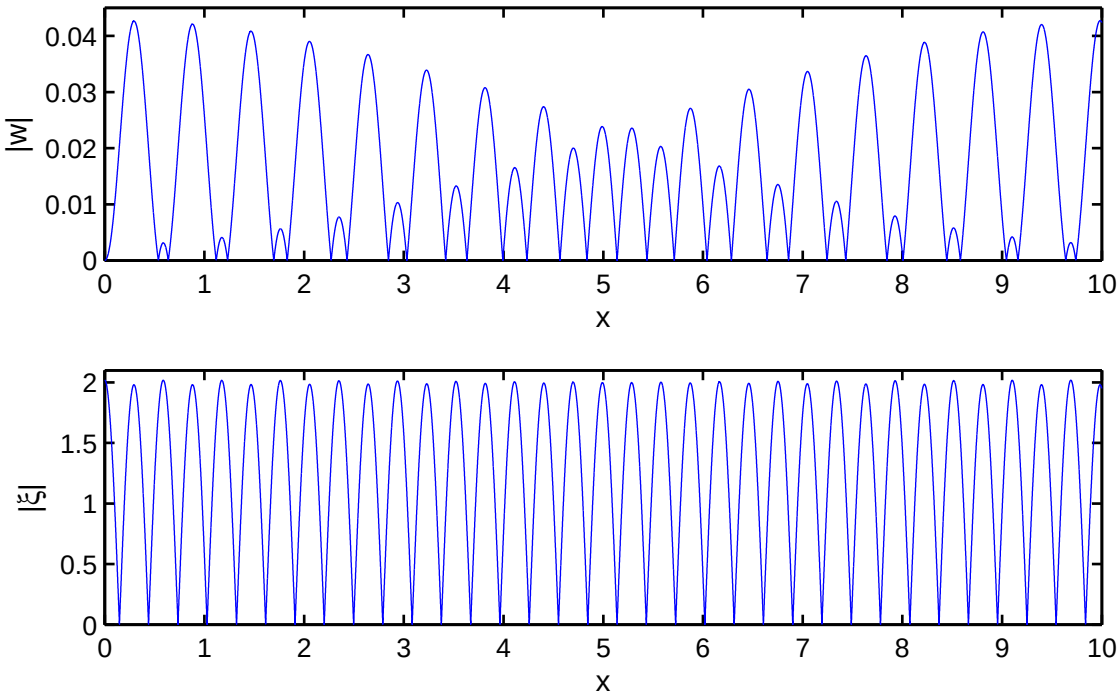

Figure 4.23: Case (iii): The plate deflection $|w(x)|$ and the interfacial deflection $|\xi(x)|$ are plotted against x. Here $\omega = 0.05\,\mathrm{s}^{-1}$, leading to $k_1 = 0.30$, $k_2 = 10.70$. The remaining parameters are set to their default values.

The strain is dimensionless, and considering our nondimensionalisation it is calculated by (Ugural, 1981)

$$\varepsilon = \frac{ah}{2H_2^2}\frac{\partial^2 w}{\partial x^2}. \tag{4.123}$$

For simplicity we take $a = 1\,\mathrm{m}$ in our calculations. Using equation (4.15) to express $w(x,t)$ in terms of $W(x)$ and using the total form of the plate deflection we have

$$\frac{\partial^2 W}{\partial x^2} = \frac{\partial^2 W_{inc}}{\partial x^2} + \frac{\partial^2 W_{ref}}{\partial x^2} + \frac{\partial^2 \hat{w}}{\partial x^2}.$$

Substituting the correct expressions using Section 4.2.8 and equation (4.114), we differentiate W twice and find that

$$\begin{aligned}\frac{\partial^2 W}{\partial x^2} &= -k_1^2 a_1^I e^{-ik_1 x} - k_2^2 a_2^I e^{-ik_2 x} - k_1^2 a_1^D e^{ik_1 x} - k_2^2 a_2^D e^{ik_2 x} \\ &\quad + \frac{2}{\pi} i(a_1^I - a_1^D)\frac{\partial^2}{\partial x^2}\int_0^\infty Q(s)\cos(sx)\,ds.\end{aligned} \tag{4.124}$$

The last term describes the interaction between the ice and the wall for small x. The integral

$$I(x) = \frac{\partial^2}{\partial x^2}\int_0^\infty Q(s)\cos(sx)\,ds \tag{4.125}$$

in this expression requires some attention. We cannot differentiate directly, as this would lead to a term $s^2 Q(s)$ in the integrand. The function $Q(s)$ decays with order s^{-2} which would leave the integral undefined. Firstly, we investigate the function

$Q(s)$ for very large s and find

$$Q(s) \to -\frac{k_1 + \hat{c}k_2}{s^2} - \frac{\hat{p}}{s^4}, \tag{4.126}$$

as $s \to \infty$. Here the constant $\hat{p}$ is given by

$$\hat{p} = \frac{\hat{c}\hat{m}_2 + \frac{M(k_1,k_2)}{k_1^2 - k_2^2}}{\gamma\chi(k_2)\tanh(k_2\bar{H})k_2}. \tag{4.127}$$

Note that even though the second term in equation (4.126) is of order s^{-4}, the constant $\hat{p}$ is so large that this term cannot be neglected (this is due to the term $\chi(k_2)$ in the denominator of $\hat{p}$ and the fact that γ is also very small). We now define

$$q(s) = Q(s) + \frac{k_1 + \hat{c}k_2}{s^2 + 1} + \frac{\hat{p}}{s^4 + 1},$$

and substitute into equation (4.125) to give

$$\begin{aligned}
I(x) &= \frac{\partial^2}{\partial x^2}\int_0^\infty \left(q(s) - \frac{k_1 + \hat{c}k_2}{s^2+1} - \frac{\hat{p}}{s^4+1} \right) \cos(sx)\, ds \\
&= \frac{\partial^2}{\partial x^2}\left(\int_0^\infty q(s)\cos(sx)\, ds - (k_1 + \hat{c}k_2)\int_0^\infty \frac{\cos(sx)}{s^2+1}\, ds \right. \\
&\quad \left. - \hat{p}\int_0^\infty \frac{\cos(sx)}{s^4+1}\, ds \right) \\
&= -\int_0^\infty s^2 q(s)\cos(sx)\, ds - (k_1 + \hat{c}k_2)\frac{\partial^2}{\partial x^2}\int_0^\infty \frac{\cos(sx)}{s^2+1}\, ds \\
&\quad - \hat{p}\frac{\partial^2}{\partial x^2}\int_0^\infty \frac{\cos(sx)}{s^4+1}\, ds \\
&= -\tilde{I}(x) - (k_1 + \hat{c}k_2)\frac{\partial^2}{\partial x^2}\left(\frac{\pi}{2}\, e^{-x} \right) \\
&\quad - \hat{p}\frac{\partial^2}{\partial x^2}\left(\frac{\pi\sqrt{2}}{4}\, e^{-x/\sqrt{2}}\Big(\cos(x/\sqrt{2}) + \sin(x/\sqrt{2})\Big) \right) \\
&= -\tilde{I}(x) - (k_1 + \hat{c}k_2)\left(\frac{\pi}{2}\, e^{-x} \right) \\
&\quad - \hat{p}\left(\frac{\pi\sqrt{2}}{4}\, e^{-x/\sqrt{2}}\Big(\cos(x/\sqrt{2}) - \sin(x/\sqrt{2})\Big) \right).
\end{aligned}$$

Here we have used the standard results

$$\begin{aligned}
\int_0^\infty \frac{\cos(sx)}{s^2+1}\, ds &= \frac{\pi}{2}\, e^{-x}, \\
\int_0^\infty \frac{\cos(sx)}{s^4+1}\, ds &= \frac{\pi\sqrt{2}}{4}\, e^{-x/\sqrt{2}}\Big(\cos(x/\sqrt{2}) - \sin(x/\sqrt{2})\Big),
\end{aligned}$$

given in Gradshteyn & Ryzhik (2007). The only integral left to evaluate is

$$\tilde{I}(x) = \int_0^\infty s^2 q(s) \cos(sx)\, ds,$$

which may be calculated directly because $q(s)$ decays with $O(s^{-5})$. The strain may now be calculated using equations (4.123) and by taking the real part of (4.124).

Case (i): $a_1^I = 1$, $a_2^I = 0$.

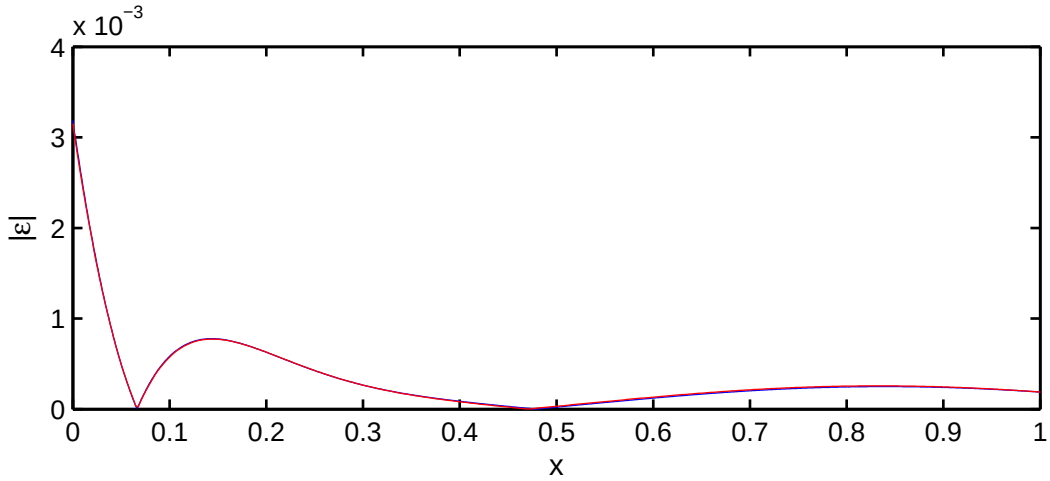

Figure 4.24: Case (i): The strain in the ice sheet $|\varepsilon|$ is plotted against x. The red curve shows the strain calculated for the two-layer model, with $\omega = 0.35\,\mathrm{s}^{-1}$ giving $k_1 = 4.4$ and $k_2 = 368.9$. The blue curve (underneath the red curve) shows the strain for the one-layer model of Chapter 2 with $k = 4.4$.

Figure 4.24 compares the strain between the two-layer and one-layer models. We take the wavenumber k from the one-layer model to be equal to k_1. There is perfect agreement between the two models. This has two implications: firstly, that in the short-wave limit for k_2, the internal waves do not penetrate to the surface and therefore have no effect on the strain in the ice sheet. Secondly, the fact that the two curves were plotted with different models and different numerical codes gives verification to the two-layer computation. The strain is highest at $x = 0$ due to the ice–clamping condition, before the strain settles down to a regular wave further away from the wall. Recall that although the strain at $x = 0$ is high, the incident amplitude a can be scaled to a more realistic value which would lower the strain considerably. From Chapter 2 our estimate for the critical strain is $\varepsilon_{cr} = 8 \times 10^{-5}$, so a value of $a = 0.01$ m would mean that the strain is below its critical value for Figure 4.24.

Figure 4.25 shows the strain $|\varepsilon|$ plotted against x for $\omega = 0.1\mathrm{s}^{-1}$, giving $k_1 = 0.64$ and $k_2 = 31$. The curve is split into two sections to show the contrast between the strain close to the vertical wall and the strain far from the wall. Despite the fact that k_2 waves were not present in the deflection for this value of ω (see Figure 4.12), its influence can be seen in the strain. However, the strain is already too small for the disturbance to be significant.

Case (ii): $a_1^I = 0$, $a_2^I = f_3^{-1}(k_2)$.

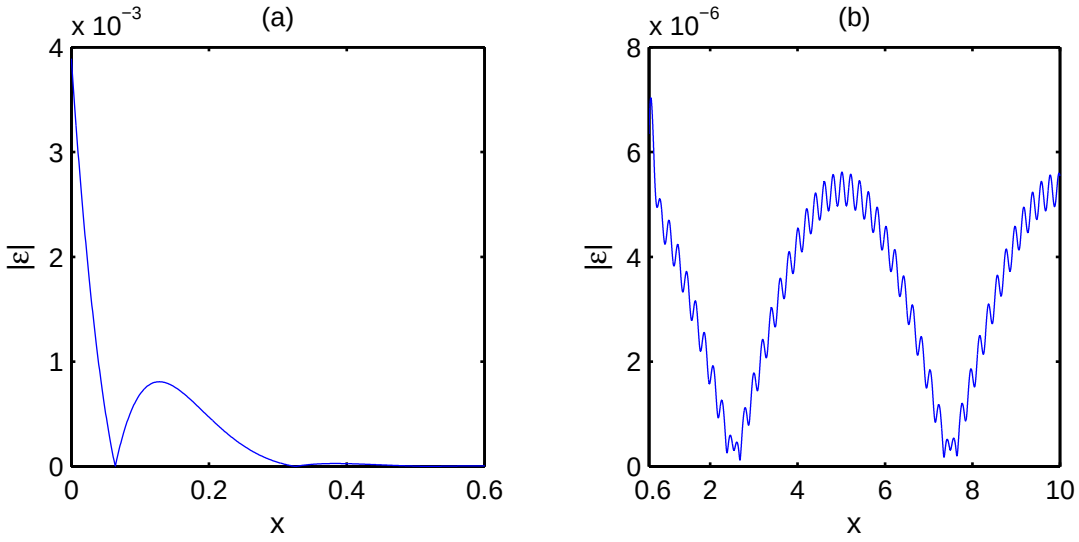

Figure 4.25: Case (i): The strain in the ice sheet $|\varepsilon|$ is plotted against x for $\omega = 0.1\,\mathrm{s}^{-1}$. The graph is split into (a) $x = 0 - 0.6$ and (b) $x = 0.6 - 10$ due to the high peak at $x = 0$.

Figure 4.26 shows the strain for case (ii), incident waves of mode k_2 only, for $\omega = 0.05\,\mathrm{s}^{-1}$ and $\omega = 0.1\,\mathrm{s}^{-1}$. With reference to Figures 4.18 and 4.17 showing the deflection for we see that k_2 is the dominant mode at the surface in both cases. For $\omega = 0.05\,\mathrm{s}^{-1}$, the highest strain is at $x = 0$, and although there were no incident waves of mode k_1 we see that k_2 has penetrated to the surface enough to contribute significant strain in the ice sheet. For $\omega = 0.1\,\mathrm{s}^{-1}$, the highest strain is no longer at $x = 0$. This is because the dominant term in equation (4.124) is now $-k_2^2 a_2^I e^{-ik_2 x}$, as opposed to the integral term (representing the contribution close to the wall) which has dominated thus far.

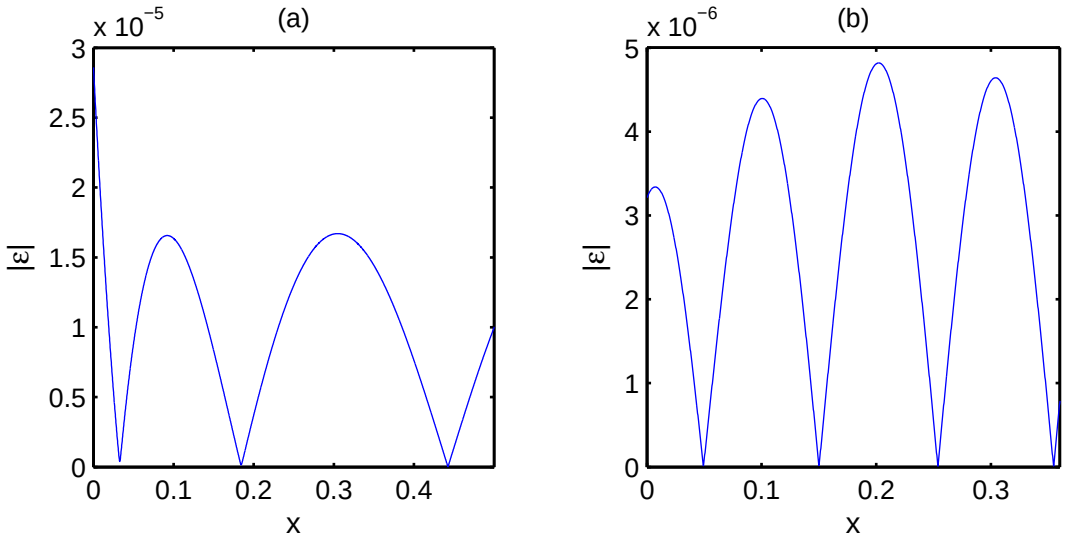

Figure 4.26: Case (ii): The strain in the ice sheet $|\varepsilon|$ is plotted against x for (a) $\omega = 0.05\,\mathrm{s}^{-1}$ and (b) $\omega = 0.1\,\mathrm{s}^{-1}$

Case (iii): $a_1^I = 0.01$, $a_2^I = f_3^{-1}(k_2)$. We now consider the strain for the case of incident waves of both modes k_1 and k_2. The strain is plotted in Figure 4.27 for $\omega = 0.05\,\mathrm{s}^{-1}$ and $\omega = 0.1\,\mathrm{s}^{-1}$. For $\omega = 0.05\,\mathrm{s}^{-1}$ the deflection is plotted in Figure

4.23. For the equivalent strain curve we see that the strain caused by the mode k_2 is dominant over the strain caused by the ice–clamping condition. For $\omega = 0.1\,\mathrm{s}^{-1}$, the opposite is true; as we can see in Figure 4.22 the mode k_2 is less prevalent in the ice deflection and hence contributes less to the strain.

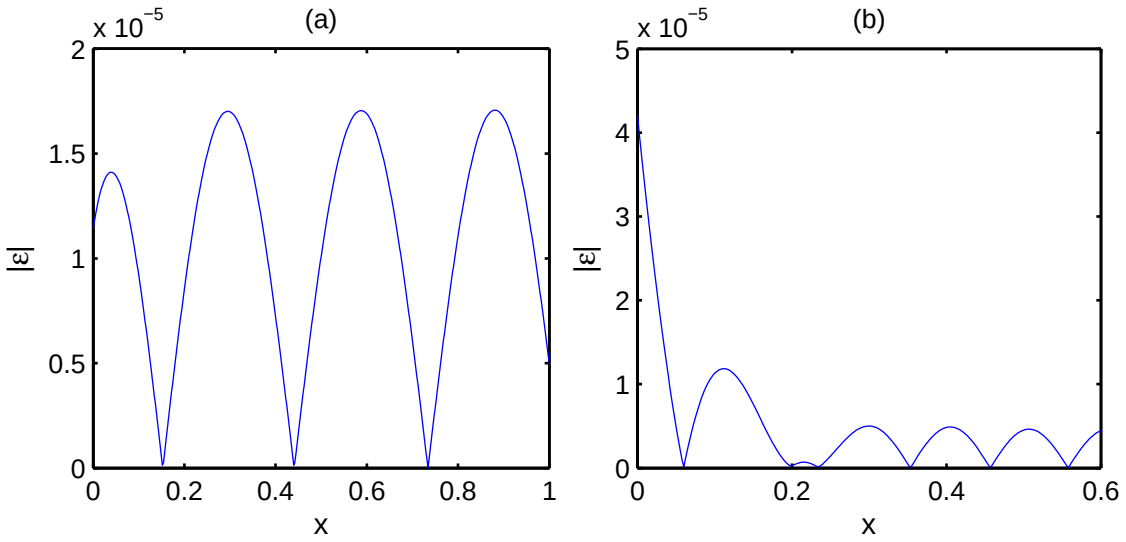

Figure 4.27: Case (iii): The strain in the ice sheet $|\varepsilon|$ is plotted against x for (a) $\omega = 0.05\,\mathrm{s}^{-1}$ and (b) $\omega = 0.1\,\mathrm{s}^{-1}$

4.4.3 Shear force

The shear force is defined as the vertical lifting force acting on the vertical wall generated by the ice–clamping condition. It is calculated in dimensionless form by (Ugural, 1981):

$$V^{SH} = -\frac{\partial^3 w(0,t)}{\partial x^3}. \tag{4.128}$$

Recalling that $w_{xxx}(0,t) = \Re(iW_{xxx}(0)e^{-it})$ and using the total form for the plate deflection we have

$$W_{xxx}(0) = \frac{\partial^3 W_{inc}}{\partial x^3} + \frac{\partial^3 W_{ref}}{\partial x^3} + \frac{\partial^3 \hat{w}}{\partial x^3}.$$

Note that we do not have to use an inverse transform to calculate $\hat{w}_{xxx}(0)$ as it is already given by equation (4.105). This avoids any difficulty with convergence that would have occurred in the resulting integrand. Recalling that we define the constant $\hat{p}$ in equation (4.127), substituting the respective expressions for W_{inc} and W_{ref} and differentiating gives

$$W_{xxx}(0) = i(a_1^I - a_1^D)(k_1^3 + \hat{c}k_2^3 - \hat{p}). \tag{4.129}$$

The maximum shear force with respect to time is then given by

$$|V^{SH}| = (k_1^3 + \hat{c}k_2^3 - \hat{p})\sqrt{a_I^2 + (a_R - a_1^I)^2}. \tag{4.130}$$

In the following figures we present the dimensionless shear force (unlike in previous chapters), because the amplitude a appears in its dimensional form, which varies in each case (i)–(iii).

Case (i): $a_1^I = 1$, $a_2^I = 0$. For case (i) the shear force is plotted against ω in Figure 4.28. The values of the shear force show excellent agreement with the equivalent one-layer model, indicating that the contribution from the waves of mode k_2 is small for this case. The shear force is higher for longer waves. We vary ρ_1 and H_1, the interfacial parameters, and confirm that they have little effect on the shear force for the incident wave under consideration.

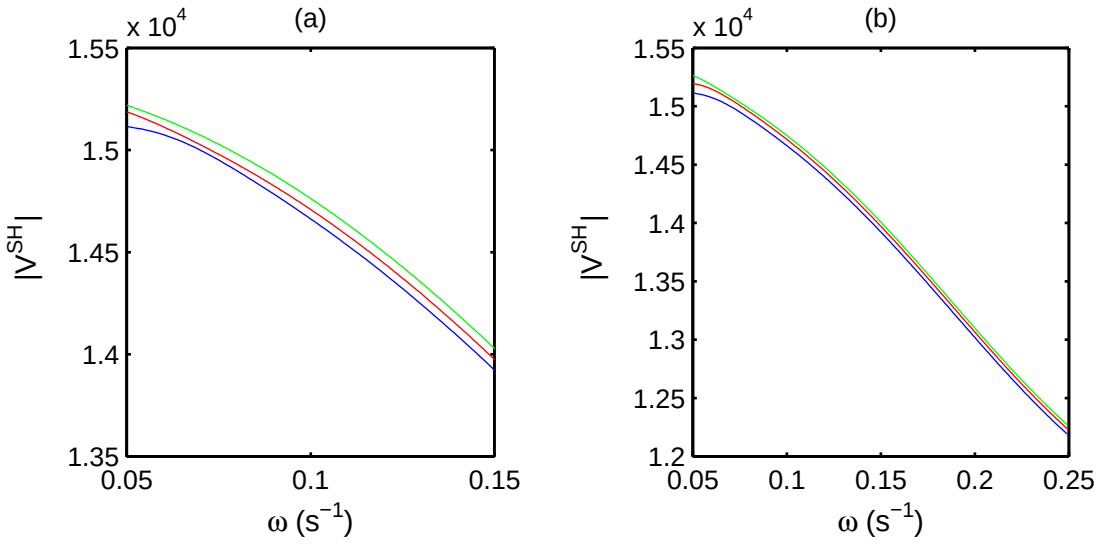

Figure 4.28: Case (i): The shear force $|V^{SH}|$ is plotted against ω for varying parameters. (a) ρ_1 is given by 1000 kgm^{-3} (blue), 1010 kgm^{-3} (red) and 1020kg m^{-3} (green). (b) H_1 is given by 20m (blue), 10m (red) and 5m (green).

Case (ii): $a_1^I = 0$, $a_2^I = f_3^{-1}(k_2)$. The shear force is plotted against ω for case (ii) in Figure 4.29. Here there are only incident waves of mode k_2. Smaller values of ω permit waves of k_2 to exist on the surface, which causes considerable shear force on the wall. However as ω increases, the k_2 waves no longer penetrate to the surface and the shear force tends to zero. We also see that as $\bar{\rho}$ approaches 1, the interfacial waves have less effect on the shear force as expected. When varying the depth H_1 we note that a depth of 5m gives the lowest shear force of the depths considered.

Case (iii): $a_1^I = 0.01$, $a_2^I = f_3^{-1}(k_2)$. Figure 4.30 shows the shear force plotted against ω for case (iii), incident waves of both modes. To compare directly with case (i), recall that the surface waves were scaled to 1 for that case, whereas here the surface waves are scaled to 0.01. We see some interesting behaviour in the long-wave limit of ω. For $\rho_1 = 1000\,\mathrm{kgm}^{-3}$ the maximum shear force actually approaches zero at $\omega = 0.06\,\mathrm{s}^{-1}$. This is because $|a_1^I - a_1 D|$ approaches zero at that point, implying that the contributions from the incident and reflected k_1 waves cancel each other out. We see that as ω grows, the parameter ρ_1 becomes less important due to the interfacial waves dying on the surface. Figure 4.30(b) shows that the depth H_1 has little influence on the maximum shear force.

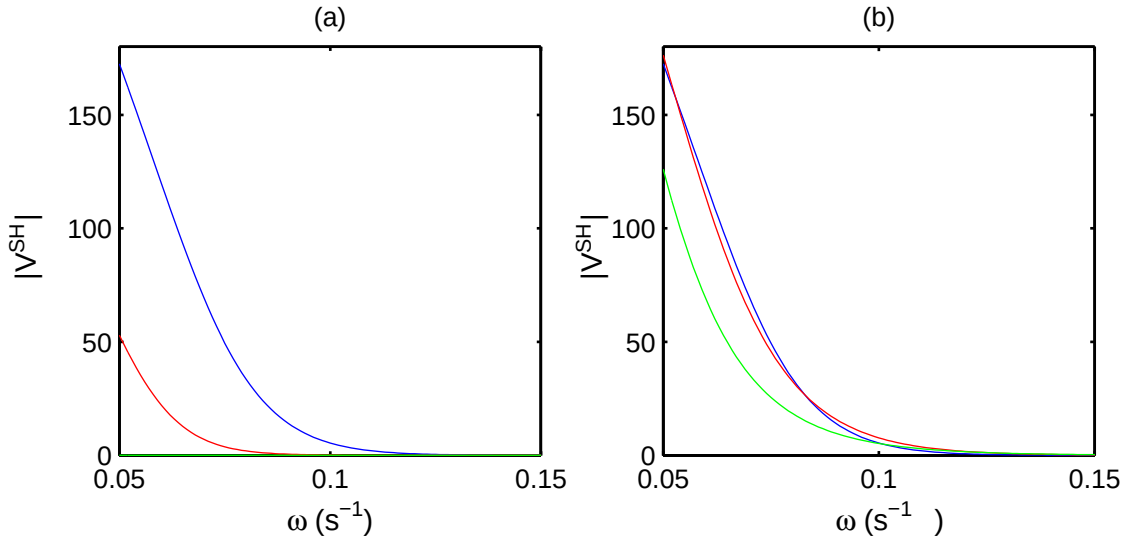

Figure 4.29: Case (ii): The shear force $|V^{SH}|$ is plotted against ω for varying parameters. (a) ρ_1 is given by 1000 kgm^{-3} (blue), 1010 kgm^{-3} (red) and 1020 kgm^{-3} (green). (b) H_1 is given by 20 m (blue), 10 m (red) and 5 m (green).

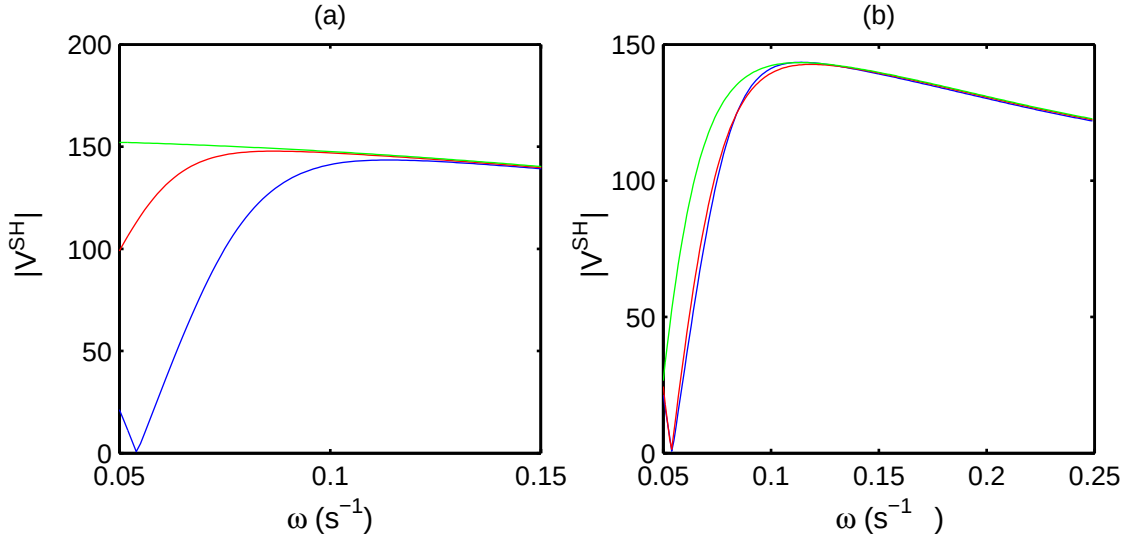

Figure 4.30: Case (iii): The shear force $|V^{SH}|$ is plotted against ω for varying parameters. (a) ρ_1 is given by 1000 kgm^{-3} (blue), 1010 kgm^{-3} (red) and 1020 kgm^{-3} (green). (b) H_1 is given by 20 m (blue), 10 m (red) and 5 m (green).

4.5 Summary

The problem of hydroelastic wave interaction with a vertical wall was extended to consider a two–layer fluid, which is expected to better describe the flow under the ice cover. The fluid was of finite depth and the ice sheet was clamped to the vertical wall. The problem was formulated and solved within linear hydroelastic wave theory. Due to the two fluid layers, there are two solutions in the dispersion relation, giving one wavenumber representing surface waves and another representing interfacial waves.

The problem was solved by Fourier transform after using linear superposition to separate the incident and reflected waves. This method led to an explicit solution in terms of integral quadratures. The integrals converge reasonably quickly, and the computational time involved was therefore short. The method was algebraically cumbersome but this is unavoidable due to the complicated physical formulation. The method allowed the incident and reflected wave-amplitude coefficients of both modes to be written explicitly. This is one advantage over methods such as an eigenfunction expansion or a Green's function formulation. In hydroelastic models, there can be difficulties with calculating the strain or the shear force, which require calculation of the second and third derivative of the ice deflection. In the present formulation, the explicit solution allows asymptotic expressions to assist in the calculation of the strain. The Fourier transform method also leads to a concise algebraic expression for the vertical shear force, sidestepping the usual problems with convergence.

Three cases were considered for results: (i) incident waves of the surface mode k_1, (ii) incident waves of the interfacial mode k_2 and (iii) incident waves of both modes. For case (i), the results were consistent with those of Chapter 2, the equivalent one-layer fluid problem. However, it was shown that the ice–wall interaction can generate interfacial waves of mode k_2, and the amplitude of these waves is considerable and similar to the surface wave amplitude. This is especially pronounced for low frequency ω and when the two layers have a more pronounced density difference. For this case the generated interfacial mode fails to have much influence on the ice deflection because the waves are not strong enough to penetrate to the ice cover.

For case (ii) we saw that reflection of incident waves of mode k_2 do not generate significant waves of mode k_1. The k_1 waves exist, but they are dwarfed by the influence of the mode k_2. For higher values of ω especially, the surface response from both modes is negligible and the disturbance is localised at the interface between the two fluid layers. However, it was shown that for small ω, waves of mode k_2 can still contribute significant strain in the ice sheet due to their short wavelength, but this strain is not above the critical strain for ice. Case (iii) shows the most interaction between the two wave modes. For small values of ω it was shown that waves of k_1 and k_2 have similar amplitude at the surface. The interfacial deflection however was dominated by the mode k_2, partly due to the scaling chosen for this case.

The results show that even if there are only incident waves of one mode, reflected waves of both modes can be generated. This is especially true for lower frequencies which usually characterise hydroelastic problems. We conclude that if the fluid under an ice sheet has stratified into two layers, and if the density difference between the two layers is pronounced, then the effect of this stratification cannot be neglected.

Chapter 5

Hydroelastic waves generated by a moving load in the vicinity of a vertical wall: linear formulation

5.1 Introduction

In this chapter the one-layer fluid formulation is reconsidered. Thus far throughout this thesis we have considered problems with regular incident waves that are periodic. Now we are concerned with waves generated by a moving load on an ice sheet in three dimensions. This area of mathematics has many applications as discussed in Section 1. We first investigate a moving load on a semi–infinite expanse of open ice with no obstacles. We then proceed to study a load moving in the vicinity of a vertical wall. In both cases, the load has constant velocity and exerts a downwards force on the ice sheet, acting as a wave source. In the vertical wall case the ice sheet is frozen to the vertical wall. The fluid is of finite depth in both cases. We are interested in the shape and magnitude of the ice deflection, and what factors influence them. Also of interest is whether the motion of the moving load can generate large enough surface response to break the ice connection to the vertical wall. Key parameters under investigation include the distance of the load from the wall and the speed at which the load is moving.

We introduce a simple viscoelastic formulation which takes into account ice relaxation time. This has two benefits: firstly, it ensures that the hydroelastic waves decay at a distance from the source. Since the source of the waves is no longer periodic as in previous chapters, this is a necessary constraint. In addition, incorporating viscoelasticity adds further realism to the model, as ice has been shown to behave viscoelastically in practice, as discussed in Chapter 1. We will also introduce a moving frame of reference to assist in the solution of the problem and provide clarity to the results.

In this chapter, the problem is formulated within linear hydroelastic theory. Chapter 6 addresses the nonlinear formulation of the same problem. The assump-

tions on the fluid and ice sheet made in Section 2.1 apply here also. We will derive the solution for the deflection of the ice sheet and the velocity potential. The deflection of the ice sheet will be analysed for various parameters. For the vertical wall case we will also investigate the strain in the ice sheet, with particular attention to the strain along the wall. By estimating a maximum strain for the ice we will investigate the conditions under which this connection is likely to break.

The default set of parameter values is taken from Table 2.1(a) with the depth chosen as $H = 100$ m. This shallower depth is chosen with consideration of the intended applications of the problem, as discussed in Section 1.

Section 5.2 analyses the case of open ice without a vertical wall present. We outline the governing equations and boundary conditions. The method of solution is introduced and results are presented for the ice deflection. We move on to the primary focus of this chapter, the vertical wall case, described in Section 5.3. The formulation is similar to the open ice case but with extra boundary conditions to account for the vertical wall. Results are presented in more detail, including results for the ice deflection and strain in the ice sheet. A summary is given in Section 5.4.

5.2 Open ice case

5.2.1 Mathematical formulation

5.2.1.1 Schematic, parameters and governing equations

In order to gain familiarity and experience with moving load problems, we first solve the problem without a vertical wall present. The geometry of the problem and co-ordinate system are shown in Figure 5.1.

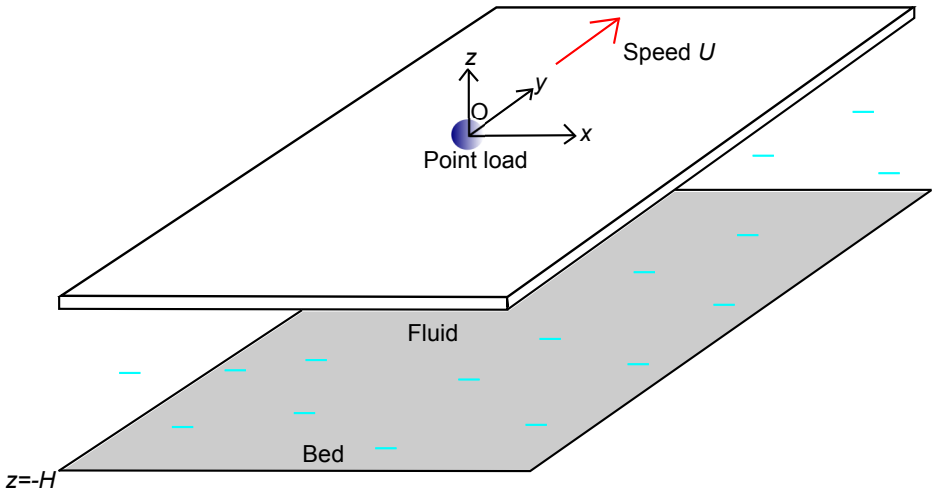

Figure 5.1: Three–dimensional schematic of a plane unbounded ice sheet, with a point load moving in the positive y direction.

We introduce Cartesian coordinates with the origin coinciding with the position of the point load. The load moves in the positive y direction. The z-axis is directed vertically upwards, with the bottom of the unperturbed ice sheet at $z = 0$. We now

introduce various physical parameters and variables, some recapped from previous chapters and some introduced for the first time. The fluid bed is flat and the fluid has depth H. Time is denoted by t. The moving load is modelled by an external pressure $P(x, y, t)$. The pressure in the fluid is defined $p(x, y, z, t)$. The external load has mass m^V, and is moving with speed U. The density of the fluid is ρ. The flow velocity $\mathbf{V}(x, y, z, t)$ is equal to the gradient of the velocity potential $\phi(x, y, z, t)$, hence $\nabla\phi = \mathbf{V}$. The vertical deflection of the ice sheet (the distance the ice sheet is displaced relative to its position at rest) is denoted by $z = w(x, y, t)$. The ice has mass per unit length M, where $M = \rho_i h$, ρ_i is the ice density and h is the ice thickness. The ice sheet has flexural rigidity EJ, where E is Young's modulus and $J = h^3/[12(1 - \nu^2)]$, where ν is Poisson's ratio. The downward acceleration due to gravity is denoted g. In addition we introduce the ice relaxation time τ, defined below.

The velocity potential ϕ must satisfy Laplace's equation in the fluid:

$$\nabla^2\phi = 0, \qquad (-\infty < x, y < \infty,\ -H \leq z \leq 0). \tag{5.1}$$

We use the linearised Bernoulli equation to determine the pressure in the fluid:

$$p(x, y, z, t) = -\rho\phi_t - \rho g z, \qquad (-\infty < x, y < \infty,\ -H \leq z \leq 0). \tag{5.2}$$

We introduce a simple viscoelastic formulation, utilising the Kelvin-Voigt model for an elastic material (see for example Zhestkaya, 1999). For a general system with stress σ, strain ε, Young's modulus E and viscosity η we have:

$$\begin{aligned}\sigma(t) &= E\varepsilon(t) + \eta\frac{d\varepsilon(t)}{dt},\\ &= E\left(1 + \tau\frac{d}{dt}\right)\varepsilon.\end{aligned}$$

Here the relaxation time $\tau = \eta/E$. Applying this model in the present problem, the plate equation becomes (Zhestkaya, 1999):

$$\begin{aligned}EJ\left(1 + \tau\frac{\partial}{\partial t}\right)\nabla^4 w + Mw_{tt} &= P(x, y, t) + p(x, y, z, t),\\ &(-\infty < x, y < \infty,\ z = 0).\end{aligned} \tag{5.3}$$

Here the biharmonic operator ∇^4 is defined as

$$\nabla^4 = \frac{\partial^4}{\partial x^4} + 2\frac{\partial^4}{\partial x^2\partial y^2} + \frac{\partial^4}{\partial y^4}.$$

The boundary conditions for Laplace's equation (5.1) are given by the kinematic

condition at the ice-fluid interface and the fluid bed respectively:

$$\phi_z = w_t, \qquad (z = 0), \tag{5.4}$$

$$\phi_z = 0, \qquad (z = -H). \tag{5.5}$$

Conditions in the far field are defined later.

5.2.1.2 Critical speeds

The dispersion relation for the viscoelastic ice plate governed by equation (5.3) can by derived by setting $P = 0$ (no load) and considering waves propagating in the x direction. Substituting $w = e^{i(kx-\omega t)}$ into equations (5.1)-(5.5), we obtain

$$EJ(1 - i\omega\tau)k^4 + \rho g - M\omega^2 = \frac{\rho\omega^2}{k\tanh(kH)}. \tag{5.6}$$

This is the viscoelastic dispersion relation which allows us to compute the wavenumber k for a given frequency ω. Note that ω is real and positive. The term with the relaxation time τ shows that k is a complex number. It is the same as the hydroelastic dispersion relation for a one-layer fluid considered in previous chapters, with the addition of a term representing viscoelastic decay. Experiments conducted in Japan (Takizawa, 1985) observe a lag in the position of maximum ice depression directly behind the moving load that was unexplained by the elastic formulation. Hosking et al. (1988) suggest that viscoelastic theory can account for this lag. Takizawa (1985) propose that the lag time should be comparable with the relaxation time, which should hence range from roughly 0.2 s to 0.8 s.

As discussed in Chapter 1, one feature of problems involving moving loads of ice sheets is the appearance of certain critical speeds, at which the linear theory breaks down. The first critical speed occurs when the load moves with speed c_{min}, where c_{min} is the minimum phase speed of hydroelastic waves. Setting $\tau = 0$, the phase speed $c = \omega/k$ and the group speed $c_g = d\omega/dk$ are plotted against k in Figure 5.2. For the parameters under consideration, $c_{min} = 18.05\,\mathrm{ms}^{-1}$. It is well known that a source speed $U = c_{min}$ results in increased ice deflections (Squire et al., 1996). Davys et al. (1985) explain thus: "for a source travelling at the critical speed energy is radiated directly forward at the same speed and will continuously accumulate underneath the source". At the value $U = c_{min}$, Davys et al. (1985) and Milinazzo et al. (1995) report unbounded deflection. However, Hosking et al. (1988) incorporated a viscoelastic formulation and found that this forces a finite response at the critical speed.

Many authors such as Schulkes & Sneyd (1988), Părău & Vanden-Broeck (2011), Milinazzo et al. (1995) have noted the differing shapes of deflection above and below the critical speed. At load speeds above c_{min}, two different wave systems appear: shorter, faster waves that are elastic dominated and propagate ahead of the source, and longer, slower gravity-dominated waves behind the source. In addition, fast load

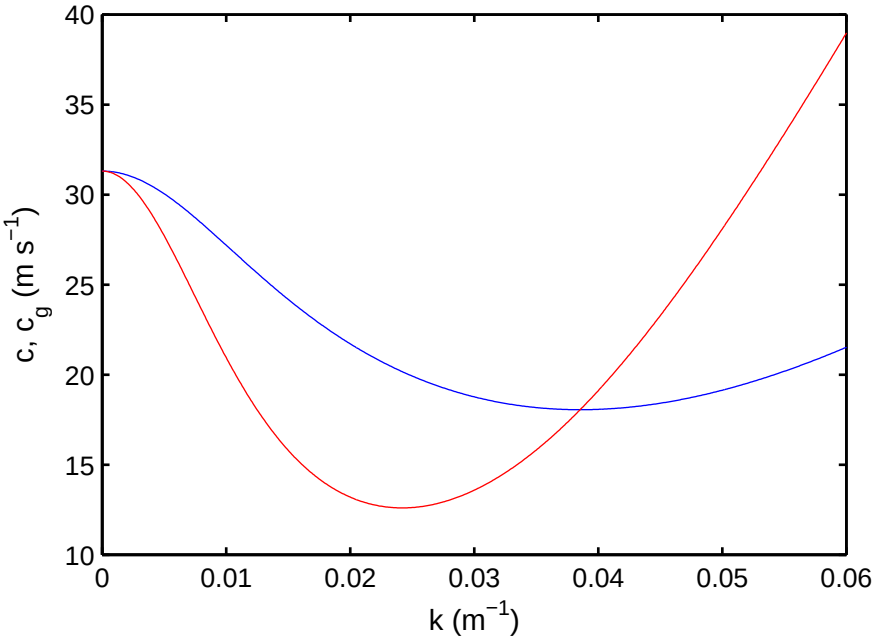

Figure 5.2: The phase (red) and group (blue) speeds plotted against the wavenumber k. Parameter values are from Table 2.1(a) with $H = 100$ m.

speeds generate a wave profile that is curved around the moving load. Below c_{min}, there is only one wave system and the wave pattern is regular, moving perpendicular to the direction of load movement.

Schulkes & Sneyd (1988) noted another possible sub-critical speed given by $\sqrt{gH}$. This is the speed at which gravity waves propagate on shallow water of uniform depth. However, they state that it is possible $\sqrt{gH}$ is not a critical speed for two–dimensional point sources, but only for line sources. Also, time-dependence seems to be a factor in qualifying this critical speed (Schulkes & Sneyd (1988) were studying the time-dependent response of an ice sheet to a moving load). Milinazzo et al. (1995) concluded that a steady solution does exist when the speed U approaches $\sqrt{gH}$, but such a solution is not realisable since the solution may grow with time.

5.2.1.3 Nondimensionalisation & expression for the moving load

As in previous chapters, we continue to use the total depth H as a length scale. We introduce a frame of reference moving with speed U by defining:

$$x^* = \frac{x}{H}, \quad y^* = \frac{y - Ut}{H}, \quad z^* = \frac{z}{H}.$$

In addition dimensionless time and dimensionless relaxation time are defined:

$$t^* = \frac{U}{H}t, \quad \tau^* = \frac{U}{H}\tau.$$

The moving load is modelled using the Dirac delta function, and can be expressed in dimensional variables as

$$P(x,y,t) = -\frac{m^V g}{H^2}\,\delta\Big(\frac{y-Ut}{H}\Big)\delta\Big(\frac{x}{H}\Big), \qquad (-\infty < x < \infty,\ -\infty < y < \infty). \quad (5.7)$$

Here m^V is the mass of the moving load. The minus in the right hand side indicates that the force is applied in a *downwards* direction. The Dirac delta function is defined as

$$\delta(x) = \begin{cases} \infty, & \text{x=0} \\ 0, & \text{otherwise,} \end{cases} \quad (5.8)$$

with the integral

$$\int_{-\infty}^{\infty} \delta(x)\,dx = 1. \quad (5.9)$$

Hence we have

$$P^*(x^*,y^*,t^*) = \frac{H^2}{m^V g} P(x,y,t) = -\delta(y^*)\delta(x^*). \quad (5.10)$$

The dimensionless deflection and velocity potential are defined as

$$w^*(x^*,y^*) = \frac{\rho U^2 H}{m^V g} w(x,y,t), \quad \phi^*(x^*,y^*,z^*) = \frac{\rho U H}{m^V g}\phi(x,y,z,t).$$

We also define several dimensionless parameters, given by

$$\alpha = \frac{M}{\rho H}, \quad \beta = \frac{gH}{U^2}, \quad \gamma = \frac{EJ}{\rho U^2 H^3}.$$

The asterisks are henceforth dropped in the following, and all variables/parameters are assumed dimensionless. We now rewrite the boundary value problem (5.1)-(5.5) in terms of the dimensionless variables and parameters:

$$\gamma\left(1-\tau\frac{\partial}{\partial y}\right)\nabla^4 w + \alpha w_{yy} + \beta w - \phi_y = -\delta(y)\delta(x), \qquad (-\infty < x,y < \infty,\ z = 0), \quad (5.11)$$

$$\nabla^2\phi = 0, \quad (-\infty < x,y < \infty,\ -1 \le z \le 0), \quad (5.12)$$

$$\phi_z = -w_y, \quad (z = 0), \quad (5.13)$$

$$\phi_z = 0, \quad (z = -1), \quad (5.14)$$

$$w \to 0, \quad (x^2+y^2) \to \infty, \quad (5.15)$$

$$\phi \to 0, \quad (x^2+y^2) \to \infty. \quad (5.16)$$

Here we have introduced conditions (5.15)-(5.16) ensuring that all waves decay far from the load. The above boundary value problem (5.11)-(5.16) describes the pattern of hydroelastic waves in the moving co–ordinate system.

5.2.2 Solution by double Fourier transform

We apply Fourier transforms in both the x and y directions. Using ξ as the transform variable in the x direction we define:

$$w^X(\xi, y) = \frac{1}{\sqrt{2\pi}} \int_{-\infty}^{\infty} w(x, y)\, e^{-i\xi x}\, dx, \tag{5.17}$$

with the corresponding inverse transform given by

$$w(x, y) = \frac{1}{\sqrt{2\pi}} \int_{-\infty}^{\infty} w^X(\xi, y)\, e^{i\xi y}\, d\xi. \tag{5.18}$$

Using transform variable η, in the y direction we define:

$$w^Y(x, \eta) = \frac{1}{\sqrt{2\pi}} \int_{-\infty}^{\infty} w(x, y)\, e^{-i\eta y}\, dy, \tag{5.19}$$

with inverse transform

$$w(x, y) = \frac{1}{\sqrt{2\pi}} \int_{-\infty}^{\infty} w^Y(x, \eta)\, e^{i\eta y}\, d\eta. \tag{5.20}$$

We now seek to obtain an expression for a Fourier transform acting on a derivative of x or y. For example, defining $F(w)$ as Fourier transform (5.19) acting on the function $w(x, y)$ to give $F(w) = w^Y$, we have:

$$\begin{aligned} F\left(\frac{\partial w}{\partial y}\right) &= \frac{1}{\sqrt{2\pi}} \int_{-\infty}^{\infty} w_y(x, y)\, e^{-i\eta y}\, dy \\ &= \frac{1}{\sqrt{2\pi}} \left((we^{-i\eta y})_{-\infty}^{\infty} + i\eta \int_{-\infty}^{\infty} w(x, y)\, e^{-i\eta y}\, dy \right) \\ &= i\eta \int_{-\infty}^{\infty} w(x, y)\, e^{-i\eta y}\, dy \\ &= i\eta w^Y. \end{aligned} \tag{5.21}$$

Here we have used integration by parts and the fact that w decays in the far field (5.16). We may use (5.21) to give an expression for $F(w_{yy})$; defining $g(y) = w_y$ we have:

$$F(w_{yy}) = F(g_y) = i\eta F(g) = (i\eta)^2 w^Y = -\eta^2 w^Y.$$

We use a similar process to obtain the expression

$$F(w_{yyyy}) = \eta^4 w^Y.$$

We also note that the Fourier transform in the x direction has no effect on y derivatives and vice versa; for example, $F(w_x) = w_x^Y$, etc.

5.2.2.1 Velocity potential

Using the facts derived in the above subsection, we apply the transforms to Laplace's equation (5.12), given by

$$\phi_{xx} + \phi_{yy} + \phi_{zz} = 0.$$

Applying both integral transforms (5.17) and (5.19) to the variable $\phi(x, y, z)$, we obtain:

$$-\xi^2\phi^{XY} - \eta^2\phi^{XY} + \phi_{zz}^{XY} = 0.$$

Applying the transforms to the boundary conditions (5.13) and (5.14), we have the following BVP for the variable $\phi^{XY}(\xi, \eta, z)$:

$$\phi_{zz}^{XY} - (\xi^2 + \eta^2)\phi^{XY} = 0, \quad (-1 \leq z \leq 0), \tag{5.22}$$

$$\phi_z^{XY} = -i\eta w^{XY}, \quad (z = 0), \tag{5.23}$$

$$\phi_z^{XY} = 0, \quad (z = -1). \tag{5.24}$$

With consideration of boundary condition (5.24), the general solution to equation (5.22) is given by

$$\phi^{XY} = A\cosh\big(\sqrt{\xi^2 + \eta^2}(z + 1)\big),$$

where A is an unknown function of ξ and η. Application of the boundary condition (5.23) gives

$$A = \frac{-i\eta w^{XY}}{\sqrt{\xi^2 + \eta^2}\sinh\big(\sqrt{\xi^2 + \eta^2}\big)}. \tag{5.25}$$

Hence, ϕ^{XY} is given by

$$\phi^{XY} = -i\eta\,\psi(z)\,w^{XY}, \tag{5.26}$$

where we have defined

$$\psi(z) = \frac{\cosh\big(\sqrt{\xi^2 + \eta^2}(z + 1)\big)}{\sqrt{\xi^2 + \eta^2}\sinh\big(\sqrt{\xi^2 + \eta^2}\big)}. \tag{5.27}$$

Equation (5.26) defines the velocity potential ϕ^{XY} in terms of the plate deflection w^{XY} which is still to be determined.

5.2.2.2 Plate deflection

We now apply the transforms to the left hand side of the plate equation (5.11), given by:

$$\text{LHS} = \gamma\left(1 - \tau\frac{\partial}{\partial y}\right)(w_{xxxx} + 2w_{xxyy} + w_{yyyy}) + \alpha w_{yy} + \beta w - \phi_y.$$

After applying both transforms (5.17) and (5.19) we obtain:

$$\text{LHS} = \gamma(1 - i\eta\tau)(\xi^4 w^{XY} + 2\xi^2\eta^2 w^{XY} + \eta^4 w^{XY}) - \alpha\eta^2 w^{XY} + \beta w^{XY} - i\eta\phi^{XY}. \tag{5.28}$$

We now apply both transforms to the right hand side of equation (5.11), given by

$$\text{RHS} = -\delta(x)\delta(y).$$

Using the property of the Dirac delta function given by equation (5.9), after applying the integral transforms we arrive at

$$\text{RHS} = -\frac{1}{2\pi}. \tag{5.29}$$

Combining the LHS and the RHS and substituting for ϕ^{XY} using equation (5.26), we have

$$w^{XY}\Big(\gamma(1-i\eta\tau)(\xi^4+2\eta^2\xi^2+\eta^4)+\beta-\alpha\eta^2-\eta^2\psi(0)\Big) = -\frac{1}{2\pi}.$$

We substitute the expression for ψ using equation (5.27) and define the function $Q(\xi,\eta)$ as

$$Q(\xi,\eta) = \gamma(1-i\eta\tau)(\xi^4+2\eta^2\xi^2+\eta^4)+\beta-\alpha\eta^2-\frac{\eta^2\coth(\sqrt{\xi^2+\eta^2})}{\sqrt{\xi^2+\eta^2}}. \tag{5.30}$$

After performing inverse transforms defined in equations (5.18) and (5.20), we arrive at the final solution for the ice deflection, which can be expressed as

$$w(x,y) = -\frac{1}{4\pi^2}\int_{-\infty}^{\infty}\left\{\int_{-\infty}^{\infty}\frac{e^{i\eta y}}{Q(\xi,\eta)}\,d\eta\right\}e^{i\xi x}\,d\xi. \tag{5.31}$$

5.2.2.3 Method of residues

The integral with respect to η in equation (5.31) is suitable for the application of complex integration by the method of residues. There are poles in the complex plane, which can be calculated readily. The poles arise due to the zeros of the function Q in the complex plane. The value of the integral can then be calculated by summing the contribution to the integral from each pole and applying the Cauchy residue theorem. Defining

$$Q = Q_R + i\,Q_I,$$
$$\eta = a + i\,b,$$

the poles occur when $Q = 0$, at the values of a and b for which

$$Q_R(\xi,a,b) = Q_I(\xi,a,b) = 0.$$

Figure 5.3 shows the location of the poles graphically. For all parameter values, there are 6 poles that have both a real and imaginary part. As U increases, or as τ decreases, the upper pair of poles in the lower half plane appraoch the real axis. However, as long as τ is non-zero, there are no poles *on* the real axis. The poles are

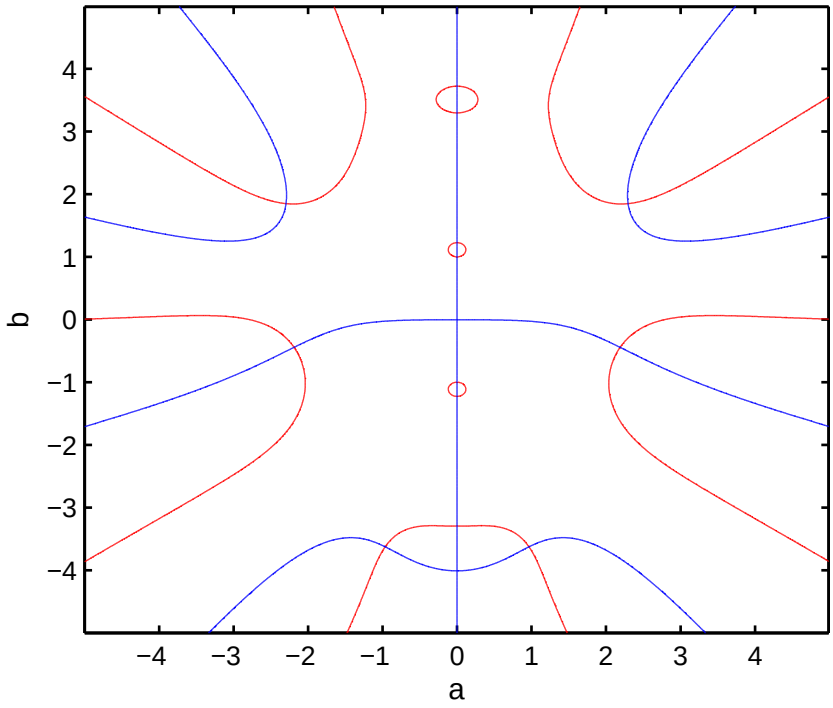

Figure 5.3: The complex η plane a vs b, showing the location of the poles in the integrand of (5.31). The blue lines represent the contour $Q_I = 0$, and the red lines represent the contour $Q_R = 0$. Poles occur at the intersections of these two lines. Here $U = 20\ \mathrm{ms}^{-1}$, $\tau = 10\ \mathrm{s}$, $\xi = 1$, and other parameters are taken from Table 2.1(a) with $H = 100\ \mathrm{m}$.

symmetric about the imaginary axis.

In addition to these 6 poles, there is an infinite set of purely imaginary poles. These can be located by setting $\eta = ib$ in the expression for $Q(\xi, \eta)$, and the poles occur where:

$$Q(\xi, ib) = 0 = \gamma(1 + b\tau)(\xi^4 - 2\xi^2 b^2 + b^4) + \beta + \alpha b^2 + \frac{b^2 \coth(\sqrt{\xi^2 - b^2})}{\sqrt{\xi^2 - b^2}}. \quad (5.32)$$

Equation (5.32) has no roots for $\xi > b$, but when $b > \xi$, and using $\coth(i\theta) = -i\cot(\theta)$ it becomes

$$\frac{\gamma}{b^2}(1 + b\tau)(\xi^4 - 2\xi^2 b^2 + b^4) + \frac{\beta}{b^2} + \alpha = \frac{\cot(\sqrt{b^2 - \xi^2})}{\sqrt{b^2 - \xi^2}}. \quad (5.33)$$

Equation (5.33) has an infinite set of solutions, shown graphically in Figure 5.4. This set of poles is not symmetric about the real axis, but differ slightly due to the $b\tau$ term in equation (5.33).

The locations of the poles are straightforward to calculate using root–finding algorithms. Each pole is denoted (a_p, b_p), where $p = 1, 2...6$ represents the poles with real and imaginary parts, and $p = 7, ...n$ represents the infinite set of imaginary poles. Once the poles are calculated, we draw the integral contour shown in Figure 5.5; a large semi-circle of radius R. For positive y, the semicircle is as shown, and for

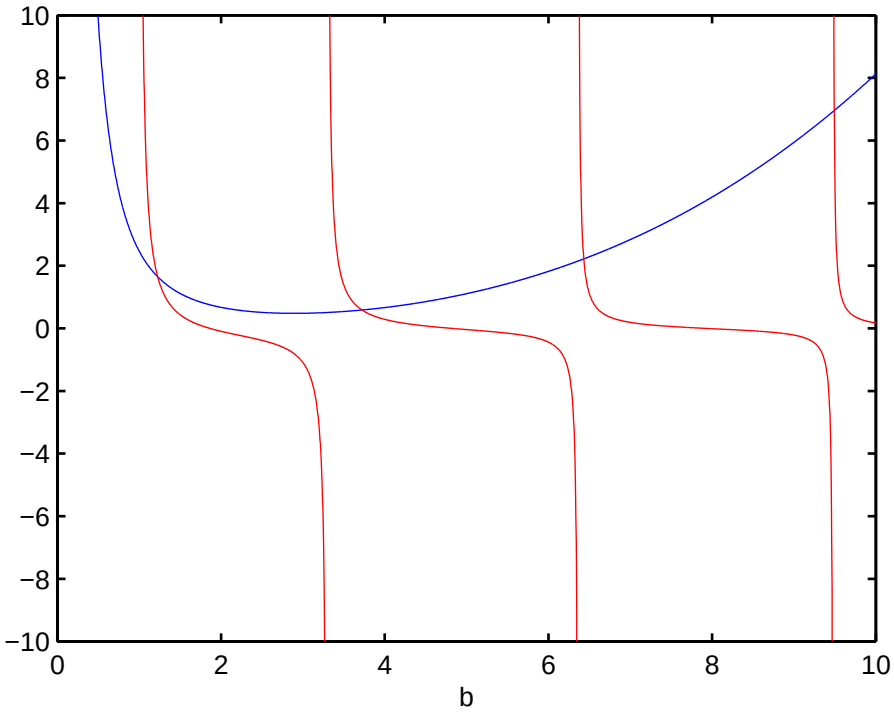

Figure 5.4: A graphical representation of the infinite set of purely imaginary poles. The blue line represents the left hand side of (5.33), and the red line represents the right hand side. Poles occur at the intersection of these two lines. Here $U = 20\,\mathrm{ms}^{-1}$, $\tau = 10\,\mathrm{s}$, $\xi = 1$, and other parameters are taken from Table 2.1(a) with $H = 100\,\mathrm{m}$.

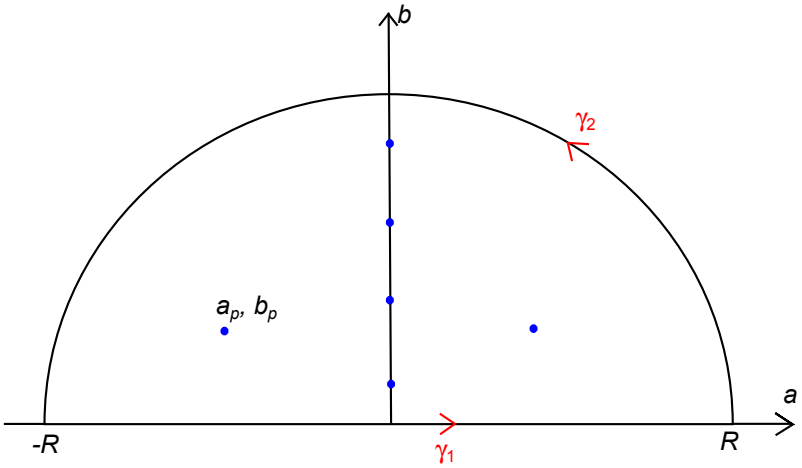

Figure 5.5: Integration contour for the application of the method of residues. The path γ_1 is the line on the real axis from $-R$ to R, and the path γ_2 is a semi–circle of radius R centred at O.

negative y, the contour is closed below the real axis. The Cauchy residue theorem (Jeffrey, 2002) states:

$$\int_{\gamma_1+\gamma_2} \frac{e^{i\eta y}}{Q(\xi,\eta)}\, d\eta = 2\pi i \sum_{p=1}^{n} \mathrm{Res}(a_p, b_p), \tag{5.34}$$

where the paths γ_1 and γ_2 are as defined in Figure 5.5. Here "Res" denotes the residue at each pole. All of the poles are simple poles (poles of order 1), and the residue is hence calculated (see Jeffrey, 2002) by

$$\mathrm{Res}(a_p, b_p) = e^{iy(a_p+ib_p)} \frac{\partial Q}{\partial \eta}^{-1}_{(a_p,b_p)}. \tag{5.35}$$

We now take the limit $R \to \infty$. The contribution from the integral path γ_2 vanishes in this limit by Jordan's lemma (Jeffrey, 2002), due to the fact that Q is of order η^5 as $\eta \to \infty$. Hence we are left with

$$\int_{-\infty}^{\infty} \frac{e^{i\eta y}}{Q(\xi,\eta)}\, d\eta = 2\pi i \sum_{p=1}^{n} \mathrm{Res}(a_p, b_p). \tag{5.36}$$

The convergence of the series (5.36) is fast, and n is usually taken as 15, by which time the contribution from the poles (a_n, b_n) is negligible. The resultant ξ integral in (5.31) is smooth and can be calculated by standard methods; note that the integrand is even and hence its symmetry can be exploited. The imaginary part of both integrands is odd and hence disappear due to the symmetric integration limits, and $w(x, y)$ is hence real.

5.2.3 Numerical results for the ice deflection

The primary focus of this chapter is the vertical wall model, presented in Section 5.3. For open ice, the problem has been solved previously by Hosking et al. (1988), albeit using a slightly different two–parameter viscoelastic model. However, the solution for the point-source part of this work was only approximated asymptotically. In addition, no three-dimensional graphs were presented. Hence several results are presented here for the open ice case. This also helps indicate the effect of the load speed U and serves as a build-up to the vertical wall case. We fix the viscoelastic time τ at $\tau = 0.1$ s. The effect of viscoelasticity will be studied in more detail for the vertical wall case.

The deflection is plotted in Figure 5.6 for speed $U = 15\,\mathrm{ms}^{-1}$, which is less than the critical speed c_{min}. We see that the waves in front and behind the source have comparable magnitudes, but the wave behind the source is slightly larger. This is due to the viscoelastic parameter τ in the formulation: with $\tau = 0$ the waves are symmetric. The waves decay a short distance from the source.

Figure 5.7 shows the deflection for the load speed $U = 25\,\mathrm{ms}^{-1}$, with $\tau = 0.1$ s. Recall that $c_{min} = 18.05\,\mathrm{ms}^{-1}$ for the default data set, so the speed U considered

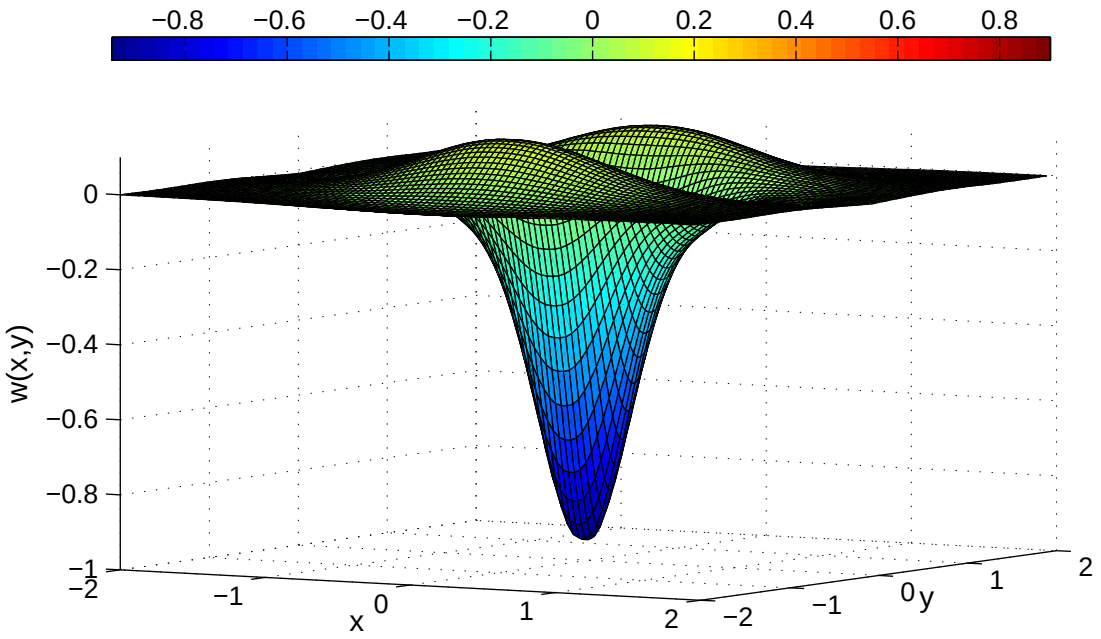

Figure 5.6: The deflection $w(x, y)$ is plotted against x and y. Here $U = 15\,\mathrm{ms}^{-1}$, $\tau = 0.1\,\mathrm{s}$, and other parameters are fixed at their default values.

is faster than the critical speed. We clearly see two wave modes; shorter, fast (predominantly elastic) waves that propagate ahead of the source, and longer, slower (predominantly gravity) waves that are behind the source. The surface pattern is also radically changed for speeds $U > c_{min}$; the wave pattern is curved around the moving load, and the decay occurs much farther from the load. The viscoelastic formulation ensures that the waves decay far from the source. There is more rapid decay in the shorter waves ahead of the source than in the longer waves behind the source.

The deflection for the load speed $U = 40\,\mathrm{ms}^{-1}$ is shown in Figure 5.8, for $\tau = 0.1\,\mathrm{s}$. The deflection becomes more curved as the speed increases. In addition, the magnitude of the peaks in deflection increase for higher speeds. The waves directly ahead of the source seem to be most affected by the viscoelasticity and decay very quickly. The same short waves that propagate sideways away from the source do not decay as fast. Figures 5.6-5.8 are qualitatively similar to the figures presented in Milinazzo et al. (1995). The shape of the ice deflection and the behaviour for different speeds are the same. However, the present formulation includes viscous effects and hence the rate of decay is different to the graphs presented in Milinazzo et al. (1995).

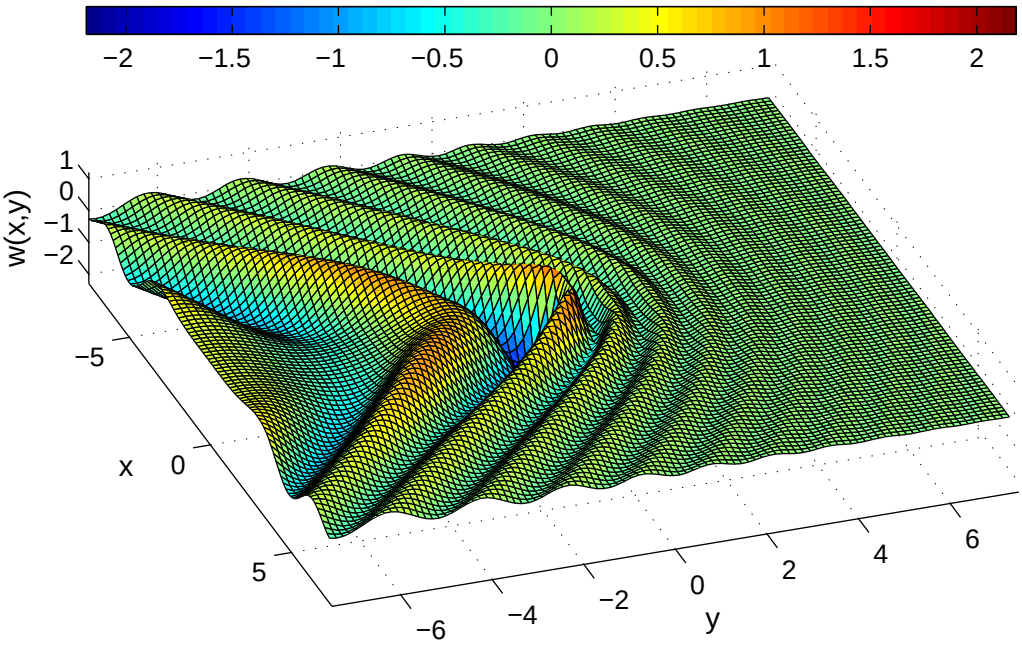

Figure 5.7: The deflection $w(x, y)$ is plotted against x and y. Here $U = 25\,\mathrm{ms}^{-1}$, $\tau = 0.1\,\mathrm{s}$, and other parameters are fixed at their default values.

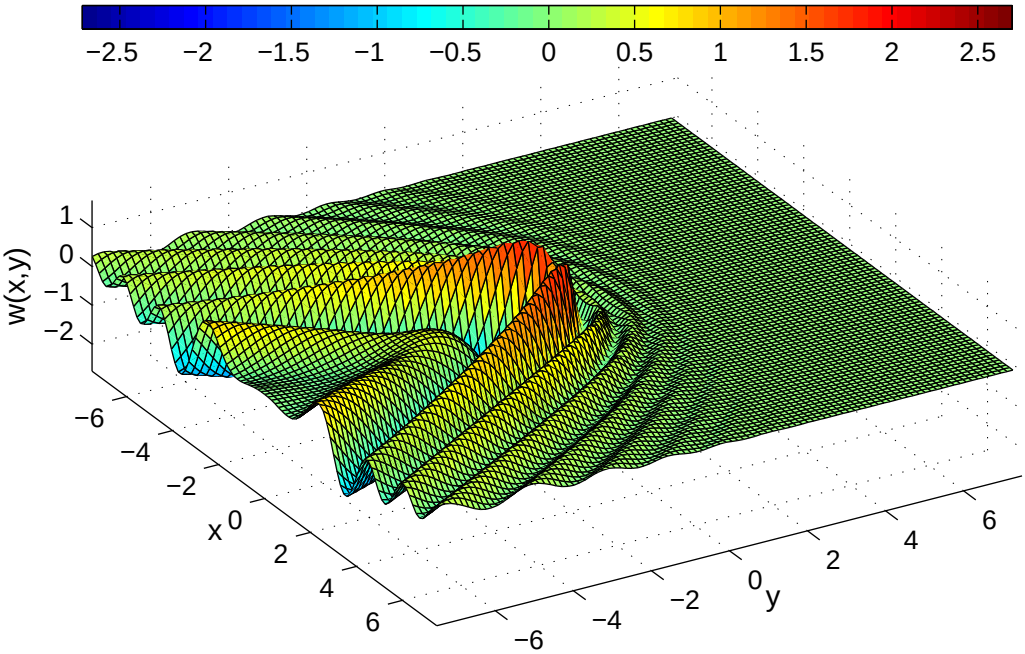

Figure 5.8: The deflection $w(x, y)$ is plotted against x and y. Here $U = 40\,\mathrm{ms}^{-1}$, $\tau = 0.1\,\mathrm{s}$, and other parameters are fixed at their default values.

5.3 Vertical wall case

5.3.1 Mathematical formulation: schematic and governing equations

With key ideas established for the formulation and solution methodology for hydroelastic problems involving moving loads, we proceed to the vertical wall formulation. The geometry of the problem and co-ordinate system are shown in Figure 5.9.

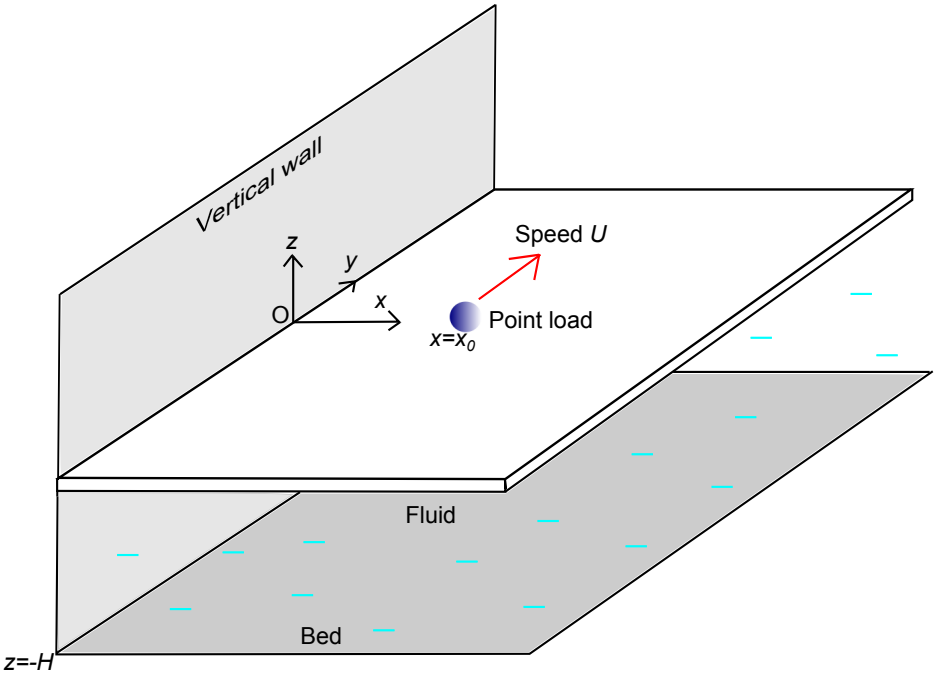

Figure 5.9: Schematic of a semi–infinite ice sheet meeting a vertical wall in three dimensions, with a load on the ice sheet moving parallel to the vertical wall.

Parameters defined for the open ice case in Section 5.2.1.1 are the same here. Note that it is convenient to move the origin so the vertical wall is at $x = 0$. The ice is fixed to the vertical wall. The load moves in the positive y direction, in a direction parallel to the vertical wall at a constant distance x_0 from the wall. The pressure due to the moving load hence becomes (in dimensional form):

$$P(x,y,t) = -\frac{m^V g}{H^2}\,\delta\Big(\frac{y-Ut}{H}\Big)\delta\Big(\frac{x-x_0}{H}\Big), \qquad (x>0,\ -\infty<y<\infty). \tag{5.37}$$

The dimensionless parameters remain the same as defined in Section 5.2.1.3, with the addition $x_0^* = x_0/H$. Following equation (5.10) from the previous section, in dimensionless form the pressure defined in equation (5.37) becomes

$$P^*(x^*,y^*,t^*) = -\delta(y^*)\delta(x^*-x_0^*), \qquad (x>0,\ -\infty<y<\infty). \tag{5.38}$$

We drop the asterisks and the variables are henceforth assumed dimensionless. We recap in full the governing equations that remain unchanged from (5.11)-(5.16), noting the change in the range of x:

$$\gamma\left(1-\tau\frac{\partial}{\partial y}\right)\nabla^4 w+\alpha w_{yy}+\beta w-\phi_y=-\delta(y)\delta(x-x_0),$$

$$(x>0,\ -\infty<y<\infty,\ z=0), \tag{5.39}$$

$$\nabla^2\phi=0, \quad (x>0,\ -\infty<y<\infty,\ -1\leq z\leq 0), \tag{5.40}$$

$$\phi_z=-w_y, \quad (z=0), \tag{5.41}$$

$$\phi_z=0, \quad (z=-1), \tag{5.42}$$

$$w,\to 0, \quad |x|,|y|\to\infty. \tag{5.43}$$

$$\phi\to 0, \quad |x|,|y|\to\infty. \tag{5.44}$$

In addition, there is a boundary condition ensuring no flow through the vertical wall at $x=0$:

$$\phi_x=0, \quad (x=0). \tag{5.45}$$

We also have two conditions along the wall owing to the ice clamping, given by

$$w=0, \quad (x=0), \tag{5.46}$$

$$w_x=0, \quad (x=0). \tag{5.47}$$

Equations (5.39)-(5.47) provide the dimensionless BVP to be solved, which is an extension of the BVP solved in Section 5.2 to include the effect of a vertical wall.

5.3.2 Solution by double Fourier transform

Unlike for the open ice case of Section 5.2, in the x direction we use a cosine Fourier transform due to the boundary conditions available and the range of x. Using ξ as the transform variable we define:

$$w^c(\xi,y)=\sqrt{\frac{2}{\pi}}\int_0^\infty w(x,y)\ \cos(\xi x)\,dx, \tag{5.48}$$

with inverse transform

$$w(x,y)=\sqrt{\frac{2}{\pi}}\int_0^\infty w^c(\xi,y)\,cos(\xi x)\,d\xi. \tag{5.49}$$

In the y direction we apply a standard Fourier transform, with transform variable η:

$$w^f(x,\eta)=\frac{1}{\sqrt{2\pi}}\int_{-\infty}^\infty w(x,y)\,e^{-i\eta y}\,dy. \tag{5.50}$$

with inverse transform

$$w(x,y)=\frac{1}{\sqrt{2\pi}}\int_{-\infty}^\infty w^f(x,\eta)\,e^{i\eta y}\,d\eta. \tag{5.51}$$

We define the action of applying transform (5.48) to a general variable θ as $C(\theta)$. Similarly the application of transform (5.50) is defined as $F(\theta)$. We apply the Fourier transforms to the governing equations and boundary conditions (5.39)-(5.47). Firstly we seek to find an expression for $C(w_{xx})$ and $C(w_{xxxx})$. We have

$$\begin{aligned}
C(w_{xx}) &= \sqrt{\frac{2}{\pi}} \int_0^\infty w_{xx}(x,y)\ \cos(\xi x)\, dx \\
&= \sqrt{\frac{2}{\pi}} \left(\big(w_x \cos(\xi x)\big)_0^\infty + \xi \int_0^\infty w_x(x,y)\ \sin(\xi x)\, dx \right) \\
&= \sqrt{\frac{2}{\pi}} \Bigg(-w_x(0,y) + \xi \Big(\big(w \sin(\xi x)\big)_0^\infty \\
&\quad - \xi \int_0^\infty w(x,y)\ \cos(\xi x) \Big) \Bigg)\, dx \\
C(w_{xx}) &= -\sqrt{\frac{2}{\pi}}\, w_x(0,y) - \xi^2 w^c, \qquad (5.52)
\end{aligned}$$

where we have used equation (5.44). Redefining $g(x) = w_{xx}$ we can utilise (5.52) to write:

$$\begin{aligned}
C(g_{xx}) &= -\sqrt{\frac{2}{\pi}}\, g_x(0,y) - \xi^2 C(g) \\
&= -\sqrt{\frac{2}{\pi}}\, w_{xxx}(0,y) - \xi^2 \left(-\sqrt{\frac{2}{\pi}}\, w_x(0,y) - \xi^2 w^c \right), \\
C(w_{xxxx}) &= -\sqrt{\frac{2}{\pi}}\, w_{xxx}(0,y) + \xi^4 w^c, \qquad (5.53)
\end{aligned}$$

where we have used boundary condition (5.47).

5.3.2.1 Velocity potential

Using the formulae derived in the above subsection, we apply the transforms to Laplace's equation (5.40), given by

$$\phi_{xx} + \phi_{yy} + \phi_{zz} = 0.$$

Applying the cosine transform and using equation (5.52) we obtain

$$-\sqrt{\frac{2}{\pi}}\, \phi_x(0,y) - \xi^2 \phi + \phi^c_{yy} + \phi^c_{zz} = 0,$$

and using (5.45) we have $\phi_x(0,y) = 0$. We now apply the Fourier transform to give:

$$-\xi^2 \phi^{cf} - \eta^2 \phi^{cf} + \phi^{cf}_{zz} = 0.$$

Hence, the expression for ϕ^{cf} is identical as for the open ice Section 5.2.2.1, though the the velocity potentials would differ for each section after inverse transforms. The

velocity potential for the vertical wall case is therefore given by

$$\phi^{cf} = -i\eta\,\psi(z)\,w^{cf}, \tag{5.54}$$

where $\psi(z)$ is given by equation (5.27). As before, the transformed deflection w^{cf} is unknown at this point.

5.3.2.2 Plate deflection

We now apply the transforms to the left hand side of the plate equation (5.39), given by

$$\text{LHS} = \gamma\left(1 - \tau\frac{\partial}{\partial y}\right)(w_{xxxx} + 2w_{xxyy} + w_{yyyy}) + \alpha w_{yy} + \beta w - \phi_y.$$

Starting by applying the Fourier cosine transform (5.48), we obtain

$$C(\text{LHS}) = \gamma\left(1 - \tau\frac{\partial}{\partial y}\right)\left(-\sqrt{\frac{2}{\pi}}w_{xxx}(0,y) + \xi^4 w^c - 2\xi^2 w^c_{yy} + w^c_{yyyy}\right) + \alpha w^c_{yy}\beta w^c - \phi^c_y. \tag{5.55}$$

Applying the Fourier transform (5.50) to equation (5.55) gives

$$\begin{aligned} F(C(\text{LHS})) = \gamma(1 - \tau i\eta)&\left((\xi^4 + 2\eta^2\xi^2 + \eta^4)w^{cf} - \sqrt{\frac{2}{\pi}}\,w^f_{xxx}(0,y)\right) \\ &- \alpha\eta^2 w^{cf} + \beta w^{cf} - i\eta\phi_{cf}. \end{aligned}$$

We now apply both transforms to the right hand side of equation (5.39), starting with the cosine Fourier transform:

$$\begin{aligned} \text{RHS} &= -\delta(y)\delta(x - x_0), \\ C(\text{RHS}) &= -\sqrt{\frac{2}{\pi}}\,\delta(y)\int_0^\infty \delta(x - x_0)\cos(\xi x)\,dx \\ &= -\sqrt{\frac{2}{\pi}}\,\delta(y)\,\cos(\xi x_0), \end{aligned} \tag{5.56}$$

where we have used the sifting property of the Dirac delta function (Bracewell, 1999). Applying the Fourier transform to equation (5.56) gives

$$\begin{aligned} F(C(\text{RHS})) &= -\sqrt{\frac{2}{\pi}}\frac{1}{\sqrt{2\pi}}\cos(\xi x_0)\int_{-\infty}^{\infty}\delta(y)e^{-i\eta y}\,dy \\ &= -\frac{1}{\pi}\cos(\xi x_0). \end{aligned} \tag{5.57}$$

Combining the LHS and the RHS and substituting for ϕ^{cf} using equation (5.54), we arrive at

$$w^{cf} = \frac{\sqrt{\frac{2}{\pi}}(1 - i\eta\tau)\gamma w^f_{xxx}(0,\eta) - \frac{1}{\pi}\cos(\xi x_0)}{Q(\xi,\eta)}.$$

Here the function $Q(\xi,\eta)$ is defined as before (see equation 5.30).

We still have one unknown quantity, namely $w^f_{xxx}(0,y)$. Using boundary condition (5.46) and performing an inverse Fourier cosine transform using equation (5.49), we have

$$w(0,y) = \sqrt{\frac{2}{\pi}} \int_0^\infty w^c(\xi, y)\, d\xi = 0. \tag{5.58}$$

Equation (5.58) directly implies that

$$\int_0^\infty w^{cf}(\xi, \eta)\, d\xi = 0,$$

and we rearrange to obtain

$$\sqrt{\frac{2}{\pi}}(1 - i\eta\tau)\gamma w^f_{xxx}(0,y) = \frac{\int_0^\infty \cos(\xi x_0) Q^{-1}(\xi,\eta)\, d\xi}{\pi \int_0^\infty Q^{-1}(\xi,\eta)\, d\xi}. \tag{5.59}$$

Defining the right hand side of equation (5.59) as

$$L(\eta) = \frac{\int_0^\infty \cos(\xi x_0) Q^{-1}(\xi,\eta)\, d\xi}{\pi \int_0^\infty Q^{-1}(\xi,\eta)\, d\xi}, \tag{5.60}$$

we reach the final solution for the plate deflection, given by

$$w^{cf}(\xi,\eta) = \frac{L(\eta) - \frac{1}{\pi}\cos(\xi x_0)}{Q(\xi,\eta)}. \tag{5.61}$$

We arrive at $w(x,y)$ by performing two inverse transforms given by equations (5.49) and (5.51) on equation (5.61). We have

$$w(x,y) = \frac{1}{\pi} \int_0^\infty \left(\int_{-\infty}^\infty w^{cf} e^{i\eta y}\, d\eta \right) \cos(\xi x)\, d\xi, \tag{5.62}$$

which is the final solution for the deflection $w(x,y)$ for the vertical wall case.

5.3.2.3 Difficulties using the method of residues

In the previous Section 5.2, the integrals similar to those in (5.62) were evaluated using the method of residues. However, in the present problem, the integrand contains the function $L(\eta)$, which contains integrals with respect to ξ (see equation 5.60). These ξ integrals are difficult to calculate by the method of residues, due to the fact that the poles are harder to locate. Applying the method of residues would require calculation of $L(a_p + ib_p)$. Defining $\xi = c + id$, Figure 5.10 demonstrates the difficulties in this calculation. The infinite set of poles that were found on the imaginary axis for integrals with respect to η now have both imaginary and real parts, making them hard to calculate efficiently. In addition, there are now poles on the real axis which complicate the calculations.

Hence, in the interest of efficiency we are forced to proceed using standard integration techniques for the present problem.

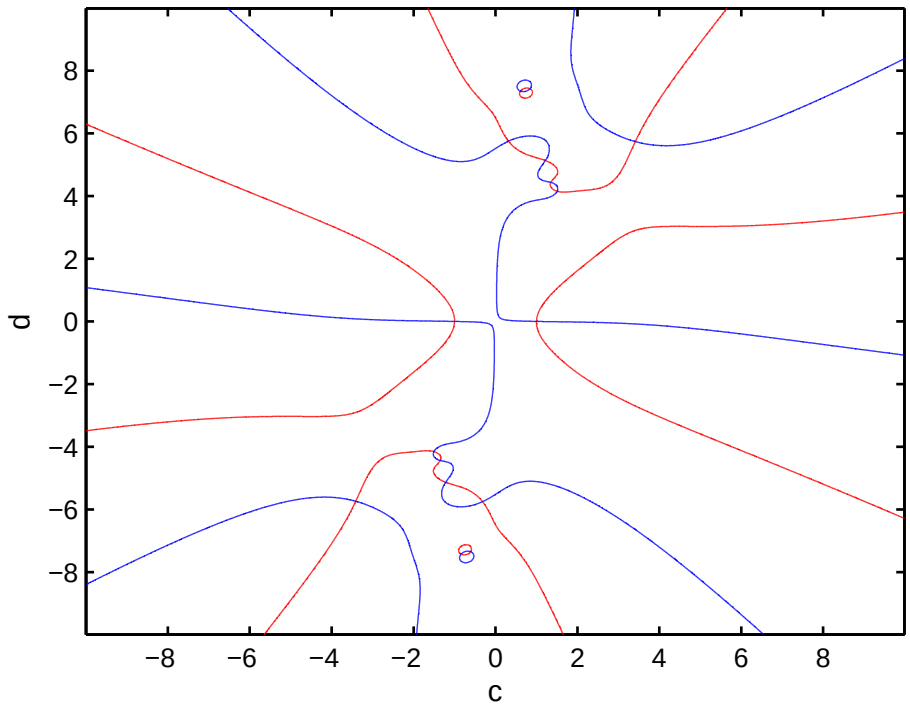

Figure 5.10: An example plot of the poles for integrals with respect to $\xi = c + id$. We again define $Q(\xi, \eta) = Q_R + iQ_I$. The red line ($Q_R = 0$) and blue line ($Q_I = 0$) intersect to show the location of the poles in the c-d plane. Here $\eta = a_p + ib_p$, where (a_p, b_p) is a pole for the $d\eta$ integral in equation (5.62).

5.3.2.4 Inverse transforms

Note that w^{cf} contains both an imaginary part and a real part. These can be resolved into

$$w^{cf} = w_R^{cf} + i\, w_I^{cf},$$

and by equation (5.62) we then have

$$w(x,y) = \frac{1}{\pi}\int_0^\infty \left(\int_{-\infty}^\infty \left(w_R^{cf}\cos(\eta y) - w_I^{cf}\sin(\eta y)\right) d\eta \right. \\ \left. + \; i\int_{-\infty}^\infty \left(w_R^{cf}\sin(\eta y) - w_I^{cf}\cos(\eta y)\right) d\eta \right) \cos(\xi x)\, d\xi. \tag{5.63}$$

Note that w_R^{cf} and cosine are even functions, whereas w_I^{cf} and sine are odd functions. The product of an even and an odd function is an odd function itself; hence, the imaginary integral in equation (5.63) has an odd integrand, and due to the symmetric limits this integral is equal to zero. The deflection $w(x, y)$ is therefore purely real.

For load speeds $U > c_{min}$, we have to be more careful in dealing with the integrals (5.62). The function Q has imaginary and real parts and can therefore be expressed as

$$Q(\xi, \eta) = Q_R(\xi, \eta) + i\, Q_I(\xi, \eta),$$

where

$$Q_R = \gamma(\xi^4 + 2\eta^2\xi^2 + \eta^4) + \beta - \alpha\eta^2 - \frac{\eta^2 \coth(\sqrt{\xi^2+\eta^2})}{\sqrt{\xi^2+\eta^2}}, \tag{5.64}$$

$$Q_I = -\eta\tau\gamma(\xi^4 + 2\eta^2\xi^2 + \eta^4). \tag{5.65}$$

For $U < c_{min}$ there are no solutions to the equation $Q_R = 0$. However, when $U > c_{min}$, there are values of ξ and η such that $Q_R = 0$. Figure 5.11 demonstrates this fact.

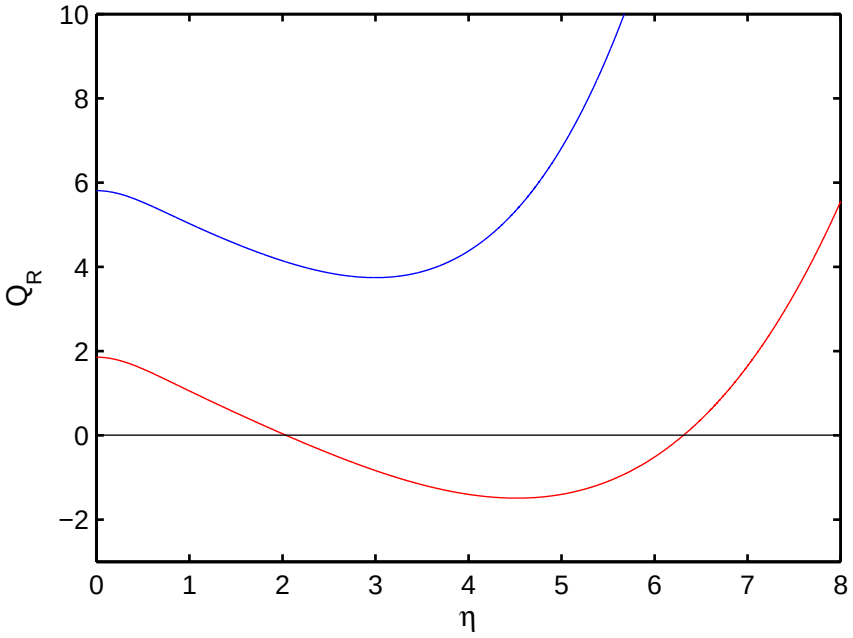

Figure 5.11: The function Q_R is plotted for $U = 13\,\mathrm{ms}^{-1}$ (blue) and $U = 23\,\mathrm{ms}^{-1}$ (red). Here ξ is fixed at $\xi = 1$. Recall that the critical speed c_{min} for the default data set is given by $c_{min} = 18.05\,\mathrm{ms}^{-1}$.

Recall that the factor $1/Q(\xi,\eta)$ appears frequently in the solution (5.61). Resolving into real and imaginary parts, we have

$$\frac{1}{Q} = \frac{Q_R}{Q_R^2 + Q_I^2} - i\,\frac{Q_I}{Q_R^2 + Q_I^2}. \tag{5.66}$$

Due to the fact that Q_I is usually small owing to its factor γ, the denominators in (5.66) are very small at the roots $Q_R = 0$. Hence, the functions $\Re(1/Q)$ and $\Im(1/Q)$ experience very sharp peaks of high magnitude for load speeds $U > c_{min}$, resulting from division by a very small number. This phenomenon is shown in Figure 5.12. Hence, the integrands involved in calculations of w^{cf} and the function $L(\eta)$ become increasingly difficult to evaluate as U grows or as the viscoelastic parameter $\tau \to 0$ (note that when the load speed is less than the critical speed, the integrands are smooth and well behaved). Special treatment of the integrals is required to accurately calculate their value. As ever, two concerns are numerical accuracy and numerical efficiency, and we seek to optimise both.

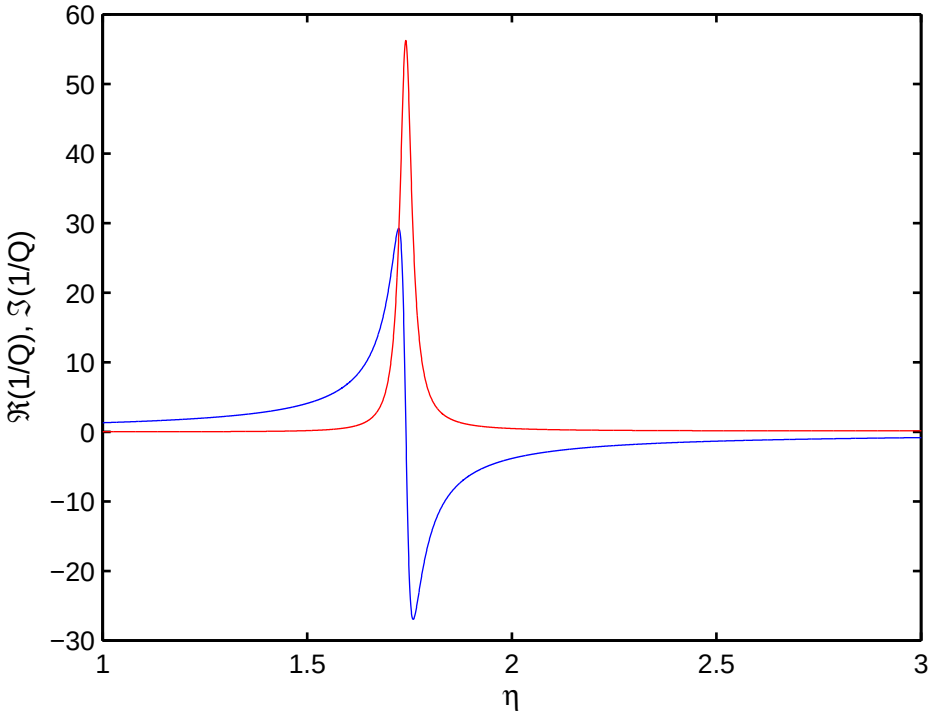

Figure 5.12: The real (blue line) and imaginary (red line) parts of $1/Q$ are plotted for fixed $\xi = 1$. Here $U = 25\,\mathrm{ms}^{-1}$ and $\tau = 1.0\,\mathrm{s}$.

The required integral with respect to η is given by equations (5.61) and (5.62):

$$I = \int_{-\infty}^{\infty} \frac{e^{i\eta y}\left(L(\eta) - \frac{1}{\pi}\cos(\xi x_0)\right)}{Q(\xi,\eta)}\, d\eta.$$

Calculation of the function $L(\eta)$ is achieved by integral subdivision. $L(\eta)$ involves integrals with respect to ξ and is given by equation (5.60). As an example, consider the denominator of L given by

$$L_D = \int_0^{\infty} Q^{-1}(\xi,\eta)\, d\xi.$$

For fixed η, there is either one or no roots to the equation $Q_R(\xi) = 0$ (depending on the value of η). Where a root exists, we define the critical value as $\hat{\xi}$ such that $Q_R(\hat{\xi}) = 0$. At this point, the integrand experiences a sharp peak, so for efficiency we subdivide the integral thus:

$$L_D = \int_0^{\hat{\xi}-\delta} Q^{-1}(\xi,\eta)\, d\xi + \int_{\hat{\xi}-\delta}^{\hat{\xi}+\delta} Q^{-1}(\xi,\eta)\, d\xi + \int_{\hat{\xi}+\delta}^{\infty} Q^{-1}(\xi,\eta)\, d\xi,$$

for a small parameter δ. In this way the function $L(\eta)$ can be calculated accurately. $L(\eta)$ is independent of x and y, and is therefore calculated at the beginning of the numerical procedure. It can then be called as needed rather than recalculated at each step.

To calculate I, we first define the location of the critical η values. For fixed ξ there are two roots to the equation $Q_R(\hat{\eta}) = 0$. The first of these roots is where the

integrand is most troublesome, and hence the integral is subdivided at $\hat{\eta}$ using the procedure outlined above. Combined with exploiting the symmetry of the integrand, these techniques allow the integrals to be calculated accurately whilst minimising the time of the computation.

5.3.3 Numerical results

Recall that the default parameters are given by Table 2.1(a) with $H = 100$ m. Parameters U, τ and x_0 will be varied frequently and are hence not given a default value but stated explicitly. For each $3D$ plot, the aspect ratio of x and y are kept equal for clarity. In each plot the colour bars are generated to have equal magnitude for depression and elevation for easy comparison. However, the colours are not consistent from plot to plot, and the scale should be consulted for each plot independently. The characteristic length scale for the default parameter set is given by $\ell = 20.01$ m, which should be borne in mind when considering values of x_0, the distance from the wall.

We begin by analysing the deflection for $U < c_{min}$. Recall that for the default data set, $c_{min} = 18.05\,\mathrm{ms}^{-1}$. We then proceed to analyse the ice deflection for load speeds greater than c_{min}. The deflections for both the open ice case and vertical wall case are then directly compared. We then investigate the strains along the vertical wall, to determine whether the ice connection will be maintained, and if not, what factors most influence the ice fracture.

5.3.3.1 Deflection

(i): $U < c_{min}$

We begin by plotting the deflection for $\tau = 0.1$ s, $U = 10\,\mathrm{ms}^{-1}$, and $x_0 = 25$ m, shown in Figure 5.13.

Recall that $H = 100$ m and hence $x_0 = 25$ m corresponds to a load at $x = 0.25$, etc. This value of x_0 places the moving load quite close to the wall, and the speed U is less than the critical speed c_{min}. For the values of the parameters given, there is little wave elevation ahead or behind the moving load. The pattern of the depression caused by the moving load is distorted from being symmetric by the ice–clamping condition. The deflection and slope of the deflection are zero along the wall due to this condition.

We increase the load speed to $U = 15\,\mathrm{ms}^{-1}$. The wave pattern for this speed is shown in Figure 5.14.

We begin to see wave elevation ahead and behind the source. Due to the viscoelastic formulation, this elevation is not symmetric: the wave elevation is slightly higher behind the load than ahead of it. The magnitude of the deflection is also considerably higher for this increased speed. Also, the depression caused by the load increases in area as the load speed increases.

We now move the load further away from the vertical wall, taking $x_0 = 75$ m,

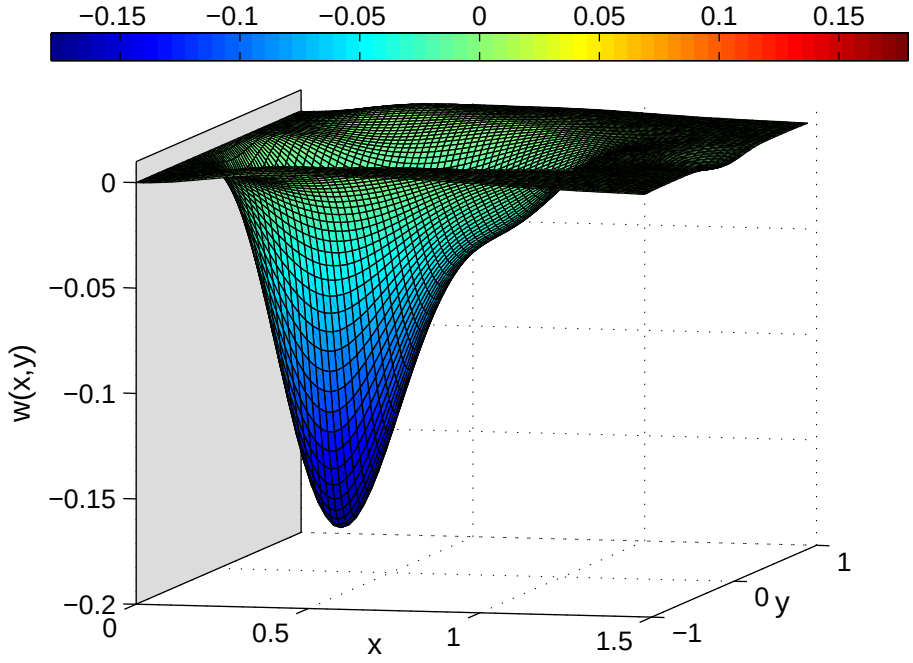

Figure 5.13: The deflection $w(x, y)$ is plotted against x and y. Here $\tau = 0.1$ s, $U = 10\,\mathrm{ms}^{-1}$, $x_0 = 25$ m.

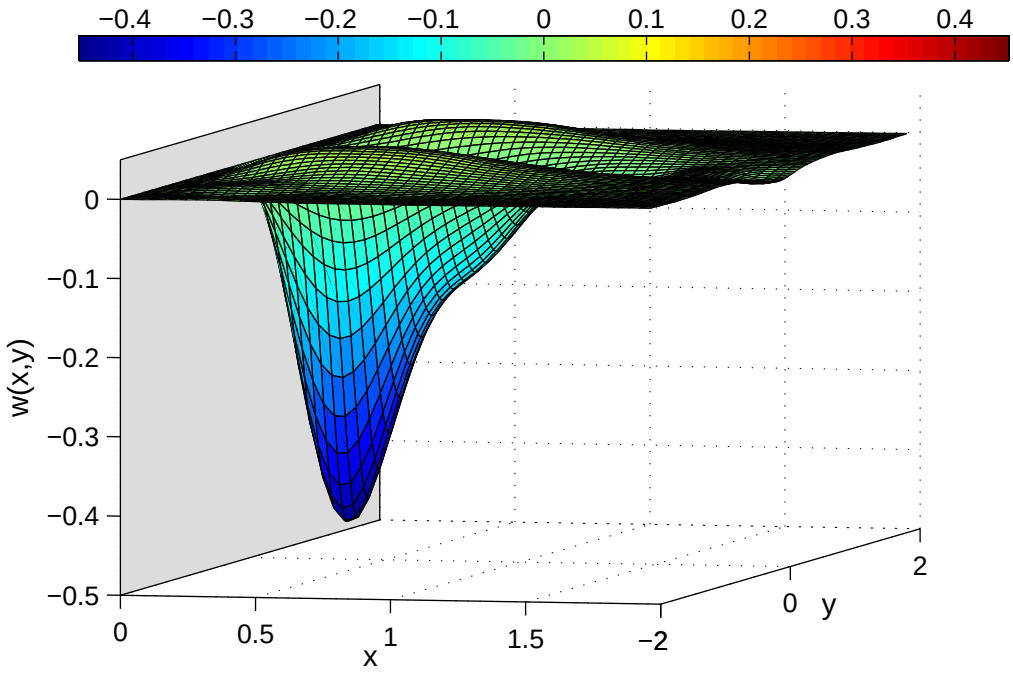

Figure 5.14: The deflection $w(x, y)$ is plotted against x and y. Here $\tau = 0.1$ s, $U = 15\,\mathrm{ms}^{-1}$, $x_0 = 25$ m.

retaining the same speed as before ($U = 15\,\mathrm{ms}^{-1}$). The resulting deflection is plotted in Figure 5.15. The wave elevation before and after the source are now seen more

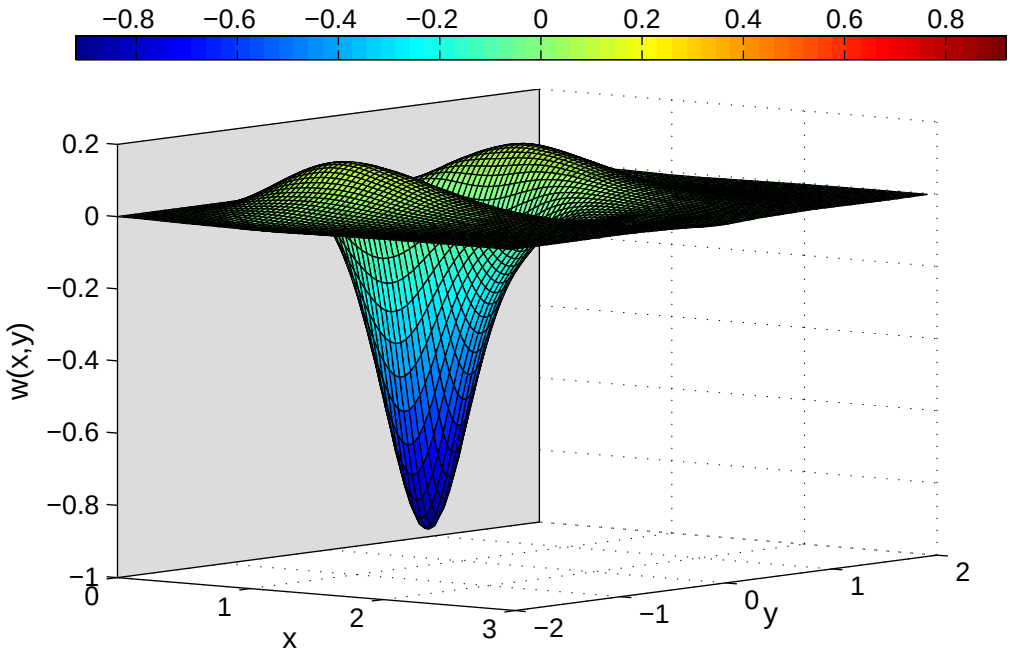

Figure 5.15: The deflection $w(x, y)$ is plotted against x and y. Here $\tau = 0.1$ s, $U = 15\,\mathrm{ms}^{-1}$, $x_0 = 75$ m.

clearly. In addition the magnitude of the depression due to the load has doubled. We also see that the pattern of deflection along the line $y = 0$ is close to symmetric, implying that the vertical wall has little effect at this distance from the source (between 3ℓ and 4ℓ factors of the characteristic length for the particular parameters under consideration).

It is clear that the distance of the source from the vertical wall affects both the shape and magnitude of the deflection pattern. Loads moving closer to the wall have smaller deflections, due to the restriction of the ice–clamping condition. However, it is expected that there will be higher strain values closer to the wall.

We now investigate the effect of changes in the viscoelastic parameter τ. Figure 5.16 shows the deflection for the value $\tau = 0.5$ s.

The speed has been increased to $U = 18\,\mathrm{ms}^{-1}$, slightly smaller than the critical speed c_{min}, and the distance from the wall is $x_0 = 100$ m. At this increased speed, the wave elevation peaks are now larger, and are closer in magnitude to the wave depression. We see that the response ahead of the source is smaller than the response behind the source, owing to the increased relaxation time; the same effect was observed by Hosking et al. (1988). In addition, increased relaxation times cause the position of maximum deflection to lag slightly behind the load. These effects are more apparent when comparing directly the centre lines through $x = x_0$. This is shown in Figure 5.17.

A similar graph is shown in Figure 5.18. The centre lines of the deflection are shown for various load speeds U for direct comparison. As expected, faster load

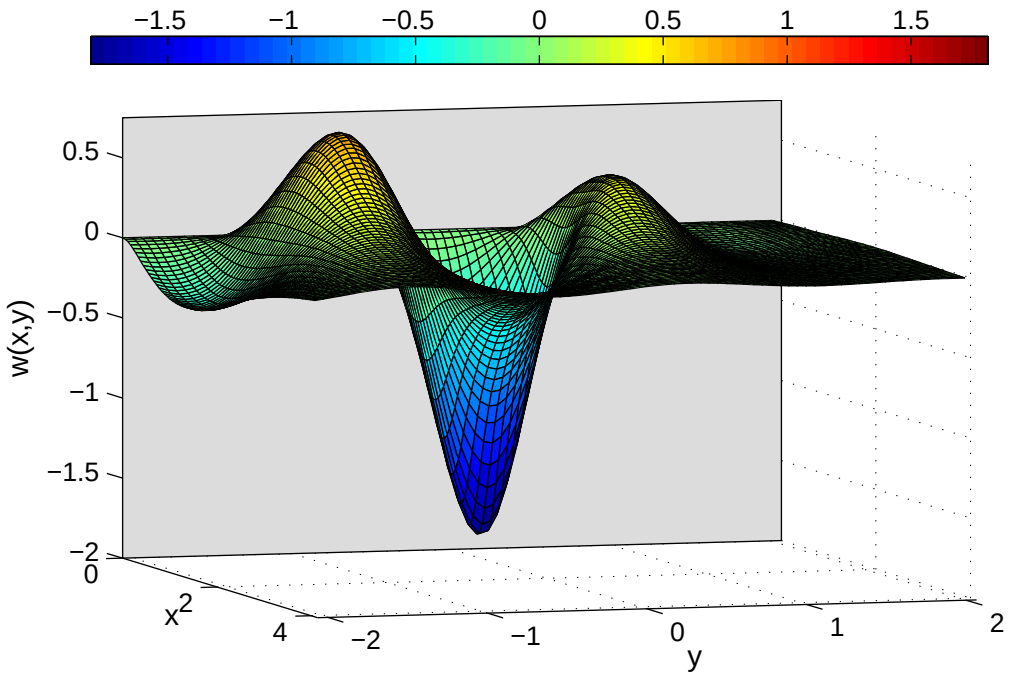

Figure 5.16: The deflection $w(x, y)$ is plotted against x and y. Here $\tau = 0.5\,\mathrm{s}$, $U = 18\,\mathrm{ms}^{-1}$, $x_0 = 100\,\mathrm{m}$.

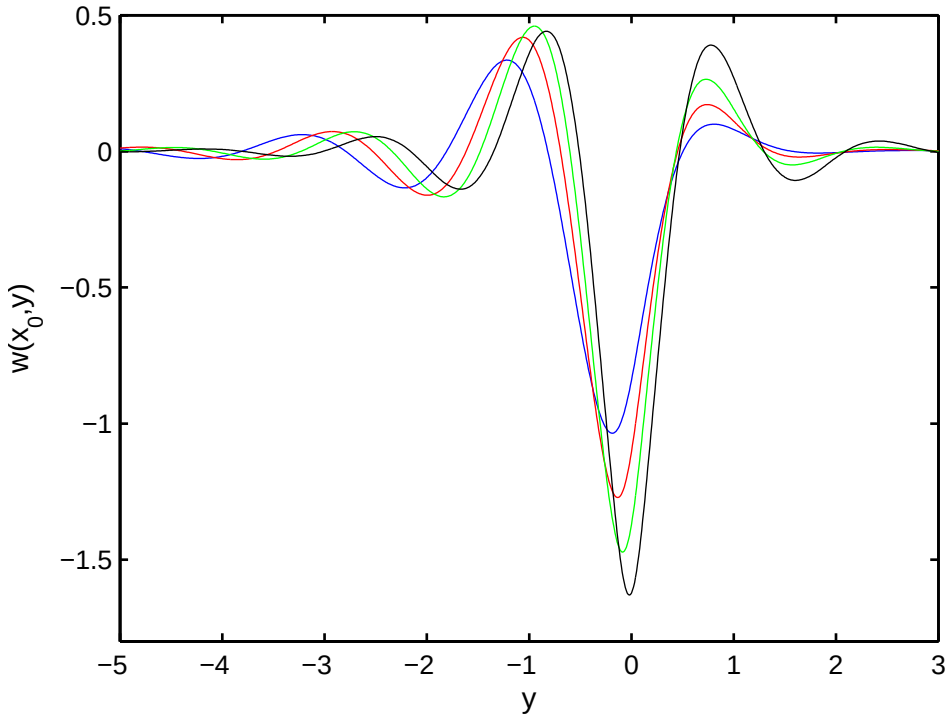

Figure 5.17: The deflection $w(x, y)$ through $x = x_0$ is plotted against y. Here $x_0 = 200\,\mathrm{m}$, $U = 17\,\mathrm{ms}^{-1}$. Relaxation time τ is given by: $\tau = 2.0\,\mathrm{s}$ (blue), $\tau = 1.0\,\mathrm{s}$ (red), $\tau = 0.5\,\mathrm{s}$ (green), $\tau = 0.1\,\mathrm{s}$ (black).

speeds incite higher surface response. The load speed U is more important than τ in deciding how fast the waves decay far behind the load.

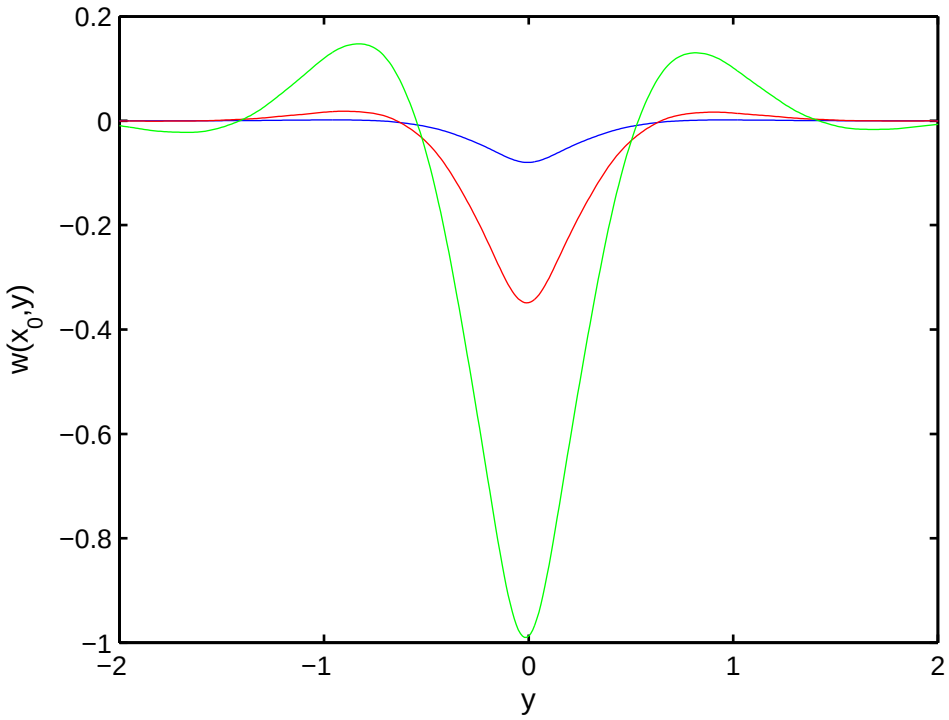

Figure 5.18: The deflection $w(x, y)$ through $x = x_0$ is plotted against y. Here $x_0 = 200$ m, and $\tau = 0.1$ s . The load speed U is given by: $U = 5\,\mathrm{ms}^{-1}$ (blue), $U = 10\,\mathrm{ms}^{-1}$ (red), $U = 15\,\mathrm{ms}^{-1}$ (green).

We have seen that for load speeds $U < c_{min}$ the shape and magnitude of the deflection depend sensitively on three parameters; the distance from the wall, the load speed and the relaxation time τ. We now proceed to investigate speeds $U > c_{min}$.

(ii): $U > c_{min}$

Figure 5.19 shows the ice deflection for a load moving with speed $U = 20\,\mathrm{ms}^{-1}$. Here

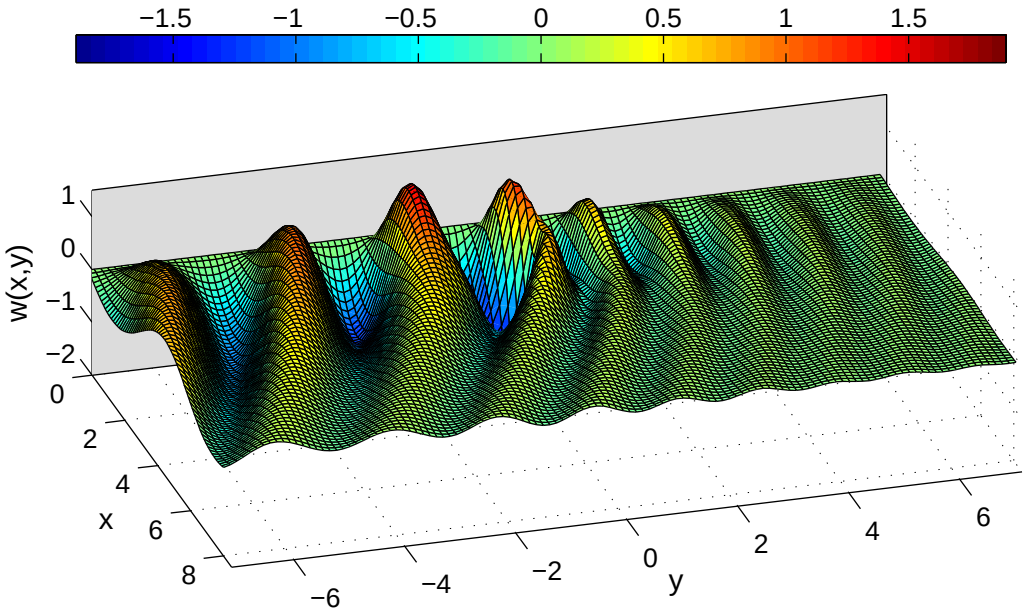

Figure 5.19: The deflection $w(x, y)$ plotted against x and y for the load speed $U = 20\,\mathrm{ms}^{-1}$, with $\tau = 0.1$ s and $x_0 = 200$ m.

the relaxation time is $\tau = 0.1$ s and the load is 200 m from the wall. We observe a drastic change in the deflection pattern; the waves decay much slower and propagate further from the source. In addition the waves are no longer straight but are curved, both ahead and behind the source. There is strong interaction with the vertical wall despite the increased distance x_0. As we are quite close to the critical speed c_{min}, the waves ahead and behind the source have comparable wavelength, but the waves ahead of the source have slightly smaller wavelength.

Figure 5.20 shows the deflection for the load speed $U = 26\,\mathrm{ms}^{-1}$, with $\tau = 0.1$ s and $x_0 = 600$ m. Similar to the open ice case in Section 5.2, both wave modes are visible and the wave pattern is curved. The waves decay faster ahead of the source than behind the source as before. However, there is now a region between the vertical wall and the moving load where considerable disturbance is present. Recall that the graphs are for a moving frame of reference, moving with speed U. Hence the disturbance can be explained as standing waves trapped between the vertical wall and the wave source, the moving load.

Figure 5.21 shows the deflection for the load speed $U = 30\,\mathrm{ms}^{-1}$, with $\tau = 0.1$ s and $x_0 = 600$ m. The wave pattern becomes even more curved. The deflection is high at the point where the longer wave behind the load is close to the vertical wall. In a similar fashion as for the open ice case, we observe that the viscoelastic decay affects the waves ahead of the source more as U increases.

We now investigate the effect of τ for high load speeds. Figure 5.22 compares the deflection through the centre line $x = x_0$ for various values of τ. Here $x_0 = 400$ m and $U = 25\,\mathrm{ms}^{-1}$. The viscoelasticity strongly affects the shorter waves ahead of the source; for $\tau = 1.0$ s the waves decay almost immediately. Behind the source,

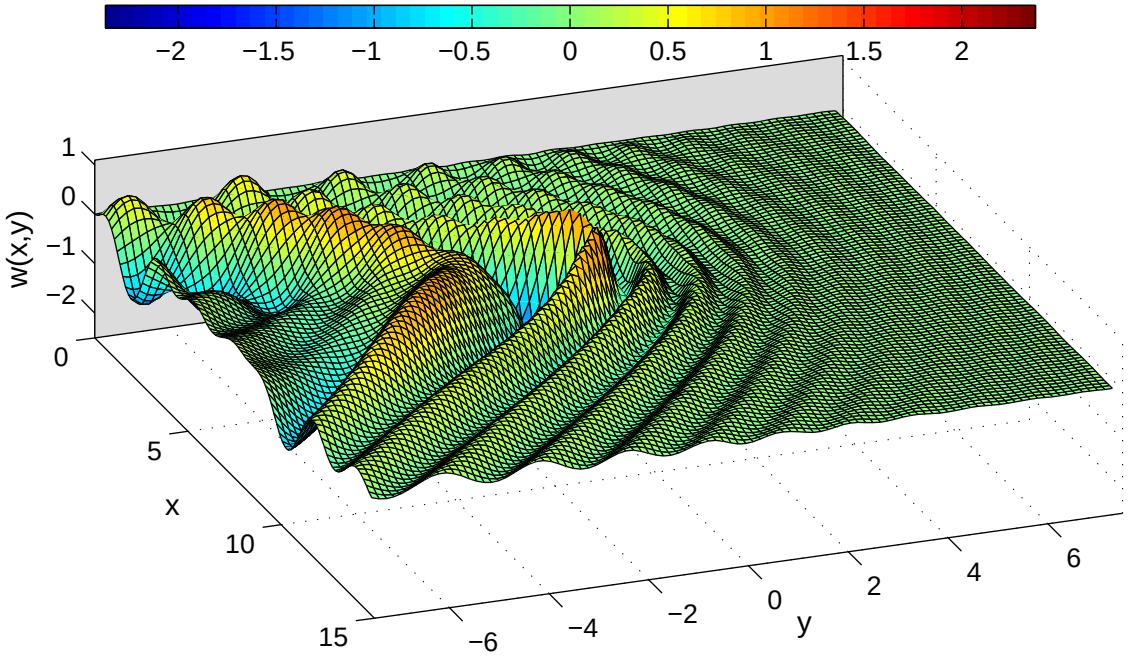

Figure 5.20: The deflection $w(x, y)$ plotted against x and y for the load speed $U = 26\,\mathrm{ms}^{-1}$, with $\tau = 0.1\,\mathrm{s}$ and $x_0 = 600\,\mathrm{m}$.

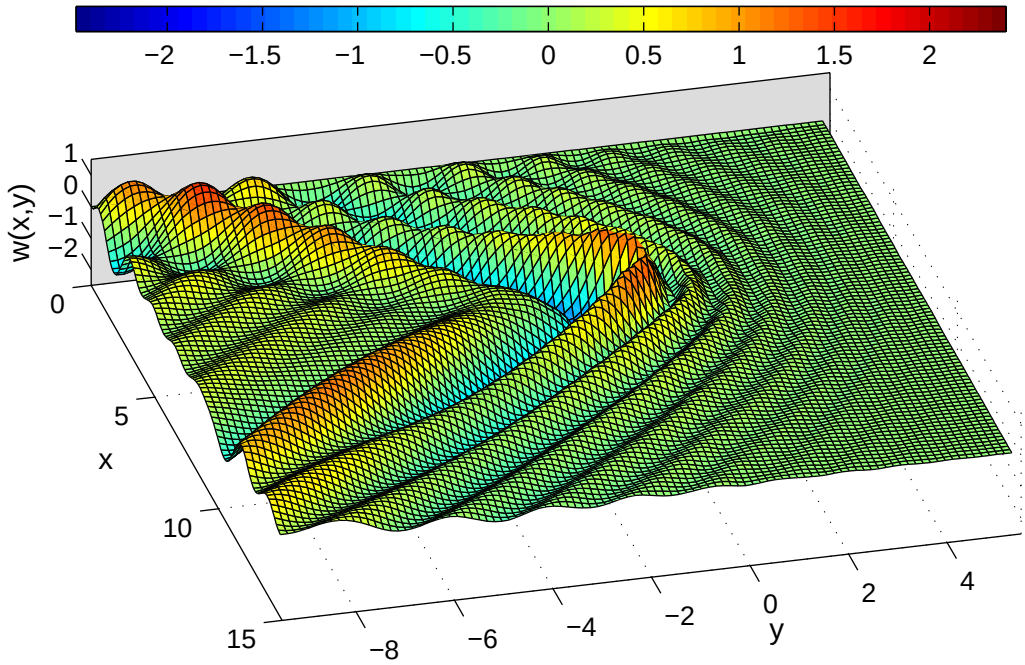

Figure 5.21: The deflection $w(x, y)$ plotted against x and y for the load speed $U = 30\,\mathrm{ms}^{-1}$, with $\tau = 0.1\,\mathrm{s}$ and $x_0 = 600\,\mathrm{m}$.

the deflections are similar for the $\tau = 0.5\,\mathrm{s}$ and $\tau = 1.0\,\mathrm{s}$ cases. However, for the $\tau = 0.1\,\mathrm{s}$ case, we see disturbances caused by the vertical wall. The magnitude of the largest deflection, directly behind the source, is almost unaffected by changes in τ.

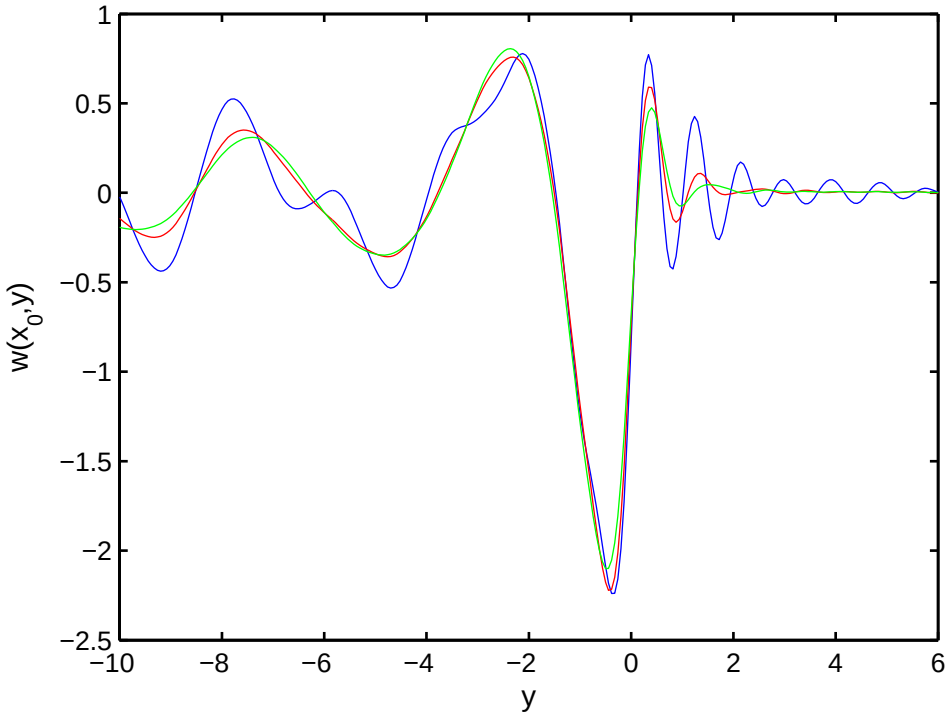

Figure 5.22: The deflection centre line $w(x_0, y)$ plotted against y for the load speed $U = 25\,\mathrm{ms}^{-1}$, and $x_0 = 400\,\mathrm{m}$. Here the relaxation time is given by $\tau = 0.1\,\mathrm{s}$ (blue), $\tau = 0.5\,\mathrm{s}$ (red), $\tau = 1.0\,\mathrm{s}$ (green).

Finally we investigate the deflection for a load moving with high speed closer to the vertical wall, $x_0 = 200\,\mathrm{m}$. This is shown in Figure 5.23. In this case the longer waves behind the source propagate away from the wall and, due to their altered angle, begin to merge with the shorter waves.

We now plot the maximum deflection $|w(x, y)|$ as a function of U in the vicinity of the critical speed $c_{min} = 18.05\,\mathrm{ms}^{-1}$. The maximum depression always occurs directly behind the moving load. To begin we take $x_0 = 50\,\mathrm{m}$: the result is shown in Figure 5.24. Note that we plot the dimensional deflection, due to the fact that U appears in the dimensionless expression for w. Here, we take a mass $m^V = 2000\,\mathrm{kg}$ to represent a large car or truck moving along the ice. The relaxation time τ is varied. We see that the peak deflection occurs $2-3\,\mathrm{ms}^{-1}$ higher than the calculated minimum speed in the elastic limit, c_{min}.

Given that the peak of each curve moves farther away from c_{min} as τ increases, it is plausible to suppose that viscoelasticity is partially responsible for this shift. Indeed, without viscoelasticity, the deflection would become unbounded precisely at the value $U = c_{min}$. However, even for $\tau = 0.1\,\mathrm{s}$ there is significant shift, suggesting another factor. It is likely that the close proximity to the wall is causing this lag, a suspicion confirmed in Figure 5.25.

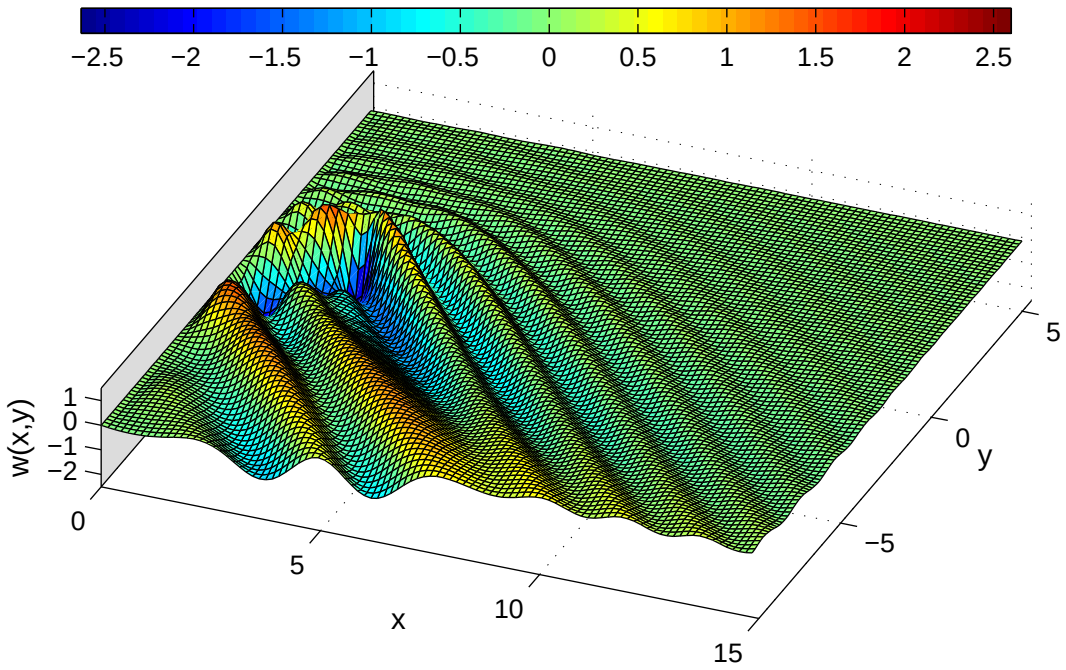

Figure 5.23: The deflection $w(x, y)$ plotted against y for the load speed $U = 30\,\mathrm{ms}^{-1}$. Here $\tau = 0.1$ s and $x_0 = 200$ m.

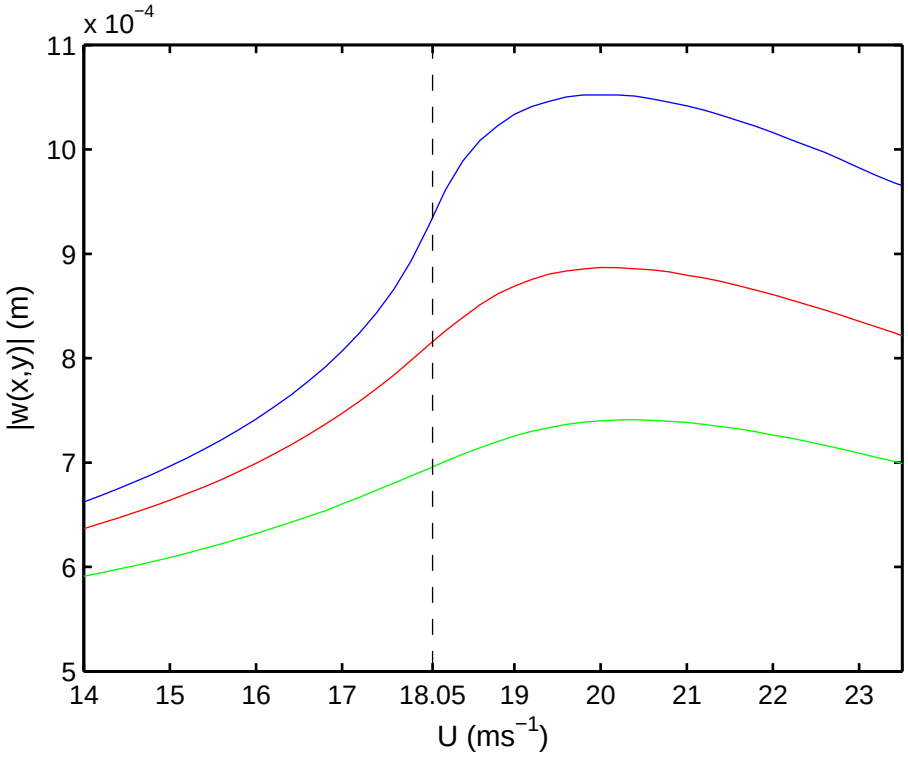

Figure 5.24: The maximum deflection $|w(x, y)|$ is plotted against the load speed U, for $\tau = 0.1$ s (blue), $\tau = 0.5$ s (red) and $\tau = 1.0$ s (green). Here $x_0 = 50$ m.

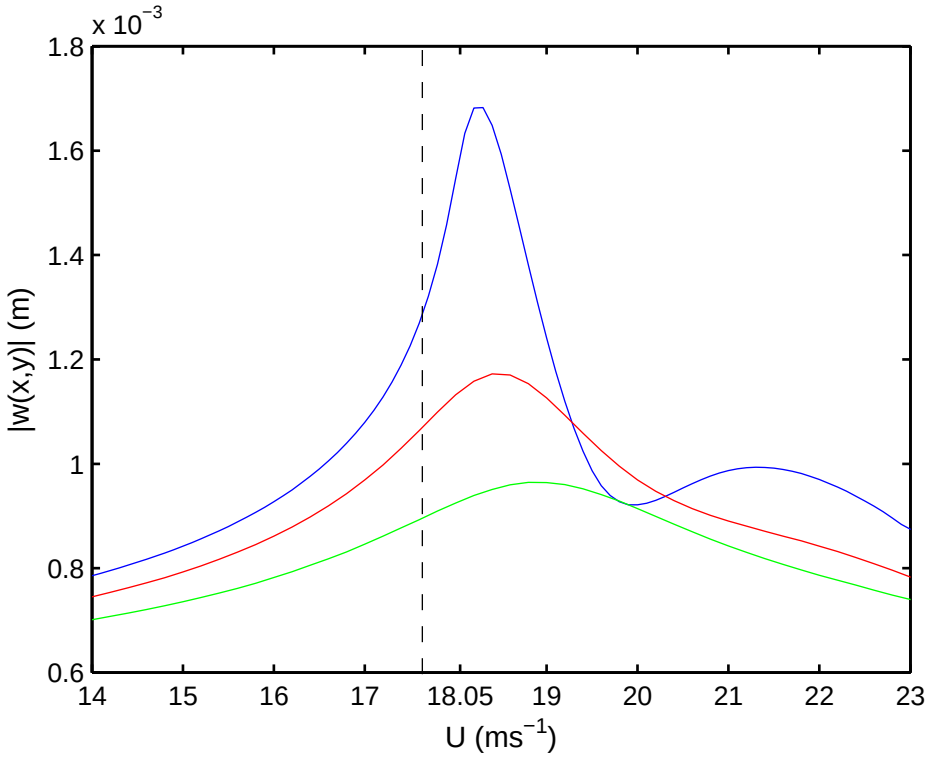

Figure 5.25: The maximum deflection $|w(x, y)|$ is plotted against the load speed U, for $\tau = 0.1$ s (blue), $\tau = 0.5$ s (red) and $\tau = 1.0$ s (green). Here $x_0 = 200$ m.

Figure 5.25 repeats the graph of Figure 5.24 for a distance further away from the wall, $x_0 = 200$ m. At this larger value of x_0 the effect of the critical speed more prevalent for $\tau = 0.1$ s; the peak of the deflection for this curve is much larger and sharper. There is interesting behaviour above the critical speed for this value of τ, where the maximum deflection has a local maximum and a local minimum. This is likely due to the influence of the vertical wall and the specific parameters chosen.

5.3.3.2 Strain in the ice sheet

We now calculate the strain in the ice sheet at the point of contact with the vertical wall. Since the ice is fixed to the wall at $x = 0$, we expect the strain to be highest at this point (see Brocklehurst et al., 2010). The strain in the x direction is given in dimensionless form as

$$\varepsilon_x = -\frac{\chi}{2}\frac{\partial^2 w}{\partial x^2},$$

where the dimensionless coefficient χ is given by

$$\chi = \frac{hm^V g}{\rho U^2 H^3}. \tag{5.67}$$

From previous chapters, we retain our estimate of the yield strain of ice to be $\varepsilon_{cr} = 8 \text{ x } 10^{-5}$, the critical strain beyond which the ice is more likely to fracture. We will investigate the strain along the wall under variation of the parameters U, x_0 and τ to estimate the conditions under which the ice-wall connection will break. We note that the strain ε_x has a linear dependence on the mass of the vehicle m^V.

We begin by investigating the strain for the default data set of Table 2.1(a) with $H = 100$ m. We choose the parameters $U = 17\,\mathrm{ms}^{-1}$, $\tau = 0.1$ s and $x_0 = 50$ m. In addition we take $m^V = 2000$ kg to represent a heavy car or truck. The strain is plotted along the line $x = 0$ and is shown in Figure 5.26. We see that despite the

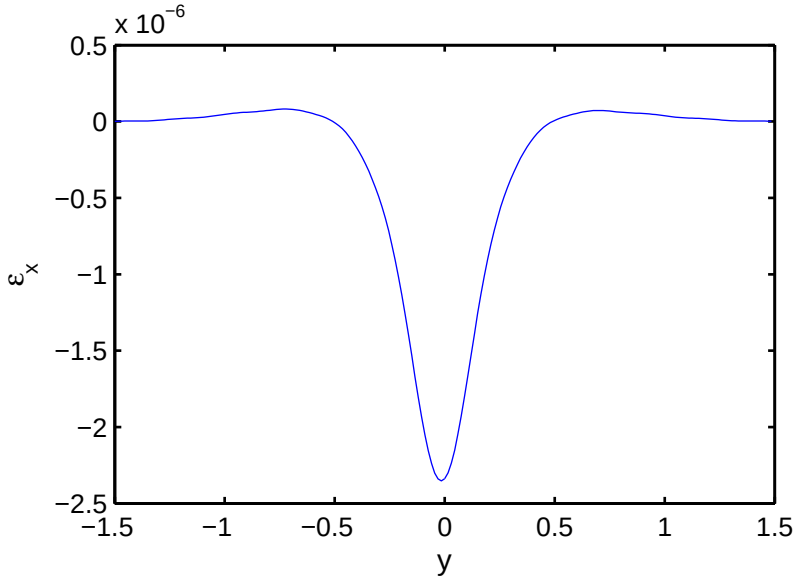

Figure 5.26: The strain ε_x is plotted against y along the line $x = 0$. Here $\tau = 0.1$ s, $x_0 = 50$ m, $U = 17\,\mathrm{ms}^{-1}$ and $m^V = 2000$ kg. Other parameters are taken from Table 2.1(a) with $H = 100$ m.

heavy load moving quite close to the vertical wall, the strain is still well below its critical value (the maximum strain here being 2.4×10^{-6}), predicting that the ice is likely to remain frozen to the wall under these conditions. This is due to the fact that the ice thickness $h = 1.6$ m is large enough to support very heavy loads.

With the proposed applications discussed in Section 1.6 in mind, the data set of Takizawa (1985) seems more appropriate. Taken from experiments on Lake Saroma, Japan, this data set is characterised by shallower water ($H = 6.8$ m) and thinner ice ($h = 0.175$ m) than the McMurdo Sound set. The full set of parameters is found in Table 2.1(b). The critical speed for this data set is calculated numerically as $c_{min} = 5.98\,\mathrm{ms}^{-1}$ and the characteristic length $\ell = 2.23$ m. Takizawa (1985) was driving a skidoo of weight $m^V = 235$ kg and investigating the waves incited by this moving load.

The strain along the wall for the new data set is found in Figure 5.27. Here $\tau = 0.1$ s, $U = 5\,\mathrm{ms}^{-1}$ and the distance from the wall x_0 is varied from $2.5 - 7.5$ m. As expected, the strain is highest when the moving load is closest to the vertical wall. For $x_0 = 2.5$ m the strain is beyond the yield strain $\varepsilon_{cr} = 8 \times 10^{-5}$, suggesting that the ice connection is likely to fracture. The dependence on the distance x_0 proves quite sensitive, as seen by the strain for $x_0 = 7.5$ m having strain below the yield strain. There is a small lag from the position of the load to the position of maximum strain. As shown in (5.27) the distance x_0 does not affect this lag, implying another cause for this phenomenon.

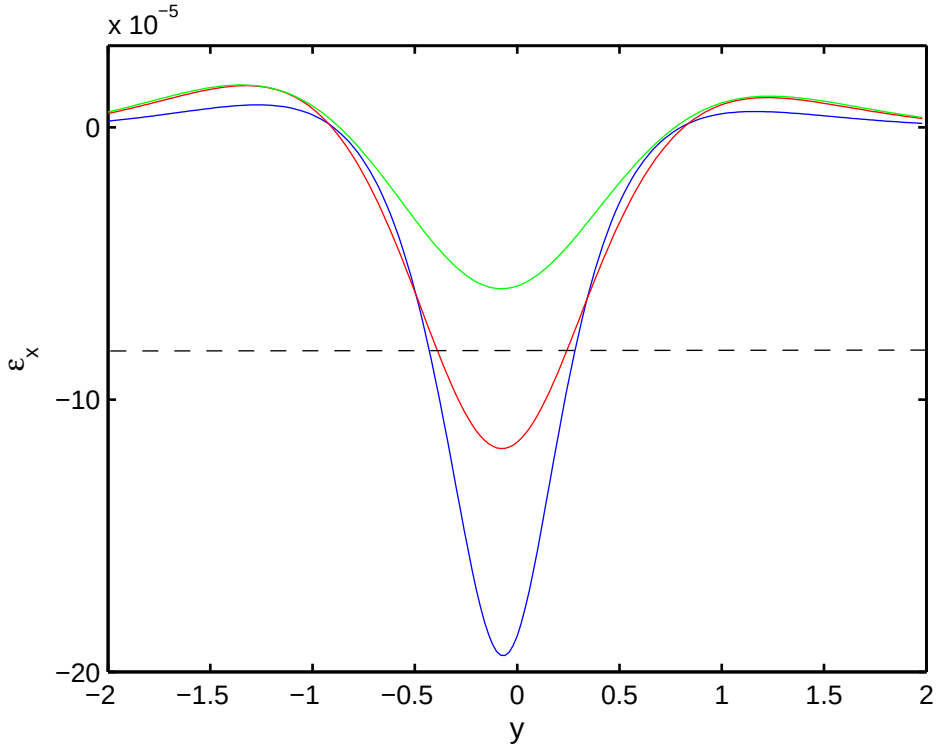

Figure 5.27: The strain ε_x is plotted against y along the line $x = 0$. Here $\tau = 0.1$ s, $U = 5$ ms^{-1} and $m^V = 235$ kg. The distance from the wall x_0 is given by 2.5 m (blue), 5 m (red) and 7.5 m (green). Other parameters are taken from Table 2.1(b). Here the dotted black line indicates the yield strain ε_{cr}.

Another important factor for deciding whether the ice will fracture is the amount of time that the ice is above its yield strain. If this proves to be a short time, it is conceivable that the ice connection may survive. Retaining starred variables for clarity, the time taken for the load to pass between two points y_1^* and y_2^* is

$$t = \frac{H(y_2^* - y_1^*)}{U}.$$

For Figure 5.27, we see that when $x_0 = 2.5$ m, the strain will be over its yield value for approximately 1 second. Although not large, given the peak magnitude of this strain, it is likely to be substantial enough to fracture the ice, though this is speculative.

Figure 5.28 varies the speed U to investigate its effect on the strain along the wall. The parameters are $\tau = 0.1$ s, $x_0 = 5$ m and U is varied from $3 - 5$ ms^{-1} (all of which are below the critical speed c_{min}). We see that faster load speeds cause more strain at the ice-wall connection, which is to be expected. However, the effect of varying U is not quite as profound as varying x_0 in terms of the magnitude of the strain. In all cases there is a small area close to $y = 0$ where the ice is likely to fracture for the parameter values considered.

We now investigate the effect of the relaxation time τ on the strain along the wall, shown in Figure 5.30. Parameters are set to $U = 5$ ms^{-1}, $x_0 = 5$ m, and τ is varied from $0.1 - 1.0$ s. We see that τ also affects the strain magnitude, with

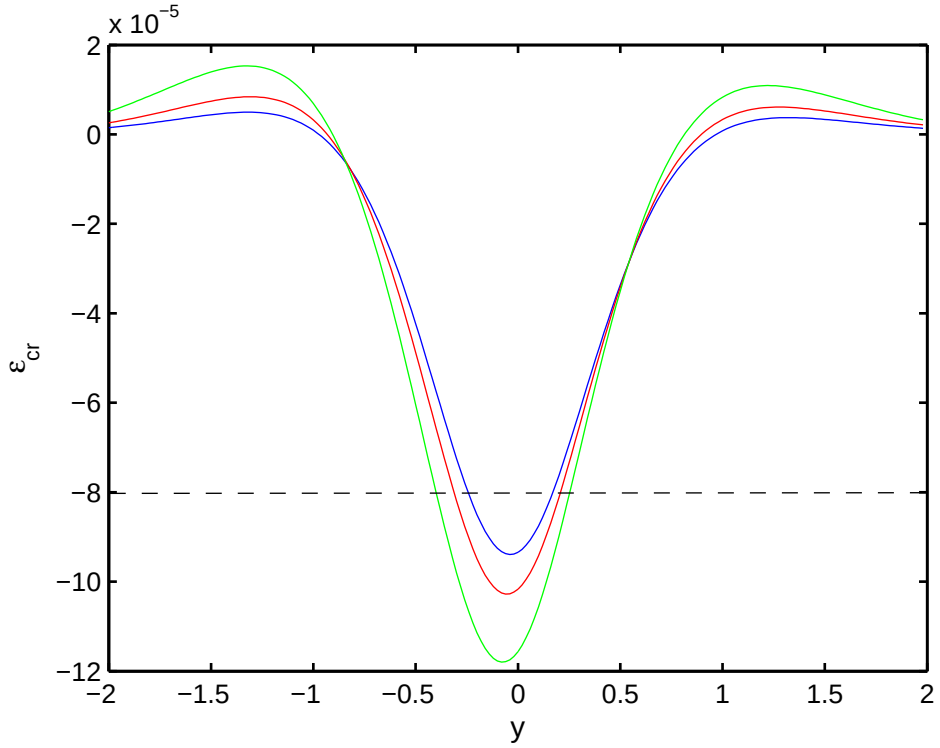

Figure 5.28: The strain ε_x is plotted against y along the line $x = 0$. Here $\tau = 0.1\,\mathrm{s}$, $x_0 = 5\,\mathrm{m}$ and $m^V = 235\,\mathrm{kg}$. The speed U of the moving load is given by $3\,\mathrm{ms}^{-1}$ (blue), $4\,\mathrm{ms}^{-1}$ (red) and $5\,\mathrm{ms}^{-1}$ (green). Other parameters are taken from Table 2.1(b).

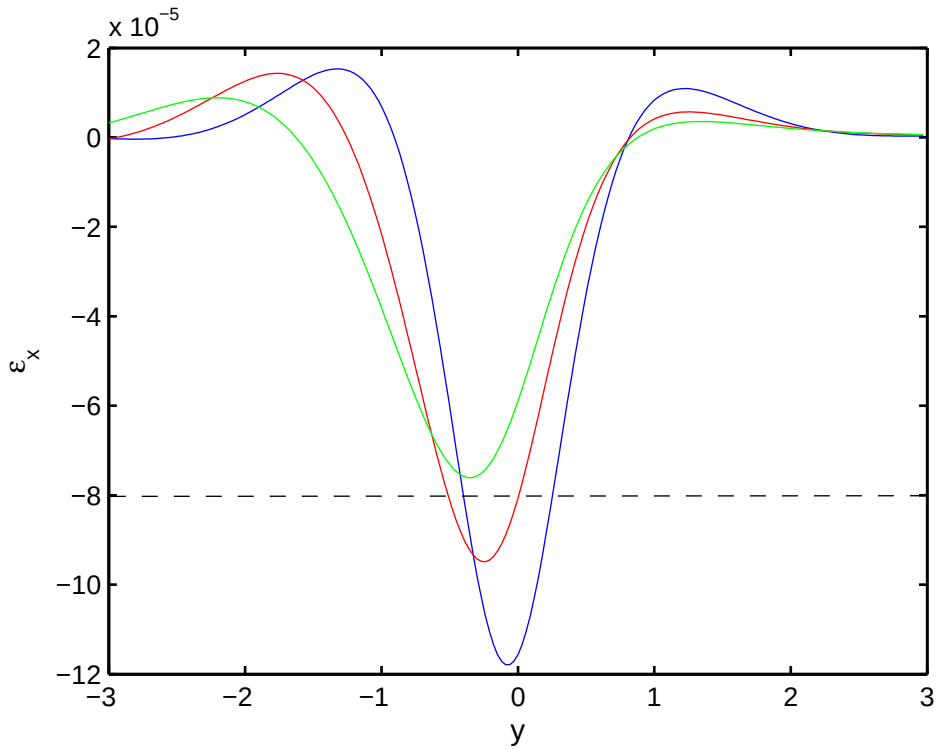

Figure 5.29: The strain ε_x is plotted against y along the line $x = 0$. Here $U = 5\mathrm{ms}^{-1}$, $x_0 = 5\,\mathrm{m}$ and $m^V = 235\,\mathrm{kg}$. The relaxation time τ of the ice is given by $0.1\,\mathrm{s}$ (blue), $0.5\,\mathrm{s}$ (red) and $1.0\,\mathrm{s}$ (green). Other parameters are taken from Table 2.1(b).

lower values of τ causing higher peaks in the strain. In addition, we see that the viscoelasticity is responsible for the lag between the load location $y = 0$ and the location of maximum strain. This is expected since other authors have speculated that the viscoelasticity was responsible for the lag effect in the deflection caused by the moving load (Hosking et al., 1988; Takizawa, 1985).

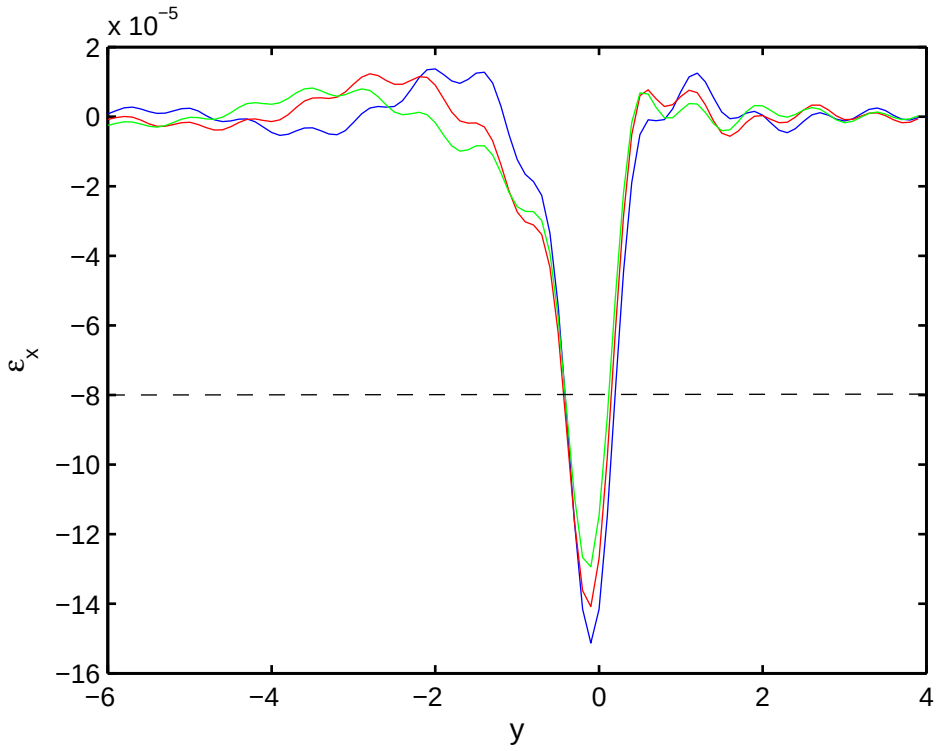

Figure 5.30: The strain ε_x is plotted against y along the line $x = 0$. Here $\tau = 0.1\,\text{s}$, $x_0 = 5\,\text{m}$ and $m^V = 235\,\text{kg}$. The load speed U of the moving load is given by $6.5\,\text{ms}^{-1}$ (blue), $7.5\,\text{ms}^{-1}$ (red) and $8.5\,\text{ms}^{-1}$ (green). Other parameters are taken from Table 2.1(b).

Figure 5.31 investigates the strain along the wall for speeds greater than the minimum speed $c_{min} = 5.98\,\text{ms}^{-1}$. Here, the other parameters are fixed as $\tau = 0.1\,\text{s}$, $x_0 = 10\,\text{m}$ and the load speed U varies between $6.5 - 8.5\,\text{ms}^{-1}$. In the vicinity of $y = 0$, the peaks in deflection are similar for each value of U. Even though x_0 is slightly higher than in the previous graphs, the strain has a higher magnitude and is likely to fracture the ice for the parameter values considered. However, we see that faster speeds cause slightly lower maximum strain. As the speed increases, we move further from the critical speed, at which the deflection (and hence strain along the wall) is highest. There is disturbance both ahead and behind the moving load. Ahead of the load we see the shorter waves that propagate ahead of the source as seen in Section 5.3.3.1. Shorter waves are also visible in the strain profile at the wall for $y < 0$: this is due to the curved wave profile for higher speeds. The longer wavelength is still visible but decays quickly.

We are also interested in the strain in the ice near the moving load. The strain along the line $y = 0$ is plotted in Figure 5.31. We see that the strain is above critical strain at the ice connection to the wall, but also above the critical strain

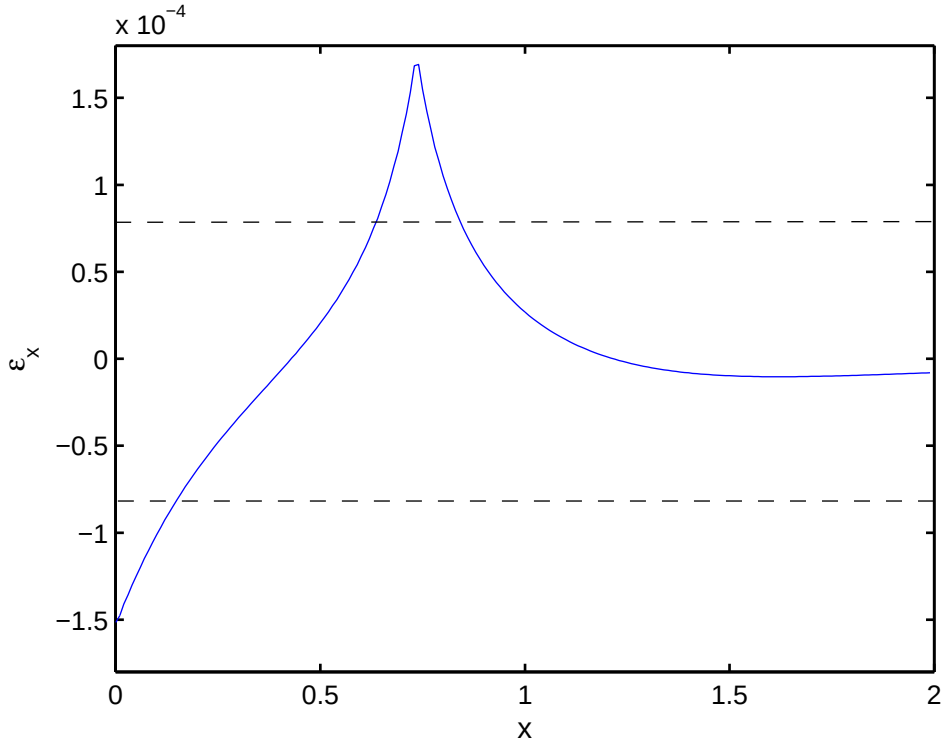

Figure 5.31: The strain ε_x is plotted against x along the line $y = 0$. Here $\tau = 0.1\,\mathrm{s}$, $x_0 = 5\,\mathrm{m}$ and $m^V = 235\,\mathrm{kg}$. The load speed is $U = 6.5\,\mathrm{ms}^{-1}$. Other parameters are taken from Table 2.1(b).

near the location of the load, $x = 0.735$. However, it is certain that the strain is over-estimated at this point due to the point-load formulation. The entirety of the mass is focused to one infinitesimally small point due to the nature of the Dirac delta function used to model the point load. In reality the load would be spread over an area which would dampen the strain at this point. Indeed, Takizawa (1985) has ridden a skiddoo of mass $m^V = 235\,\mathrm{kg}$ without any reported fracture.

5.3.4 Comparison between vertical wall and open ice case

We now compare directly the results from Sections (5.2) and (5.3); the open ice case and the vertical wall case. The deflection for each case is plotted in Figure 5.32 for a speed $U = 15\,\mathrm{ms}^{-1}$. As expected, the two cases are very similar, and are almost identical to the right of the load. For Figure 5.32(a) the presence of a vertical wall breaks the symmetry and also makes the deflection pattern slightly more circular near the vertical load.

This comparison is repeated in Figure 5.33 for a higher load speed $U = 25\,\mathrm{ms}^{-1}$. In this case, the differences are more profound. However, the region to the right of the moving load is still very similar to each other, indicating that for the value of x_0 considered, the influence of the vertical wall is confined mostly to the zone between the wall and the moving load.

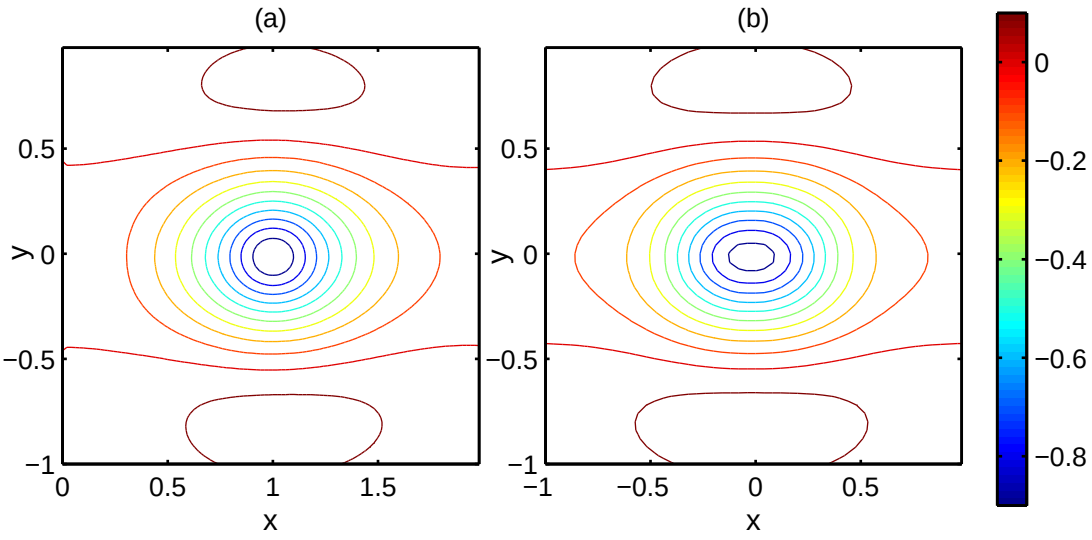

Figure 5.32: Contour plot for the ice deflection for comparison between (a) the vertical wall case and the (b) open ice case. Here $x_0 = 100\,\mathrm{m}$, $U = 15\,\mathrm{ms}^{-1}$ and $\tau = 0.1\,\mathrm{s}$.

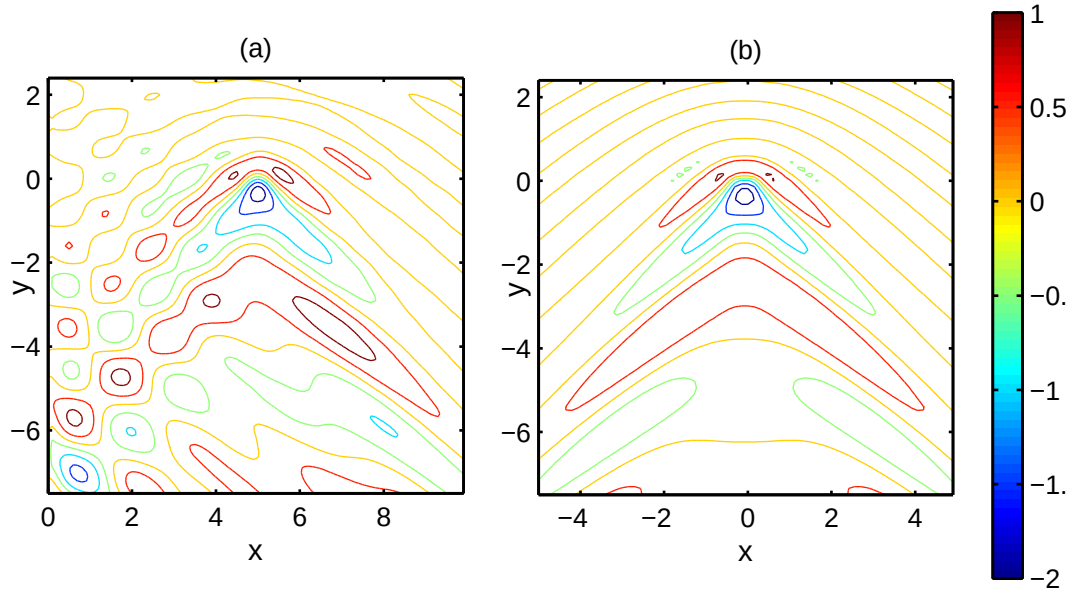

Figure 5.33: Contour plot for the ice deflection for comparison between (a) the vertical wall case and the (b) open ice case. Here $x_0 = 500\,\mathrm{m}$, $U = 25\,\mathrm{ms}^{-1}$ and $\tau = 0.1\,\mathrm{s}$.

5.4 Summary

The problem of a moving load on an ice sheet was solved within the linear theory of hydroelasticity, both in open ice and near a vertical wall. For the latter case, the ice was frozen to the vertical wall. The moving load incites a response in the ice sheet in the form of outgoing waves. In both cases a simple viscoelastic model was introduced, adding further realism to the formulation. Both cases were solved by applying Fourier transforms in the x and y directions along the plane of the ice sheet. For the open ice case, the resulting integral transforms were calculated using the method of residues and the application of the Cauchy residue theorem. For the vertical wall case, the integrals were solved by standard integration techniques and integrand subdivision. The deflection in the ice sheet was studied extensively under variation of important parameters. The strain in the ice sheet was studied, with particular attention to the strain along the vertical wall to assess whether the ice connection would be maintained.

For problems involving moving loads on ice sheets, there exists a critical speed c_{min}, corresponding to the minimum phase speed of hydroelastic waves. Ice has been proven experimentally to produce abnormally high deflections close to this critical speed. If the load moves at this speed, the viscoelastic formulation is necessary to find a bounded solution. The effect of viscoelasticity on the deflection at speeds $U = c_{min}$ was studied. In addition, whether the load moves at speed above or below this critical speed has a dramatic impact on the shape of the deflection pattern, and the decay of the waves in the far field. For slow load speeds, the waves are mostly localised. For speeds $U > c_{min}$, there are two visible sets of waves; faster waves ahead of the source that have smaller wavelength and are elastic-dominated, and slower waves behind the source that have a longer wavelength and are gravity-dominated.

The effect of a vertical wall on the ice deflection for slow load speeds is mostly dampening; if the load is close to the vertical wall, the magnitude of the ice response is smaller because of the restriction of the ice being frozen to the wall. For faster speeds, there is considerable interaction between the vertical wall and the generated waves, causing wave reflection and visible disturbance in the vicinity of the wall.

For slow load speeds, the viscoelasticity causes the response ahead of the moving load to become smaller than the response behind, whereas these would usually be symmetric in the elastic limit. In addition the viscoelasticity causes a lag between the moving load and the position of maximum deflection. For fast load speeds, the viscoelasticity affects the waves ahead of the source most profoundly, and the decay there is quite fast. Lower values of viscoelastic parameter τ markedly increase the disturbance in the wave pattern.

The strain along the wall was studied for both data sets in Table 2.1. For the parameter set from McMurdo Sound, we conclude that only a very heavy load moving very close to the vertical wall would produce enough strain to fracture the ice, due to the thickness of the ice in this data set. For the data from Lake Saroma,

a vehicle of mass $m^V = 235\,\mathrm{kg}$ could be enough to fracture the ice-wall connection, provided it is driven close enough to the vertical wall and at sufficient speed. The exact effect of the distance from the wall, the load speed and the viscoelasticity were studied in detail.

Chapter 6

Hydroelastic waves generated by a moving load in the vicinity of a vertical wall: nonlinear formulation

6.1 Introduction

We extend the model of Section 5.3 to consider nonlinear effects. A semi–infinite ice sheet meets a vertical wall, to which the ice is frozen. We investigate the effect of a load moving close to the wall. In this chapter the fluid is considered to be of infinite depth. This assumption is justified by the deep water of the default data set, for which we will be taking the data from McMurdo Sound, Table 2.1(a). Other features of the model are the same as the previous section; the fluid is incompressible, inviscid and irrotational flow is assumed. The load moves parallel to the wall, a constant distance from it, with constant velocity. The motion of the load generates hydroelastic waves which are studied in detail.

The model for the ice sheet is the same linear thin elastic plate model used in all previous chapters. However, we now consider fully nonlinear equations for the fluid flow beneath the plate. The nonlinear Bernoulli and kinematic conditions replace their linear counterparts. The introduction of this nonlinearity means that integral transforms used in the previous chapters cannot be used as the method of solution. Instead we utilise a boundary integral equation method, after application of Green's second identity using a suitable free-surface Green's function. The solution is then computed numerically using Newton's method. The method is based on work by Părău & Vanden-Broeck (2011) who solved the problem of hydroelastic waves due to a moving load without a vertical wall present. Their solution was in turn based on Forbes (1989) who developed a method to solve problems involving nonlinear free-surface flows.

Another change from the linear formulation of Chapter 5 is the definition of

the pressure. Instead of using the Dirac delta function which facilitated a solution by Fourier transform, we define the moving load by a simple exponential function acting over a designated compact region. This adds more realism to the model. As discussed in Chapter 5, the solution becomes unstable close to the critical speed c_{min} without dissipative effects. Hence, we introduce an artificial viscosity to the plate equation, following Părău et al. (2007).

We will analyse the pattern and magnitude of the ice deflection and compare the results with the corresponding linear formulation of Chapter 5. Section 6.2 outlines the mathematical formulation of the problem and introduces parameters. We then outline the boundary value problem to be solved. Section 6.3 demonstrates the method of solution. Numerical results are then presented and discussed in Section 6.4. A summary and conclusion of the chapter are given in Section 6.5.

6.2 Mathematical formulation

6.2.1 Schematic and parameters

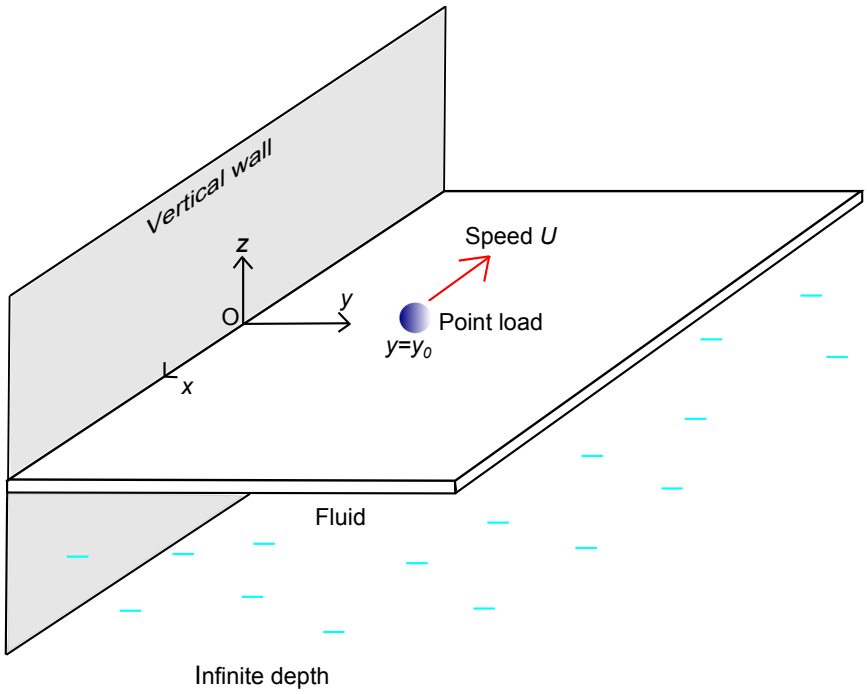

Figure 6.1: Schematic of a semi–infinite ice sheet meeting a vertical wall in three dimensions, with a load on the ice sheet moving parallel to the vertical wall. The fluid is of infinite depth.

The orientation of the axes as well as some of the definitions for the variables and parameters are redefined from Chapter 5 to align with the notation of Părău & Vanden-Broeck (2011). The geometry of the problem and co-ordinate system are shown in Figure 6.1. We introduce Cartesian coordinates with the origin located at the vertical wall. The vertical wall is along the line $y = 0$. The load moves in the negative x direction at a constant distance y_0 from the vertical wall. The z-axis is

directed vertically upwards, with the bottom of the unperturbed ice sheet at $z = 0$. The fluid has infinite depth. Time is denoted by t. The moving load is defined as an external pressure $P(x, y, t)$, and the pressure in the fluid is defined $p(x, y, z, t)$. The moving load has magnitude P_0 and is moving with speed U. The size of the support of the pressure is defined L. The density of the fluid is ρ. The fluid velocity $\mathbf{V}(x, y, z, t)$ is equal to the gradient of the velocity potential $\Phi(x, y, z, t)$, hence $\nabla\Phi = \mathbf{V}$. The vertical deflection of the ice sheet (the distance the ice sheet is displaced relative to its position at rest) is denoted by $w(x, y, t)$. The ice has mass per unit length M, where $M = \rho_i h$, ρ_i is the ice density and h is the ice thickness. The ice sheet has flexural rigidity EJ, where E is Young's modulus and $J = h^3/[12(1 - \nu^2)]$, where ν is Poisson's ratio. The acceleration due to gravity is denoted g. In addition we introduce the artificial viscosity μ, defined below.

6.2.2 Governing equations and boundary conditions

We now introduce nonlinear versions of the governing equations, as opposed to their linearised counterparts which have been used in the previous chapters. Note that we retain the linear elastic plate model, but the fluid is fully nonlinear. Due to this nonlinear model, the boundary conditions applied at the surface are applied at $z = w(x, y, t)$ instead of $z = 0$ as for the linear models.

The velocity potential $\Phi(x, y, z, t)$ must satisfy Laplace's equation in the fluid:

$$\nabla^2\Phi = 0, \quad (-\infty < x < \infty,\ 0 < y < \infty,\ -\infty < z < 0). \tag{6.1}$$

The plate equation is given by

$$EJ\nabla^4 w = p(x, y, z, t) + P(x, y, t), \quad (-\infty < x < \infty,\ 0 < y < \infty,\ z = 0). \tag{6.2}$$

Following Părău & Vanden-Broeck (2011) we neglect the inertia of the thin plate, and hence the acceleration term Mw_{tt} is not considered. According to Schulkes & Sneyd (1988), this is justified "provided the wavelength of the surface displacement is much larger than the ice thickness h. Since the water motion penetrates to a depth comparable with one wavelength, the inertia of the thin ice plate will then be small compared with that of the moving-water layer".

The nonlinear Bernoulli equation gives the pressure in the fluid as

$$p(x, y, z, t) = -\rho g z - \rho\Phi_t - \frac{\rho}{2}|\nabla\Phi|^2, \quad (-\infty < x < \infty,\ 0 < y < \infty). \tag{6.3}$$

The nonlinear kinematic condition is

$$w_t + \Phi_x w_x + \Phi_y w_y = \Phi_z, \quad (-\infty < x < \infty,\ 0 < y < \infty,\ z = w(x, y, t)). \tag{6.4}$$

Equations (6.2) and (6.3) combine to give the dynamic condition at the plate-fluid

interface:

$$\rho\Phi_t + \frac{\rho}{2}\left(\Phi_x^2 + \Phi_y^2 + \Phi_z^2\right) + \rho g w + EJ\nabla^4 w = P(x,y,t),$$
$$(-\infty < x < \infty,\ 0 < y < \infty,\ z = w(x,y,t)). \tag{6.5}$$

From Forbes (1989), when the free surface is described by $z = w(x,y,t)$, it is necessary to impose an upstream radiation condition:

$$w \to 0,\ |\nabla\Phi| \to 0, \quad (x \to -\infty). \tag{6.6}$$

We also have the condition of no flow through the vertical wall:

$$\Phi_y = 0, \quad (y = 0). \tag{6.7}$$

There is zero flow in the water far below the ice, so

$$|\nabla\Phi| \to 0, \quad (z \to -\infty). \tag{6.8}$$

The ice clamping gives two boundary conditions, namely

$$w = 0, \quad (y = 0), \tag{6.9}$$
$$w_y = 0, \quad (y = 0). \tag{6.10}$$

Equations (6.1)-(6.10) define the nonlinear boundary value problem to be solved.

6.2.3 Dispersion relation and critical speed

By linearising equations (6.1)-(6.10) and looking for waves of the form $e^{i(lx+my-\omega t)}$, we obtain the dispersion relation for infinite depth (Părău & Vanden-Broeck, 2011):

$$\omega^2 = gk + \frac{EJk^5}{\rho}, \tag{6.11}$$

where $k^2 = l^2 + m^2$. Note that this dispersion relation could also be derived from taking the limit $H \to \infty$ in the equation for the hydroelastic dispersion relation for finite depth (2.22), and neglecting the mass of the plate. The phase speed $c = \omega/k$ is therefore given by

$$c^2(k) = \frac{EJk^3}{\rho} + \frac{g}{k}.$$

By differentiating with respect to k and after some algebra, we obtain a concise expression for the minimum phase speed, given by

$$c_{min} = \sqrt{\frac{4}{3}}\left(\frac{3EJg^3}{\rho}\right)^{\frac{1}{8}}.$$

We note that for the data of Table 2.1(a) with infinite depth, the critical speed $c_{min} = 18.55\,\mathrm{ms}^{-1}$.

6.2.4 Nondimensionalisation & expression for the moving load

Recall that L is defined as the size of the support for the moving pressure. We use L as the length scale and the load speed U as the velocity scale. We also introduce a moving frame of reference, moving with speed U, noting that the load moves in the negative x direction. Hence we have

$$x^* = \frac{x+Ut}{L}, \quad y^* = \frac{y}{L}, \quad z^* = \frac{z}{L}, \quad t^* = \frac{Ut}{L}.$$

The dimensionless velocity potential and plate deflection are given by

$$\Phi^*(x^*, y^*, z^*) = \frac{\Phi(x, y, z, t) + Ux}{LU}, \quad w^* = \frac{w}{L}.$$

In terms of the new dimensionless moving frame, the derivatives are given by

$$\frac{\partial}{\partial t} = \frac{U}{L}\frac{\partial}{\partial x^*}, \quad \frac{\partial}{\partial x} = \frac{1}{L}\frac{\partial}{\partial x^*}, \quad \frac{\partial}{\partial y} = \frac{1}{L}\frac{\partial}{\partial y^*}, \quad \frac{\partial}{\partial z} = \frac{1}{L}\frac{\partial}{\partial z^*}.$$

Applying these changes to the kinematic condition and substituting $\Phi = LU\Phi^* - LU(x^* + t^*)$ and $w = Lw^*$ gives

$$\begin{aligned}&\frac{U}{L}\frac{\partial}{\partial x^*}\Big(Lw^*\Big) + \frac{1}{L^2}\frac{\partial}{\partial x^*}\Big(LU\Phi^* - LU(x^*+t^*)\Big)\frac{\partial}{\partial x^*}\Big(Lw^*\Big)\\ &+ \frac{1}{L^2}\frac{\partial}{\partial y^*}\Big(LU\Phi^* - LU(x^*+t^*)\Big)\frac{\partial}{\partial y^*}\Big(Lw^*\Big) = \frac{1}{L}\frac{\partial}{\partial z^*}\Big(LU\Phi^* - LU(x^*+t^*)\Big).\end{aligned}$$

Hence we have

$$\frac{\partial w^*}{\partial x^*} + \left(\frac{\partial \Phi^*}{\partial x^*} - 1\right)\frac{\partial w^*}{\partial x^*} + \frac{\partial \Phi^*}{\partial y^*}\frac{\partial w^*}{\partial y^*} = \frac{\partial \Phi^*}{\partial z^*},$$

and after cancellation the kinematic condition in dimensionless form is given by

$$\Phi^*_{x^*} w^*_{x^*} + \Phi^*_{y^*} w^*_{y^*} = \Phi^*_{z^*}. \tag{6.12}$$

We proceed to nondimensionalise the dynamic condition (6.5). Substituting for x^*, y^* and z^* we have:

$$-\frac{U\rho}{L}\Phi_{x^*} + \frac{\rho}{2L^2}\left(\Phi^2_{x^*} + \Phi^2_{y^*} + \Phi^2_{z^*}\right) + \rho g w + EJ\nabla^{*4} w = P.$$

We now substitute $\Phi = LU\Phi^* - LU(x^* + t^*)$, $w = Lw^*$ and $P = P_0 P^*$ (where P_0 is the magnitude of the moving pressure) to give

$$U^2\rho(\Phi^*_{x^*} - 1) + \frac{U^2\rho}{2}\left(\Phi^{*2}_{x^*} - 2\Phi^*_{x^*} + 1 + \Phi^{*2}_{y^*} + \Phi^{*2}_{z^*}\right) + \rho g L w^* + \frac{EJ}{L^3}\nabla^{*4} w^* = P_0 P^*.$$

Rearranging and dividing by $U^2\rho$ gives

$$\frac{1}{2}\left(|\nabla^{*2}\Phi^*|-1\right)+\frac{gL}{U^2}w^*+\frac{EJ}{U^2\rho L^3}\nabla^{*4}w^*=\frac{P_0}{\rho U^2}P^*.$$

This gives rise to several dimensionless parameters, namely

$$f_L=\frac{gL}{U^2},\quad \beta=\frac{EJ}{\rho U^2L^3},\quad \epsilon=\frac{P_0}{\rho U^2}.$$

To summarise, we drop the asterisks, and the dimensionless boundary value problem to be solved is:

$$\begin{aligned}
\nabla^2\Phi=0,\quad & (-\infty<x<\infty,\\
& 0<y<\infty,\ -\infty<z<0), && (6.13)\\
\Phi_x w_x+\Phi_y w_y=\Phi_z,\quad & (z=w(x,y)), && (6.14)\\
\frac{1}{2}\left(|\nabla^2\Phi|-1\right)+f_L w+\beta\nabla^4 w=\epsilon P,\quad & (z=w(x,y)), && (6.15)\\
(\Phi_x,\Phi_y,\Phi_z)\to(1,0,0),\quad & (z\to-\infty), && (6.16)\\
w\to 0,\ (\Phi_x,\Phi_y,\Phi_z)\to(1,0,0),\quad & (x\to-\infty) && (6.17)\\
\Phi_y=0,\quad & (y=0), && (6.18)\\
w=0,\quad & (y=0), && (6.19)\\
w_y=0,\quad & (y=0). && (6.20)
\end{aligned}$$

Here and in the rest of thesis, we have used the standard notation $(a,b,c)=a\mathbf{i}+b\mathbf{j}+c\mathbf{k}$ for scalars a, b and c. Vectors are indicated by bold font, and $\mathbf{i}$, $\mathbf{j}$ and $\mathbf{k}$ are the vectors in the x, y, and z direction respectively.

We now choose the form of the expression for the moving load. In dimensionless form, we take

$$P(x,y)=\begin{cases}-\exp\left(\dfrac{1}{x^2-1}+\dfrac{1}{(y-y_0)^2-1}\right), & |x|<1 \text{ and } |y-y_0|<1,\\ 0, & \text{otherwise,}\end{cases} \qquad (6.21)$$

with the negative sign indicating the *downwards* pressure. An illustration of this pressure distribution is found in Figure 6.2.

6.3 Solution

6.3.1 Green's second identity

We consider a general region V bounded by a surface S. We assume that throughout V the complex-valued functions α and β are twice continuously differentiable. Then,

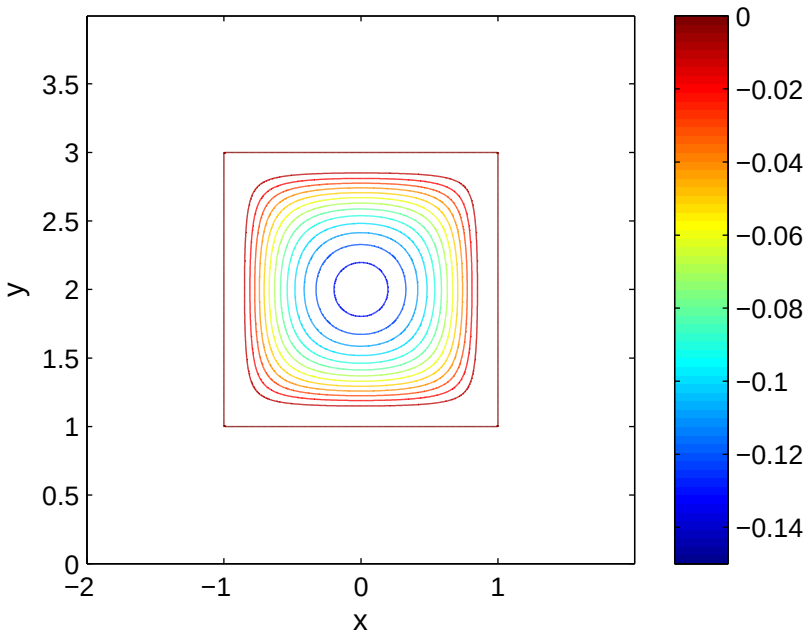

Figure 6.2: An illustration of the pressure distribution for $y_0 = 2$.

α and β must satisfy Green's second identity (Linton & McIver, 2001):

$$\iiint_V \left(\alpha\nabla^2\beta - \beta\nabla^2\alpha\right) dV = \iint_S \left(\alpha\frac{\partial\beta}{\partial\mathbf{n}} - \beta\frac{\partial\alpha}{\partial\mathbf{n}}\right) dS, \tag{6.22}$$

where $\mathbf{n}$ is the unit vector normal to the surface. The Green's function for the present problem is the linear combination of the three-dimensional free-space Green's function (Părău & Vanden-Broeck, 2011) plus its image in the y plane, to account for the vertical wall:

$$\begin{aligned} G(Q,\tilde{Q}) = &\frac{1}{4\pi\Big((x-\tilde{x})^2 + (y-\tilde{y})^2 + (z-\tilde{z})^2\Big)^{\frac{1}{2}}} \\ &+ \frac{1}{4\pi\Big((x-\tilde{x})^2 + (y+\tilde{y})^2 + (z-\tilde{z})^2\Big)^{\frac{1}{2}}}. \end{aligned} \tag{6.23}$$

The Green's function G is the linear sum of two fractions. In the first fraction, the denominator represents 4π multiplied by the distance between two points, $Q = (x, y, z)$ and $\tilde{Q} = (\tilde{x}, \tilde{y}, \tilde{z})$. The second fraction represents 4π multiplied by the image of the first fraction in the $y = 0$ plane. We substitute $G = \beta$ and $\Phi - x = \alpha$ into Green's second identity (6.22):

$$\iiint_V \left((\Phi - x)\nabla^2 G - G\nabla^2(\Phi - x)\right) dV = \iint_S \left((\Phi - x)\frac{\partial G}{\partial\mathbf{n}} - G\frac{\partial(\Phi - x)}{\partial\mathbf{n}}\right) dS. \tag{6.24}$$

G satisfies $\nabla^2 G = 0$, and by equation (6.13) we have $\nabla^2(\Phi - x) = \nabla^2(\Phi) = 0$. Hence, the left hand side of (6.24) is equal to zero.

For the application of Green's second identity to the present problem, we choose the region sketched in Figure 6.3. The region V consists of half of a large hemisphere

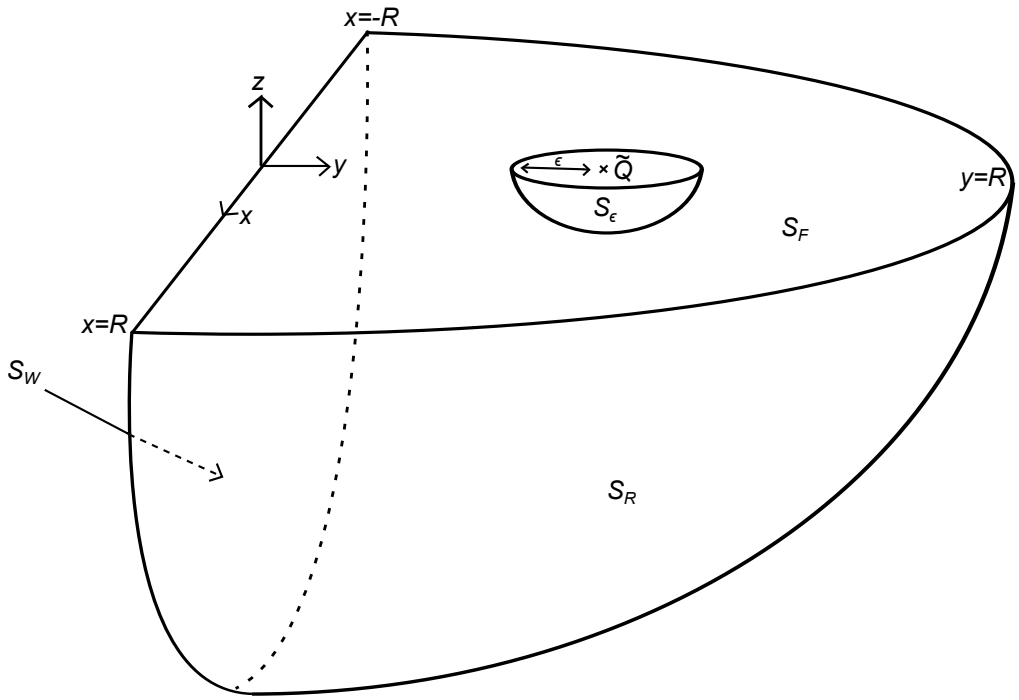

Figure 6.3: The region V for the application of Green's second identity.

of radius R centred around the origin, with a smaller hemisphere of radius ε centred at $\tilde{Q}$ excluded from the region. The large hemisphere is divided in half by the vertical wall along the line $y = 0$. The surface is bounded above by the ice sheet. The surface S therefore comprises 4 surfaces:

- S_W, the flat section which is the union of the vertical wall and the large hemisphere
- S_R, the circular surface of the large hemisphere
- S_ε, the circular surface of the small hemisphere around the point $\tilde{Q}$
- S_F, the ice-water interface.

Hence, we have

$$I = \iint_{S_W+S_R+S_\varepsilon+S_F} \left((\Phi - x)\frac{\partial G}{\partial \mathbf{n}} - G\frac{\partial(\Phi - x)}{\partial \mathbf{n}} \right) dS = 0. \tag{6.25}$$

We choose the unit normal $\mathbf{n}$ for each surface to point *into* the fluid.

The Green's function is designed such that it is singular at the point $\tilde{Q}$. For the application of Green's second identity, if $\tilde{Q}$ lies on or within S then it must be excluded from the domain V (Linton & McIver, 2001). As we will see, an expression for the velocity potential Φ at the point $\tilde{Q}$ can extracted by taking the limit $\varepsilon \to 0$ and $R \to \infty$. The point $\tilde{Q}$ can be moved arbitrarily to give Φ everywhere on the free surface.

6.3.2 Each surface integral evaluated

6.3.2.1 The surface S_W

We wish to calculate the calculation to the integral due to the surface S_W:

$$\iint_{S_W} \left((\Phi - x) \frac{\partial G}{\partial \mathbf{n}} - G \frac{\partial (\Phi - x)}{\partial \mathbf{n}} \right) \, dS. \tag{6.26}$$

For the surface S_W, the unit normal pointing into the fluid is given by $\mathbf{n} = \mathbf{j}$. We have

$$\begin{aligned} \frac{\partial G}{\partial \mathbf{n}} = \nabla(G).\mathbf{n} &= \left(\frac{\partial G}{\partial x} \frac{\partial G}{\partial y}, \frac{\partial G}{\partial z} \right).(0,1,0) \\ &= \frac{\partial G}{\partial y} \\ &= -\frac{1}{4\pi} \Big((x-\tilde{x})^2 + (y-\tilde{y})^2 + (z-\tilde{z})^2 \Big)^{-\frac{3}{2}} (y - \tilde{y}) \\ &\quad - \frac{1}{4\pi} \Big((x-\tilde{x})^2 + (y+\tilde{y})^2 + (z-\tilde{z})^2 \Big)^{-\frac{3}{2}} (y + \tilde{y}). \end{aligned}$$

On the vertical wall, $y = 0$, and hence we are left with

$$\frac{\partial G}{\partial \mathbf{n}} = (\tilde{y} - \tilde{y}) \Big((x-\tilde{x})^2 + \tilde{y}^2 + (z-\tilde{z})^2 \Big)^{-\frac{3}{2}} = 0. \tag{6.27}$$

Also,

$$\begin{aligned} \frac{\partial (\Phi - x)}{\partial \mathbf{n}} = \nabla(\Phi - x).\mathbf{n} &= \left(\frac{\partial (\Phi - x)}{\partial x}, \frac{\partial (\Phi - x)}{\partial y}, \frac{\partial (\Phi - x)}{\partial z} \right).(0,1,0) \\ &= \frac{\partial (\Phi - x)}{\partial y} = \frac{\partial \Phi}{\partial y}. \end{aligned} \tag{6.28}$$

By equation (6.7), $\Phi_y = 0$ when $y = 0$. Hence, the contribution to the integral I from the surface S_W is equal to zero.

6.3.2.2 The surface S_R

The required calculation is

$$\iint_{S_R} \left((\Phi - x) \frac{\partial G}{\partial \mathbf{n}} - G \frac{\partial (\Phi - x)}{\partial \mathbf{n}} \right) \, dS. \tag{6.29}$$

The equation for the large spherical surface S_R is given by

$$x^2 + y^2 + z^2 = R^2. \tag{6.30}$$

When a surface can be expressed in the form of a function $f = 0$, the unit normal vector $\mathbf{n}$ is (see for example Jeffrey, 2002):

$$\mathbf{n} = \frac{\nabla f}{|\nabla f|}. \tag{6.31}$$

In this case, since we require the inwardly oriented normal, we have

$$\mathbf{n} = \frac{\nabla(R^2 - x^2 - y^2 - z^2)}{|\nabla(R^2 - x^2 - y^2 - z^2)|} = \frac{(-2x, -2y, -2z)}{(4x^2 + 4y^2 + 4z^2)} = -\frac{1}{R}(x, y, z).$$

For the first term in the integral, we have

$$\begin{aligned}
\frac{\partial G}{\partial \mathbf{n}} &= \nabla(G).\mathbf{n} = \left(\frac{\partial G}{\partial x}, \frac{\partial G}{\partial y}, \frac{\partial G}{\partial z}\right).(x, y, z)\left(-\frac{1}{R}\right) \\
&= \frac{1}{4\pi R}\Big((x-\tilde{x})^2 + (y-\tilde{y})^2 + (z-\tilde{z})^2\Big)^{-\frac{3}{2}}\Big(x(x-\tilde{x}) + y(y-\tilde{y}) + z(z-\tilde{z})\Big) \\
&+ \frac{1}{4\pi R}\Big((x-\tilde{x})^2 + (y+\tilde{y})^2 + (z-\tilde{z})^2\Big)^{-\frac{3}{2}}\Big(x(x-\tilde{x}) + y(y+\tilde{y}) + z(z-\tilde{z})\Big).
\end{aligned}$$

We take the limit $R \to \infty$. In this limit, $\tilde{x}$, $\tilde{y}$ and $\tilde{z}$ are negligible in comparison with x, y, and z. Hence in the limit $R \to \infty$:

$$\begin{aligned}
\frac{\partial G}{\partial \mathbf{n}} &\sim \frac{1}{4\pi R}\Big((x)^2 + (y)^2 + (z)^2\Big)^{-\frac{3}{2}}\Big(x(x) + y(y) + z(z)\Big) \\
&\quad + \frac{1}{4\pi R}\Big((x)^2 + (y)^2 + (z)^2\Big)^{-\frac{3}{2}}\Big(x(x) + y(y) + z(z)\Big) \\
&= \frac{1}{4\pi R}\Big(R^2\Big)^{-\frac{3}{2}}R^2 + \frac{1}{4\pi R}\Big(R^2\Big)^{-\frac{3}{2}}R^2 \\
\frac{\partial G}{\partial \mathbf{n}} &= \frac{1}{2\pi}\frac{1}{R^2}.
\end{aligned} \tag{6.32}$$

Clearly equals zero in the limit $R \to \infty$.

For the second term in the required integral over S_R, we have

$$G\frac{\partial(\Phi - x)}{\partial \mathbf{n}} = G\nabla(\Phi - x).\mathbf{n} = G(\Phi_x - 1, \Phi_y, \Phi_z).(x, y, z)\left(-\frac{1}{R}\right). \tag{6.33}$$

In the limit $R \to \infty$, using the same argument as before, $G \sim (2\pi R)^{-1}$ and so we have

$$G\frac{\partial(\Phi - x)}{\partial \mathbf{n}} \sim -\frac{1}{2\pi}\frac{1}{R^2}\Big(x(\Phi_x - 1) + y\Phi_y + z\Phi_z\Big),$$

which tends to zero in the limit $R \to \infty$. Hence, the contribution to I from the surface S_R is zero.

6.3.2.3 The surface S_ε

We evaluate the integral over the surface S_ε:

$$\iint_{S_\varepsilon}\left((\Phi - x)\frac{\partial G}{\partial \mathbf{n}} - G\frac{\partial(\Phi - x)}{\partial \mathbf{n}}\right) dS. \tag{6.34}$$

The equation for this spherical surface centred around the point $\tilde{Q}$ is

$$\varepsilon^2 = (x-\tilde{x})^2 + (y-\tilde{y})^2 + (z-\tilde{z})^2,$$

and the normal pointing into the fluid is given by

$$\mathbf{n} = \frac{\Big(2(x-\tilde{x}), 2(y-\tilde{y}), 2(z-\tilde{z})\Big)}{\Big(4(x-\tilde{x})^2 + 4(y-\tilde{y})^2 + 4(z-\tilde{z})^2\Big)^{\frac{1}{2}}} = \frac{(x-\tilde{x}, y-\tilde{y}, z-\tilde{z})}{\varepsilon}.$$

We split the Green's function into $G = G_1 + G_2$, where

$$G_1 = \frac{1}{4\pi\Big((x-\tilde{x})^2 + (y-\tilde{y})^2 + (z-\tilde{z})^2\Big)^{\frac{1}{2}}},$$
$$G_2 = \frac{1}{4\pi\Big((x-\tilde{x})^2 + (y+\tilde{y})^2 + (z-\tilde{z})^2\Big)^{\frac{1}{2}}}.$$

Equation (6.34) is then written as

$$\begin{aligned} 0 = &\iint_{S_\varepsilon} (\Phi - x)\frac{\partial G_2}{\partial \mathbf{n}}\, dS - \iint_{S_\varepsilon} G_2 \frac{\partial(\Phi - x)}{\partial \mathbf{n}}\, dS \\ &+ \iint_{S_\varepsilon} \left((\Phi - x)\frac{\partial G_1}{\partial \mathbf{n}} - G_1\frac{\partial(\Phi - x)}{\partial \mathbf{n}}\right) dS = I_1 - I_2 + I_3, \end{aligned} \tag{6.35}$$

respectively.

To begin, we evaluate I_1. We have

$$\begin{aligned} \frac{\partial G_2}{\partial \mathbf{n}} = \nabla G_2.\mathbf{n} &= -\frac{1}{4\pi}\frac{1}{\varepsilon}\frac{\Big((x-\tilde{x})^2 + (y+\tilde{y})(y-\tilde{y}) + (z-\tilde{z})^2\Big)}{\Big((x-\tilde{x})^2 + (y+\tilde{y})^2 + (z-\tilde{z})^2\Big)^{\frac{3}{2}}} \\ &= -\frac{1}{4\pi}\frac{1}{\varepsilon}\frac{\Big((x-\tilde{x})^2 + (y-\tilde{y})^2 + (z-\tilde{z})^2 + (y+\tilde{y})(y-\tilde{y}) - (y-\tilde{y})^2\Big)}{\Big((x-\tilde{x})^2 + (y-\tilde{y})^2 + (z-\tilde{z})^2 + (y+\tilde{y})^2 - (y-\tilde{y})^2\Big)^{\frac{3}{2}}} \\ &= -\frac{1}{4\pi}\frac{1}{\varepsilon}\frac{\Big(\varepsilon^2 + (y+\tilde{y})(y-\tilde{y}) - (y-\tilde{y})^2\Big)}{\Big(\varepsilon^2 + (y+\tilde{y})^2 - (y-\tilde{y})^2\Big)^{\frac{3}{2}}} \\ &= -\frac{1}{4\pi}\frac{1}{\varepsilon}\frac{\Big(\varepsilon^2 + 2\tilde{y}y - 2\tilde{y}^2\Big)}{\Big(\varepsilon^2 + 4\tilde{y}y\Big)^{\frac{3}{2}}}. \end{aligned}$$

Hence we have

$$I_1 = -\frac{1}{4\pi}\iint_{s_\varepsilon} \frac{\Phi - x}{\varepsilon}\frac{\Big(\varepsilon^2 + 2\tilde{y}y - 2\tilde{y}^2\Big)}{\Big(\varepsilon^2 + 4\tilde{y}y\Big)^{\frac{3}{2}}}\, dS. \tag{6.36}$$

We need to project the surface onto the x-y plane. To achieve this, we use the

formula (see for example Forbes, 1989)

$$dS = \frac{dxdy}{|\mathbf{k}.\mathbf{n}|}, \tag{6.37}$$

and in the case of the current surface, we have

$$dS = \frac{dxdy}{\frac{(z-\tilde{z})}{\varepsilon}} = \frac{\varepsilon}{\left(\varepsilon^2 - (x-\tilde{x})^2 - (y-\tilde{y})^2\right)^{\frac{1}{2}}} dxdy.$$

The mean value theorem for double integrals states that for a general function f which is continuous over a region D, we have (Stewart, 2011)

$$\iint_D f(x,y)\, dxdy = f(x_0, y_0)A(D), \tag{6.38}$$

where (x_0, y_0) is some point in D and $A(D)$ denotes the area of D. In the present problem, we define the function $f(x,y)$ as

$$f(x,y) = \frac{\left(\varepsilon^2 + 2\tilde{y}y - 2\tilde{y}^2\right)}{\left(\varepsilon^2 + 4\tilde{y}y\right)^{\frac{3}{2}}} \frac{\Phi - x}{\left(\varepsilon^2 - (x-\tilde{x})^2 - (y-\tilde{y})^2\right)^{\frac{1}{2}}}.$$

Application of the mean value theorem to the integral I_1 (equation (6.36)) gives

$$I_1 = -\frac{1}{4\pi} f(x_0, y_0)A(D) = -\frac{1}{4\pi} f(x_0, y_0)\pi\varepsilon^2.$$

We intend to take the limit $\varepsilon \to 0$. In this limit, the only possible choice for x_0 and y_0 become $\tilde{x}$ and $\tilde{y}$ respectively. Hence we have

$$\lim_{\varepsilon\to 0}(I_1) \approx -\frac{1}{4\pi} \lim_{\varepsilon\to 0}\left(f(\tilde{x},\tilde{y})\pi\varepsilon^2\right) = -\frac{1}{4\pi} \lim_{\varepsilon\to 0}\left(\frac{\left(\Phi(\tilde{x},\tilde{y},\tilde{z}) - \tilde{x}\right)\pi\varepsilon^3}{(\varepsilon^2 + 4\tilde{y}^2)^{\frac{3}{2}}}\right) = 0. \tag{6.39}$$

Thus we see that the contribution from I_1 is zero as we collapse the surface S_ε to the point $\tilde{Q}$.

Recall that the integral I_2 is given by

$$I_2 = \iint_{S_\varepsilon} G_2 \frac{\partial(\Phi - x)}{\partial \mathbf{n}}\, dS.$$

We have

$$\frac{\partial(\Phi - x)}{\partial \mathbf{n}} = \nabla(\Phi - x).\mathbf{n} = (\Phi_x - 1, \Phi_y, \Phi_z).\frac{(x-\tilde{x}, y-\tilde{y}, z-\tilde{z})}{\varepsilon}.$$

Hence

$$I_2 = \iint_{S_\varepsilon} \frac{1}{4\pi}\frac{1}{\varepsilon}\left(\frac{(\Phi - x)(x-\tilde{x}) + \Phi_y(y-\tilde{y}) + \Phi_z(z-\tilde{z})}{\Big((x-\tilde{x})^2 + (y+\tilde{y})^2 + (z-\tilde{z})^2\Big)^{\frac{1}{2}}}\right) dS$$

$$= \iint_{S_\varepsilon} \frac{1}{4\pi}\frac{1}{\varepsilon}\left(\frac{(\Phi - x)(x-\tilde{x}) + \Phi_y(y-\tilde{y}) + \Phi_z(z-\tilde{z})}{\Big(\varepsilon^2 + (y+\tilde{y})^2 - (y-\tilde{y})^2\Big)^{\frac{1}{2}}}\right) dS$$

$$= \iint_{S_\varepsilon} \frac{1}{4\pi}\left(\frac{(\Phi - x)(x-\tilde{x}) + \Phi_y(y-\tilde{y}) + \Phi_z(z-\tilde{z})}{\Big(\varepsilon^2 + 4\tilde{y}y\Big)^{\frac{1}{2}}\Big(\varepsilon^2 - (x-\tilde{x})^2 - (y-\tilde{y})^2\Big)^{\frac{1}{2}}}\right) dxdy$$

$$I_2 = \frac{1}{4\pi}\iint_D g(x,y)\, dxdy, \tag{6.40}$$

where we have projected the surface onto the x-y plane. Application of the mean value theorem for double integrals as before leads to

$$I_2 = \frac{1}{4\pi} g(x_0, y_0)\pi\varepsilon^2,$$

where x_0 and y_0 are some point within the region D. We collapse the surface S_ε and hence $(x_0, y_0) \to (\tilde{x}, \tilde{y})$ as before, leading to

$$\lim_{\varepsilon\to 0} I_2 \approx \frac{1}{4}\lim_{\varepsilon\to 0}\Big(g(\tilde{x},\tilde{y})\varepsilon^2\Big) = 0. \tag{6.41}$$

We are left with the integral I_3, the part of the integral over S_ε containing G_1 terms:

$$\iint_{S_\varepsilon}\left((\Phi - x)\frac{\partial G_1}{\partial \mathbf{n}} - G_1\frac{\partial(\Phi - x)}{\partial \mathbf{n}}\right) dS. \tag{6.42}$$

We have

$$\frac{\partial G_1}{\partial \mathbf{n}} = \nabla G_1 . \mathbf{n} = (\frac{\partial G_1}{\partial x}, \frac{\partial G_1}{\partial y}, \frac{\partial G_1}{\partial z}) . \frac{(x-\tilde{x}, y-\tilde{y}, z-\tilde{z})}{\varepsilon}$$

$$= -\frac{1}{4\pi}\frac{1}{\varepsilon}\frac{(x-\tilde{x})^2 + (y-\tilde{y})^2 + (z-\tilde{z})^2}{\Big((x-\tilde{x})^2 + (y-\tilde{y})^2 + (z-\tilde{z})^2\Big)^{\frac{3}{2}}}$$

$$= -\frac{1}{4\pi}\frac{1}{\varepsilon}\frac{\varepsilon^2}{(\varepsilon^2)^{\frac{3}{2}}} = -\frac{1}{4\pi}\frac{1}{\varepsilon^2}.$$

Substituting this into equation (6.42) and projecting onto the x-y plane gives

$$I_3 = \frac{1}{4\pi}\iint_{D_\varepsilon}\left(-\frac{\Phi - x}{\varepsilon^2} - \frac{1}{\varepsilon}\frac{\partial(\Phi - x)}{\partial \mathbf{n}}\right)\frac{\varepsilon}{\Big(\varepsilon^2 - (x-\tilde{x})^2 - (y-\tilde{y})^2\Big)^{\frac{1}{2}}}\, dxdy.$$

We introduce cylindrical polar co-ordinates and substitute $dxdy = r\, drd\theta$. Then I_3

becomes

$$I_3 = \frac{1}{4\pi}\int_0^{\varepsilon}\int_0^{2\pi}\left(-\frac{\Phi - x}{\varepsilon} - \frac{\partial(\Phi - x)}{\partial \mathbf{n}}\right)\frac{r\,drd\theta}{(\varepsilon^2 - r^2)^{\frac{1}{2}}}$$
$$= \frac{1}{2}\int_0^{r}\left(-\frac{\Phi - x}{\varepsilon} - \frac{\partial(\Phi - x)}{\partial \mathbf{n}}\right)\frac{r\,dr}{(\varepsilon^2 - r^2)^{\frac{1}{2}}}.$$

Shrinking the surface S_ε such that $(x, y, z) \to (\tilde{x}, \tilde{y}, \tilde{z})$, we have

$$I_3 \approx \frac{1}{2}\left(-\frac{\Phi(\tilde{x}, \tilde{y}, \tilde{z}) - \tilde{x}}{\varepsilon} - \frac{\partial(\Phi(\tilde{x}, \tilde{y}, \tilde{z}) - \tilde{x})}{\partial \mathbf{n}}\right)\int_0^{\varepsilon}\frac{r}{(\varepsilon^2 - r^2)^{\frac{1}{2}}}\,dr. \tag{6.43}$$

The integration is equal to

$$\int_0^{\varepsilon}\frac{r}{(\varepsilon^2 - r^2)^{\frac{1}{2}}}\,dr = \Big(-(\varepsilon^2 - r^2)^{\frac{1}{2}}\Big)_0^{\varepsilon} = \varepsilon.$$

Hence we have

$$I_3 \approx \frac{1}{2}\left(-\Big(\Phi(\tilde{x}, \tilde{y}, \tilde{z}) - \tilde{x}\Big) - \varepsilon\,\frac{\partial(\Phi(\tilde{x}, \tilde{y}, \tilde{z}) - \tilde{x})}{\partial \mathbf{n}}\right), \tag{6.44}$$

and taking the limit $\varepsilon \to 0$ gives

$$\lim_{\varepsilon \to 0}(I_3) = -\frac{1}{2}\Big(\Phi(\tilde{x}, \tilde{y}, \tilde{z}) - \tilde{x}\Big).$$

Hence, the total contribution to I from the surface S_ε is $-\frac{1}{2}\Big(\Phi(\tilde{x}, \tilde{y}, \tilde{z}) - \tilde{x}\Big)$.

6.3.2.4 The surface S_F

In the previous sections, we showed that the contributions to I from S_R and S_W are zero, and that the contribution from S_ε is $-\frac{1}{2}\Big(\Phi(\tilde{x}, \tilde{y}, \tilde{z}) - \tilde{x}\Big)$. Only the integral over the surface S_F remains. We have

$$\iint_{S_F}\left((\Phi - x)\frac{\partial G}{\partial \mathbf{n}} - G\frac{\partial(\Phi - x)}{\partial \mathbf{n}}\right)\,dS. \tag{6.45}$$

The equation for the surface S_F is given by $z = w(x, y)$. Therefore, the normal pointing into the fluid is given by

$$\mathbf{n} = \frac{\nabla(w(x, y) - z)}{|\nabla(w(x, y) - z)|} = \frac{(w_x, w_y, -1)}{(w_x^2 + w_y^2 + 1)^{\frac{1}{2}}}.$$

We have

$$\frac{\partial(\Phi - x)}{\partial \mathbf{n}} = \nabla(\Phi - x).\mathbf{n} = \frac{w_x(\Phi_x - 1) + w_y\Phi_y - \Phi_z}{(w_x^2 + w_y^2 + 1)^{\frac{1}{2}}}.$$

Using the kinematic condition (6.14) to simplify the numerator leads to

$$\frac{\partial(\Phi - x)}{\partial \mathbf{n}} = -\frac{Gw_x}{(w_x^2 + w_y^2 + 1)^{\frac{1}{2}}}.$$

We also have

$$\begin{aligned}\frac{\partial G}{\partial \mathbf{n}} = \nabla G.\mathbf{n} = &-\frac{1}{4\pi}\frac{(x-\tilde{x})w_x + (y-\tilde{y})w_y - (z-\tilde{z})}{\left((x-\tilde{x})^2 + (y-\tilde{y})^2 + (z-\tilde{z})^2\right)^{\frac{3}{2}}(w_x^2 + w_y^2 + 1)^{\frac{1}{2}}} \\ &- \frac{1}{4\pi}\frac{(x-\tilde{x})w_x + (y+\tilde{y})w_y - (z-\tilde{z})}{\left((x-\tilde{x})^2 + (y+\tilde{y})^2 + (z-\tilde{z})^2\right)^{\frac{3}{2}}(w_x^2 + w_y^2 + 1)^{\frac{1}{2}}}.\end{aligned}$$

We project the surface onto the x-y plane using the formulae:

$$dS = \frac{dxdy}{|\mathbf{k}.\mathbf{n}|} = (w_x^2 + w_y^2 + 1)^{\frac{1}{2}}dxdy.$$

Hence, the contribution to I from the surface S_F is given by

$$\begin{aligned}\frac{1}{4\pi}\int_0^\infty \int_{-\infty}^\infty \Bigg(&(\Phi - x)\frac{z - \tilde{z} - (x-\tilde{x})w_x - (y-\tilde{y})w_y}{\left((x-\tilde{x})^2 + (y-\tilde{y})^2 + (z-\tilde{z})^2\right)^{\frac{3}{2}}} \\ &+ (\Phi - x)\frac{z - \tilde{z} - (x-\tilde{x})w_x - (y+\tilde{y})w_y}{\left((x-\tilde{x})^2 + (y+\tilde{y})^2 + (z-\tilde{z})^2\right)^{\frac{3}{2}}} \\ &+ \frac{w_x}{\left((x-\tilde{x})^2 + (y-\tilde{y})^2 + (z-\tilde{z})^2\right)^{\frac{1}{2}}} \\ &+ \frac{w_x}{\left((x-\tilde{x})^2 + (y+\tilde{y})^2 + (z-\tilde{z})^2\right)^{\frac{1}{2}}}\Bigg)\, dxdy. \qquad (6.46)\end{aligned}$$

6.3.3 Formulating the numerical procedure

To simplify the formulation and reduce the computation time, Forbes (1989) combined the kinematic and dynamic boundary conditions into one formula. This was achieved by introducing a new variable, the velocity potential at the ice surface:

$$\phi(x, y) = \Phi(x, y, w(x, y)). \qquad (6.47)$$

Recall that the dynamic boundary condition (6.15) is given by

$$\frac{1}{2}\left(\Phi_x^2 + \Phi_y^2 + \Phi_z^2 - 1\right) + f_L w + \beta\nabla^4 w = \epsilon P, \quad (z = w(x, y)), \qquad (6.48)$$

and the kinematic boundary condition (6.14) is

$$\Phi_x w_x + \Phi_y w_y = \Phi_z, \quad (z = w(x, y)). \qquad (6.49)$$

Using equation (6.47), applying the chain rule of calculus gives

$$\frac{\partial \phi}{\partial x} = \frac{\partial \Phi}{\partial z}\frac{\partial w}{\partial x} + \frac{\partial \Phi}{\partial x}, \tag{6.50}$$

$$\frac{\partial \phi}{\partial y} = \frac{\partial \Phi}{\partial z}\frac{\partial w}{\partial y} + \frac{\partial \Phi}{\partial y}. \tag{6.51}$$

Substituting (6.50)-(6.51) into equation (6.49) gives

$$\begin{aligned}
\Phi_z &= (\phi_x - \Phi_z w_x)w_x + (\phi_y - \Phi_z w_w)w_y, \\
\Phi_z &= \frac{\phi_x w_x + \phi_y w_y}{1 + w_x^2 + w_y^2}.
\end{aligned} \tag{6.52}$$

We also use (6.50)-(6.51) to give

$$\begin{aligned}
\Phi_x^2 + \Phi_y^2 + \Phi_z^2 &= (\Phi_x - w_x\Phi_z)^2 + (\phi_y - \Phi_z w_y)^2 + \Phi_z^2 \\
&= \phi_x^2 + \phi_y^2 - 2\Phi_z(\phi_x w_x + \phi_y w_y) + \Phi_z^2(1 + w_x^2 + w_y^2) \\
&= \phi_x^2 + \phi_y^2 + \frac{(\phi_x w_x + \phi_y w_y)^2}{1 + w_x^2 + w_y^2} - 2\frac{(\phi_x w_x + \phi_y w_y)^2}{(1 + w_x^2 + w_y^2)} \\
&= \frac{1}{1 + w_x^2 + w_y^2}\Big((\phi_x^2 + \phi_y^2)(1 + w_x^2 + w_y^2) - (\phi_x w_x + \phi_y w_y)^2\Big) \\
\Phi_x^2 + \Phi_y^2 + \Phi_z^2 &= \frac{1}{1 + w_x^2 + w_y^2}\Big(\phi_x^2(1 + w_y^2) + \phi_y^2(1 + w_x^2) - 2\phi_y w_y \phi_x w_x\Big).
\end{aligned} \tag{6.53}$$

where we have used equation (6.52) to substitute for Φ_z. Substituting equation (6.53) into equation (6.48) gives the dynamic boundary condition in terms of $\phi(x, y)$:

$$\frac{1}{2}\left(\frac{\phi_x^2(1 + w_y^2) + \phi_y^2(1 + w_x^2) - 2\phi_y w_y \phi_x w_x}{1 + w_x^2 + w_y^2} - 1\right) + f_L w + \beta\nabla^4 w + \epsilon p = 0. \tag{6.54}$$

Substituting (6.47) into (6.46), and using the results from Sections (6.3.2.1)-(6.3.2.4), equation (6.25) becomes:

$$2\pi(\phi(\tilde{x}, \tilde{y}) - \tilde{x}) = I_A + I_B, \tag{6.55}$$

where

$$I_A = \int_0^\infty \int_{-\infty}^\infty \Big(\phi(x, y) - x\Big) K_A \, dxdy, \tag{6.56}$$

$$I_B = \int_0^\infty \int_{-\infty}^\infty w_x K_B \, dxdy, \tag{6.57}$$

where the kernel functions are given by

$$
\begin{aligned}
K_A &= \frac{w(x,y) - w(\tilde{x},\tilde{y}) - (x-\tilde{x})w_x - (y-\tilde{y})w_y}{\Big((x-\tilde{x})^2 + (y-\tilde{y})^2 + (w(x,y) - w(\tilde{x},\tilde{y}))^2\Big)^{\frac{3}{2}}} \\
&\quad + \frac{w(x,y) - w(\tilde{x},\tilde{y}) - (x-\tilde{x})w_x - (y+\tilde{y})w_y}{\Big((x-\tilde{x})^2 + (y+\tilde{y})^2 + (w(x,y) - w(\tilde{x},\tilde{y}))^2\Big)^{\frac{3}{2}}}, \\
K_B &= \frac{1}{\Big((x-\tilde{x})^2 + (y-\tilde{y})^2 + (w(x,y) - w(\tilde{x},\tilde{y}))^2\Big)^{\frac{1}{2}}} \\
&\quad + \frac{1}{\Big((x-\tilde{x})^2 + (y+\tilde{y})^2 + (w(x,y) - w(\tilde{x},\tilde{y}))^2\Big)^{\frac{1}{2}}}.
\end{aligned} \tag{6.58}
$$

The integral I_A can be rewritten as

$$
I_A = \int_0^\infty \int_{-\infty}^\infty \Big(\phi(x,y) - \phi(\tilde{x},\tilde{y}) - x + \tilde{x}\Big) K_A \, dxdy + (\phi(\tilde{x},\tilde{y}) - \tilde{x}) \int_0^\infty \int_{-\infty}^\infty K_A \, dxdy. \tag{6.59}
$$

This technique, used by Forbes (1989), renders I_A less singular. The second integral in (6.59) can be evaluated:

$$
\int_0^\infty \int_{-\infty}^\infty K_A \, dxdy = \iint_{S_F} \frac{\partial G}{\partial \mathbf{n}} \, dS = 0. \tag{6.60}
$$

Forbes (1989) showed this result by using the Gauss flux theorem and the fact that G is harmonic within V. Hence, the final expression for I_A is

$$
I_A = \int_0^\infty \int_{-\infty}^\infty \Big(\phi(x,y) - \phi(\tilde{x},\tilde{y}) - x + \tilde{x}\Big) K_A \, dxdy. \tag{6.61}
$$

The integral I_A is now non-singular, whereas I_B is singular at $x = \tilde{x}$, $y = \tilde{y}$. Following Forbes (1989), we rewrite the integral I_B as

$$
I_B = I'_B + I''_B, \tag{6.62}
$$

where

$$
I'_B = \int_0^\infty \int_{-\infty}^\infty \Big(w_x(x,y) K_B - w_x(\tilde{x},\tilde{y}) S\Big) \, dxdy, \tag{6.63}
$$

$$
I''_B = w_x(\tilde{x},\tilde{y}) \int_0^\infty \int_{-\infty}^\infty S \, dxdy. \tag{6.64}
$$

Here S is given by

$$S = \frac{1}{\Big(A(x-\tilde{x})^2 + B(x-\tilde{x})(y-\tilde{y}) + C(y-\tilde{y})^2\Big)^{\frac{1}{2}}} + \frac{1}{\Big(A(x-\tilde{x})^2 + B(x-\tilde{x})(y+\tilde{y}) + C(y+\tilde{y})^2\Big)^{\frac{1}{2}}},$$

where

$$\begin{aligned} A &= 1 + w_x^2(\tilde{x},\tilde{y}), \\ B &= 2w_x(\tilde{x},\tilde{y})w_y(\tilde{x},\tilde{y}), \\ C &= 1 + w_y^2(\tilde{x},\tilde{y}). \end{aligned}$$

The integral I_B'' can be integrated directly in closed form by using the standard result (Forbes, 1989):

$$\begin{aligned} \iint \frac{dsdt}{\sqrt{As^2+bst+Ct^2}} = &\frac{t}{\sqrt{A}} \ln\Big(2As + Bt + 2\sqrt{A(As^2+Bst+Ct^2)}\Big) \\ &+ \frac{s}{\sqrt{C}} \ln\Big(2Ct + Bs + 2\sqrt{A(As^2+Bst+Ct^2)}\Big), \end{aligned}$$

which can be exploited after the integrals are truncated later.

6.3.4 The numerical scheme

We aim to set up a numerical scheme to computationally solve equation (6.55), where the integrals are given by (6.61) and (6.62)-(6.64), combined with the dynamic boundary condition (6.54). Following Părău & Vanden-Broeck (2011) we truncate the intervals $-\infty < x < \infty$ and $0 < y < \infty$ to $x_1 < x < x_N$ and $y_1 < y < y_M$ respectively. We introduce the mesh points $x_i = x_1 + (i-1)\Delta x$, $i = 1, 2, ..., N$ and $y_j = y_1 + (j-1)\Delta y$, $j = 1, 2, ..., M$.

The $2NM$ unknowns are given by

$$\mathbf{u} = (w_{x_{1,1}}, w_{x_{1,2}}, ..., w_{x_{N,M-1}}, w_{x_{N,M}}, \phi_{x_{1,1}}, ..., \phi_{x_{N,M}})^T.$$

We evaluate the (now truncated) integrals (6.61) and (6.62)-(6.64) as well as the dynamic condition (6.54) at the midpoints $(x_{i+1/2}, y_j)$, $i = 1, ..., N-1$, $j = 1, ..., M$, so we have $2(N-1)M$ equations. The values of w and ϕ at the midpoints were obtained by interpolation. Following Părău & Vanden-Broeck (2011) we also impose a radiation condition (from equation (6.6)) on the first row upstream: $w_{x_{1j}} = 0$, $\phi_{x_{1j}} = 1$, $j = 1, ..., M$, giving another $2M$ equations. We integrate w_x and ϕ_x with respect to x by the trapezoidal rule to give the values of w and ϕ.

We now state the conditions imposed on the boundaries of the grid. With respect to the stated upstream radiation condition (6.6) and the dynamic boundary

condition (6.54), the integration is started by taking the following values for the first row (along $i = 1$ for $j = 1, ..., M$):

$$w_{1,j} = 0, \quad w_{x_{1,j}} = 0, \quad w_{y_{1,j}} = 0, \tag{6.65}$$

$$\phi_{1,j} = x_1, \quad \phi_{x_{1,j}} = 1, \quad \phi_{y_{1,j}} = 0. \tag{6.66}$$

Following Părău & Vanden-Broeck (2011), we also impose a radiation condition downstream, and for the final row we take (along $i = N$ for $j = 1, ..., M$):

$$w_{x_{N,j}} = 0, \quad \phi_{x_{N,j}} = 0. \tag{6.67}$$

Finally the clamped–ice conditions (6.10) require that along the vertical wall we have (along $j = 1$ for $i = 1, M$):

$$w_{i,1} = 0, \quad w_{x_{i,1}} = 0. \tag{6.68}$$

Inside the grid, the values of the other derivatives, w_y, ϕ_y and $\nabla^4 w$ are calculated using central finite differences, utilising formulae from Abramowitz & Stegun (1972). For example, the bi-Laplacian is approximated by

$$\begin{aligned}\nabla^4 w = &\frac{1}{(\Delta x)^4}(w_{i+2,j} - 4w_{i+1,j} + 6w_{i,j} - 4w_{i-1,j} + w_{i-2,j}) \\ &+ \frac{1}{(\Delta y)^4}(w_{i,j+2} - 4w_{i,j+1} + 6w_{i,j} - 4w_{i,j-1} + w_{i,j-2}) \\ &+ \frac{1}{(\Delta y)^2(\Delta x)^2}(4w_{i,j} - 2w_{i+1,j} - 2w_{i-1,j} - 2w_{i,j+1} - 2w_{i,j-1} \\ &+ w_{i+1,j+1} + w_{i+1,j-1} + w_{i-1,j+1} + w_{i-1,j-1}).\end{aligned}$$

Along the edges of the grid we use extrapolation, except for along the vertical wall where we use forward finite differences.

We then solve the $2NM$ equations by using Newton's method for a system of nonlinear equations. After each step, a correction vector $\mathbf{c}$ is added to the vector $\mathbf{u}$ of unknowns, where c is given by solving the matrix equation (Forbes, 1989)

$$\mathbf{J(u)\ c} = -\mathbf{E(u)}.$$

Here $\mathbf{E}$ defines the error vector. We continue this procedure until the magnitude of the error vector $||\mathbf{E}|| < 10^{-20}$.

For load speeds $U > c_{min}$, the solution will not converge without dissipation of some kind. This was also true in Chapter 5, where the viscoelastic relaxation time $\tau \neq 0$ was necessary to find a solution for fast speeds. Therefore for fast load speeds, we follow Părău et al. (2007) and introduce an artificial viscosity μ, known as the Rayleigh viscosity. This was first introduced by Rayleigh (1883) to obtain a unique solution for linear problems involving gravity-capillary waves by taking the

limit $\mu \to 0$. For speeds $U > c_{min}$, the dynamic boundary condition (6.54) becomes

$$\frac{1}{2}\left(\frac{\phi_x^2(1+w_y^2)+\phi_y^2(1+w_x^2)-2\phi_y w_y \phi_x w_x}{1+w_x^2+w_y^2}-1\right)+f_L w+\beta\nabla^4 w+\epsilon p+\mu(\phi-x)=0. \tag{6.69}$$

This dissipative term allows the solution to converge for fast load speeds.

6.4 Numerical results

In this section we present numerical results for the regime outlined in Section 6.3.4. The default parameters are taken from Table 2.1(a), with infinite fluid depth. We fix the length scale in the present problem at $L = 20\,\text{m}$. This choice allows us to keep Δx and Δy small, while also allowing the grid to fully capture the ice deflection. The values of the load speed U and the distance from the wall y_0 are quoted for each graph. The parameters of the grid Δx, Δy, m and n are stated for each graph.

6.4.1 Deflection

For this section, the value of P_0 is arbitrary, as varying P_0 affects the magnitude of the deflection much more than its pattern, which we are interested in here. We take the mass of the moving load to be such that $m^V g = 50000\,\text{N}$, giving $m^V \approx 5200\,\text{kg}$. This represents a large vehicle or truck on the ice. Using the length scale $L = 20\,\text{m}$, this corresponds to a value $P_0 = 641\,\text{Nm}^{-2}$.

(i): $U < c_{min}$

We begin by plotting the deflection for low source speeds $U < c_{min}$. In the following, it is assumed that the artificial viscosity $\mu = 0$. Figure 6.4 shows the ice deflection for the load speed $U = 10\,\text{ms}^{-1}$ and distance from the wall $y_0 = 100\,\text{m}$. We see that the surface elevation response is small for such a low speed U. The deformation is localised around the position of the load. The pattern in the depression caused by the moving load is similar to those observed for low source speeds for the linear formulation of Chapter 5. The position of maximum depression is at the position of the load (at $x = 0$), in contrast to the slight lag exhibited by the linear model due to the viscoelastic formulation.

We now shift the load to a distance $y_0 = 80\,\text{m}$ from the wall, retaining the load speed $U = 10\,\text{ms}^{-1}$. The resulting deflection is shown in Figure 6.5. The wave pattern behind the moving load is altered due to this change in y_0. A wave has appeared in close proximity to the vertical wall. The maximum depression is unchanged from the $y = 100\,\text{m}$ case. The surface response ahead of the load is still negligible. To investigate this phenomenon further, the distance y_0 is decreased to $y_0 = 50\,\text{m}$. Figure 6.6 shows the resulting ice deflection. The waves behind the source have further increased in amplitude. In the present nonlinear formulation, it appears that the load, when moving in close proximity to the vertical wall, causes increased deflections in the wake of the load. This is in contrast to the linear model

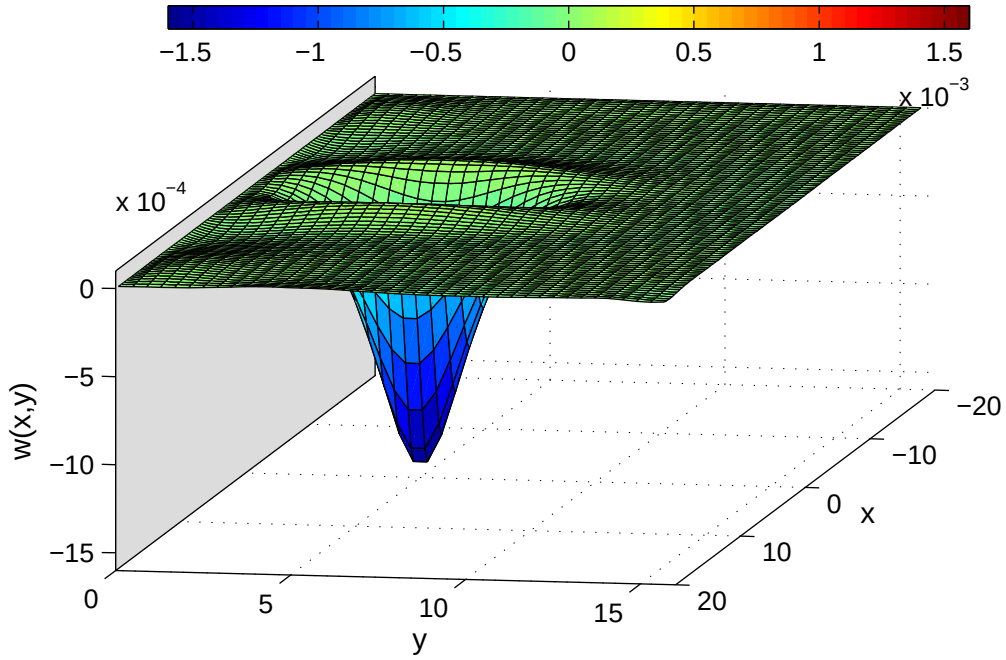

Figure 6.4: The deflection of the ice sheet is plotted for $U = 10\,\mathrm{ms}^{-1}$. Here $\Delta x = \Delta y = 0.4$, $n = 100$, $m = 40$ and $y_0 = 100\,\mathrm{m}$.

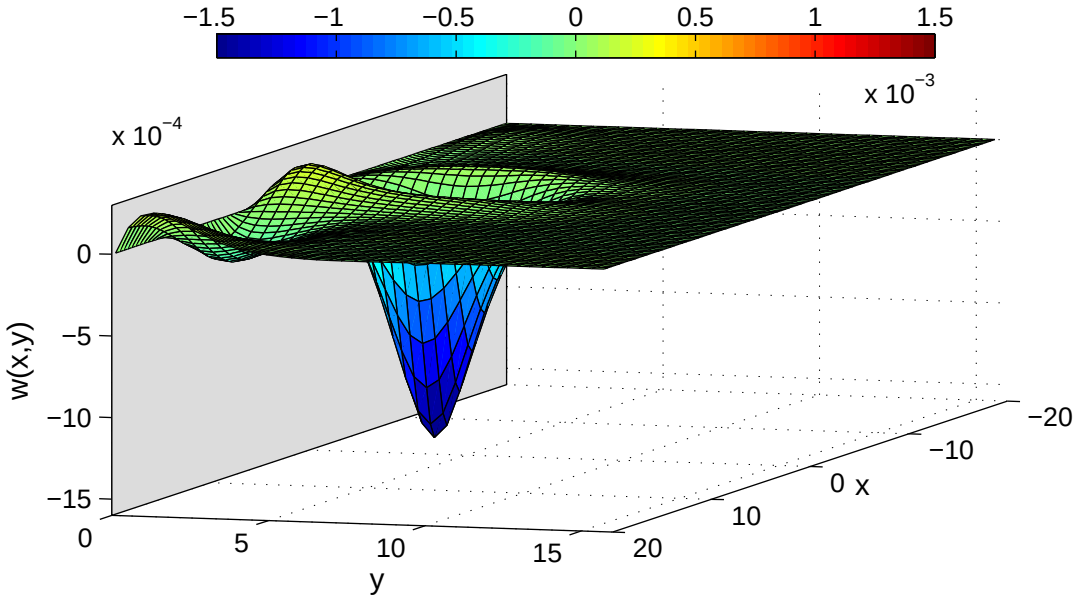

Figure 6.5: The deflection of the ice sheet is plotted for $U = 10\,\mathrm{ms}^{-1}$. Here $\Delta x = \Delta y = 0.4$, $n = 100$, $m = 40$ and $y_0 = 80\,\mathrm{m}$.

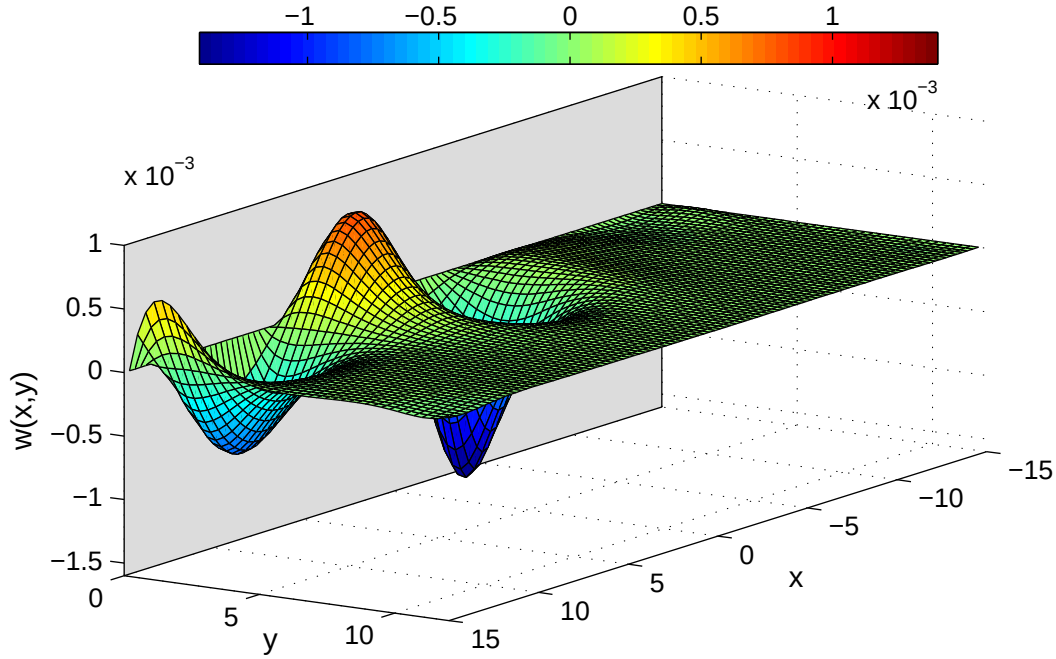

Figure 6.6: The deflection of the ice sheet is plotted for $U = 10\,\mathrm{ms}^{-1}$. Here $\Delta x = \Delta y = 0.3$, $n = 100$, $m = 40$ and $y_0 = 50\,\mathrm{m}$.

of Chapter 5, where a small distance from the wall to the load led to a smaller depression in the ice, and a differing shape of that depression. The explanation for this discord could lie in the nonlinear wave interaction with the wall, or the more sophisticated model for the moving pressure load adopted in the present problem.

We now investigate the effect of increasing the load speed to $U = 15\,\mathrm{ms}^{-1}$, and we set the distance $y_0 = 100\,\mathrm{m}$. The computed solution is shown in Figure 6.7. We observe an increase in the maximum depression caused by the moving load.

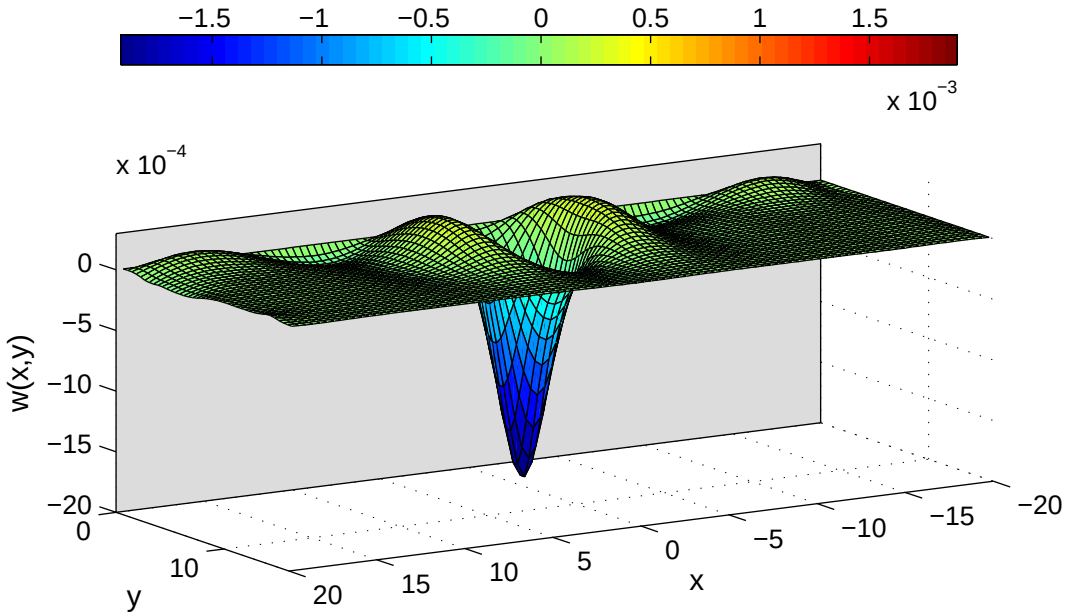

Figure 6.7: The deflection of the ice sheet is plotted for $U = 15\,\mathrm{ms}^{-1}$. Here $\Delta x = \Delta y = 0.4$, $n = 100$, $m = 40$ and $y_0 = 100\,\mathrm{m}$.

In addition we now see elevation both behind and ahead of the source due to the

motion of the load. Both of these trends were also present for the linear formulation. However, in Figure 6.7, the waves take longer to decay than for the linear case, and there is a disturbance reaching the edges of the grid ahead and behind the source, close to the wall.

(ii): $U > c_{min}$

We now investigate load speeds faster than the critical speed c_{min}. The artificial viscosity μ must now be present for the solution to converge. To begin, we plot the deflection for the parameters $U = 20\,\text{ms}^{-1}$ and $y_0 = 200\,\text{m}$, shown in Figure 6.8. By now we are familiar with the change in deflection magnitude and varied

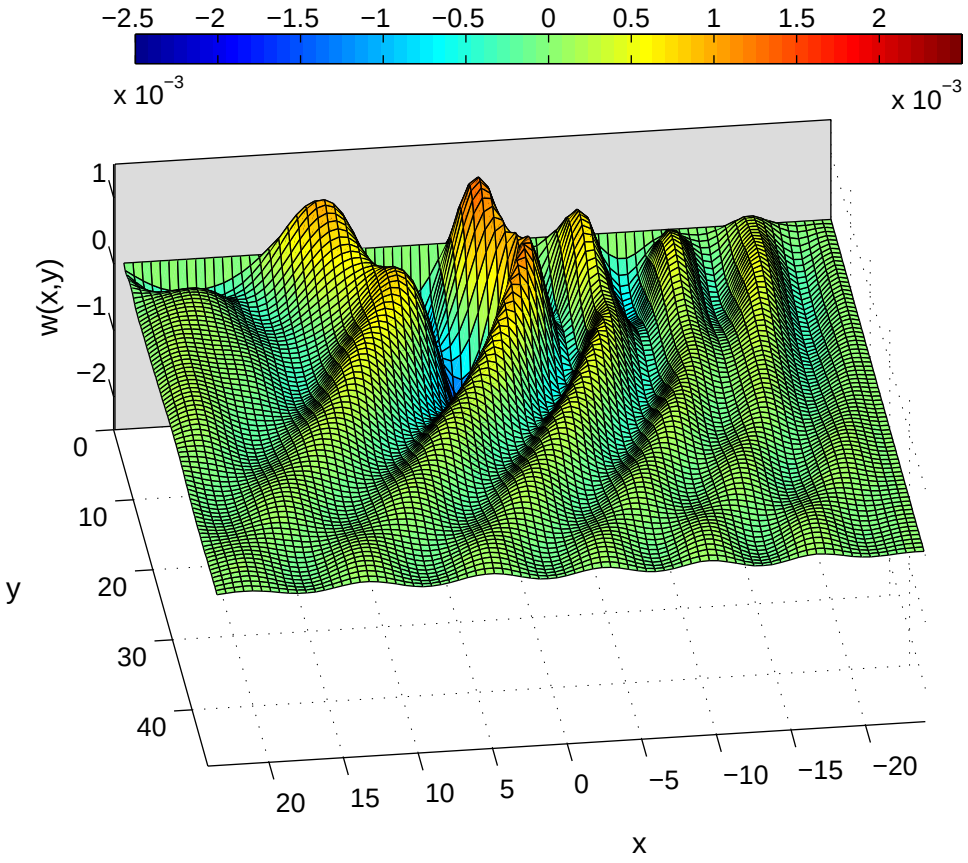

Figure 6.8: The deflection of the ice sheet is plotted for $U = 20\,\text{ms}^{-1}$. Here $\Delta x = \Delta y = 0.6$, $n = 80$, $m = 80$ and $y_0 = 200\,\text{m}$. The artificial viscosity is given by $\mu = 0.1$.

pattern caused by load speeds $U > c_{min}$. The maximum deflection has increased, and the waves generated by the moving load propagate further than for the case $U < c_{min}$. The wave profile is more curved owing to the increased speed. The solution regime of shorter, elastic waves ahead of the source and slower, gravity waves behind the source that was observed in the linear model is also present in the nonlinear formulation. We note that the solution decays towards the edges of the grid, owing to the artificial viscosity and radiation conditions. In general the behaviour is very similar to that of the equivalent linear graph shown in Figure 5.19. However, in Figure 6.8 there are fewer long waves behind the source than for the linear case. This is due to the fact that the grid is smaller, because we are now more constrained by computational restrictions: for a solution to be realistic and to

converge, the parameters Δx and Δy must be small. In addition, grid sizes larger than 80x80 are not numerically feasible.

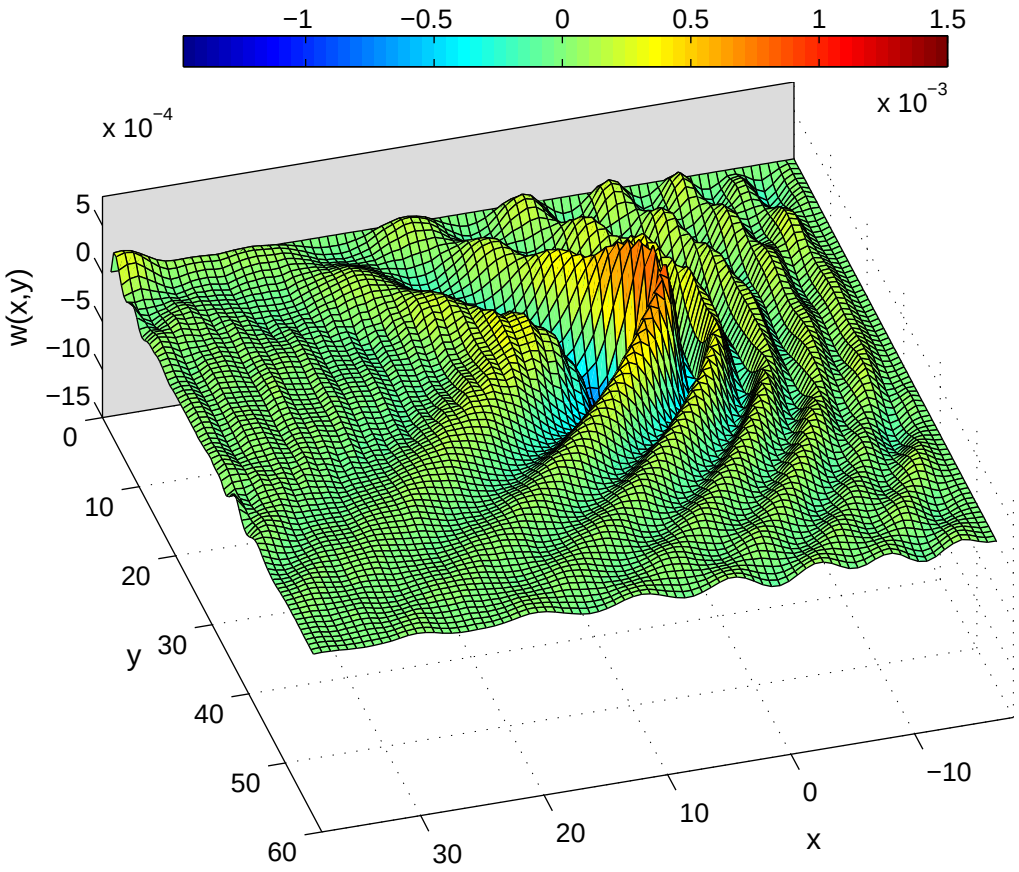

Figure 6.9: The deflection of the ice sheet is plotted for $U = 25\,\mathrm{ms}^{-1}$. Here $\Delta x = \Delta y = 0.7$, $n = 80$, $m = 80$ and $y_0 = 400\,\mathrm{m}$. The artificial viscosity is given by $\mu = 0.2$.

Finally we plot the deflection for a fast load speed $U = 25\mathrm{ms}^{-1}$ and distance from the wall $y_0 = 400\,\mathrm{m}$, the solution for which is shown in Figure 6.9. The disparity in wavelength between the shorter and longer waves is more apparent. We begin to see significant disturbance between the vertical wall and the moving load, owing to wave reflection by the wall. This is similar to the behaviour shown in Chapter 5 for fast load speeds, indicating that this phenomenon is not purely linear. Only one long wave appears behind the source, and its amplitude is small compared to the wave peak ahead of the load or the wave depression caused by the load.

6.4.2 Comparison with linear model

In this section we compare the results between the present nonlinear model and the linear model of Chapter 5. Such a comparison is difficult to interpret because there are many differences between the two models. For example, the expression for the pressure is a point load in the linear formulation, whereas it is modelled as a non-uniform distribution over a prescribed rectangle in the nonlinear formulation. The linear model assumes finite depth, whereas the nonlinear model does not. The linear model includes a term for the plate acceleration whereas the nonlinear model

neglects this term. Finally, in the linear model the dissipation is inherent in the viscoelastic plate equation, whereas for the nonlinear model we add an artificial viscosity. Hence, while assessing any disparity between the two models it is difficult to determine whether nonlinear effects are responsible, or one of the other differences mentioned above.

For this comparison we would like to set the relevant parameters such that the two expressions for the moving loads are equivalent. Because one is a point load and the other is a load distribution, we achieve this by requiring that

$$\iint_R P_L \, dxdy = \iint_R P_N \, dxdy, \tag{6.70}$$

where R is the region occupied by the ice sheet in each case. Here P_L is the expression for the load in the linear formulation given by equation (5.38), and P_N is the expression for the load in the nonlinear formulation given by equation (6.21). The left hand side of (6.70) is therefore given by (in dimensionless variables and in the notation of Chapter 5):

$$\frac{m^V g}{H^2} \int_{-\infty}^{\infty} \int_0^{\infty} -\delta(x - x_0)\delta(y) \, H^2 dxdy = -m^V g. \tag{6.71}$$

The right hand side of (6.70) becomes (in dimensionless variables)

$$-P_0 L^2 \int_{y_0-1}^{y_0+1} \int_{-1}^{1} \exp\left(\frac{1}{x^2-1} + \frac{1}{(y-y_0)^2-1}\right) dxdy. \tag{6.72}$$

The integral in equation (6.72) may be computed numerically as $c = 0.1971305088$, and is independent of y_0. Hence, equating (6.71) and (6.72), we arrive at

$$P_0 L^2 c = m^V g. \tag{6.73}$$

We may then select a mass m^V for the load in the linear formulation and, using equation (6.73), calculate the value of P_0 such that the nonlinear load is equivalent. For this comparison, as before we take the value $m^V g = 50000\,\mathrm{N}$ leading to $P_0 = 641\,\mathrm{Nm}^{-2}$.

We may now compare the results directly. Firstly we select a load speed $U = 15\,\mathrm{ms}^{-1}$ and a distance from the wall of 100 m. In both models there is no dissipation (ie. $\tau = 0$ for the linear model and $\mu = 0$ for the nonlinear model). The deflection through the centre line $x = 0$ is given in Figure 6.10. There is excellent agreement between the two data sets. The value of the deflection at $y = y_0$ is slightly smaller for the nonlinear model. The maximum ice excursion predicted for these parameters is approximately 2mm for each model. We repeat this comparison, instead plotting the deflection through the centre line $y = y_0$, shown in Figure 6.11. Again we experience near-perfect agreement between the two models, giving credence to both.

We repeat this comparison, increasing the speed of the load to $U = 20\,\mathrm{ms}^{-1}$ and

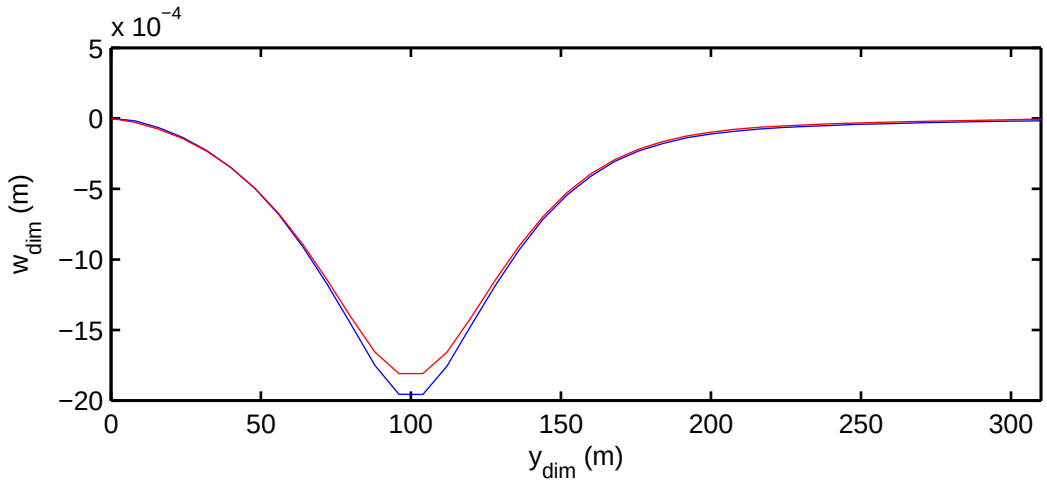

Figure 6.10: The deflection of the ice sheet is plotted through the centre line $x = 0$ for $U = 15\,\mathrm{ms}^{-1}$, $y_0 = 100\,\mathrm{m}$. The blue line represents the linear model, and the red line represents the nonlinear model.

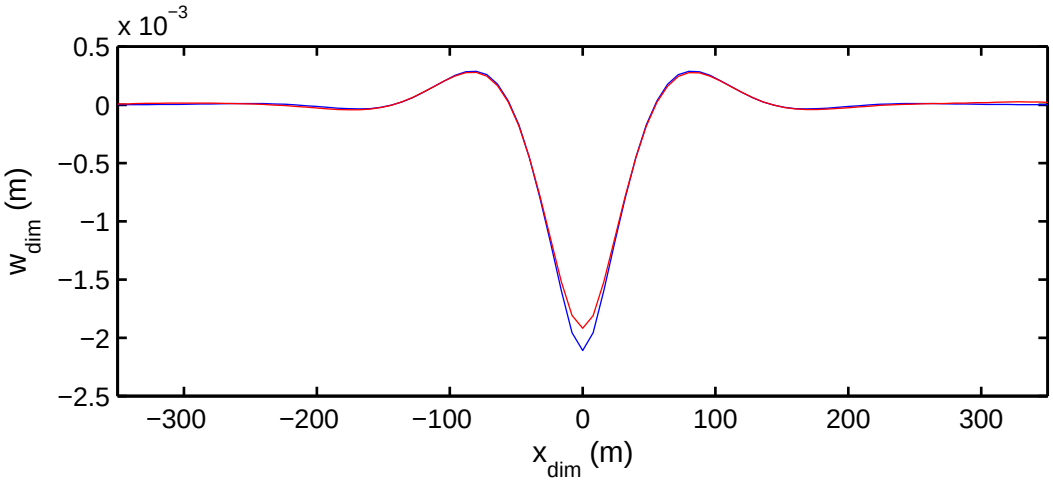

Figure 6.11: The deflection of the ice sheet is plotted through the centreline $y = y_0$ for $U = 15\,\mathrm{ms}^{-1}$, $y_0 = 100\,\mathrm{m}$. The blue line represents the linear model, and the red line represents the nonlinear model.

the distance from the wall to $y_0 = 200\,\text{m}$. This speed is slightly above the critical speed, and hence we require the presence of viscosity in each model for bounded solutions. We therefore select $\tau = 0.1\,\text{s}$ and $\mu = 0.1$. The deflection through the centre line $x = 0$ is shown in Figure 6.12. For these parameters, the agreement

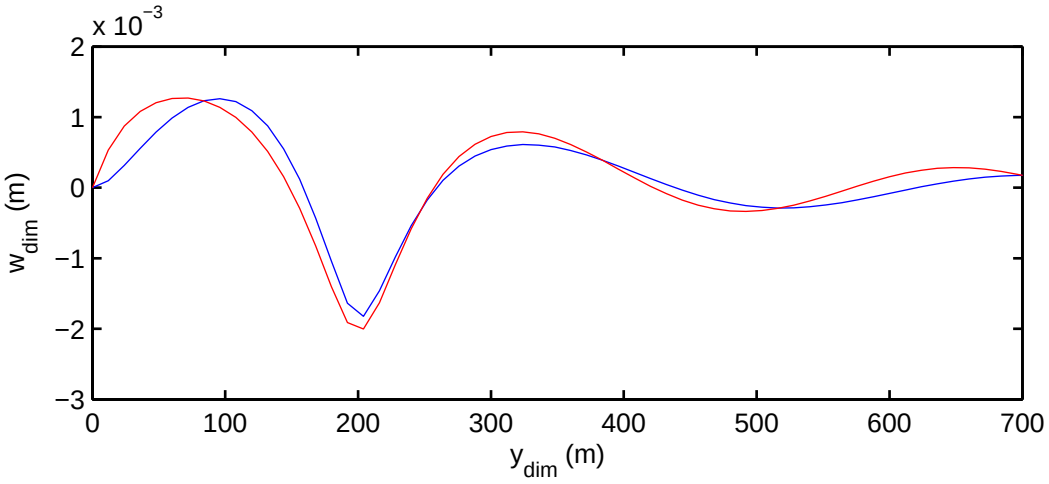

Figure 6.12: The deflection of the ice sheet is plotted through the centre line $x = 0$ for $U = 20\,\text{ms}^{-1}$, $y_0 = 200\,\text{m}$. The blue line represents the linear model, and the red line represents the nonlinear model.

between the two models is still excellent, though slightly worse than for slower load speeds. In this case the nonlinear model predicts a slightly higher surface depression at the point of the load. There is also a steeper rise in deflection at the vertical wall in the nonlinear model. Once again, the maximum ice excursion is approximately 2mm for each model. For further comparison, the centre line through $y = y_0$ is shown in Figure 6.13. The agreement in this case is fairly good, though some disagreement

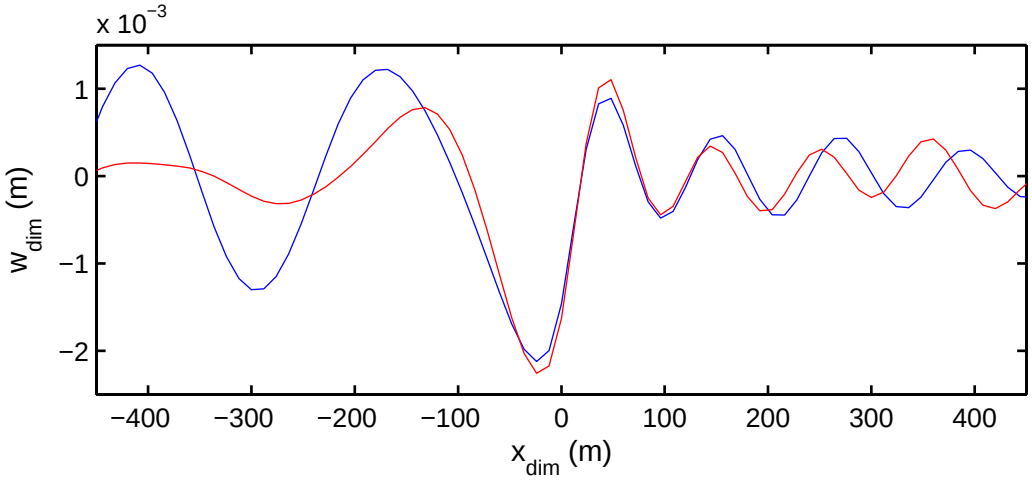

Figure 6.13: The deflection of the ice sheet is plotted through the centreline $y = y_0$ for $U = 20\,\text{ms}^{-1}$, $y_0 = 200\,\text{m}$. The blue line represents the linear model, and the red line represents the nonlinear model.

starts to appear towards the edges of the grid. Behind the load, the nonlinear model predicts smaller wave amplitudes. This is likely due to the truncation of the grid in the nonlinear model, and the radiation condition imposed downstream. Ahead

of the load, the linear model predicts slightly longer wavelengths, though the wave amplitudes are similar in each case. This discrepancy is likely due to the differing expressions for the moving pressure. Towards the centre of the grid, there is excellent agreement.

6.5 Summary

The problem of a moving load on an ice sheet was solved for fully nonlinear fluid equations. The ice was frozen to the vertical wall. The fluid was of infinite depth. This chapter represents an extension of the linear model in Chapter 5. Based on the work of Forbes (1989) and Părău & Vanden-Broeck (2011), the problem was solved by application of Green's theorem using the free–surface Green's function, and use of a boundary integral method. The introduction of a vertical wall complicates the problem, but choice of a suitable surface over which to apply Green's theorem leads to a solution. Some elegant simplifications introduced by Forbes (1989) led to further efficiency in the method, and the numerical computations involved are not overly cumbersome. The deflection of the ice sheet was studied in detail for various load speeds, and a comparison with the linear theory was presented.

In general the response of the ice sheet to the moving load followed the trends introduced in Chapter 5. Whether the load moves with speed above or below the critical speed c_{min} is the most important factor governing the shape of the deflection pattern. For slow load speeds, the surface response is mostly localized around the support of the pressure. However, placing the load closer to the wall increases the deflections in the wake of the moving load. This was not the case in the linear formulation, indicating that nonlinearity is responsible for this behaviour. For fast load speeds, the deflection becomes curved and the waves propagate at a further distance from the load. For certain values of the load speed and the distance from the wall, disturbance exists between the load and the wall, representing trapped standing waves due to the interaction with the vertical wall.

Direct comparison with the linear theory yields good agreement, despite the differences in the two models. This agreement is better for slower load speeds, where the shape and magnitude of the deflection in both cases agrees almost perfectly. For faster load speeds, we begin to see some disparity, though in the vicinity of the load the predicted ice response is the same.

Chapter 7

Final discussion

7.1 Summary and conclusions

Hydroelastic waves can propagate over long distances in polar regions owing to the flexural nature of ice sheets. In any situation in which a fixed vertical boundary exists near ice–covered water, we expect interaction between the boundary and hydroelastic waves. This thesis investigated such interactions for several physical scenarios. There is a wide variety of motivation for the work, the chief of which being construction of offshore oil–gas platforms and wind turbines in ice–covered water, as discussed in Section 1.6.

By modelling the ice as a thin floating elastic plate, equations were derived that govern the behaviour of the ice–structure system under the effect of waves. The system is comprised of a fourth–order governing equation for the plate deflection, coupled to the equations of fluid motion, and accompanied by appropriate boundary conditions on the structure. This thin–plate assumption neglects some of the more inhomogeneous properties of ice sheets, but allows explicit solutions to be found. The incident waves are considered to propagate either from infinity towards the structure or are generated by a moving load. In the former case we assume time–harmonic motion, which allows the velocity potential and ice deflection to be separated into a time–independent part. In the latter case, a moving frame of reference is adopted.

For the linear formulations of Chapters 2-5 an exact analytic solution was found by applying integral transforms. This approach presents several advantages. In general the method proves effective and concise. The ice deflection and velocity potential are then expressed in terms of integral quadratures. These integrals often have rapid convergence and, where this is not the case, techniques were outlined to improve the convergence. Hence, the numerical computation involved was relatively minimal, even for the three–dimensional formulations. Although we have focused on ice clamping boundary conditions, it is important to note that the methods used could also solve free edge conditions without increase in difficulty.

The linear superposition of the incident and reflected waves reduces the boundary value problems such that we are solving for an unknown extra function which governs the ice and fluid behaviour in the vicinity of the structure. This gives clarity to

the problem and later allows us to analyse the contribution from each part of the solution. The integral transform solution method leads to simple expressions for the forces on the structure. Through eliminating a singularity in Fourier space, we were able to define algebraic expressions for the third derivative of the ice deflection, giving the vertical shear force. This allows us to sidestep the convergence difficulties that may have arisen from evaluating such a derivative. The method also allows simple expressions for the horizontal force (as well as for the phase shift between the incident and reflected waves) to be defined which may then be studied easily.

For the nonlinear study of Chapter 6, a solution is found by application of Green's second identity to a suitable Green's function. The numerical procedure and solution are based on that of Părău & Vanden-Broeck (2011) and Forbes (1989), where a boundary element method is utilised and finite difference techniques are applied. While computationally intense, the Green's theorem / boundary element approach is a powerful method which adeptly deals with the complicated nonlinear fluid equations. The solution is not exact but may be computed to extreme accuracy.

Many results describing the features of the ice–structure problems were presented. Primarily the focus was on the following:

- The ice deflection field caused by the reflection or diffraction of hydroelastic waves
- The strain in the ice sheet due to the curvature caused by these waves
- The vertical lifting force caused by the waves, which exists due to the ice being frozen to the structure
- The horizontal force on the wall caused by the waves.

Detailed conclusions and summaries may be found at the end of each chapter, and we therefore only discuss broad trends and the salient conclusions of each chapter here.

For Chapter 2, we considered hydroelastic incident waves propagating towards a vertical wall in two dimensions. The ice was frozen to the wall which introduces a specific effect on the ice deflection. The deflection and slope of the ice are both zero at the ice–wall boundary, restricting the motion of the ice sheet in the vicinity of the structure. The first wave peak nearest the wall was diminished, and there is disturbance in subsequent waves due to interaction with the wall. The deflection pattern was shown to depend more on ice thickness than on the finite fluid depth. The strain in the ice sheet was shown to be roughly 2–3 times higher in magnitude at the ice–wall connection point than far from the wall. However, it was shown that the ice–clamping condition can be maintained provided the amplitude of the incident wave is small enough. The strain also sensitively depends on the incident wavenumber k. The value of k also effects the vertical and horizontal forces. The vertical force on the wall is in general higher for short waves than for long waves,

whereas the opposite is true for the horizontal force. In general the horizontal and shear forces are similar in magnitude, and they may reach substantial quantity.

Chapter 3 extended the study to three dimensions, solving the problem of hydroelastic wave diffraction by a vertical cylinder. We conclude that for long incident waves, the cylinder has a small effect on the wave pattern as it passes the cylinder. This is due to the cylinder radius being generally small in comparison with the incident wavelength. For shorter waves, there is much more pronounced disturbance due to wave reflection and evanescent outgoing waves from the cylinder. In particular, the deflection is diminished in the wake of the cylinder. The strain in the ice due to the ice–clamping condition can reach high levels, particularly at $\theta = \pi$, the direction from which the incident wave approaches. We conclude that the ice is unlikely to remain frozen to the cylinder unless the wave amplitudes are only several millimetres, or if the wavelength is long. The vertical and horizontal forces were shown to depend on a number of parameters. They were both highest at $\theta = \pi$, and behind the cylinder the forces were smaller by up to half. Other dependences on the cylinder radius b and the ice thickness were investigated. Once again we note that the wave forces on the cylinder can reach surprisingly high magnitude.

In Chapter 4 we adopt a two–layer fluid model, motivated by density stratification that often occurs underneath an ice sheet. This entails two free surfaces; one at the ice–cover and the other at the interface between the two fluid layers. The dispersion relation has two modes corresponding to a surface wavenumber (characterised by longer, smaller–amplitude waves) and an interfacial wavenumber (characterised by larger–amplitude short waves). It is shown that after wave reflection by the wall, incident interfacial waves can generate waves in the ice cover, and vice versa. Further, waves of either mode may propagate at either free surface under various conditions. The effect this two–layer formulation has on the strain in the ice and forces on the wall was analysed. It is concluded that if stratification exists and the two fluids have distinct densities then the effect of the stratification should not be ignored.

We consider the linear formulation of waves generated by a moving load on an ice sheet near a vertical wall in Chapter 5. A simple viscoelastic model was introduced to account for wave attenuation in the ice sheet. It is well documented that the wave profiles depend on the speed of the moving load, and whether this speed is above or below the critical speed c_{min}. In the elastic limit the deflection is unbounded at c_{min}, but the viscoelastic formulation renders a finite response there. Speculation from other authors regarding a potential second critical speed is not shared by the present study and we report only one critical speed c_{min}. The load speed that produces maximum ice deflection is perturbed slightly above c_{min} due to the viscoelasticity. For any given speed, the position of maximum deflection lags slightly behind the load. Close proximity of the load to the wall causes damped wave deflection due to the ice–clamping condition. The introduction of a vertical wall means that for faster load speeds we observe disturbance due to wave reflection and trapping. Whether

the moving load will fracture the ice–wall connection depends on the mass and speed of the load, together with its distance from the wall. Various parameter changes were analysed using the data set of Takizawa (1985), taken from a frozen lake in Japan.

The same problem was studied in Chapter 6 with fully nonlinear fluid equations. The model also uses a more sophisticated expression for the moving pressure. The solution displayed the same traits as its linear counterpart. The two models behave slightly differently as the load is moved close to the wall, with the nonlinear theory predicting increased deflection in the wake of the load. The trapped wave phenomenon observed in the linear formulation (for high load speeds) was also observed in the nonlinear formulation. Direct comparison between models showed excellent agreement in the shape and magnitude of the surface response. For faster speeds the agreement is slightly worse towards the edges of the grid, though it is hard to say which of the differences between the two models is responsible.

In conclusion, the present study helps elucidate the numerous factors that govern hydroelastic wave interaction with structures. The rigorous formulation and solution of the pertinent boundary value problems means that all aspect of the wave interaction can be described. Results for the ice deflection and incited forces are expected to assist in the wave–consideration aspect of designing structures to be built in ice–covered regions.

7.2 Future work

There are a multitude of options when considering enhancement of the models used here. The introduction of vertical boundaries meant it was necessary to apply certain simplifications to facilitate concise solutions. We may for example replace the assumption that the ice has constant thickness, and investigate the effect of an ice sheet of varying thickness. Similarly the effect of variable bottom topography has been included by several authors and could be applied to the present problem. The assumption of non–zero draught could also be studied and its validity assessed. The mathematical theory for these suggestions is already in place, though their inclusion in wave–structure interaction problems would present a challenge.

Regarding ice–structure interaction in three dimensions, one problem that warrants study is a multiple–cylinder model, representing structures that have more than one support. We expect that some wave trapping may occur between the cylinders, in view of the work done in water wave scattering theory. A multipole approach may be necessary to solve the problem, or we may exploit the rapid decay of the function Q in the solution of Chapter 3 to consider each cylinder independently. Free edge conditions must be considered in addition to the clamped–ice condition, bearing in mind the conclusions of Chapter 3.

Alternatively we may envisage a situation where an ice sheet is partially frozen to a vertical cylinder; that is, free edge conditions for a prescribed interval of θ

and clamped edge conditions elsewhere. Matching across these mixed boundary conditions would mean the problem would be challenging to solve. A related problem is also relevant: considering a non-continuous ice sheet, so that the ice only partially covers the free surface. Further research must certainly be made into the fracture process of ice, to improve the naive assumption we use that the yield strain has a constant value. Investigation must be made into the variety of factors that affect ice fracture.

One problem plaguing hydroelasticity from a broad standpoint is the paucity of realistic field experiments that have been conducted on waves in ice sheets or ice floes, something which must be rectified in future to ensure that the theory is credible. For the particular theory of ice–structure interaction, forces due to the crushing of ice into a structure have been studied experimentally, but not forces due to waves in ice.

Other inhomogeneous aspects of the ice must be taken into account for the accuracy of the models to improve. Although the thin plate equation has been proven to be accurate in certain circumstances, for others the assumptions of small–deflection theory may prove inappropriate. A more sophisticated plate equation, incorporating the effect of thick ice, shear stresses or nonlinear effects must be adopted. Further, we could include a viscous layer on the underside of the ice sheet, modelling the semi–frozen slush that accumulates there. It is certain that such changes would require more advanced solution methods. The development of numerical methods such as finite or boundary element methods is likely to play a large role in the future of hydroelastic research. Nonlinear effects of either the ice sheet or the fluid motion may be of crucial importance to the problems studied here and elsewhere within hydroelasticity.

Bibliography

Abramowitz M. & Stegun I., 1972. *Handbook of mathematical functions with formulas, graphs and mathematical tables*. Dover Publications.

Andrianov A., 2005. *Hydroelastic Analysis of Very Large Floating Structures*. Ph.D. thesis, Delft University of Technology, The Netherlands.

Andrianov A. & Hermans A., 2003. The influence of water depth on the hydroelastic response of a very large floating platform. *Marine Structures*, 16:355–371.

Arrigo K., van Dijken G., Ainley D., Fahnestock M. & Markus T., 2002. Ecological impact of a large antarctic iceberg. *Geophys. Res. Letters*, 29(7):1104.

Ashton G., 1986. *River and lake ice engineering*. Water Resources Pubns.

Athanassoulis M. & Belibassakis K., 2009. A novel coupled-mode theory with application to hydroelastic analysis of thick, non-uniform floating bodies over general bathymetry. *Proceedings of the Institution of Mechanical Engineers, Part M: Journal of Engineering for the Maritime Environment*, 223(3):419–438.

Balmforth N. & Craster R., 1999. Ocean waves and ice sheets. *J. Fluid Mech.*, 395(1):89–124.

Barrett M. & Squire V., 1996. Ice-coupled wave propagation across an abrupt change in ice rigidity, density, or thickness. *Journal of Geophysical Research*, 101(C9):20825–20832.

Bates H. & Shapiro L., 1980. Long–period gravity waves in ice–covered sea. *J. Geophys. Res.*, 85(C2):1095–1100.

Battisti L., Fedrizzi R., Brighenti A. & Laakso T., 2006. Sea ice and icing risk for offshore wind turbines. In *Proceedings of the OWEMES*, pages 20–22.

Belibassakis K. & Athanassoulis G., 2005. A coupled-mode model for the hydroelastic analysis of large floating bodies over variable bathymetry regions. *J. Fluid. Mech.*, 531:221–250.

Bennetts L., 2007. *Wave scattering by ice sheets of varying thickness*. Ph.D. thesis, University of Bristol, England.

Bennetts L., Peter M., Squire V. & Meylan M., 2010. A three-dimensional model of wave attenuation in the marginal ice zone. *J. Geophys. Res*, 115:C12043.

Bennetts L. & Squire V., 2009. Wave scattering by multiple rows of circular ice floes. *J. Fluid Mech.*, 639(1):213–238.

Bennetts L. & Squire V., 2010. Linear wave forcing of an array of axisymmetric ice floes. *IMA J. App. Math.*, 75(1):108–138.

Bennetts L. & Williams T., 2010. Wave scattering by ice floes and polynyas of arbitrary shape. *J. Fluid Mech.*, 662:5–35.

Bennetts L., Williams T. & Squire V., 2009. An approximation to wave scattering by an ice polynya. In *Proceedings 24th International Workshop on Water Waves and Floating Bodies. University of East Anglia, Zelenogorsk, Russia*, page 4.

Bhattacharjee J. & Guedes-Soares C., 2012. Flexural gravity waves over a floating ice sheet near a vertical wall. *J. Eng. Math.*, 75:29–48.

Bhattacharjee J. & Sahoo T., 2008. Flexural gravity wave problems in two-layer fluids. *Wave Motion*, 45(3):133–153.

Blyth M., Părău E. & Vanden-Broeck J.M., 2011. Hydroelastic waves on fluid sheets. *Journal of Fluid Mechanics*, 689:541–551.

Bonnefoy F., Meylan M. & Ferrant P., 2009. Nonlinear higher-order spectral solution for a two-dimensional moving load on ice. *J. Fluid Mech.*, 621(1):215–242.

Bowman F., 1958. *Introduction to Bessel functions*. Dover Publications.

Bracewell R., 1999. *The Fourier Transform & Its Applications*. McGraw-Hill, third edition.

Brevdo L. & Il'ichev A., 2006. Uni-modal destabilization of a visco-elastic floating ice layer by wind stress. *European Journal of Mechanics-A/Solids*, 25(3):509–525.

Brocklehurst P., Korobkin A. & Părău E., 2010. Interaction of hydro-elastic waves with a vertical wall. *J. Eng. Math.*, 68:215–231.

Brocklehurst P., Korobkin A. & Părău E., 2011. Hydroelastic wave diffraction by a vertical cylinder. *Phil. Trans. Roy. Soc. Lond. A*, 369:2832–2851.

Cammaert A. & Muggeridge D., 1988. *Ice interaction with offshore structures*. Van Nostrand Reinhold Co. Inc., New York, NY.

Chakrabarti A., Ahluwalia D. & Manam S., 2003. Surface water waves involving a vertical barrier in the presence of an ice cover. *Int. Journal of Eng. Sci.*, 41:1145–1162.

Chung H. & Fox C., 2002. Calculation of wave-ice interaction using the wiener-hopf technique. *New Zealand J. Math*, 31(1):1–18.

Chung H. & Linton C., 2005. Reflection and transmission of waves across a gap between two semi-infinite elastic plates on water. *Quart. J. Mech. Appl. Math.*, 58:1–15.

Crocker R.M.G., 1992. Ice floe collisions interpreted from accelerometer data during limex. *Atmos. -Ocean*, 30(2):246–269.

Croteau P., 1983. *Dynamic interactions between floating ice and offshore structures*. Ph.D. thesis, Univ. of California, Berkeley, CA, USA.

Czipott P., Levine M., Paulson C., Menemenlis D., Farmer D. & Williams R., 1991. Ice flexure forced by internal wave packets in the arctic ocean. *Science*, 254:832–834.

Davys J., Hosking R. & Sneyd A., 1985. Waves due to a steadily moving source on a floating ice plate. *J. Fluid Mech.*, 158:269–287.

Downer J. & Haskell T., 2001. Ice-floe kinematics in the ross sea marginal ice zone using gps and accelerometers. *Annals of Glaciology*, 33(1):345–349.

Duffy D., 1996. On the generation of internal waves beneath sea ice by a moving load. *Cold Reg. Sci. Tech.*, 24(1):29–39.

Dumont D., Kohout A. & Bertino L., 2011. A wave-based model for the marginal ice zone including a floe breaking parameterization. *J. Geophys. Res*, 116:C04001.

Ehrenmark U. & Porter D., 2012. Water wave scattering by a floating elastic plate over a plane incline. *Quart. J. Mech. App. Math.*, 65(3):409–434.

El-Reedy M., 2012. *Offshore Structures: Design, Construction and Maintenance*. Gulf Professional Publishing.

Emmerhoff O. & Sclavounos P., 1992. The slow-drift motion of arrays of vertical cylinders. *J. Fluid Mech.*, 242:31–50.

Emmerson C. & Lahn G., 2012. *Arctic Opening: Opportunity and Risk in the High North*. Lloyds, Chatham House.

Evans D. & Davies T., 1968. Wave-ice interaction. Technical Report 1313, New Jersey:Davidson Lab, Stevens Inst. of Tech.

Evans D. & Porter R., 2003. Wave scattering by narrow cracks in ice sheets floating on water of finite depth. *J. Fluid Mech.*, 484:143–165.

Ewing M. & Crary A., 1934. Propagation of elastic waves in ice, ii. *Physics*, 5:181–184.

Fletcher N., 1970. *The Chemical Physic of Ice*. Cambridge University Press.

Forbes L., 1986. Surface waves of large amplitude beneath an elastic sheet. part 1. high-order series solution. *J. Fluid Mech*, 169:409–428.

Forbes L., 1988. Surface waves of large amplitude beneath an elastic sheet. part 2. galerkin solution. *J. Fluid Mech.*, 188(1):491–508.

Forbes L., 1989. An algorithm for 3-dimensional free-surface problems in hydrodynamics. *J. Comp. Phys.*, 82:330–347.

Fox C. & Squire V., 1990. Reflection and transmission characteristics at the edge of shore fast sea ice. *J. Geophys. Res.*, 95:11629–11639.

Fox C. & Squire V., 1991a. Coupling between an ocean and an ice shelf. *Ann. Glaciol.*, 15:101–108.

Fox C. & Squire V., 1991b. Strain in shore fast ice due to incoming ocean waves and swell. *J. Geophys. Res.*, 96(C3):4531–4547.

Fox C. & Squire V., 1994. On the oblique reflexion and transmission of ocean wave at shore fast sea ice. *Phil. Trans. R. Soc. Lond. A*, 347:185–218.

Frankenstein G. & Garner R., 1967. Equations for determining the brine volume of sea ice from -0.5c to -22.9c. *J. Glaciology*, 6:934–944.

Glen J., 1987. Fifty years of progress in ice physics. *Journal of Glaciology*, Special Issue:52–59.

Goodman D., Wadhams P. & Squire V., 1980. The flexural response of a tabular ice island to ocean swell. *Annals of Glaciology*, 1:23–27.

Gradshteyn I. & Ryzhik I., 2007. *Table of Integrals, Series, and Products*. Academic Press (Elsevier), seventh edition.

Gravesen H., Petersen B., Søresen S. & Vølund P., 2003. Ice forces on wind turbine foundations in denmark. In *Proceedings of the International Conference on Port and Ocean Engineering under Arctic Conditions*, 17.

Gravesen H., Sørensen S., Vølund P., Barker A. & Timco G., 2005. Ice loading on danish wind turbines: Part 2. analyses of dynamic model test results. *Cold regions science and technology*, 41(1):25–47.

Greenhill A., 1887. Wave motion in hydrodynamics. *Am. J. Math.*, 9:62–112.

Griggs J. & Bamber J., 2011. Antarctic ice–shelf thickness from satellite radar altimetry. *Journal of Glaciology*, 57:485–498.

Gürtner A., 2009. *Experimental and Numerical Investigations of Ice-Structure Interaction*. Ph.D. thesis, Norwegian University of Science and Technology, Norway.

Hassan M., Meylan M. & Peter M., 2009. Water-wave scattering by submerged elastic plates. *Quart. J. Mech. App. Math.*, 62(3):321–344.

Hegarty G. & Squire V., 2004. On modelling the interaction of large amplitude waves with a solitary floe. In *Proceedings of the 14th international offshore and polar engineering conference*, volume 1, pages 845–850.

Hegarty G. & Squire V., 2008. A boundary-integral method for the interaction of large-amplitude ocean waves with a compliant floating raft such as a sea-ice floe. *J. of Eng. Math.*, 62(4):355–372.

Hendrickson J. & Webb L., 1963. Theoretical investigation of semi-infinite ice floes in water of infinite depth. *Rep. NBy–32225,Natl. Engng. Sci. Co., Pasadena, CA*.

Hosking R., Sneyd A. & Waugh D., 1988. Viscoelastic response of a floating ice plate to a steadily moving load. *J. Fluid. Mech.*, 196:409–430.

Hunkins K., 1962. Waves on the arctic ocean. *J. Geophys. Res.*, 67:2477–2489.

Ikebe T., 1960. Eigenfunction expansions associated with the schroedinger operators and their applications to scattering theory. *Archive for Rational Mechanics and Analysis*, 5(1):1–34.

ISO19906, 2010. *Petroleum and natural gas industries: Arctic offshore structures*. BSI.

Jeffrey A., 2002. *Advanced Engineering Methods*. Harcourt / Academic Press.

Jordaan I., 2001. Mechanics of ice-structure interaction. *Engineering Fracture Mechanics*, 68(17-18):1923–1960.

Karr D., Troesch A. & Wingate W., 1993. Nonlinear dynamic response of a simple ice-structure interaction model. *Journal of Offshore Mechanics and Arctic Engineering*, 115(4):246–252.

Kashiwagi M., 1998. A new solution method for hydroelastic problems of a very large floating structure in waves. In *OMAE 1998: 17th International Conference on Offshore Mechanics and Arctic Engineering*, page 1998.

Kashiwagi M., 2000. Research on hydroelastic responses of vlfs: recent progress and future work. *Int. J. Off. Pol. Eng.*, 10(2):81–90.

Keller J., 1998. Gravity waves on ice-covered water. *J. Geophys. Res.*, 103:7663–7669.

Kerr A., 1976. The bearing capacity of floating ice plates subjected to static or quasi-static loads. *Journal of Glaciology*, 17(76).

Kerr A. & Haynes F., 1988. On the determination of the average young's modulus for a floating ice cover. *Cold Reg.Sci. Tech.*, 15(1):39–43.

Kerr A. & Palmer W., 1972. The deformations and stresses in floating ice plates. *Acta Mech.*, 15:57–72.

Khabakhpasheva T. & Korobkin A., 2002. Hydroelastic behaviour of compound floating plate in waves. *J. Eng. Math.*, 44(1):21–40.

Kim J. & Ertekin R., 1998. An eigenfunction-expansion method for predicting hydroelastic behavior of a shallow-draft vlfs. In *Proceedings of the 2nd International Conference on Hydroelasticity in Marine Technology*, pages 47–59.

Kohout A. & Meylan M., 2008. An elastic plate model for wave attenuation and ice floe breaking in the marginal ice zone. *J. Geophys. Res*, 113:C09016.

Korobkin A., 2000. Unsteady hydroelasticity of floating plates. *Journal of Fluids and Structures*, 14(7):971–991.

Korobkin A., Părău E. & Vanden-Broeck J., 2011. The mathematical challenges and modelling of hydroelasticity. *Phil. Trans. Roy. Soc. Lond. A*, 369(1947):2803–2812.

Kouzov D., 1963a. Diffraction of a plane hydro–acoustic wave on the boundary of two elastic plates. *Prikl. Mat. Mekh*, 27:541–546.

Kouzov D., 1963b. Diffraction of a plane hydroelastic wave at a crack in an elastic plate. *Prikl. Mat. Mekh*, 27:1037–1043.

Kwok R., Cunningham G., Wensnahan M., Rigor I., Zwally H., Yi D. et al., 2009a. Thinning and volume loss of the arctic ocean sea ice cover: 2003–2008. *J. Geophys. Res*, 114(C7):C07.

Kwok R., Rothrock D. et al., 2009b. Decline in arctic sea ice thickness from submarine and icesat records: 1958–2008. *Geophys. Res. Lett.*, 36(15):L15501.

Lamb H., 1932. *Hydrodynamics 6th ed.*. Cambridge University Press.

Lange M., 1989. Development of sea ice in the weddell sea. *Annals of Glaciology*, 12:92–96.

Lewis E. & Walker E., 1970. The water structure under a growing sea ice sheet. *J. Geophys. Res.*, 75(33):6836–6845.

Linton C. & Chung H., 2003. Reflection and transmission at the ocean/sea-ice boundary. *Wave motion*, 38(1):43–52.

Linton C. & Evans D., 1990. The interaction of waves with arrays of vertical circular cylinders. *J. Fluid Mech.*, 215(1):549–569.

Linton C. & McIver M., 1995. The interaction of waves with horizontal cylinders in two-layer fluids. *J. Fluid Mech.*, 304(1):213–229.

Linton C. & McIver P., 2001. *Mathematical techniques for wave/structure interactions*. Chapman and Hall/CRC.

Lucas S., 1995. Evaluating infinite integrals involving products of bessel functions. *J. Comp. Appl. Math.*, 64:269–282.

Malenica S. & Korobkin A., 2003. Water wave diffraction by vertical circular cylinder in partially frozen sea. *Proc. 18th International Workshop on Water Waves and Floating Bodies, LeCroisic, France.*

Marchenko A., 1996. Swell wave propagation in an inhomogeneous ice sheet. *Fluid Dynamics*, 31(5):761–767.

Marchenko A., 1997. Flexural-gravity wave diffraction at linear irregularities in sheet ice. *Fluid Dynamics*, 32(4):548–560.

Marchenko A. & Voliak K., 1997. Surface wave propagation in shallow water beneath an inhomogeneous ice cover. *Journal of Physical Oceanography*, 27(8):1602–1613.

Marko J., 2003. Observations and analyses of an intense waves-in-ice event in the sea of okhotsk. *J. Geophys. Res*, 108:3296.

Martin S. & Becker P., 1987. High–frequency ice floe collisions in the greenland sea during the 1984 marginal ice zone experiment. *J. Geophys. Res.*, 92(C7):7071–7084.

Martin S. & Becker P., 1988. Ice floe collisions and relation to ice deformation in the bering sea. *J. Geophys. Res.*, 93(C2):1303–1315.

Martin S. & Kauffman P., 1981. A field and laboratory study of wave damping by grease ice. *J. Glaciol.*, 27(96):283–313.

Masuda K. & Miyazaki T., 1999. A study on estimation of wave exciting forces on floating structure under tsunami. *Proc 3rd Int Wksp Very Large Floating Structures, Honolulu, Hawaii, USA, September*, pages 22–24.

Matlock H., Dawkins W. & Panak J., 1969. A model for the prediction of ice-structure interaction. In *Offshore Technology Conference.*

Matlock H., Dawkins W. & Panak J., 1971. Analytical model for ice-structure interaction. *J. Eng. Mech. Div.*, 97(4):1083–1092.

McCamy R., 1954. Wave forces on a pile: a diffraction theory. Technical Report 69, U.S. Army Corp. of Engineers.

Mei C., 1983. *The Applied Dynamics of Ocean Surface Waves.* John Wiley and Sons.

Menemenlis D., Farmer D. & Czipott P., 1995. A note on infragravity waves in the arctic ocean. *J. Geophys. Res.*, 100:7089–7093.

Meylan M., 2002. Wave response of an ice floe of arbitrary geometry. *J. Geophys. Res.*, 107(1).

Meylan M., Hazard C. & Loret F., 2004. Linear time-dependent motion of a two-dimensional floating elastic plate in finite depth water using the laplace transform. In *Proceedings 19th International Workshop on Water Waves and Floating Bodies, Cortona, Italy.*

Meylan M. & Masson D., 2006. A linear boltzmann equation to model wave scattering in the marginal ice zone. *Ocean Modelling*, 11(3):417–427.

Meylan M. & Squire V., 1993a. A model for the motion and bending of an ice floe in ocean waves. *Proc. 3rd. Int. Offshore and Polar Eng. Conf., Golden, Colo.*, II:718–723.

Meylan M. & Squire V., 1993b. A model for the motion and bending of an ice floe in ocean waves. *Int. J. Offshore Polar Eng.*, 3(4):322–323.

Meylan M. & Squire V., 1994. The response of ice floes to ocean waves. *J. Geophys. Res.*, 99:891–900.

Meylan M. & Sturova I., 2009. Time-dependent motion of a two-dimensional floating elastic plate. *Journal of Fluids and Structures*, 25(3):445–460.

Milinazzo F., Shinbrot M. & Evans N., 1995. A mathematical analysis of the steady response of floating ice to the uniform motion of a rectangular load. *Journal of Fluid Mechanics*, 287:173–197.

Mohapatra S. & Bora S., 2009. Propagation of oblique waves over small bottom undulation in an ice-covered two-layer fluid. *Geophysical and Astrophysical Fluid Dynamics*, 103(5):347–374.

Mollazadeh M., Khanjani M. & Tavakoli A., 2011. Applicability of the method of fundamental solutions to interaction of fully nonlinear water waves with a semi-infinite floating ice plate. *Cold Reg. Sci. Tech.*

Montiel F., Bonnefoy F., Bennetts L., Squire V., Ferrant P. & Marsault P., 2011. Experimental validation of a linear numerical model for the water wave scattering by a compliant floating disk. In *Proc. 26th Int. Workshop on Water Waves and Floating Bodies, Athens, Greece*, pages 17–20.

Muzylev S., 2007. Internal waves under an ice cover. *Oceanology*, 418:145–148.

Newman J., 1997. *Marine Hydrodynamics*. The MIT Press, Cambridge, USA.

Nzokou F., Morse B. & Quach-Thanh T., 2009. River ice cover flexure by an incoming wave. *Cold Reg. Sci. Tech.*, 55(2):230–237.

Ogasawara T. & Sakai S., 2006. Numerical analysis of the characteristics of waves propagating in arbitrary ice-covered sea. *Annals of Glaciology*, 44(1):95–100.

Oliver J., Crary A. & Cotell R., 1954. Elastic waves in arctic pack ice. *Eos Trans. AGU*, 35:282–292.

Omer Jr G. & Hall H., 1949. The scattering of a tsunami by a cylindrical island. *Bulletin of the Seismological Society of America*, 39(4):257–260.

Părău E. & Dias F., 2002. Nonlinear effects in the response of a floating ice plate to a moving load. *J. Fluid Mech.*, 460:281–305.

Părău E. & Vanden-Broeck J.M., 2011. Three-dimensional waves beneath an ice sheet due to a steadily moving pressure. *Phil. Trans. R. Soc*, 369:2973–2988.

Părău E., Vanden-Broeck J.M. & Cooker M., 2007. Three-dimensional capillary-gravity waves generated by a moving disturbance. *Phys. fluids*, 19:082102.

Peake N., 2001. Nonlinear stability of a fluid-loaded elastic plate with mean flow. *J. Fluid Mech.*, 434:101–118.

Peter M. & Meylan M., 2004. Infinite-depth interaction theory for arbitrary floating bodies applied to wave forcing of ice floes. *J. Fluid Mech.*, 500:145–167.

Peter M. & Meylan M., 2009. Water-wave scattering by vast fields of bodies. *SIAM J. App. Math.*, 70(5):1567.

Peter M., Meylan M. & Chung H., 2004. Wave scattering by a circular elastic plate in water of finite depth: a closed form solution. *Int. J. Offshore Polar Eng.*, 14(2):81–85.

Peters A., 1950. The effect of a floating mat on water waves. *Commun. Pure Appl. Maths*, 3:319–354.

Phillips O., 1977. *The dynamics of the upper ocean.* Cambridge University Press, 2nd edition.

Plotnikov P. & Toland J., 2011. Modelling nonlinear hydroelastic waves. *Phil. Trans. Roy. Soc. Lond. A*, 369(1947):2942–2956.

Porter D. & Porter R., 2004. Approximations to wave scattering by an ice sheet of variable thickness over undulating bed topography. *J. Fluid Mech.*, 509(1):145–179.

Porter R. & Evans D., 2007. Diffraction of flexural waves by finite straight cracks in an elastic sheet over water. *Journal of Fluids and Structures*, 23(2):309–327.

Povzner A., 1953. On the expansion of arbitrary functions in characteristic functions of the operator -δu+cu. *Matematicheskii Sbornik*, 74(1):109–156.

Press F., Crary A., Oliver J. & Katz S., 1951. Air–coupled flexural waves in floating ice. *Eos Trans. AGU*, 32:166–172.

Press F. & Ewing M., 1951. Propagation of elastic waves in a floating ice sheet. *Eos Trans. AGU*, 32:673–678.

Prinsenberg S. & Peterson I., 2011. Observing regional-scale pack-ice decay processes with helicopter-borne sensors and moored upward-looking sonars. *Annals of Glaciology*, 52(57):35–42.

Rayleigh L., 1883. The form of standing waves on the surface of running water. *Proc. Lond. Math. Soc.*, 15:69–78.

Robin G., 1963. Wave propagation through fields of pack ice. *Phil. Trans. R. Soc. Lond. A*, 255:313–339.

Rottier P., 1992. Floe pair interaction event rates in the marginal ice zone. *J. Geophys. Res.*, 97(C6):9391–9400.

Sahoo T., Yip T. & Chwang A., 2001. Scattering of surface waves by a semi-infinite floating elastic plate. *Physics of Fluids*, 13:3215.

Sanderson T., 1988. *Ice mechanics and risks to offshore structures.* Kluwer Academic Publishers, Norwell, MA.

Schulkes R., Hosking R. & Sneyd A., 1987. Waves due to a steadily moving source on a floating ice plate. part 2. *J. Fluid. Mech.*, 180:297–318.

Schulkes R. & Sneyd A., 1988. Time-dependent response of floating ice to a steadily moving load. *Journal of Fluid Mechanics*, 186:25–46.

Schulz-Stellenfleth J. & Lehner S., 2002. Spaceborne synthetic aperture radar observations of ocean waves travelling into sea ice. *J. Geophys. Res*, 107(C8):10–1029.

Serreze M., Holland M. & Stroeve J., 2007. Perspectives on the arctic's shrinking sea-ice cover. *Science*, 315(5818):1533–1536.

She Y., Tanekou F., Hicks F., Morse B., Keller D., Abarca N., Krath C., Nolin S., Stander E., Andrishak R. et al., 2007. Ice jam formation and release events on the athabasca river, 2007. *Proceedings of the 14th Workshop on River Ice. 20-22 June 2007, Quebec City.*

Spring B. & Monkmeyer P., 1974. Interaction of plane waves with vertical cylinders. In *Proceeding of the Fourteenth International Conference on Coastal Engineering*, pages 1828–1847.

Squire V., 1984a. How waves break up inshore fast ice. *Polar Rec.*, 22(138):281–285.

Squire V., 1984b. On the critical angle for waves entering shore fast ice. *Cold Reg. Sci. Tech.*, 10(1):59–68.

Squire V., 1984c. Sea ice. *Sci. Prog. Oxford*, 69:19–43.

Squire V., 1984d. A theoretical, laboratory and field study of ice–coupled waves. *J. Geophys. Res.*, 89(C5):8069–8079.

Squire V., 1993a. The breakup of shore fast sea ice. *Cold Reg. Sci. and Tech.*, 21:211–218.

Squire V., 1993b. A comparison of the mass–loading and elatic–plate models of an ice field. *Cold Reg. Sci. and Tech.*, 21:219–229.

Squire V., 2007. Of ocean waves and sea ice revisited. *Cold Reg. Sci. and Tech.*, 49(2):110–133.

Squire V., 2008. Synergies between vlfs hydroelasticity and sea ice research. *Int. J. Offshore Polar Eng.*, 18(4):241–253.

Squire V., 2011. Past, present and impendent hydroelastic challenges in the polar and subpolar seas. *Phil. Trans. Roy. Soc. Lond. A*, 369(1947):2813–2831.

Squire V. & Dixon T., 2000. An analytical model for wave propagation across a crack in an ice sheet. *International Journal of Offshore and Polar Engineering*, 10:173–176.

Squire V. & Dixon T., 2001. How a region of cracked sea ice affects ice-coupled wave propagation. *Annals of Glaciology*, 33(1):327–332.

Squire V., Dugan J., Wadhams P., Rottier P. & Liu A., 1995. Of ocean waves and ice sheets. *Annu. Rev. Fluid Mech.*, 27:115–168.

Squire V. & Fox C., 1992. On ice–coupled waves: a comparison of data and theory. *Advances in Ice technology, Proc. 2nd Int. Conf. on Ice. Tech., Boston: Comp. Mech.*, pages 269–280.

Squire V., Hosking R., Kerr A. & Langhorne P., 1996. *Moving Loads on Ice Plates.* Kluwer Academic Publishers.

Squire V. & Martin S., 1980. A field study of the physical properties, response to swell, and subsequent fracture of a single ice floe in the winter bering sea. Technical Report 18, Univ. Wash. Sci.

Squire V., Robinson W., Langhorne P. & Haskell T., 1988. Vehicles and aircraft on floating ice. *Nature*, 333:159–161.

Squire V., Rottier P. & Fox C., 1994. A first look at some wave-ice interaction data from mcmurdo sound, antarctica. In *In Sea Ice Observations and Modelling - Proceedings of the 93's International Symposium on Sea Ice. Y. Zhouwen, C.L. Tang, R.H. Preller, W. Huiding eds China Ocean Press, Beijing*, pages 19–33.

Stewart J., 2011. *Multivariable calculus*. Thomas Brookes/Cole, seventh edition.

Stoker J., 1957. *Water Waves*. Interscience Publishers Inc.

Stroeve J., Holland M., Meier W., Scambos T. & Serreze M., 2007. Arctic sea ice decline: Faster than forecast. *Geophysical Research Letters*, 34(9):9501.

Sturova I., 1999. Oblique incidence of surface waves on an elastic strip. *Zh. Prikl. Mekh. Tekh. Fiz*, 40(4):62–68.

Sturova I., 2009. Time-dependent response of a heterogeneous elastic plate floating on shallow water of variable depth. *J. Fluid Mech.*, 637(1):305–325.

Sundararajan C. & Reddy D., 1973. Stochastic analysis of ice-structure interaction. In *Proceedings of the Second International Conference on Port and Ocean Engineering Under Arctic Conditions*.

Takizawa T., 1985. Deflection of a floating sea ice sheet induced by a moving load. *Cold Regions Sci. Tech.*, 11:171–180.

Teng B., Cheng L., Liu S. & Li F., 2001. Modified eigenfunction expansion methods for interaction of water waves with a semi-infinite elastic plate. *Applied Ocean Research*, 23(6):357–368.

Timco G. & Weeks W., 2010. A review of the engineering properties of sea ice. *Cold Reg. Sci. Tech.*, 60(2):107–129.

Timokov L. & Kheisin D., 1987. *Dynamics of sea ice*. Leningrad: Gidrometeoizdat.

Timoshenko S., Woinowsky-Krieger S. & Woinowsky S., 1959. *Theory of plates and shells*, volume 2. McGraw-hill New York.

Tkacheva L., 2001. Surface wave diffraction on a floating elastic plate. *Fluid Dyn.*, 36:776–789.

Tkacheva L., 2004. The diffraction of surface waves by a floating elastic plate at oblique incidence. *J. App. Math. Mech.*, 68(3):425–436.

Tsuchiya M., Kanie S., Ikejiri K., Ikejiri A. & Saeki H., 1985. An experimental study on ice-structure interaction. In *Offshore Technology Conference*.

Ugural A., 1981. *Stresses in Plates and Shells*. McGraw Hill Book Company.

Utsunomiya T., Watanabe E. & Taylor R., 1998. Wave response analysis of a box-like vlfs close to a breakwater. In *OMAE 1998: 17th International Conference on Offshore Mechanics and Arctic Engineering*, page 1998.

Vaughan G., Bennetts L. & Squire V., 2009. The decay of flexural-gravity waves in long sea ice transects. *Proc. Roy. Soc. Lond. A*, 465(2109):2785–2812.

Vaughan G. & Squire V., 2011. Wave induced fracture probabilities for arctic sea-ice. *Cold Reg. Sci. Tech.*

Ventsel E. & Krauthammer T., 2001. *Thin plates and shells: theory, analysis, and applications*. CRC.

Venturella M., Patil M. & McCue L., 2011. Modal analysis of the ice-structure interaction problem. *J. Offshore Mech. Arc. Eng.*, 133:041501.

Wadhams P., 1972. Measurement of wave attenuation in pack ice by inverted echo sounding. In *Sea Ice (Proceedings of an international conference), National Research Council, Rejkjavik, Iceland*, pages 255–260.

Wadhams P., 1973. Attentuation of swell by sea ice. *J. Geophys. Res.*, 78(18):3552–3563.

Wadhams P., 1975. Airborne laser profiling of swell in an open ice field. *J. Geophys. Res.*, 80(33):4520–4528.

Wadhams P., 1990. *Waves in frazil and pancake ice and their detection in seasat synthetic aperture radar imagery.* Ice Technology for Polar Operations, Computational Mechanics Publications.

Wadhams P., 2004. Recent observations on arctic ocean ice thickness. *Gayana (Concepción)*, 68(2):572–575.

Wadhams P. & Holt B., 1991. Waves in frazil and pancake ice and their detection in seasat synthetic aperture radar imagery. *J. Geophys. Res.*, 96:8835–8852.

Wang C. & Meylan M., 2002. The linear wave response of a floating thin plate on water of variable depth. *App. Ocean. Res.*, 24(3):163–174.

Wang C. & Meylan M., 2004. A higher-order-coupled boundary element and finite element method for the wave forcing of a floating elastic plate. *J. Fluids and Structures*, 19(4):557–572.

Wang R. & Shen H., 2010. Experimental study on surface wave propagating through a grease-pancake ice mixture. *Cold Reg. Sci. Tech.*, 61(2-3):90–96.

Watanabe E., Utsunomiya T. & Wang C., 2004. Hydroelastic analysis of pontoon-type vlfs: a literature survey. *Eng. Structures*, 26:245–256.

Weir P., Bennetts L. & Squire V., 2011. Nonlinear fem approach to the analysis of the hydroelastic behaviour of floating beams. In *The 10th International Conference on Mathematical and Numerical Aspects of Waves*, pages 189–192.

Weitz M. & Keller J., 1950. Reflection of water waves from floating ice in water of finite depth. *Commun. Pure Appl. Maths*, 3:305–318.

Williams T., Bennetts L., Dumont D., Squire V. & Bertino L., 2012. Towards the inclusion of wave-ice interactions in large-scale models for the marginal ice zone. *arXiv:1203.2981.*

Williams T. & Meylan M., 2011. The wiener–hopf and residue calculus solutions for a submerged semi-infinite elastic plate. *J. Eng. Math.*, pages 1–26.

Williams T. & Porter R., 2009. The effect of submergence on the scattering by the interface between two semi-infinite sheets. *Journal of Fluids and Structures*, 25(5):777–793.

Williams T. & Squire V., 2002. Ice coupled waves near a deep water tide crack or ice jetty. In *Ice in the Environment: Proceedings of the 16th IAHR International Symposium on Ice*, pages 318–326.

Williams T. & Squire V., 2004. Oblique scattering of plane flexural–gravity waves by heterogeneities in sea–ice. *Proc. Roy. Soc. Lond. A*, 460(2052):3469–3497.

Williams T. & Squire V., 2006. Scattering of flexural–gravity waves at the boundaries between three floating sheets with applications. *J. Fluid Mech.*, 569(1):113–140.

Williams T. & Squire V., 2008. The effect of submergence on wave scattering across a transition between two floating flexible plates. *Wave Motion*, 45(3):361–379.

Wilson J., 1958. *Moving loads on floating ice sheets*. University of Michigan Research Institute (UMRI Project 2432).

Wu C., Watanabe E. & Utsunomiya T., 1995. An eigenfunction expansion-matching method for analyzing the wave-induced responses of an elastic floating plate. *Applied Ocean Research*, 17(5):301–310.

Xia X. & Shen H., 2002. Nonlinear interaction of ice cover with shallow water waves in channels. *J. Fluid Mech.*, 467:259–268.

Xu F. & Lu D., 2009. An optimization of eigenfunction expansion method for the interaction of water waves with an elastic plate. *Journal of Hydrodynamics, Ser. B*, 21(4):526–530.

Zhestkaya V., 1999. Numerical solution of the problem of an ice sheet under a moving load. *J. App. Mech. and Tech. Phys.*, 40:770–775.